Understanding the Role of Human TRPV1 S1-S4 Membrane Domain in Temperature and Ligand Activation

by

Minjoo Kim

A Dissertation Presented in Partial Fulfillment
of the Requirements for the Degree
Doctor of Philosophy

Approved October 2019 by the
Graduate Supervisory Committee:

Wade D. Van Horn, Chair
Xu Wang
Wei Liu

ARIZONA STATE UNIVERSITY

December 2019

ABSTRACT

Transient receptor potential vanilloid member 1 (TRPV1) is a membrane protein ion channel that functions as a heat and capsaicin receptor. In addition to activation by hot temperature and vanilloid compounds such as capsaicin, TRPV1 is modulated by various stimuli including acidic pH, endogenous lipids, diverse biological and synthetic chemical ligands, and modulatory proteins. Due to its sensitivity to noxious stimuli such as high temperature and pungent chemicals, there has been significant evidence that TRPV1 participates in a variety of human physiological and pathophysiological pathways, raising the potential of TRPV1 as an attractive therapeutic target. However, the polymodal nature of TRPV1 function has complicated clinical application because the TRPV1 activation mechanisms from different modes have generally been enigmatic. Consequently, tremendous efforts have put into dissecting the mechanisms of different activation modes, but numerous questions remain to be answered.

The studies conducted in this dissertation probed the role of the S1-S4 membrane domain in temperature and ligand activation of human TRPV1. Temperature-dependent solution nuclear magnetic resonance (NMR) spectroscopy for thermodynamic and mechanistic studies of the S1-S4 domain. From these results, a potential temperature sensing mechanism of TRPV1, initiated from the S1-S4 domain, was proposed. Additionally, direct binding of various ligands to the S1-S4 domain were used to ascertain the interaction site and the affinities (K_d) of various ligands to this domain. These results are the first to study the isolated S1-S4 domain of human TRPV1 and many

results indicate that the S1-S4 domain is crucial for both temperature-sensing and is the general receptor binding site central to chemical activation.

Dedicated to my family and friends

ACKNOWLEDGEMENTS

My Ph.D. experience has been one of the most valuable experiences I have had, and without these people, the completion would not have been possible. I would like to really express my gratitude to my advisor, Dr. Wade Van Horn. He has been extremely supportive throughout my entire Ph.D. career, and has trained me to become a better scientist. I am also thankful for my committee members, Dr. Xu Wang and Dr. Wei Liu, for providing helpful feedback. I also want to acknowledge Dr. Julian Chen and Dr. Giovanna Ghirlanda for being very generous and giving me chance to show that I am capable of problem solving. I have had an opportunity to interact with many faculties in Personalized Diagnoistics at Biodesign, and would like to thank Dr. Joshua LaBaer for giving me opportunities to present my work in front of the audience that is outside of my field and providing kind words as my reference. I must acknowledge Dr. Chris Diehnelt and Dr. Rajeev Misra for teaching me the research.

I was lucky to have awesome lab mates to share this adventure with. My previous colleagues, now Dr. Jacob Hilton and Dr. Nicholas Sisco, were intelligent and hard-working scientists that provided good advice and encouragement over a number of years. My current colleagues, Dustin Luu, Camila Montano, Aerial Pratt and Mubark Mebret, have also been pleasure to work with. I would also like to thank Dr. Samrat Amin for nice chats during coffee break.

I would like to thank my family, especially my mother and my sister, for their support. They could never understand what I was experiencing, but they listened without scolding or judging. Every time when I faced major obstacles, they encouraged me to

continue pursuing this journey, and reminded me of the goals I want to achieve in my life. My friends, especially Kaylyn Riggs, Samantha Day and Melinda Fraser, also deserve acknowledgement because they told me I am doing great and I should never give up. Special gratitude goes to Raul Yanez, who helped me continue to pursue my other passion, jazz piano. Music occupied a major part during my PhD journey, and I would love to acknowledge Hiromi and Chick Corea for making heartfelt music that have been the driving force to spend countless hours on experiments and analysis.

Finally, I am grateful to have Daniel Jungkind, my dear partner. Even though he wasn't there the whole time, he lifted my mood in times of frustration, reminded me of my capability, and believed in me. I would also like to thank the Jungkinds for being generous and supportive.

TABLE OF CONTENTS

CHAPTER Page

CHAPTER Page

LIST OF TABLES

LIST OF FIGURES

CHAPTER 1

GENERAL INTRODUCTION

Higher organisms are surrounded by various stimuli. Detecting and responding to stimuli are crucial in biology to survive and adapt in the environment. At the molecular level, the transient receptor potential (TRP) ion channel superfamily is responsible for various sensations. TRP channels are widely expressed in various cells and tissues, and they are sensitive to various stimuli from temperature to chemical ligands. This ion channel superfamily is divided into subfamilies based on the homology [1]. In general, the architecture of TRP channels resembles that of voltage-gated potassium ion channels (VGICs), including six transmembrane helices. In VGICs, first four transmembrane helices (S1 through S4) form the voltage sensing domain (VSD), which corresponds to the S1-S4 domain, or voltage sensor-like domain in TRP channels. Following transmembrane helices, S5-S6, form the pore domain (PD). One common feature in TRP channels is a post S6 amphipathic helix, TRP helix. This helix is conserved throughout the TRP channel superfamily. These ion channels are tetrameric, meaning that the four PDs ensemble together to form a functional channel [2].

Transient receptor potential vanilloid 1 (TRPV1) is the most extensively studied member among TRP channels. From its vanilloid sensitivity, it inherited the name vanilloid receptor 1 (VR1), serving as the founding member of TRPVs [3]. Besides vanilloid compounds, a variety of chemical and physical stimuli such as heat [3], protons [4, 5], endogenous lipids [6], weak voltage and membrane proteins like PIRT [7] modulate TRPV1 function. Because of the sensitivity to various noxious stimuli, TRPV1

functions as a nociceptor and is also involved in human diseases and physiology from obesity [8], cancer [9], to inflammation [10, 11], making TRPV1 an attractive novel therapeutic target. For the past several decades, thousands of studies have been conducted to understand the various functions of TRPV1 from different angles such as the mode of activation, novel drug discovery, and role in human physiology and diseases. With tremendous effort, we are now starting to understand the mechanism of this ion channel in more detail.

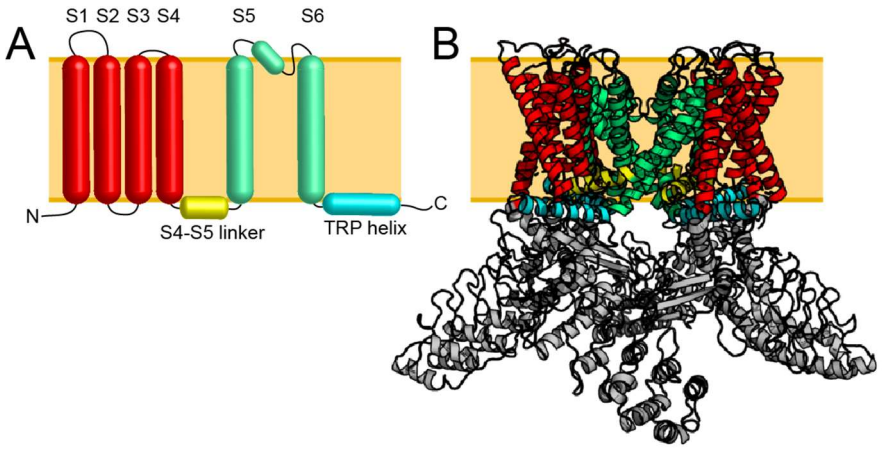

Figure 1.1 General architecture of TRP channels. (A) A TRP channel has six transmembrane helices. The S1-S4 domain (red) is coupled to the pore domain (PD, green) by the S4-S5 linker (yellow). Followed by the S6 helix in the PD, there is a conserved TRP helix (cyan) that is crucial in TRP channel function. (B) The structure of rat TRPV1 determined by cryo electron microscopy. The full channel is in the tetrameric form.

One main topic in TRPV1 research is probing and understanding the mechanism of temperature activation. Intrinsically heat sensitive, TRPV1 functions as a primary heat sensor in humans [3, 12]. TRPV1 is one of a handful thermosensitive TRP channels (thermoTRPs), which possess strong temperature dependence to initiate the channel gating. One simple way to understand the thermodynamics of temperature gating is that

there are two conformation states, open and close. In the case of TRPV1, as temperature increases, open probability of the channel increases. This results in a sigmoidal-shaped curve when P_o is plotted against temperature. The P_o can be defined as below:

$$P_o = \frac{1}{1 + e^{\frac{\Delta G^o}{RT}}} \quad [1]$$

where ΔG^o is the change in free energy that is evolved from the opening and closing of the channel, R is the ideal gas constant, and T is temperature. Applying that ΔG^o is related to the changes in enthalpy (ΔH^o) and the changes in entropy (ΔS^o) ($\Delta G^o = \Delta H^o - T\Delta S^o$), the equation [1] for P_o can be re-written:

$$P_o = \frac{1}{1 + e^{\frac{\Delta H^o}{RT} - \frac{\Delta S^o}{R}}} \quad [2]$$

This equation indicates that transition between open and closed states of the ion channel is related to ΔH and ΔS. From this sigmoidal curve, two key parameters are the slope of the curve and the midpoint of the slope (T_{50}). At the midpoint of the slope, T_{50}, ΔG^o equals zero, and the equation can be rearranged as follows:

$$T_{50} = \frac{\Delta H^o}{\Delta S^o} \quad [3]$$

The slope of the sigmoidal curve can be described by taking the derivative of the equation [2]:

$$\frac{dP_o}{d\left(\frac{1}{T}\right)} = -\left(P_o(1 - P_o)\right)\left(\frac{\Delta H^o}{R}\right) \quad [4]$$

Given that $P_o = 0.5$ at the midpoint, the slope at the midpoint can be defined as follows:

$$-0.5(1-0.5)\left(\frac{\Delta H}{R}\right) = -\frac{0.25\Delta H}{R} = \frac{\Delta H^o}{4R} \quad [5]$$

This implies that at the midpoint, the slope of the sigmoid is proportional to the changes in enthalpy, making the ΔH a measurement of thermosensitivity [13]. Thermosensitive TRP channels tend to have large Δ*H* magnitudes, and for TRPV1, the average Δ*H* is approximately 90 kcal/mol [12, 14-17].

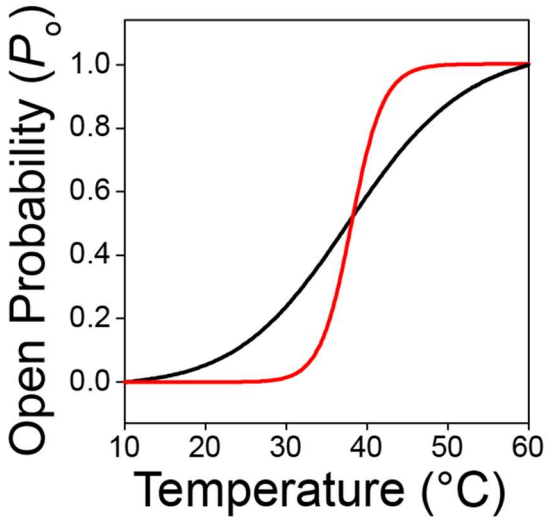

Figure 1.2 Simulated open probability (P_o) as a function of temperature. The slope of the sigmoidal curve represents the changes in enthalpy (Δ*H*), which functions as the measurement of thermosensitivity. The more thermosensitive the channel is, the higher Δ*H* becomes. Simulated red curve has Δ*H* of approximately 100 kcal/mol, while the black curve has Δ*H* = 30 kcal/mol.

There are several hypotheses on how the thermosensitive TRP channels (thermoTRPs) have large enthalpic changes. The large thermodynamic signature could arise from the changes in protein conformations, and changes in heat capacity [18]. The Chanda group manipulated the residues in the VSD of Shaker Kv channel to engineer a thermosensitive Shaker Kv channel [19]. This work was conducted based on the assumption that the protein undergoes structural rearrangement as the thermal stimulus is applied, resulting in changes in solvent accessibility in certain regions of the protein. When the polarities of amino acid residues in the VSD were modified, the Shaker Kv

channel exhibited temperature-induced activation [19]. This work is remarkable in that it tested the physical principal of the temperature activation.

Despite the interest, it has been challenging to pinpoint a specific region that functions as a main heat sensor in TRPV1. Countless researchers have had different hypotheses, have performed experiments and have suggested the locations of the "thermo-switch" in TRPV1 [14, 20-22]. However, all these efforts have produced contradictory results, leaving the temperature gating mechanism of TRPV1 unknown. One study generated a chimera between TRPV1 and TRPM8, a cold sensing TRP channel, swapping the C-terminus [20]. This study resulted in the reversed temperature sensitivity; TRPV1 with TRPM8 C-terminus was activated at cold temperature and vice versa, suggesting that this C-terminal region is the key to temperature sensing in thermoTRPs. Unfortunately, this intriguing result has not been reproduced by any groups since its publication, making the results questionable. Another potential region that researchers are focusing on is the membrane proximal domain (MPD), N-terminal region that is prior to the Pre-S1 helix. One study inserted the MPD of TRPV1 into TRPV3 to dissect the molecular determinant of temperature activation. TRPV3 is a warm temperature sensitive channel, and its activation has been reported to be the use-dependent, which means that the channel becomes sensitized over repeated stimulation. To understand its complex thermal activation mechanism, Qin and coworker noticed that in the membrane proximal region of TRPV3, one amino acid residue was deleted, while it was present in TRPV1 (S404). The insertion of this residue in TRPV3 resulted in a more stable temperature activation, indicating that this single residue plays a role in use-

dependent activation of TRPV3 [23]. Furthermore, a few molecular dynamics studies have shown that the MPD exhibits the large heat-induced motion after performing three sets of ten MD simuations at 200 ns timescale at three temperatures, 30, 60 and 72 °C, suggesting that this region may participate in thermosensing [24]. The pore domain also has gained attention for its role in temperature activation. Some studies suggested that the pore turret, 20 amino acid residues between the S5 helix and the pore helix, is the key thermosensor as replacement of 14 amino acids in the pore turret with an artificial sequence, $G_4PG_4SG_4S$, caused the abolition of heat sensitivity [14]. Ironically, the truncated rat TRPV1 construct that was used for cryo-EM omits the entire pore turret, and this minimal construct remained heat sensitive [21]. Interestingly, a recent study has highlighted the intrinsic thermosensitive nature of the pore domain (PD) [22]. This work created a chimeric ion channel between TRPV1 and Shaker potassium channel that is not activated by the thermal stimulus. The transplant of TRPV1 PD in Shaker channel inherited the heat sensitivity, concluding that the PD is the main source of heat sensing in TRPV1 [22]. As seen above, the temperature sensing mechanism is extremely complex, and new theories emerge, but the consensus indicates that the temperature sensing arises from the transmemebrane domain (TMD) [2]. As an example, a rodent TRPV1 isoform is naturally expressed with the deletion of majority of N-terminus; it is missing four of the Ankyrin repeat domain, but it remains thermosensitive, and it also is pressure sensitive [25]. Furthermore, TRPA1 is either hot or cold sensing TRP channel, depending on species [26]. Although a few mutations in the N-terminus can switch the nature of

temperature sensitivity, i.e. from cold sensing to warm temperature sensing [27], deletion of the whole N-terminus didn't abrogate the thermosensitive nature of TRPA1 [28].

Another "hot" topic in TRPV1 studies is its interaction with vanilloid compounds and other ligands. The most well-known agonist of TRPV1 is capsaicin, a chemical of pungency. Some vanilloid analogues include capsiate, chemical very similar to capsaicin, but does not have pungency, and resiniferatoxin (RTX), much more potent than capsaicin. Unlike the temperature activation, the capsaicin activation mechanism is relatively well understood. The Julius group first discovered the molecular determinant of capsaicin sensitivity in TRPV1 [29]. While TRPV subfamily is named with "vanilloid" due to the sequence homology, only TRPV1 is sensitive to vanilloid compounds. Naturally, chicken are insensitive to capsaicin, but retains the sensitivity to heat and protons, suggesting that there may be a rudimentary vanilloid binding site in chick TRPV1 [29]. The chicken TRPV1 ortholog (*Gallus gallus*, gTRPV1) has relatively high amino acid sequence similarity (~79%) to the mammalian TRPV1 (rat or human), and TRPV2, initially referred as VRL1, shows approximately 50% sequential similarity to rTPV1. Leveraging these differences, various chimeras between rTRPV1 and gTRPV1, and rTRPV1 and rTRPV2, were generated, and the key region that influence capsaicin sensitivity was narrowed down to the S2-S4 transmembrane helices [29].

A main contributing piece of work that aided the determination of the molecular determinant of capsaicin was the crystal structure of capsaicin-bound reaction center (RC) of photosystem [30]. Using the chemical structure of capsaicin that resembles the characteristics of some inhibitors of photosystem II, one group tested capsaicin as an

inhibitor of the photosynthetic activity. The residues in the RC that bound capsaicin had specific interactions with three major functional moieties of capsaicin. First, the vanilloid moiety formed pi-electron interactions with an aromatic residue, second, the amide neck interacted with polar residues by forming a hydrogen bond, and lastly, the carbon chain had hydrophobic interactions [30]. Julius and coworker realized that the S3 helix of TRPV1 was in the similar size of capsaicin binding site in the RC, and focused on this region to further dissect the molecular determinant of capsaicin in TRPV1. Based on these results, next investigation looked for the residues that are different in rTRPV2, yet conserved in gTRPV1. One of the amino acids that satisfied all these qualifications was Y511, a residue that resides in intracellular side and initiates the S3 helix. The mutation of this residue to alanine led to a significant loss in capsaicin sensitivity, indicating that Y511 is a key residue for capsaicin sensitivity [29]. Using a similar approach, a couple of amino acid residues in the S4 helix (M547 and T550) that affect capsaicin sensitivity were identified using the rabbit TRPV1 ortholog (*Oryctolagus cuniculus*, oTRPV1), which is less sensitive to capsaicin than the rat and human TRPV1, but more capsaicin-sensitive than the chicken TRPV1 [31].

These key residues in vanilloid sensing were confirmed with the ligand-bound TRPV1 cryo-EM structures [32, 33]. The cryo-EM structures in atomic resolution ranging from 2.9 to 4.4 Å have allowed researchers to perform computational studies to investigate the putative capsaicin activation mechanism. The capsaicin-bound TRPV1 cryo-EM structure (PDB ID: 3J5R) was informative in that the capsaicin binding leads partial opening of the channel [32]. However, the capsaicin molecule was poorly resolved

to understand in what orientation this molecule is binding. The Zheng group used the capsaicin-bound cryo-EM structure (PDB ID: 3J5R) to dock capsaicin, and revealed that the capsaicin binds in the binding pocket in head-down, tail-up orientation [34]. In more detail, the vanilloid head group forms a hydrogen bond with Y511, and the amide in the neck also forms a hydrogen bond with T550. This agrees with the trend shown in capsaicin-bound photosystem reaction center. Furthermore, this study suggested a potential capsaicin mechanism by comparing different states that were simulated by Rosetta docking method. Based on the structural analysis of these different states, the initial hydrogen bond seems to be formed between the neck of capsaicin and T550 in the S4 helix. Following capsaicin occupation in the putative binding pocket induces the movement of S4-S5 linker, resulting in the opening of the lower gate [34]. This was further studied in the later study using phi analysis where it showed that the conformational wave initiates from the capsaicin binding to T550 [35]. While the capsaicin activation mechanism is fairly well understood, how other types of ligands such as lipids, cannabinoids and antagonists modulate TRPV1 is at its infancy.

The majority of work presented here was achieved by a biophysical technique, solution nuclear magnetic resonance (NMR)

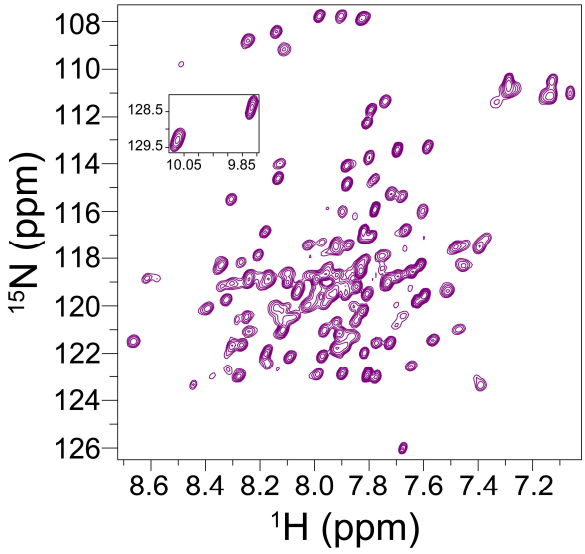

Figure 1.3 Heteronuclear single quantum coherence (HSQC) spectrum of the S1-S4 domain of human TRPV1. The amide proton is irradiated by the radiofrequency, and the magnetization is transferred to the amide nitrogen. The amide proton and nitrogen bond appears as a peak, or resonance, on a two-dimensional spectrum, which corresponds to an amino acid in the protein.

spectroscopy. Solution NMR is a powerful tool to study protein dynamics and structure. NMR utilizes the energy difference between two spin states of spin ½ nuclei induced by the magnetic field. The most commonly performed NMR experiment in structural biology is heteronuclear single quantum coherence (HSQC), which detects the bond between amide proton and nitrogen that transfer magnetization to each other (Figure 1.3). The spectrum resembles a contour map, including two dimensions, and each peak, or resonance, corresponds to one amino acid in the protein. Since the HSQC spectrum displays resonances from the amide backbone, it is considered as a fingerprint of the protein.

The protein of interest can be isotopically labeled with both ^{13}C and ^{15}N for triple-dimensional experiments that allow magnetization to transfer over the peptide bonds. The minimum experiments that are required for this amide backbone assignments include HNCA, HN(co)CA, HNCACB, CBCAcoNH, and HNCO, and all these experiments have a carbon (Cα, Cβ, Co) that is tied to the ^{1}H-^{15}N plane. These experiments provide the whole picture of how the atoms are linked to each other through bond, and this enables the assignment of each amide backbone, which provides specific amino acid information. In addition, the chemical shifts of all the atoms can be useful to predict the secondary structure or predict dihedrals of the protein by using a software TALOS-N [36].

Another benefit of using NMR is that a wide range of temperature is accessible. This allows the collection of ^{1}H-^{15}N HSQC spectra at different temperatures (temperature titration). As temperature increases, changes in chemical shifts and changes in resonance intensity evolve. As temperature increases, changes in hydrogen bonding networks occur,

which enhances the changes in chemical shifts. Also, protein molecule tumbles faster at higher temperature, decreasing the transverse relaxation rate (R_2) and increasing the resonance intensity. The transverse relaxation rate has been considered to be sensitive to the changes in protein dynamics such as a protein conformational change. Therefore, monitoring the changes in resonance intensities as a function of temperature could provide thermodynamic properties of a protein. This work is extensively studied in Chapter 3.

A series of ^{1}H-^{15}N HSQC can be useful to monitor the interactions between a ligand and a protein [37]. For a ligand L and a receptor protein P, a reversible reaction between P and L can be written as follows:

$$P + L \leftrightarrow PL \quad [6]$$

where P is a protein of interest, L is the ligand to be tested, and PL is the protein-ligand complex. When this reaction is at equilibrium, the association constant (K_a) is:

$$K_a = \frac{[PL]}{[P][L]} \quad [7]$$

In reverse, dissociation constant (K_d) is a parameter that informs how tightly or weakly a ligand binds to protein, and it can be written:

$$K_d = \frac{[P][L]}{[PL]} \quad [8]$$

In NMR-detected ligand experiment, the chemical shifts are sensitive to the local environment of the nuclei; therefore, addition of a ligand would cause some changes in chemical shift, $\Delta\delta$. The trend of chemical shift perturbations can be different depending

on the off-rate. If the off-rate is greater than the on-rate, the chemical shifts of the ligand-bound protein would deviate as a function of ligand concentration. On the other hand, if the off-rate is slower than the on-rate, this indicates that it takes longer for a ligand to detach from the target, which also means that the ligand binds to protein tightly. Because the exchange rate between the ligand and protein is slow, two signals can arise, one from the free protein, and another from the ligand-bound protein. As a ligand is titrated, the signals of free protein would decrease, while the signals from the ligand-bound protein would increase simultaneously [37]. In general, fast-exchange is more commonly observed in NMR-based ligand titration. Since the chemical shifts occur in two dimensions, chemical shift perturbations can be calculated with the following equation:

$$\Delta\delta_{obs} = \sqrt{(\Delta\delta_H)^2 + \frac{1}{5}(\Delta\delta_N)^2} \quad [9]$$

where $\Delta\delta_{obs}$ is the change in chemical shifts from the free state, $\Delta\delta_H$ is the change in proton chemical shifts, and $\Delta\delta_N$ is the change in nitrogen chemical shifts (Figure 1.4). Because the magnitudes of nitrogen chemical shifts are bigger than protons, the changes in nitrogen chemical shifts are scaled by multiplying 0.2. The $\Delta\delta_{obs}$ at each titration point can be plotted as a function of ligand concentration, and the resulting plot will resemble a hyperbolic curve if a ligand binds specifically to the target. To calculate the binding dissociation constant, K_d, assuming that the ligand and protein are in 1:1 ratio upon binding, following equation can be used:

$$\Delta\delta_{obs} = \frac{\Delta\delta_{max} \cdot x}{K_d + x} \quad [10]$$

where $\Delta\delta_{obs}$ is the chemical shift perturbation induced by ligand binding, $\Delta\delta_{max}$ is the maximum chemical shift perturbation, x is the ligand concentration, and K_d is the dissociation constant. The work presented in Chapter 4 heavily involves the NMR monitored ligand interaction with the S1-S4 domain of human TRPV1.

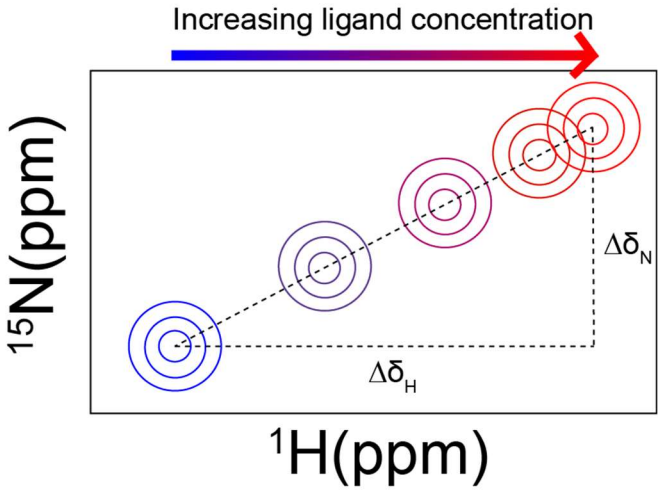

Figure 1.4 NMR ligand titration in fast exchange system. As the concentration of ligand increases, it promotes changes in chemical shifts. The $\Delta\delta_{obs}$ represents a chemical shift from free-state of the protein, and in the fast exchange system, the k_{off} is larger than k_{on}, the chemical shifts travel from the ligand-free state to the ligand-bound state.

The work presented in this dissertation mainly focuses on the S1-S4 domain of human TRPV1. Chapter 2 presents the review of recently determined cryo-EM structures of TRP channels and how these structures have been informative in understanding the mechanisms of TRP channel gating. Chapter 3 includes a study to investigate the role of S1-S4 membrane domain of human TRPV1 in thermosensing. Chapter 4 presents a study that explores the interaction between the human TRPV1 S1-S4 domain and various ligands such as vanilloid compounds, antagonists such as capsazepine and ABT-102, and cannabinoids. Chapter 5 includes miscellaneous work including the expression and purification of a membrane protein enzyme vitamin K epoxide reductase (VKOR). At last, Chapter 6 concludes this work and suggests future directions.

1.1 References

1. Nilius, B. and G. Owsianik, The transient receptor potential family of ion channels. *Genome Biol,* 2011. **12**(3): p. 218.

2. Hilton, J.K., M. Kim, and W.D. Van Horn, Structural and Evolutionary Insights Point to Allosteric Regulation of TRP Ion Channels. *Acc Chem Res,* 2019. **52**(6): p. 1643-1652.

3. Caterina, M.J., et al., The capsaicin receptor: a heat-activated ion channel in the pain pathway. *Nature,* 1997. **389**(6653): p. 816-24.

4. Jordt, S.E., M. Tominaga, and D. Julius, Acid potentiation of the capsaicin receptor determined by a key extracellular site. *Proc Natl Acad Sci U S A,* 2000. **97**(14): p. 8134-9.

5. Tominaga, M., et al., The Cloned Capsaicin Receptor Integrates Multiple Pain-Producing Stimuli. *Neuron,* 1998. **21**(3): p. 531-543.

6. Lukacs, V., et al., Dual regulation of TRPV1 by phosphoinositides. *J Neurosci,* 2007. **27**(26): p. 7070-80.

7. Kim, A.Y., et al., Pirt, a phosphoinositide-binding protein, functions as a regulatory subunit of TRPV1. *Cell,* 2008. **133**(3): p. 475-85.

8. Suri, A. and A. Szallasi, The emerging role of TRPV1 in diabetes and obesity. *Trends Pharmacol Sci,* 2008. **29**(1): p. 29-36.

9. Weber, L.V., et al., Expression and functionality of TRPV1 in breast cancer cells. *Breast Cancer (Dove Med Press),* 2016. **8**: p. 243-252.

10. Kim, J.H., The Emerging Role of TRPV1 in Airway Inflammation. *Allergy Asthma Immunol Res,* 2018. **10**(3): p. 187-188.

11. Yoshida, A., et al., TRPV1 is crucial for proinflammatory STAT3 signaling and thermoregulation-associated pathways in the brain during inflammation. *Sci Rep,* 2016. **6**: p. 26088.

12. Cao, E., et al., TRPV1 channels are intrinsically heat sensitive and negatively regulated by phosphoinositide lipids. *Neuron,* 2013. **77**(4): p. 667-79.

13. Feng, Q., Temperature sensing by thermal TRP channels: thermodynamic basis and molecular insights. *Curr Top Membr,* 2014. **74**: p. 19-50.

14. Yang, F., et al., Thermosensitive TRP channel pore turret is part of the temperature activation pathway. *Proc Natl Acad Sci U S A,* 2010. **107**(15): p. 7083-8.

15. Liu, B., K. Hui, and F. Qin, Thermodynamics of Heat Activation of Single Capsaicin Ion Channels VR1. *Biophysical Journal,* 2003. **85**(5): p. 2988-3006.

16. Vlachová, V., et al., Functional Role of C-Terminal Cytoplasmic Tail of Rat Vanilloid Receptor 1. *The Journal of Neuroscience,* 2003. **23**(4): p. 1340-1350.

17. Yao, J., B. Liu, and F. Qin, Kinetic and energetic analysis of thermally activated TRPV1 channels. *Biophys J,* 2010. **99**(6): p. 1743-53.

18. Clapham, D.E. and C. Miller, A thermodynamic framework for understanding temperature sensing by transient receptor potential (TRP) channels. *Proc Natl Acad Sci U S A,* 2011. **108**(49): p. 19492-7.

19. Chowdhury, S., B.W. Jarecki, and B. Chanda, A molecular framework for temperature-dependent gating of ion channels. *Cell,* 2014. **158**(5): p. 1148-1158.

20. Brauchi, S., et al., A hot-sensing cold receptor: C-terminal domain determines thermosensation in transient receptor potential channels. *J Neurosci,* 2006. **26**(18): p. 4835-40.

21. Liao, M., et al., Structure of the TRPV1 ion channel determined by electron cryo-microscopy. *Nature,* 2013. **504**(7478): p. 107-12.

22. Zhang, F., et al., Heat activation is intrinsic to the pore domain of TRPV1. *Proc Natl Acad Sci U S A,* 2018. **115**(2): p. E317-E324.

23. Liu, B. and F. Qin, Single-residue molecular switch for high-temperature dependence of vanilloid receptor TRPV3. *Proc Natl Acad Sci U S A,* 2017. **114**(7): p. 1589-1594.

24. Wen, H. and W. Zheng, Decrypting the Heat Activation Mechanism of TRPV1 Channel by Molecular Dynamics Simulation. *Biophys J,* 2018. **114**(1): p. 40-52.

25. Zaelzer, C., et al., DeltaN-TRPV1: A Molecular Co-detector of Body Temperature and Osmotic Stress. *Cell Rep,* 2015. **13**(1): p. 23-30.

26. Laursen, W.J., et al., Species-specific temperature sensitivity of TRPA1. *Temperature (Austin),* 2015. **2**(2): p. 214-26.

27. Jabba, S., et al., Directionality of temperature activation in mouse TRPA1 ion channel can be inverted by single-point mutations in ankyrin repeat six. *Neuron,* 2014. **82**(5): p. 1017-31.

28. Moparthi, L., et al., Human TRPA1 is intrinsically cold- and chemosensitive with and without its N-terminal ankyrin repeat domain. *Proc Natl Acad Sci U S A,* 2014. **111**(47): p. 16901-6.

29. Jordt, S.-E. and D. Julius, Molecular Basis for Species-Specific Sensitivity to "Hot" Chili Peppers. *Cell,* 2002. **108**(3): p. 421-430.

30. Spyridaki, A., et al., The natural product capsaicin inhibits photosynthetic electron transport at the reducing side of photosystem II and purple bacterial reaction center: structural details of capsaicin binding. *Biochimica et Biophysica Acta (BBA) - Bioenergetics,* 2000. **1459**(1): p. 69-76.

31. Gavva, N.R., et al., Molecular determinants of vanilloid sensitivity in TRPV1. *J Biol Chem,* 2004. **279**(19): p. 20283-95.

32. Cao, E., et al., TRPV1 structures in distinct conformations reveal activation mechanisms. *Nature,* 2013. **504**(7478): p. 113-8.

33. Gao, Y., et al., TRPV1 structures in nanodiscs reveal mechanisms of ligand and lipid action. *Nature,* 2016. **534**(7607): p. 347-51.

34. Yang, F., et al., Structural mechanism underlying capsaicin binding and activation of the TRPV1 ion channel. *Nat Chem Biol,* 2015. **11**(7): p. 518-524.

35. Yang, F., et al., The conformational wave in capsaicin activation of transient receptor potential vanilloid 1 ion channel. *Nat Commun,* 2018. **9**(1): p. 2879.

36. Shen, Y. and A. Bax, Protein backbone and sidechain torsion angles predicted from NMR chemical shifts using artificial neural networks. *J Biomol NMR,* 2013. **56**(3): p. 227-41.

37. Williamson, M.P., Using chemical shift perturbation to characterise ligand binding. *Prog Nucl Magn Reson Spectrosc,* 2013. **73**: p. 1-16.

CHAPTER 2

STRUCTURAL AND EVOLUTIONARY INSIGHTS POINT TO ALLOSTERIC REGULATION OF TRP ION CHANNELS

2.1 Conspectus

The familiar pungent taste of spicy food, the refreshing taste of mint, and many other physiological phenomena are mediated by transient receptor potential (TRP) ion channels. TRP channels are a superfamily of ion channels that are sensitive to diverse chemical and physical stimuli and play diverse roles in biology. In addition to chemical regulation, some family members also sense common physical stimuli, such as temperature or pressure. Since their discovery and cloning in the 1990s and 2000s, understanding the molecular mechanisms governing TRP channel function and polymodal regulation has been a consistent but challenging goal. Until recently, a general lack of high-resolution TRP channel structures had significantly limited a molecular understanding of their function.

In the past few years, a flood of TRP channel structures have been released, made possible primarily by advances in cryo-electron microscopy (cryo-EM). The boon of many structures has unleashed unparalleled insight into TRP channel architecture. Substantive comparative studies between TRP structures provide snapshots of distinct states such as ligand-free, stabilized by chemical agonists, or antagonists, partially illuminating how a given channel opens and closes. However, the now ~75 TRP channel

structures have ushered in surprising outcomes, including a lack of an apparent general mechanism underlying the channel opening and closing among family members. Similarly, the structures reveal a surprising diversity in which chemical ligands bind TRP channels.

Several TRP channels are activated by temperature changes in addition to ligand binding. Unraveling mechanisms of thermosensation have proven an elusive challenge to the field. Although some studies point to thermosensitive domains in the transmembrane region of the channels, results have sometimes been contradictory and difficult to interpret; in some cases, a domain that proves essential for thermal sensitivity in one context can be entirely removed from the channel without affecting thermosensation in another context. These results are not amenable to simple interpretations and point to allosteric networks of regulation within the channel structure.

TRP channels have evolved to be fine-tuned for the needs of a species in its environmental niche, a fact that has been both a benefit and burden in unlocking their molecular features. Functional evolutionary divergence has presented challenges for studying TRP channels, as orthologs from different species can give conflicting experimental results. However, this diversity can also be examined comparatively to decipher the basis for functional differences. As with structural biology, untangling the similarities and differences resulting from evolutionary pressure between species has been a rich source of data guiding the field. This Account will contextualize the existing biochemical and functional data with an eye to evolutionary data and couple these

insights with emerging structural biology to better understand the molecular mechanisms behind chemical and physical regulation of TRP channels.

2.2 Introduction

Much of biology is determined by relative concentrations of ions across biological membranes. These concentration gradients are tightly regulated and used to transmit signals typically via ion channels. Ion channels are pore-forming proteins embedded in lipid bilayer membranes. Hundreds of different ion channels exist, with vast structural and functional diversity, but in principle, all work the same way: the channel pore has one or more "gates" that can open and close in response to specific stimuli such as chemical ligands, electrical potential across the membrane, temperature, or mechanical force. When open, ions freely flow through the pore down their concentration gradient forming cascades of information transmission.

Transient receptor potential (TRP) ion channels make up a superfamily of membrane proteins that are widely expressed in higher organisms. Based on sequence homology this superfamily is divided into seven subfamilies, six of which are found in humans (Figure 2.1).[1] Canonically the best studied ion channels are “gated”, that is opened or closed, by either chemical ligands or changes in potential (i.e., voltage) across the membrane. A feature that appears common to many TRP channels is responsiveness to multiple types of stimuli, such as chemical, electrical, thermal, pH, and mechanical stimuli. Diverse classes of endogenous lipids provide a variety of regulatory effects on TRP channels and can act as cofactors required for function or even as direct agonists and

antagonists.[2, 3] Channel activity can also be modulated by phosphorylation, which can directly affect channel gating or modify membrane trafficking.[4-7] Presumably because of their role as polymodal sensors, TRP channels are expressed in a variety of tissues and function broadly in physiology. Because a given TRP channel integrates diverse physical and chemical stimuli, a thorough understanding of the molecular mechanisms, including the interplay between stimuli and the similarities and differences between TRP channels, has been complicated and often controversial.

Since the cryo-EM structures of TRPV1 reported in 2013, ~75 structures representing orthologs to about two-thirds of human TRP channels have been determined (Figure 2.1).[8, 9] This advancement has arisen primarily from developments in cryo-electron microscopy (cryo-EM). As a result, TRP channel structures with resolutions between 2.9–5 Å have provided unprecedented insight into the molecular architecture of channels from various TRP subfamilies and bound in different states to a variety to chemical ligands. These structures show that TRP channels have widely divergent termini and loop regions. The only conserved structural features across all TRP channels are two transmembrane structural domains and the amphipathic "TRP" helix (Figure 2.2). The conserved membrane regions include a four-helix bundle domain comprising the S1-S4 transmembrane helices that have been referred to nondescriptly as the S1-S4 domain or, because of homology to voltage-sensing domains found in voltage-gated channels, the voltage-sensing like domain (VSLD). The S5-S6 transmembrane helices tetramerize to form the pore domain (PD) where ion conduction occurs. Following the S6 transmembrane helix is the conserved amphipathic TRP helix that lies along the

intracellular plane of the membrane. Besides these features shared across all TRP channels, other features are also shared between a few subfamilies. TRPA, TRPM, and TRPC channels have a C-terminal coiled-coil domain, thought to mediate and stabilize the tetrameric assembly. TRPA, TRPV, and TRPN channels have N-terminal ankyrin repeats that are capable of transducing conformational change to the pore. While TRP channels are typically considered homomeric, and indeed all current structures recapitulate this, there is evidence which suggests these channels can form heteromeric channel assemblies between TRP family members[10] or complexes between two homomeric TRP channels.[11] Alternative splicing isoforms of TRP channels further increase the complexity of regulation and diversity of function.[12] TRP channel function is further fine-tuned by other protein interactions. For example, TRPV1, the canonical heat and capsaicin sensor, has been implicated in interactions with at least 94 non-TRP channel proteins.[13]

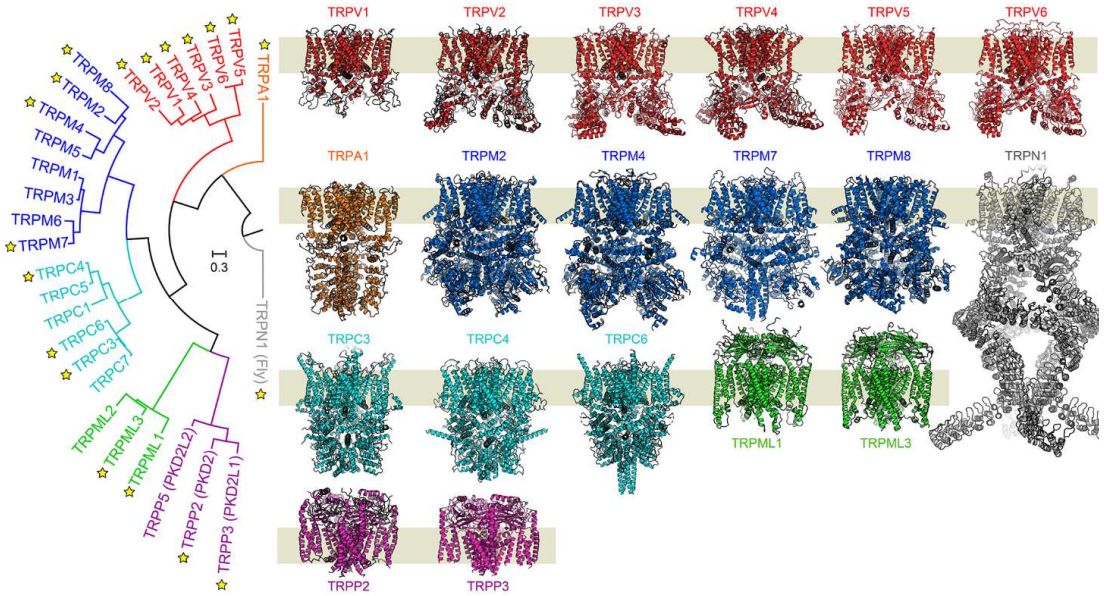

Figure 2.1 TRP channel evolutionary relationships and representative structures. Left, a phylogenetic tree of human TRP channels, including an ancestral non-mammalian TRPN1 channel (Gray). Yellow stars indicate that a structure of either the human or an ortholog channel has been determined. To date, at least two structures have been determined from each human TRP subfamily, with exception of TRPA1, where there is a lone human subfamily member. Representative structures have been determined for the entire vanilloid (TRPV) subfamily. The structures reveal a conserved general transmembrane architecture with highly diverse extramembrane loops and N- and C-terminal domains. The collective structural information has shaped understanding of how TRP channels gate in response to chemical and physical stimuli. TRPA is for ankyrin, -V for vanilloid, -M for melastatin, -C for canonical, -ML for mucolipin, -P for polycystic.

Numerous TRP channel structures have provided detailed information, such as domain architectures, domain packing, and key insights into chemical ligand-induced gating mechanisms.[8, 9] Despite significant successes in TRP channel structural biology and a well conserved transmembrane domain (TMD, helices S1-S6, Figure 2.2) architecture, surprisingly a general TRP channel gating mechanism has not emerged from the structural biology.

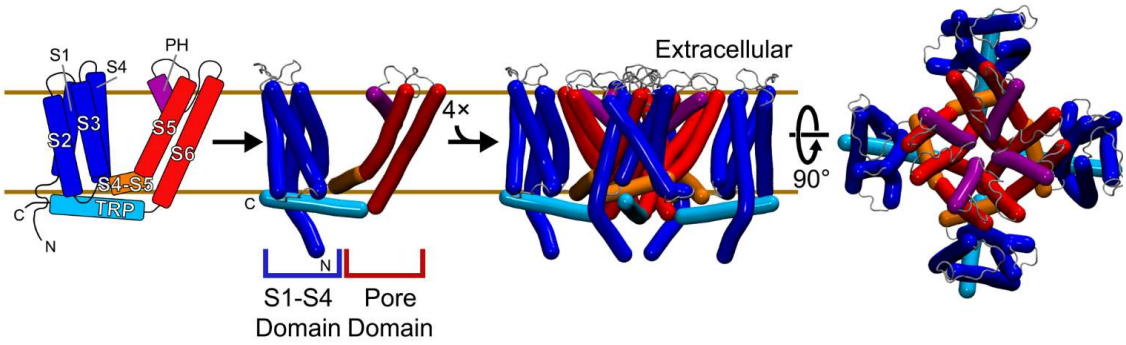

Figure 2.2 The conserved transmembrane architecture of TRP ion channels. A TRP channel monomer (left panels) contains six transmembrane helices, including two conserved structural domains. The S1-S4 ligand sensing domain (blue) is a four-helix bundle of first four transmembrane helices, S1 to S4. The last two transmembrane helices, S5 and S6, form the pore domain (PD, red) where the tetramer of the PD forms the conductance pathway of the channel. The S1-S4 domain and the PD are linked by an S4-S5 linker (orange). Two additional conserved helices are the pore helix (PH, purple) and the amphipathic TRP helix (cyan). A functional channel is composed of a domain-swapped tetramer, with the PD helices interacting with adjacent subunits (right panels). Structural and functional studies suggest that allosteric networks between binding, temperature sensing, and other stimuli regulate these channels.

Indeed, it is possible that the ability to detect a variety of stimuli and the diverse N- and C-terminal structural features preclude a single conserved gating mechanism across all the channels. Notwithstanding these challenges, and as outlined more thoroughly below, the conserved TMD seems to be central to function. Interactions between the TRP helix, the S1-S4 domain, and a linker helix between the S4 and S5 helices are crucial to transducing stimuli from peripheral domains to gate the PD. Apart from the TMD and TRP helix, there are no domains that are present in all TRP channels, indicating the importance of these regions. Coupled with the recent structural information, TRP channel function is enriched and complicated by species-specific diversity, with some channels activated by a particular chemical while the same chemical inhibits the equivalent (orthologous) channel in a different species.[14] There are also reports characterizing a given thermosensitive TRP channel as a heat sensor in one

species and a cold sensor in another.[15] Speciation can also extend to partner proteins that modulate the channels, such as opposite effects of the PIRT protein on human and mouse orthologs of TRPM8.[16] The emerging examples of species dependent function indicate that TRP channels are functionally plastic and that allosteric networks regulate channel function. In this Account, we highlight TRP channel structural and functional studies and leverage evolutionary and genetic data with the goal of identifying similarities and differences between family members. We also focus on the emerging role of allostery in functional regulation, with "function" defined as gating of the channel pore, and propose that TRP channels are a model system to probe and understand the fundamentals of allostery in biomolecular systems.

2.3 Biochemical Insights from Genetics and Evolution

After the identification of the fly *trp* gene in 1989 [17], hundreds of TRP channels have since been identified primarily from organisms in the phylogenetic kingdom of Animalia and spanning a wide variety of animals including fish, sea squirts, rodents, flies, and humans. Each species genome typically encodes about 15-30 TRP channels, with 27 found in humans. Beyond animals, a few examples of TRP channels have been identified in fungi and non-land plants.[18] To date, no TRP channels have been identified in bacteria nor archaea.

Evolutionary-based studies of protein orthologs from distinct species with variable physiologies can be leveraged to help elucidate molecular mechanisms, either through direct comparative studies or by systematic analysis to identify different regions and their susceptibility to genetic variation. Evolutionary analysis of the menthol and

cold-sensing receptor TRPM8 indicates that it is found only in vertebrates and emerged about 400 MYA during vertebrate evolution.[19] Analysis of evolutionary conservation of TRPM8 orthologs indicates that diverse regions of TRPM8 have evolved with distinct selection pressures.[20] Presumably channel regions that are most well conserved are central to core channel function. Not surprisingly, the most highly conserved TRPM8 regions are in the TMD and include the S3, S4, S5, and S6 transmembrane helices from the S1-S4 domain and the PD respectively. Two small membrane regions including the intracellular side of the S4 helix, S4-S5 loop, and intracellular S5 region that connect the S1-S4 domain to the PD appear to be completely conserved across the ~40 TRPM8 orthologs that were sequenced at the time of the study.[19] These conserved regions in TRPM8 are reminiscent of the regions in the heat and capsaicin receptor TRPV1 vanilloid binding site. Another direct result from expansive sequencing and evolutionary data is leveraged from statistical models of protein sequence evolution that can be used to identify residues that coevolve. This has been successfully employed and validated in structure prediction algorithms by identifying interacting residue pairs [21] but also provides insight into conformational changes, critical functional residues, and protein-protein interaction information.[22] Looking at the evolutionary couplings of TRPM8 and TRPV1 TMD regions, interesting patterns emerge (Figure 2.3). While the technique is typically used to identify residue-residue contacts (i.e., residues that are close in space), the TRPM8 and TRPV1 coevolutionary analysis shows that there are many evolutionary couplings that are spatially far apart. This suggests that these channels are allosterically regulated, and the patterns of evolutionary couplings are consistent with allosteric

communication between the S1-S4 domain and PD. Another feature to emerge from this analysis is that these coevolution patterns of allosteric networks between TRPV1 and TRPM8 are distinct. The differences indicate that there are likely some conserved activation and regulation mechanisms between TRPV1 and TRPM8, focused on coupling the S1-S4 domain to the PD via the S4-S5 linker. However, other distinct types of allostery and or mechanistic conformational changes might have emerged through evolution.

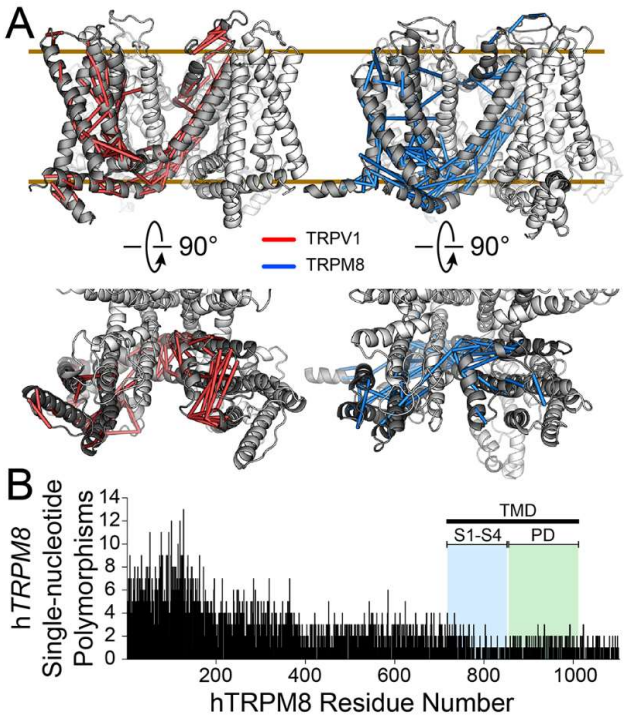

Figure 2.3 Insights from evolutionary studies. A) TRPM8 and TRPV1 show distinct patterns of co-evolution. Using GREMLIN software the 100 highest probability predicted coevolving residues were plotted on homology models of the human TRPV1 (red) and TRPM8 (blue) TMD regions (including helices S1-S6), with pseudo-bonds shown between coevolving pairs. The analysis identifies coevolution of the intracellular S1-S4 domain to the pore domain. However, patterning differences of the evolutionary constraints suggests there are distinct mechanisms and allosteric networks. B) The frequency of exonic human TRPM8 single-nucleotide polymorphisms (SNPs) as a function of residue number. A decreased SNPs frequency in the TMD indicates that this region is less tolerant of mutations. Data were aggregated from the Ensembl database searching exclusively deposited human genomes.

Significant advances in DNA sequencing technology and the ease of obtaining human genetic information can also help to elucidate regions that are most prone to mutations and therefore presumably least crucial to function. Our analysis of human genomes found in the Ensembl database identify 26,975 human TRPM8 variants including insertions, deletions, and single nucleotide polymorphisms. Analysis of the human TRPM8 variants reflects frequency and tolerance to divergence and shows that this variance is not random. Figure 2.3B plots the single nucleotide polymorphisms

(SNPs) of the human *TRPM8* gene as a function of protein residue number. As expected from protein domain conservation across species and from TRP structural studies, the TRPM8 TMD shows fewer SNPs than other domains, indicating its importance in TRPM8 function.

Analysis of TRP channel genetic data provides important insights into function, identifying the TMD as crucial to function and suggesting the importance of allosteric mechanisms. Leveraging the similarities and differences between orthologous and paralogous TRP channels has also provided biochemical insight into how these channels are gated. Although many of these channels are polymodally regulated, significant inroads have been made in understanding how chemical ligands regulate TRP channels and similarly, a framework for temperature activation is beginning to emerge. One constant from these comparative studies is that distal regulation of function, or allostery, is key in understanding the biochemical mechanism.

2.4 Mechanisms of Ligand Gating

Many TRP channels are regulated by a variety of diverse chemical ligands, and structural studies are beginning to identify intriguing mechanistic commonalities and surprising differences between TRP channels. Among the best studied is TRPV1, which is activated by elevated temperatures and sensitive to a variety of ligands including the vanilloid capsaicin. Structural, functional, and computational studies of TRPV1 have delineated a clear vanilloid binding pocket and mechanism for TRPV1 ligand activation.[23, 24] Protein engineering studies of two non-vanilloid activated channels, TRPV2 [25, 26] and TRPV3 [27], have shown that this binding site is likely conserved as

are the mechanistic framework, at least in the TRPV family and potentially other TRP channels.[28-32] One key feature that emerges from the TRPV3 vanilloid engineering study is that allostery plays a significant role in ligand activation.[27]

Highlighting the diversity of allosteric mechanisms of ligand activation, TRPA1 is uniquely activated via covalent modification by pungent electrophilic compounds such as allyl isothiocyanate and diallyl disulfide, found in wasabi, mustard oil, or garlic. These compounds covalently bond with cysteine residues in the N-terminal ankyrin repeat and pre-S1 regions. This induces conformational changes that propagate from the modification site to the pore.[33] A final unique example is allosteric regulation of TRPM7 by a kinase domain, which mediates nucleotide inhibition of the channel.[34] Human TRPM2, on the other hand has an evolutionary inactivated enzyme domain that still retains the ability to bind the historical substrate and this binding regulates channel activity allosterically.[35] Allostery seems to emerge as a key contributor in TRP channel ligand activation as highlighted below.

2.4.1 Menthol Ligand-Gating in TRPM8

While experimental, computational, and structural data identify the vanilloid binding site in TRPV1, the TRPM8 menthol binding site is more controversial. Early mutagenesis data identified residues in the S1-S4 domain that selectively abrogate TRPM8 menthol sensitivity while leaving intact cold activation.[36] From this and other studies, Y745 (S1) and Arg842 (S4) have emerged as potential TRPM8 residues involved in menthol binding. Later radioligand binding studies of ^{3}H-labeled menthol showed that the mutation Y745H decreases TRPM8 affinity for the radioligand, suggesting that it may

be directly involved in menthol binding.[37] More recently an NMR and microscale thermophoresis (MST) binding study of an isolated human TRPM8 S1-S4 domain showed that menthol and WS-12, a menthol analog and more potent TRPM8 agonist, directly bind to this domain.[38] The authors further tested the Y745H and R842H mutations in the isolated S1-S4 membrane domain, but unexpectedly neither impacted menthol affinity as monitored by NMR or MST. With the flood of TRPM cryo-EM structures, including TRPM2, TRPM4, TRPM7, and TRPM8, it is clear that the equivalent tyrosine and arginine residues for Y745 and R842 in TRPM8 are structurally conserved. These residue identities are also conserved across the human TRPM family. Given that TRPM8 is the only menthol-sensitive TRPM channel, it seems unlikely that either Y745 or R842 are key determinants for menthol selectivity. This idea is supported by the identification of a TRPM8 isoform (isoform 4) protein in epidermal cells that is missing parts of the N-terminus and a region of the TMD that includes helices S1 and S2.[39] The epidermally expressed TRPM8 isoform 4 trafficks differently from the full-length protein but retains key functions such as cold sensitivity and activation by menthol and other cooling agents, namely WS-12 and icilin. Convoluting these data are recent agonist bound structures of TRPM8 identifying overlapping but distinct binding sites for WS-12 and icilin in an intracellular side cavity of the S1-S4 domain between helices S1-S4.[40] Presumably the aggregate data suggest that Y745 modulates menthol sensitivity allosterically since mutating the residue influences TRPM8 menthol sensitivity and in the context of the full channel reduces affinity. However, TRPM8 isoform 4, which lacks the S1 helix that includes Y745, retains menthol sensitivity. It is clear from structural studies

that TRPM8 and TRPV1 have distinct agonist binding sites.[8, 40] Nonetheless, there is experimental evidence of reciprocal ligand effects between TRPM8 and TRPV1. The TRPM8 agonist menthol inhibits TRPV1 capsaicin activation, and the TRPV1 agonist capsaicin antagonizes menthol evoked TRPM8 currents.[41] Additionally, an early study published before the identification of TRPM8 used ^{3}H-labeled menthol for radioligand binding studies in whole cell membranes, and among other things noted that labeled menthol is displaced by TRPV1 agonist capsaicin and antagonist capsazepine.[42] Menthol has also been implicated in activating or inhibiting other TRP channels, like TRPV3 and TRPA1.[43, 44] While TRPM8 ligand binding is coming into focus, the allosteric relationships and mechanisms of activation are still relatively opaque.

2.4.2 The Convoluted Case of 2-APB

While the canonical vanilloid binding site seems to be conserved in TRPVs, clear mechanistic relationships between ligand regulations of TRP channels is still unresolved. The compound 2-APB (2-aminoethoxydiphenyl borate) modulates the activity of channels from at least the TRPA, -M, -V, and -C families. Such a compound presumably should provide tremendous insight into what constitutes conserved mechanisms of chemical activation. 2-APB regulates five of six TRPV family members, activating TRPV1, V2, and V3, and inhibiting TRPV5, and V6.[45-47] Structures from TRPV3 and TRPV6 have been determined in the presence of 2-APB which activates or inhibits the respective channel. The 2-APB bound TRPV6 structure identifies the inhibitor on the intracellular side in the S1-S4 domain that is distinct from the canonical vanilloid binding pocket.[47] The proposed mechanism whereby 2-APB inhibits TRPV6 is allosteric in

nature where conformational rearrangements in the S1-S4 domain, specifically motions in the S3 helix, pull on the S4-S5 linker shifting an activating lipid that binds at the interface between the S1-S4 domain and the PD, which ultimately results in channel inhibition.

In contrast, the TRPV3 structure identifies three different binding sites for 2-APB: one near, but distinct from the intracellular S1-S4 TRPV6 binding site, one below the intracellular TRP-helix, and one in the extracellular side of the S1-S4 domain (Figure 2.4A).[48] According to this proposed activation mechanism of TRPV3, 2-APB binds the extracellular side of the S1-S4 domain, causing the S1-S2 loop to move; this results in the release of an extracellular leaflet lipid which couples 2-APB binding and allosteric gating across the membrane. The authors conclude that the extracellular binding site is key for TRPV3 activation since 2-APB binding in the other two intracellular sites were populated in closed state structures.[49] We note that other TRPV structures have a lipid binding site near that in the TRPV3 structure, raising potential that this may be a non-specific binding site.

The TRPV6 residues near the 2-APB binding site were also functionally studied, and a tyrosine residue in S4 (Y467A) was identified that increases 2-APB inhibitory potency of TRPV6.[47] This tyrosine in the S4 helix is conserved across the TRPV family, and the same mutation made in mouse TRPV3 caused a 20-fold increase in 2-APB agonist potency.[48] This complicates the interpretation of 2-APB in activating TRPV3, suggesting that either TRPV6 and TRPV3 share the 2-APB binding site, in contradiction of the structural data, or imply that multiple 2-APB binding sites contribute

to TRPV3 activation but only one to TRPV6 inhibition. Another interpretation could be that regulation is achieved by allosteric coupling between the binding sites.

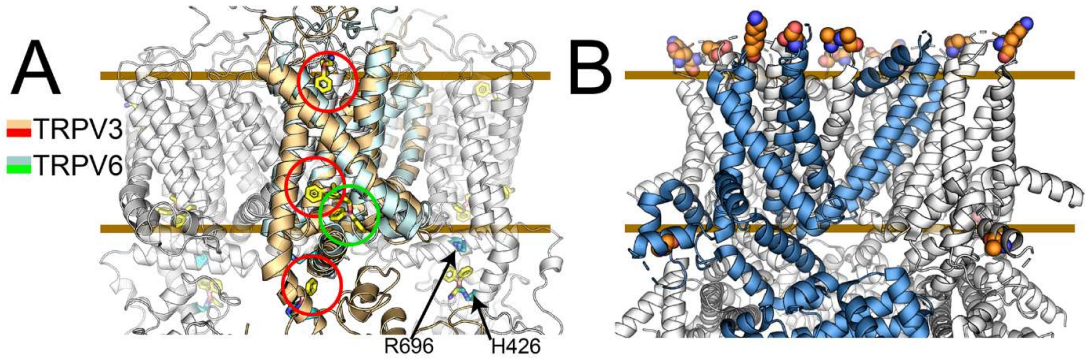

Figure 2.4 Allosteric coupling in ligand and temperature activation. Panel A shows structures of 2-APB bound TRPV3 and TRPV6 in gold and cyan respectively. Between the two structural studies four 2-APB binding sites have been identified in related TRPV channels. These coupled with functional studies suggest that in 2-APB ligand regulation of TRP channels allostery is key to modulating function. Panel B identifies residues essential to exchanging cold-sensing properties between TRPM8 channels from hibernating and non-hibernating rodents. The six residues are far away in space indicating that allosteric networks are key to deciphering these outcomes. Comparing these six mutations with human TRPM8 show that not only are allosteric networks important but also that there must be compensating pairs of residues that impact allostery.

To complicate 2-APB modulation of TRPV channels further, a high-throughput mutagenesis functional screen of ~14,000 mutations in mouse TRPV3 identified two key residues (H426 and A696) that reside near the TRP-helix 2-APB binding site that was deemed non-activating in the TRPV3 structure studies.[50] TRPV4 has not been reported to be modulated by 2-APB, however, by mutating the equivalent residues (N456 and W737) to histidine and arginine respectively, the mutated TRPV4 becomes sensitive to 2-APB activation. Taken together, these three studies suggest a complicated binding landscape for TRPV modulation by 2-APB, where allostery and multiple binding sites in and/or near the S1-S4 domain couple to channel gating in the S5-S6 PD.

These studies clearly show that allosteric coupling between distinct binding sites in the S1-S4 domain and pore domain gating is a common mechanism to regulate TRP channel function. Figure 2.5 illustrates the relative structural rearrangements of the TRPV3 and TRPV6 S1-S4 domain induced by 2-APB that results in activation and inhibition, respectively. Other motions of S1-S4 domain in TRPV family gating are also shown, highlighting the apparently disparate structural mechanisms and diverse allosteric

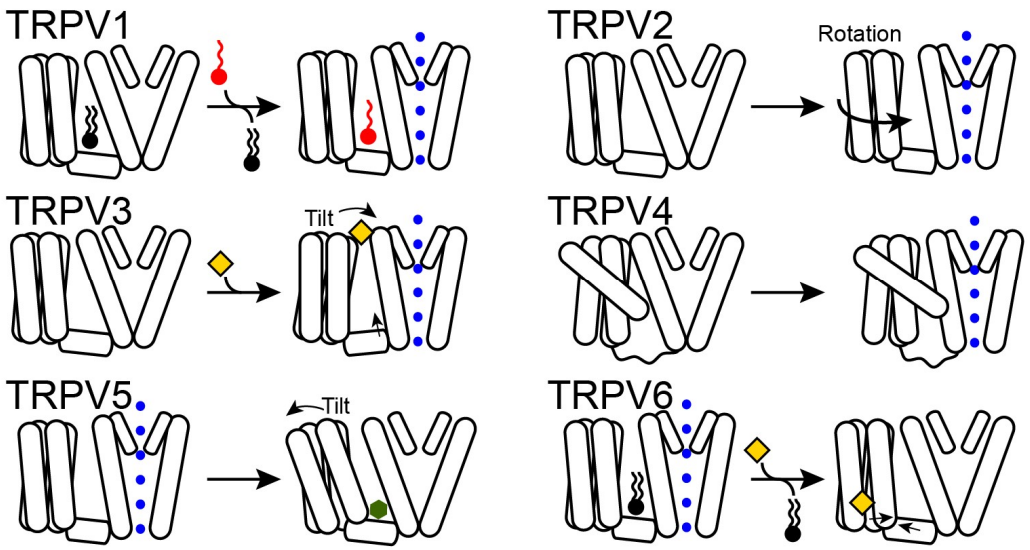

Figure 2.5 Diverse S1-S4 gating-coupled movements identified from TRPV structural studies. In TRPV1, the S1-S4 domain remains immobile while a residing lipid (black rectangle) is replaced by a vanilloid ligand (red circle). In TRPV2, the S1-S4 domain, along with intracellular ankyrin repeat domains, rotates when the lower gate opens. In TRPV3, the S1-S4 domain tilts towards the PD when the agonist 2-APB (yellow diamond) binds to the S1-S4 domain. TRPV4 gating details are presently unclear, but a unique S1-S4 arrangement causes the S3 helix to contact S6 helix. In TRPV5, the S1-S4 domain tilts away from the PD when the antagonist econazole (dark green hexagon) enters the binding pocket, causing the lower gate to close. In TRPV6, the inhibitor 2-APB (yellow diamond) causes the S3 helix to move toward S4-S5 linker to close the lower gate.

coupling TRPV channel gating.

2.5 Mechanisms of Temperature Gating

Eleven TRP channels from the TRPA, TRPV, TRPC, and TRPM families can integrate biological scale temperature changes into conformational change and eventually signal transduction. These channels, including TRPM8 and TRPV1, are inherently and acutely thermosensitive;[51, 52] however, the mechanisms and conformational changes associated with thermosensing are currently unknown. A number of studies implicate cross-talk between TRP channel thermal and ligand activation, in which small amounts of chemical agonist potentiate the channel to be more temperature sensitive.[53] This is also recapitulated in the aforementioned TRPV3 vanilloid engineering studies in which a form of TRPV3 is RTx insensitive until it has been prestimulated with heat.[27] While chemical and thermal activation are linked to some extent, there is also evidence of distinct mechanistic pathways; for example, TRPV1 channels maximally stimulated with high concentrations of capsaicin nevertheless show increased current when temperature is simultaneously elevated.[54] Reciprosity between chemical and temperature activation has also been observed at the organismal level, for example, chemical-based antagonism of TRPM8 in rodents transiently decreases body temperature.[55] Alternatively, chemical activation of TRPM8 triggers thermogenesis increasing metabolic output and has been suggested as a mechanism to chemically regulate obesity.[56, 57] Indeed, there is a correlation between a species body temperature set point and TRPM8 activation temperature, suggesting that the temperature sensitivity is relatively plastic between orthologs.[20, 58] The fact that a given thermosensitive TRP channel will respond to

temperature in a species dependent manner indicates a potential direction for investigating thermosensing mechanisms.

The regions that are directly sensitive to temperature and mechanisms that underlie the structural rearrangements are not currently clear and diverse regions have been implicated in modulating thermosensing.[14, 59-61] Nonetheless, the thermodynamics that forms the basis of TRP channel temperature sensitivity likely mirror standard protein folding/unfolding frameworks. Suitably large temperature-induced thermodynamic driving forces can arise from entropic and enthalpic contributions to charged or hydrophobic residues sequestered to or released from the hydrophobic membrane bilayer (entropic) or the aqueous environment and balanced by local changes in secondary structure, such as an α-helix forming or unfurling (enthalpic) to give biologically accessible changes in free energy. One can also think about the conformational changes in terms of changes in heat capacity (ΔCp); however, ΔCp can be thought of in terms of how temperature impacts enthalpy, entropy, or free energy. Similarly, it has long been recognized that the hydrophobic effect is temperature dependent suggesting that changes in hydrophobic exposure as a function of temperature is likely key to the high magnitude TRP channel thermosensitivity. Experimental data supporting these thermodynamic principles are beginning to emerge. For example, engineering changes in hydrophobic accessibility of a temperature insensitive voltage-gated potassium ion channel endowed the channel to be temperature sensitive.[62] A separate study performed a high-throughput functional screen of ~7,300 random mutants of rat TRPV1 for ligand and temperature sensitivity.[63] This impressive feat did not

explicitly identify the structural domains or mechanisms that give rise to thermosensitivity, but two crucial insights emerge from the data. First, TRPV1 mutations that decrease hydrophobicity are generally less tolerated for retention of temperature activation relative to chemical activation by capsaicin. Second, in general all TRPV1 regions and domains are functionally tolerant to incorporation of mutations, emphasizing that allosteric networks across the channel must be important. Still, there are hints that the core thermosensing regions are found in the TMD and that these structural domains are sufficient for temperature activation. For example, the engineered temperature-sensing voltage-gated potassium channel mentioned above, relied exclusively on mutations in the equivalent S1-S4 domain, indicating that a single domain can be sufficient to confer thermosensitivity.[62] On the other hand, transferring the TRPV1 PD to a non-thermosensitive channel scaffold is also sufficient to confer thermosensitivity.[64] Although these results implicate different regions in thermosensing, it is noteworthy that they are both in the transmembrane domain. Given that the TMD is the most conserved feature across TRP channels, it seems likely that this region is central to mechanisms of thermal activation.

While the key regions involved in thermosensing may be narrowed down to the TMD, studies attempting to identify more specific domains responsible for temperature activation have given seemingly contradictory results, as illustrated by the following examples of TRPV1, TRPM8, and TRPA1. This lack of an identified thermosensing domain suggests allosteric modulation is also present in thermosensing. The first high-resolution TRP channel structure was a cryo-EM structure of a truncated rat TRPV1.[9]

The rTRPV1 truncation removed 109 residues from the N-terminus, 23 residues from the pore turret, and, and 74 residues from the distal C-terminus. The final construct represents 632/838 residues or about 75% of the wild-type rat protein. Despite these deletions, the truncated channel behaves well structurally and recapitulates the general features of the biological channel including sensitivity to capsaicin and other vanilloids, pH, and elevated temperatures. In an unrelated study of mouse TRPV1 thermosensitivity, it was found that exchanging a 14 residue subset of the pore turret in mouse TRPV1 for an artificial polyglycine sequence abolishes temperature sensitivity while retaining vanilloid sensitivity.[54] Strikingly in the minimal rat TRPV1 structural construct, the exact pore turret region is deleted with no effect on thermosensitivity. Presumably, this suggests that parts of the pore turret in the PD form an allosteric network that modulates thermosensitivity but is not crucial mechanistically.

Differences in thermosensing between TRPM8 orthologs have been used to gain a foothold in identifying domains or residues that are mechanistically important, but again the results have been difficult to interpret. A recent study leveraged the fact that mouse TRPM8 is more cold sensitive than chicken TRPM8. Swapping the pore loop was sufficient to recapitulate the relative differences suggesting that this region either directly or allosterically modulates TRPM8 cold sensitivity.[65] This region overlaps with the pore loop in TRPV1 mentioned above that allosterically modulates thermosensitivity. Another recent study of TRPM8 orthologs showed that the TRPM8 from hibernating rodents retained menthol chemical activation but was poorly activated by temperatures.[58] By swapping the TMD from rat TRPM8, which is potently activated by

cold, that cold-sensitivity could be transferred to the less sensitive hibernating rodent TRPM8 channel. Of the 15 amino acids that vary between rat and a hibernating squirrel TRPM8, exchanging six amino acids between the rat and squirrel orthologs was sufficient to alter the cold sensitivity without affecting chemical sensitivity. All six residues were absolutely required to swap the cold sensitivity; swapping any five particular residues was not sufficient to transfer the phenotype between channels. Two key points emerge from these studies: first, allosteric coupling across the membrane likely contributes to the observed effects, because five of the six residues are on the extracellular side, one is on the intracellular side, and none reside in transmembrane helices (Figure 2.4B). Second, two of the six hibernating rodent residues are identical with the equivalent human TRPM8 residues; as human TRPM8 is robustly cold-sensitive, this suggests that not only is there allosteric coupling, but there must also be compensation between networks of residues.

TRPA1 provides a final example of thermosensation regulation by allosteric networks. TRPA1 can be either hot– or cold–sensing depending on the species.[15] Mutating three amino acid residues that cluster to a discrete soluble ankyrin repeat domain in mouse TRPA1 can flip the cold sensing channel to warm sensing.[15] However, TRPA1 truncations that completely remove this large N-terminal region result in channels that are still temperature sensitive; therefore, the fundamental origins of temperature sensitivity of TRPA1 seem to reside in the transmembrane region.[66]

2.6 Conclusions and Outlook

The intersection of structural and genetic revolutions has provided tremendous tools and insight into how TRP channels function. An emergent property of these channels is the identification of the fundamental role of allostery in function. We speculate the centrality of allosteric networks in TRP channel regulation arises primarily because of the evolution of these channels to function in thermosensing, where biologically accessible changes in temperature are poor thermodynamic driving forces. Current studies have identified the importance of both the S1-S4 and PD in sensing, binding, and coupling to gating, giving a platform to better understand the molecular mechanisms that underlie basic biological processes such as tasting spiciness or feeling cold. Despite the significant progress in recent years, there is a need to dissect these channels with spectroscopic tools such as EPR,[67] fluorescence,[68, 69] and NMR.[38] These tools should unravel the allosteric networks that seemingly make allosteric coupling so challenging to interpret from current structural and functional measurements. Understanding these basic mechanisms will provide access to the fundamental rules of mechanistic cross talk and will also reveal opportunities for pharmacological intervention and manipulation.

2.7 References

1. Nilius, B. and G. Owsianik, The transient receptor potential family of ion channels. *Genome Biol,* 2011. **12**(3): p. 218.

2. Rohacs, T., Phosphoinositide regulation of TRP channels. *Handb Exp Pharmacol,* 2014. **223**: p. 1143-76.

3. Ciardo, M.G. and A. Ferrer-Montiel, Lipids as central modulators of sensory TRP channels. *Biochim Biophys Acta Biomembr,* 2017. **1859**(9 Pt B): p. 1615-1628.

4. Numazaki, M., et al., Direct phosphorylation of capsaicin receptor VR1 by protein kinase Cepsilon and identification of two target serine residues. *J Biol Chem,* 2002. **277**(16): p. 13375-8.

5. Bhave, G., et al., Protein kinase C phosphorylation sensitizes but does not activate the capsaicin receptor transient receptor potential vanilloid 1 (TRPV1). *Proc Natl Acad Sci U S A,* 2003. **100**(21): p. 12480-5.

6. Studer, M. and P.A. McNaughton, Modulation of single-channel properties of TRPV1 by phosphorylation. *J Physiol,* 2010. **588**(Pt 19): p. 3743-56.

7. Liu, J., et al., Phosphorylation of TRPV1 by cyclin-dependent kinase 5 promotes TRPV1 surface localization, leading to inflammatory thermal hyperalgesia. *Exp Neurol,* 2015. **273**: p. 253-62.

8. Cao, E., et al., TRPV1 structures in distinct conformations reveal activation mechanisms. *Nature,* 2013. **504**(7478): p. 113-8.

9. Liao, M., et al., Structure of the TRPV1 ion channel determined by electron cryo-microscopy. *Nature,* 2013. **504**(7478): p. 107-12.

10. Hellwig, N., et al., Homo- and heteromeric assembly of TRPV channel subunits. *J Cell Sci,* 2005. **118**(Pt 5): p. 917-28.

11. Staruschenko, A., N.A. Jeske, and A.N. Akopian, Contribution of TRPV1-TRPA1 interaction to the single channel properties of the TRPA1 channel. *J Biol Chem,* 2010. **285**(20): p. 15167-77.

12. Bidaux, G., et al., Regulation of activity of transient receptor potential melastatin 8 (TRPM8) channel by its short isoforms. *J Biol Chem,* 2012. **287**(5): p. 2948-62.

13. Shin, Y.C., et al., TRIP database 2.0: a manually curated information hub for accessing TRP channel interaction network. *PLoS One,* 2012. **7**(10): p. e47165.

14. Hilton, J.K., et al., Understanding thermosensitive transient receptor potential channels as versatile polymodal cellular sensors. *Biochemistry,* 2015. **54**(15): p. 2401-13.

15. Jabba, S., et al., Directionality of temperature activation in mouse TRPA1 ion channel can be inverted by single-point mutations in ankyrin repeat six. *Neuron,* 2014. **82**(5): p. 1017-31.

16. Hilton, J.K., et al., Phosphoinositide-interacting regulator of TRP (PIRT) has opposing effects on human and mouse TRPM8 ion channels. *J Biol Chem,* 2018. **293**(24): p. 9423-9434.

17. Montell, C. and G.M. Rubin, Molecular characterization of the drosophila trp locus: A putative integral membrane protein required for phototransduction. *Neuron,* 1989. **2**(4): p. 1313-1323.

18. Lange, M., et al., The Transient Receptor Potential (TRP) Channel Family in Colletotrichum graminicola: A Molecular and Physiological Analysis. *PLoS One,* 2016. **11**(6): p. e0158561.

19. Majhi, R.K., et al., Expression of temperature-sensitive ion channel TRPM8 in sperm cells correlates with vertebrate evolution. *PeerJ,* 2015. **3**: p. e1310.

20. Myers, B.R., Y.M. Sigal, and D. Julius, Evolution of thermal response properties in a cold-activated TRP channel. *PLoS One,* 2009. **4**(5): p. e5741.

21. Ovchinnikov, S., et al., Large-scale determination of previously unsolved protein structures using evolutionary information. *Elife,* 2015. **4**: p. e09248.

22. Nicoludis, J.M. and R. Gaudet, Applications of sequence coevolution in membrane protein biochemistry. *Biochim Biophys Acta Biomembr,* 2018. **1860**(4): p. 895-908.

23. Yang, F., et al., Structural mechanism underlying capsaicin binding and activation of the TRPV1 ion channel. *Nat Chem Biol,* 2015. **11**(7): p. 518-524.

24. Yang, F., et al., The conformational wave in capsaicin activation of transient receptor potential vanilloid 1 ion channel. *Nat Commun,* 2018. **9**(1): p. 2879.

25. Yang, F., et al., Rational design and validation of a vanilloid-sensitive TRPV2 ion channel. *Proc Natl Acad Sci U S A,* 2016. **113**(26): p. E3657-66.

26. Zhang, F., et al., Engineering vanilloid-sensitivity into the rat TRPV2 channel. *Elife,* 2016. **5**.

27. Zhang, F., K.J. Swartz, and A. Jara-Oseguera, Conserved allosteric pathways for activation of TRPV3 revealed through engineering vanilloid-sensitivity. *Elife,* 2019. **8**.

28. Gao, Y., et al., TRPV1 structures in nanodiscs reveal mechanisms of ligand and lipid action. *Nature,* 2016. **534**(7607): p. 347-51.

29. Zubcevic, L., et al., Cryo-electron microscopy structure of the TRPV2 ion channel. *Nat Struct Mol Biol,* 2016. **23**(2): p. 180-186.

30. Hughes, T.E.T., et al., Structural basis of TRPV5 channel inhibition by econazole revealed by cryo-EM. *Nat Struct Mol Biol,* 2018. **25**(1): p. 53-60.

31. McGoldrick, L.L., et al., Opening of the human epithelial calcium channel TRPV6. *Nature,* 2018. **553**(7687): p. 233-237.

32. Autzen, H.E., et al., Structure of the human TRPM4 ion channel in a lipid nanodisc. *Science,* 2018. **359**(6372): p. 228-232.

33. Samanta, A., et al., Structural insights into the molecular mechanism of mouse TRPA1 activation and inhibition. *J Gen Physiol,* 2018. **150**(5): p. 751-762.

34. Demeuse, P., R. Penner, and A. Fleig, TRPM7 channel is regulated by magnesium nucleotides via its kinase domain. *J Gen Physiol,* 2006. **127**(4): p. 421-34.

35. Iordanov, I., et al., The proposed channel-enzyme transient receptor potential melastatin 2 does not possess ADP ribose hydrolase activity. *Elife,* 2016. **5**.

36. Bandell, M., et al., High-throughput random mutagenesis screen reveals TRPM8 residues specifically required for activation by menthol. *Nat Neurosci,* 2006. **9**(4): p. 493-500.

37. Voets, T., et al., TRPM8 voltage sensor mutants reveal a mechanism for integrating thermal and chemical stimuli. *Nat Chem Biol,* 2007. **3**(3): p. 174-82.

38. Rath, P., et al., Implications of Human Transient Receptor Potential Melastatin 8 (TRPM8) Channel Gating from Menthol Binding Studies of the Sensing Domain. *Biochemistry,* 2016. **55**(1): p. 114-24.

39. Bidaux, G., et al., Epidermal TRPM8 channel isoform controls the balance between keratinocyte proliferation and differentiation in a cold-dependent manner. *Proc Natl Acad Sci U S A,* 2015. **112**(26): p. E3345-54.

40. Yin, Y., et al., Structural basis of cooling agent and lipid sensing by the cold-activated TRPM8 channel. *Science,* 2019.

41. Takaishi, M., et al., Reciprocal effects of capsaicin and menthol on thermosensation through regulated activities of TRPV1 and TRPM8. *J Physiol Sci,* 2016. **66**(2): p. 143-55.

42. Wright, C.E., et al., Identification of the L-menthol binding site in guinea-pig lung membranes. *Br J Pharmacol,* 1998. **123**(3): p. 481-6.

43. Macpherson, L.J., et al., More than cool: promiscuous relationships of menthol and other sensory compounds. *Mol Cell Neurosci,* 2006. **32**(4): p. 335-43.

44. Karashima, Y., et al., Bimodal action of menthol on the transient receptor potential channel TRPA1. *J Neurosci,* 2007. **27**(37): p. 9874-84.

45. Colton, C.K. and M.X. Zhu, 2-Aminoethoxydiphenyl borate as a common activator of TRPV1, TRPV2, and TRPV3 channels. *Handb Exp Pharmacol,* 2007(179): p. 173-87.

46. Kovacs, G., et al., Inhibition of the human epithelial calcium channel TRPV6 by 2-aminoethoxydiphenyl borate (2-APB). *Cell Calcium,* 2012. **52**(6): p. 468-80.

47. Singh, A.K., et al., Structural bases of TRP channel TRPV6 allosteric modulation by 2-APB. *Nat Commun,* 2018. **9**(1): p. 2465.

48. Singh, A.K., L.L. McGoldrick, and A.I. Sobolevsky, Structure and gating mechanism of the transient receptor potential channel TRPV3. *Nat Struct Mol Biol,* 2018. **25**(9): p. 805-813.

49. Zubcevic, L., et al., Conformational ensemble of the human TRPV3 ion channel. *Nat Commun,* 2018. **9**(1): p. 4773.

50. Hu, H., et al., Two amino acid residues determine 2-APB sensitivity of the ion channels TRPV3 and TRPV4. *Proc Natl Acad Sci U S A,* 2009. **106**(5): p. 1626-31.

51. Cao, E., et al., TRPV1 channels are intrinsically heat sensitive and negatively regulated by phosphoinositide lipids. *Neuron,* 2013. **77**(4): p. 667-79.

52. Zakharian, E., et al., Inorganic polyphosphate modulates TRPM8 channels. *PLoS One,* 2009. **4**(4): p. e5404.

53. Voets, T., et al., The principle of temperature-dependent gating in cold- and heat-sensitive TRP channels. *Nature,* 2004. **430**(7001): p. 748-54.

54. Yang, F., et al., Thermosensitive TRP channel pore turret is part of the temperature activation pathway. *Proc Natl Acad Sci U S A,* 2010. **107**(15): p. 7083-8.

55. Gavva, N.R., et al., Transient receptor potential melastatin 8 (TRPM8) channels are involved in body temperature regulation. *Mol Pain,* 2012. **8**: p. 36.

56. Ma, S., et al., Activation of the cold-sensing TRPM8 channel triggers UCP1-dependent thermogenesis and prevents obesity. *J Mol Cell Biol,* 2012. **4**(2): p. 88-96.

57. Rossato, M., et al., Human white adipocytes express the cold receptor TRPM8 which activation induces UCP1 expression, mitochondrial activation and heat production. *Mol Cell Endocrinol,* 2014. **383**(1-2): p. 137-46.

58. Matos-Cruz, V., et al., Molecular Prerequisites for Diminished Cold Sensitivity in Ground Squirrels and Hamsters. *Cell Rep,* 2017. **21**(12): p. 3329-3337.

59. Yao, J., B. Liu, and F. Qin, Modular thermal sensors in temperature-gated transient receptor potential (TRP) channels. *Proc Natl Acad Sci U S A,* 2011. **108**(27): p. 11109-14.

60. Wen, H. and W. Zheng, Decrypting the Heat Activation Mechanism of TRPV1 Channel by Molecular Dynamics Simulation. *Biophys J,* 2018. **114**(1): p. 40-52.

61. Zheng, W. and H. Wen, Heat activation mechanism of TRPV1: New insights from molecular dynamics simulation. *Temperature,* 2019: p. 1-12.

62. Chowdhury, S., B.W. Jarecki, and B. Chanda, A molecular framework for temperature-dependent gating of ion channels. *Cell,* 2014. **158**(5): p. 1148-1158.

63. Sosa-Pagan, J.O., E.S. Iversen, and J. Grandl, TRPV1 temperature activation is specifically sensitive to strong decreases in amino acid hydrophobicity. *Sci Rep,* 2017. **7**(1): p. 549.

64. Zhang, F., et al., Heat activation is intrinsic to the pore domain of TRPV1. *Proc Natl Acad Sci U S A,* 2018. **115**(2): p. E317-E324.

65. Pertusa, M., et al., Critical role of the pore domain in the cold response of TRPM8 channels identified by ortholog functional comparison. *J Biol Chem,* 2018. **293**(32): p. 12454-12471.

66. Moparthi, L., et al., Human TRPA1 is intrinsically cold- and chemosensitive with and without its N-terminal ankyrin repeat domain. *Proc Natl Acad Sci U S A,* 2014. **111**(47): p. 16901-6.

67. Velisetty, P., et al., Expression and Purification of the Pain Receptor TRPV1 for Spectroscopic Analysis. *Sci Rep,* 2017. **7**(1): p. 9861.

68. Zagotta, W.N., et al., Measuring distances between TRPV1 and the plasma membrane using a noncanonical amino acid and transition metal ion FRET. *J Gen Physiol,* 2016. **147**(2): p. 201-16.

69. Steinberg, X., et al., Conformational dynamics in TRPV1 channels reported by an encoded coumarin amino acid. *Elife,* 2017. **6**: p. e28626.

CHAPTER 3

EVIDENCE THAT THE TRPV1 S1-S4 MEMBRANE DOMAIN CONTRIBUTES TO THERMOSENSING

Reproduced with permission from Minjoo Kim, Nicholas J. Sisco, Jacob K. Hilton, Camila M. Montano, Manuel A. Castro, Brian R. Cherry, Marcia Levitus, and Wade D. Van Horn. Published in bioRxiv, doi: https://doi.org/10.1101/711499

3.1 Abstract

Sensing and responding to temperature is crucial in biology. The TRPV1 ion channel is a well-studied heat-sensing receptor that is also activated by vanilloid compounds including capsaicin. Despite significant interest, the molecular underpinnings of thermosensing have remained elusive. The TRPV1 S1-S4 membrane domain couples chemical ligand binding to the pore domain during channel gating. However, the role of the S1-S4 domain in thermosensing is unclear. Evaluation of the isolated human TRPV1 S1-S4 domain by solution NMR, Far-UV CD, and intrinsic fluorescence shows that this domain undergoes a non-denaturing temperature-dependent transition with a high thermosensitivity. Further NMR characterization of the temperature-dependent conformational changes suggests the contribution of the S1-S4 domain to thermosensing shares features with known coupling mechanisms between this domain with ligand and pH activation. Taken together, this study shows that the TRPV1 S1-S4 domain contributes to TRPV1 temperature-dependent activation.

3.2 Introduction

Transient receptor potential (TRP) ion channels are a family of membrane proteins which play diverse roles in physiology [1, 2]. TRPV1, from the vanilloid subfamily, is responsive to various chemical and physical stimuli, including vanilloid ligands, elevated temperature, protons, endogenous lipids, and small modulatory membrane proteins [3-6]. While TRPV1 is expressed in neuronal and non-neuronal tissues, its role in neuronal tissues has garnered significant interest [7]. For example, in group C unmyelinated nerve tissue of the peripheral nervous system, TRPV1 is integral to nociception (pain) [8, 9]. Consequentially, there is interest in TRPV1 therapeutic intervention for various pain indications [8]. Beyond nociception, an increasing number of studies provide emerging evidence that TRPV1 is involved in diverse human physiologies and pathophysiologies including: inflammatory diseases [10-12], obesity [13, 14], diabetes [11], longevity [15], and cancer [16, 17].

Cryo-electron microscopy (cryo-EM)-based structural biology has had significant impact on understanding the molecular architecture that underlies TRP channel function [18]. These structures have shown that TRP channels resemble the transmembrane topology of voltage-gated ion channels (VGICs), with two conserved transmembrane structural domains. The S1-S4 transmembrane helices (S1-S4 domain) form a four-helix bundle that is structurally related to the voltage-sensing domain (VSD) in VGICs. In TRP channels, like their evolutionary ancestors in the VGIC superfamily, the S5-S6 transmembrane helices form the pore domain (PD), which assembles into a tetrameric channel. In addition to the identifying topological features, a number of TRPV1

structures in different states have been determined, which have provided significant insight into the molecular basis for TRPV1 chemical activation [19-21]. Canonical TRPV1 vanilloid compounds, like the pungent agonist capsaicin, bind to the S1-S4 domain which couples with the PD to open the lower and upper gates of the channel [22], thereby initiating signal transduction. The cryo-EM determined vanilloid binding site [19-21] is consistent with previous studies [23-28], which identified residues in the S3 and S4 helices of the TRPV1 S1-S4 domain as central for capsaicin activation.

Several TRP channels are exquisitely sensitive to changes in temperature and function as molecular thermometers. The temperature-induced activation of thermosensitive TRP channels generates large changes in enthalpy (ΔH) and significant compensating changes in entropy (ΔS), resulting in biologically accessible changes in free energy (ΔG) between closed and open states. Typically to assess thermosensitivity of biological systems, the temperature coefficient (Q_{10}) is measured, which is simply the ratio of equilibrium constants measured 10 °C apart. The temperature coefficient is related to the change in enthalpy [29], and thermosensitive TRP channels like TRPV1 have large Q_{10} and ΔH values of ~40 and ~100 kcal/mol, respectively [30, 31]. The physical mechanisms that underlie temperature sensitivity are thought to arise from changes in secondary structure and hydrophobic/hydrophilic accessibility, both of which have large thermodynamic signatures [1, 29, 32, 33]. Notwithstanding, the region (or regions) within TRP channels that are key to thermosensing remains controversial. As a result, the specific biochemical and structural mechanisms that give rise to TRP channel temperature sensing are also not well understood. However, important contributions have

been made to investigating TRPV1 thermosensing. For example, studies of the purified TRPV1 channel clearly show that the channel is intrinsically thermosensitive [34]. Similarly, an isoform of murine TRPV1 that lacks the majority of the N-terminus remains thermosensitive [35], suggestive that the transmembrane region is central to thermosensing. More recently, a chimeric study which swapped the TRPV1 PD into a non-thermosensing channel, was able to endow thermosensitivity in the chimeric channel [36]. Despite these studies, the mechanism of TRPV1 thermosensing has remained elusive.

Given the role of the TRPV1 S1-S4 domain (V1-S1S4) in ligand activation and the structural similarity to voltage-sensing domains in VGICs, we hypothesize that the S1-S4 domain may contribute to the thermosensitivity of TRPV1. We adopt a distinct strategy that is not reliant on mutagenesis but instead focuses on direct temperature-dependent characterization of the hV1-S1S4, an evolutionarily conserved structural domain (Fig. 1). Here, we show that an isolated hV1-S1S4 is in a biologically relevant state, is sufficient for vanilloid ligand binding, and retains the expected secondary structure and membrane topology. Temperature-dependent studies of the hV1-S1S4 using solution nuclear magnetic resonance (NMR) spectroscopy identify a two-state transition between folded conformational states. The magnitude of the NMR detected temperature sensitivity is supported by far-UV circular dichroism (CD) and intrinsic tryptophan fluorescence spectroscopy. Quantitative comparison with whole-cell patch-clamp electrophysiology experiments in mammalian cells indicates that the hV1-S1S4 significantly contributes to TRPV1 thermosensitivity. Additionally, the temperature-

dependent conformational changes were examined by NMR-based temperature-dependent distance measurements from paramagnetic relaxation enhancement (PRE), secondary structure measurements from chemical shift assignment and residual dipolar coupling, and solvent exposure from deuterium/hydrogen exchange and water–protein NOEs. To validate these outcomes, we introduced a mutation that disrupts coupling between the S1-S4 and pore domains and show that both ligand and temperature activation are abrogated in the full-length channel but retained in the isolated domain. Taken together, the data provide thermodynamic and mechanistic insight into the properties of thermosensitive TRP channels and suggests an overlap between TRPV1 ligand, proton (pH), and temperature activation.

3.3 Results

3.3.1 The Isolated hV1-S1S4 Resides in a Biologically Relevant State

3.3.1.1 The hV1-S1S4 in Isolation Retains the Expected Membrane Topology

The transmembrane hV1-S1S4 construct includes the pre-S1 helix through the S4 helix (residues 417 to 558) (Figure 3.1A). Optimization of hV1-S1S4 expression resulted in ~1.5 mg of purified protein per liter of M9 media. The identity of the hV1-S1S4 was verified by SDS-PAGE, western blot, LC-MS/MS, and ultimately NMR resonance assignment (Figure S3.1A-C). After membrane mimic screening, the hV1-S1S4 was reconstituted in LPPG (1-palmitoyl-2-hydroxy-*sn*-glycero-3-phospho-(1'-*rac*-glycerol)) lysolipid micelles, which yielded high-quality NMR spectra (Figure S3.1D). We focused on single chain membrane mimics, such as LPPG, to avoid temperature-dependent phase transitions common to lipids that could interfere with temperature-dependent

thermodynamic and biophysical characterization. TROSY-based 3D and 4D NMR experiments were carried out to assign the hV1-S1S4 amide backbone. Specifically, TROSY-based HNCA, HNCOCA, HNCO, HNCACB, CBCACONH, HNCACO, ^{15}N-edited-NOESY-TROSY, 4D HNCACO and 4D HNCOCA were used to assign 87% of backbone resonances (BMRB ID: 27029, Figure 3.1B and Figure S3.1E-J). The hV1-S1S4 membrane topology was determined from secondary structure derived from backbone chemical shift data (TALOS-N) and membrane accessibility from NMR-detected deuterium-hydrogen (D/H) exchange factors (Figure 3.1C, D). The resulting hV1-S1S4 secondary structure in solution at elevated temperature is similar to existing rat TRPV1 cryo-EM structures. Similarly, the D/H exchange factors show that the transmembrane helices have lower exchange factors than the solvent accessible loop regions, indicative of the expected membrane topology for this domain.

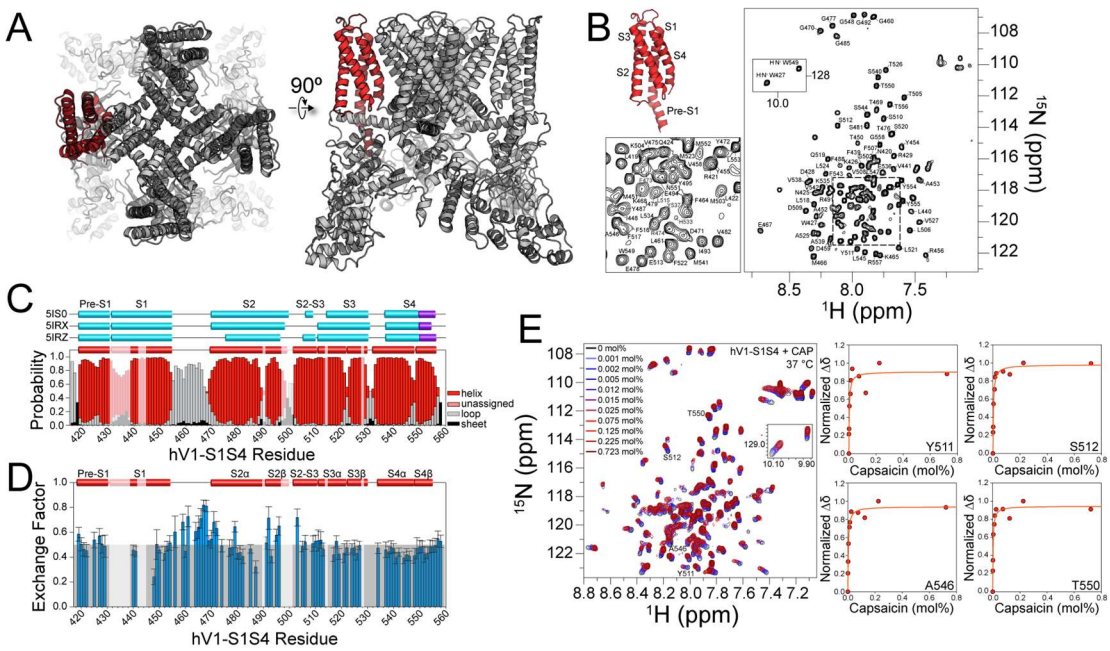

Figure 3.1 The isolated human TRPV1 S1-S4 domain is folded in a biologically relevant state and binds capsaicin at elevated temperatures. (**A**) Highlighted in red is the hV1-S1S4 construct shown in the rTRPV1 cryo-EM structure (PDB ID: 3J5P) and used throughout our studies. (**B**) Representative ^{15}N-TROSY-HSQC showing the hV1-S1S4 backbone resonance assignments at 45 °C. (**C**) Cryo-EM determined secondary structure information of rTRPV1 (cyan/purple) compared with the NMR determined secondary structure (red) from hV1-S1S4 at 45 °C identifies the similarities and differences in secondary structure. The S4 3_{10} helix is shown in purple. (**D**) Deuterium/hydrogen (D/H) exchange factors show the hV1-S1S4 solvent accessibility is consistent with the anticipated membrane topology. (**E**) Superimposed ^{1}H-^{15}N HSQC spectra of the hV1-S1S4 titration with capsaicin at 37 °C. Canonical capsaicin binding residues include Y511, S512, and T550, and A546, show saturating binding isotherms as a function of capsaicin.

3.3.1.2 The hV1-S1S4 Domain Specifically Binds Capsaicin

The isolated hV1-S1S4 solubilized in LPPG retains the ability to specifically bind capsaicin at 37 °C (Figure 3.1E). Previously identified capsaicin binding residues, Y511, S512, and T550, were used as probes of capsaicin binding. These residues showed saturable chemical shift perturbation as a function of increased capsaicin concentration

which is indicative of specific binding (Figure 3.1E). The average K_d values from the key vanilloid binding residues (Y511, S512, and T550) is 3.4 ± 0.4 mmol%. L547 (M547 in the rat ortholog) has also been ascribed importance in vanilloid binding and activation; however, due to resonance overlap this residue could not be analyzed. A neighboring residue, A546, which is located within 5 Å of vanilloid ligand as shown a vanilloid-bound TRPV1 structure (PDB ID: 5IRX), also exhibited saturating binding with a K_d value of 3.6 ± 0.5 mmol% (Figure 3.1E). Taken together, the isolated hV1-S1S4 in solution retains four transmembrane embedded helices and recapitulates expected features of capsaicin binding, indicating that the isolated hTRPV1-S1S4 retains a biologically-relevant conformation in solution and at elevated temperatures.

3.3.2 Two-State Temperature Transition and Thermodynamic Analysis of the Full-Length Human TRPV1

TRPV1 temperature-dependent electrophysiology data have been shown to fit well to a simple two-state thermodynamic model between open (active) and closed (resting) states [2]. While this is certainly an oversimplification, modeling TRPV1 temperature-dependent transitions allows for quantification of the thermosensitivity. In this two-state model the temperature-dependent slope of the transition between conformational states reflects the change in enthalpy (ΔH) [37] and is a read out of the thermosensitivity associated with the conformational change between temperatures.

To date the majority of TRPV1 thermosensing studies have focused on rodent orthologs (Table S3.1). To evaluate the thermosensitivity of the human TRPV1 ortholog, whole-cell patch-clamp electrophysiology measurements were performed using the full-

length wild-type human TRPV1 in HEK293 cells. We employed two distinct methods to measure the thermosensitivity (ΔH) of human TRPV1 in cellular conditions. First, steady-state current values were measured at +60 mV as a function of increasing temperature (Figure S3.2A). The normalized current values were plotted against temperature and fit to a two-state model representing closed (resting) and open (active) states resulting in a measured ΔH of 98 ± 12 kcal/mol (Figure 3.2A). Independently, we used a second method involving temperature ramps from 20 to 50 °C and fit the data to a pseudo-steady state thermodynamic model to obtain hTRPV1 ΔH values (see Methods), resulting in an average ΔH of 94 ± 8 kcal/mol (Figure S3.2B). The ΔH values of human TRPV1 measured from the steady-state current and the temperature ramp methods are consistent with those of rodent TRPV1 from previous studies, which is ~90 kcal/mol (Table S3.1).

3.3.3 Two-State Temperature Transition and Thermodynamic Analysis of the hV1-S1S4 Domain

To investigate a potential role of the hV1-S1S4 in thermosensitivity, far-UV circular dichroism (CD) and solution NMR spectra were recorded at 20 °C and 50 °C; temperatures that would be expected to correspond to distinct conformational states if the hV1-S1S4 were to contribute to thermosensitivity. First, the CD spectra at 20 °C and 50 °C displayed characteristic α-helical minima at 208 and 222 nm. These spectral features were retained at both high and low temperatures, suggestive that the protein does not significantly unfold under these conditions (Figure S3.2C, D). Additionally, the ^{1}H-^{15}N TROSY-HSQC NMR spectra of hV1-S1S4 at these two temperatures (20 °C and 50 °C) provide qualitative insight into potential temperature-dependent conformational change

and the foldedness of this domain at the respective temperatures (Figure S3.2E). The NMR proton resonance dispersion and resolution indicate that the hV1-S1S4 remains generally folded over this temperature range. There is also significant temperature dependent chemical shift perturbation between the spectra at 20 °C and 50 °C, which is consistent with a temperature-induced conformational change. The temperature-dependent spectral changes, in both CD and NMR, are completely reversible and indicate that the system is suitable for thermodynamic analysis to assess thermosensitivity (ΔH) of the apparent conformational change (Figure S3.2C-E).

3.3.3.1 CD-Based Temperature-Dependent Studies of hV1-S1S4

CD data collected as a function of temperature have long been used to determine thermodynamic properties of proteins [37]. The hV1-S1S4 CD data exhibit two-state behavior at 222 nm, near the characteristic α-helical minimum, as a function of temperature. Fitting the data to a two-state sigmoidal model yielded a ΔH of 19 ± 1 kcal/mol, which reflects the temperature dependence of the hV1-S1S4 change conformational states (Figure 3.2B). The KCNQ1-voltage-sensing domain (VSD, helices S1-S4) is structurally homologous to the hV1-S1S4; however, it is not directly activated (gated) by thermal stimulus. As a control, we measured the KCNQ1-VSD mean residue ellipticity (MRE) at 222 nm over the same temperature range. The hKCNQ1-VSD did not exhibit two-state behavior, but instead showed a linear temperature response over this temperature range, consistent with a general thermal expansion of the α-helical hydrogen bonds (Figure S3.3A). Comparatively, the lack of measurable thermosensitivity (ΔH) of

the KCNQ1-VSD over this temperature range suggests that the hV1-S1S4 reflects a feature of TRPV1 thermosensitivity.

3.3.3.2 Intrinsic Tryptophan Fluorescence Temperature-Dependent Studies of hV1-S1S4

The hV1-S1S4 was also subjected to temperature-dependent studies using intrinsic tryptophan fluorescence. Typically, intrinsic tryptophan has a large fluorescence transition dipole moment and the position and shape of the emission spectrum is particularly sensitive to the polarity of the environment. Tryptophan (Trp) emission maxima in an apolar (hydrophobic) environment is blue-shifted and varies from ca. 310-335 nm. Whereas emission maxima in polar (hydrogen-bonding) solvents for an unstructured Trp residue is red-shifted about 40 nm up to ca. 355 nm [38]. These characteristics are commonly exploited in protein folding studies, where the emission peak of Trp shifts towards the red as the fraction of unfolded protein increases. In the context of hV1-S1S4, this analysis allows insight into both the thermosensitivity of the transition and the environment of the Trp residues. The hV1-S1S4 has two endogenous Trp residues in the amphipathic pre-S1 helix and the transmembrane S4 helix, both of which are anticipated to be in a hydrophobic environment from cryo-EM structures. Indeed the resulting fluoresce emission spectral maxima are 328 nm at 7.4 °C and 332 nm at 52.0 °C, indicating that over the temperature range studied, the endogenous Trp residues generally retain their membrane embeddedness (Figure S3.3). This observation is consistent with the observations from CD (Figure S3.2C) and NMR (Figure S3.2D) that the hV1-S1S4 remains generally folded across this temperature range. Quantifying

the observed temperature induced spectral shifts in terms of the average emission wavelength ($\langle\lambda\rangle$) identifies a sigmoidal two-state behavior with a ΔH of 24 ± 9 kcal/mol (Figure 3.2C). This thermosensitivity is consistent with the observed CD-detected thermosensitivity (Figure 3.2B).

3.3.3.3 NMR-Detected Temperature-Dependent Studies of hV1-S1S4

A series of ^{1}H-^{15}N TROSY-HSQC spectra of hV1-S1S4 were collected at temperatures ranging from 15 °C to 50 °C (Figure S3.3D). The hV1-S1S4 resonance assignments at 45 °C (Figure 3.1B) were used to assign the temperature series spectra by chemical shift mapping, resulting in assignment of 71 resonances (~51% of the total expected resonances) across the temperature range (15 to 50 °C). The remaining resonances could not be unambiguously identified at all temperatures because of loss of resonance intensity, emergence of resonances, and/or coalescence with other resonances. The resonances that could be assigned across the temperature series show reversible two-state temperature-dependent behavior, as illustrated by representative plots of G548 (Figure 3.2D) and W549 (Figure S3.3E). The two-state temperature-dependent behavior is similar to that observed from CD and fluorescence emission experiments. Fitting the 71 assigned resonances as a function of temperature to the same two-state model used for electrophysiology, CD, and fluorescence, enabled us to evaluate the ΔH value for each individual resonance. Plotting the ΔH values as a function of frequency (Figure 3.2E) suggests the mean ΔH from NMR has similar magnitude as those observed from CD and fluorescence measurements. Fitting these data to a Gaussian distribution results in an average thermosensitivity of ΔH = 21.2 ± 0.1 kcal/mol and a mean T_{50} (reflective of the

inflection point of the sigmoid) of 40.7 ± 0.6 °C (Figure 3.2E and Figure S3.3F). To ensure that the effects observed by NMR, CD, and fluorescence arise from changes in temperature and not pH, the experiments were carried out in sodium phosphate buffer, which is relatively insensitive to temperature-induced pH changes. We measured the change in pH to be ~0.1 units when the temperature of the buffer is varied from 10 to 60 °C (Table S3.1). Also, hV1-S1S4 ^{1}H-^{15}N TROSY-HSQC NMR spectra show no detectible chemical shift perturbation over this pH range, pH 6.5 and 6.4 (Figure S3.3G). Taken together, the far-UV CD, intrinsic tryptophan fluorescence, and solution NMR data indicate that the hV1-S1S4 domain undergoes a temperature-dependent conformational change with a thermosensitivity of ~20 kcal/mol.

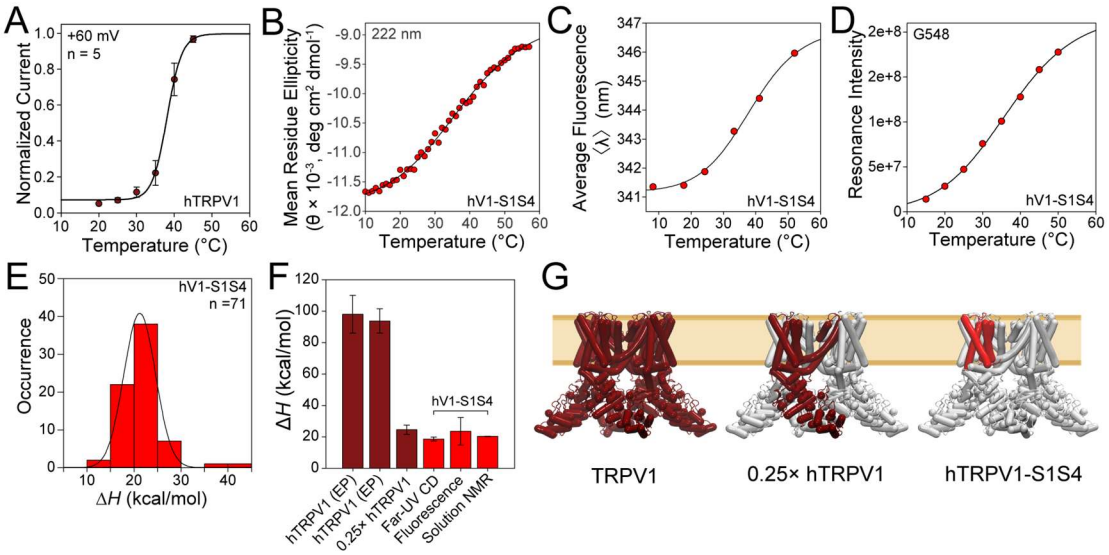

Figure 3.2 Temperature-dependent two-state behavior and thermodynamic analysis of hTRPV1 and hV1-S1S4. (**A**) Whole-cell patch-clamp electrophysiology measurements from a full-length human TRPV1 in HEK293 cells. (**B**) Temperature ramp of hV1-S1S4 monitored by far-UV circular dichroism shows two-state behavior. (**C**) The first moment of intrinsic tryptophan fluorescence of hV1-S1S4 as a function of temperature shows two-state transition similar to that identified by CD. (**D**) Representative NMR resonance intensity, G548 in the S4 helix, shows two-state behavior. G548 was chosen due to its similarity to the mean ΔH obtained from NMR. (**E**) A histogram of 71 enthalpies from NMR resonance intensities are shown in red. These data fit to a Gaussian function (black line) provide an average value of 21.2 ± 0.1 kcal/mol (**F**) Comparison of ΔH values, the first dark red two bars are from the cellular electrophysiology measurements for full-length hTRPV1 from steady state currents (**A**) and temperature ramps. A representative value for one quarter of the steady state value is also shown. The ΔH values from CD, fluorescence, and NMR are shown in red. (**G**) The left panel shows the full-length TRPV1 used for electrophysiology measurements. The middle panel shows the relative size of a TRPV1 monomer. The right panel shows the hV1-S1S4 domain in red, which has similar ΔH as the monomer, showing the relative significance of the hV1-S1S4 in thermosensitivity.

3.3.4 Insights into Temperature-Dependent Conformational Change

3.3.4.1 Differences in Secondary Structure between rTRPV1 and hV1-S1S4

The secondary structure of the hV1-S1S4 at 45 °C was determined from experimental backbone chemical shift data analyzed in TALOS-N (Figure 3.1C) [39]. Comparison of secondary structures of the isolated hV1-S1S4 in solution at elevated temperature with those of the truncated rat TRPV1 structures from cryo-EM [19-21] indicate that the transmembrane topologies are generally consistent (Figure 3.1C). Despite the similarities, there are differences in helicity between the NMR-determined secondary structure of hV1-S1S4 at 45 °C and the low temperature cryo-EM structures (Figure 3.3A). The NMR data indicate that the S2, S3, and S4 helices have short helical kinks that are absent from the TRPV1 cryo-EM structures. Among the cryo-EM structures there are also differences; for example, in the apo structure (PDB ID: 5IRZ), which is the putative resting state structure, the S2 helix begins near R474. However, in the putative ligand-bound structures (PDB ID: 5IS0 and 5IRX) the extracellular side of the S2 helix is about two helical turns longer and begins near residue K468. The NMR data at elevated temperature indicates that the S2 helical conformation reflects that of the ligand bound structures. The NMR data also identify distinct helical content in the S2-S3 linker region, which is at the heart of the vanilloid binding pocket. In the apo and antagonist-bound cryo-EM structures (PDB IDs: 5IRZ and 5IS0 respectivly), the S2-S3 linker adopts a short amphipathic helix that includes residues S505-S510 with a break prior to the start of the S3 helix. Whereas, in the agonist activated structure (PDB ID: 5IRZ), the S2-S3 linker is not helical. The NMR-determined secondary structure is

distinct and shows a near-continuous helix that begins near S502 in the S2-S3 linker and continues through the S3 helix. Additionally, the rTRPV1 structures show that the intracellular side of the S4 helix adopts a 3_{10} helical conformation (Figure 3.1C). In solution at elevated temperatures, the bottom of S4 helix does not adopt a 3_{10} helix but instead has decreased helical probability, most similar to the agonist bound S4 helix (Figure 3.1C).

To further investigate and validate the apparent differences in helicity, we analyzed the secondary amide proton chemical shifts ($\Delta\delta_{HN}$, Figure 3.3B). The proton $\Delta\delta$ values were calculated by taking the difference between an assigned resonance ^1H chemical shift and the same amino acid in a random coil conformation. $\Delta\delta_{HN}$ data typically show a characteristic periodicity in helical regions [40-42]. Changes in $\Delta\delta_{HN}$ were plotted against the hV1-S1S4 residue numbers, and each helix can be fit to a sinusoidal function for α-helices comprising the following amino acids: 419 to 430 for pre-S1, 439 to 456 for S1, 470 to 487 for S2α, 490 to 496 for S2β, 505 to 510 for S2-S3 amphipathic loop, 511 to 522 for S3α, 523 to 527 for S3β, 534 to 546 for S4α, and 547 to 553 for S4β. These data for hV1-S1S4 are consistent with the secondary structure output from TALOS-N. Additionally, the $\Delta\delta_{HN}$ data suggest that the intracellular side of the S4 helix, including residues L553 to G558, is not helical at higher temperature. This is distinct from the consensus 3_{10} helix identified over this region in the cryo-EM rTRPV1 structures. The RMSE values for corresponding helices are 0.26, 0.49, 0.18, 0.15, 0.33, 0.27, 0.22, 0.12, and 0.19 (Figure 3.3B). Helicity can also be determined from NMR residual dipolar coupling (RDC) measurements, where fitting of the data to a

helical sinusoid model can be used to identify alpha-, 3_{10}-, and pi helices. This dipolar wave analysis of RDC data can also differentiate from ideal and kinked helices [43]. ^{1}H-^{15}N RDCs were measured for hV1-S1S4 at 45 °C and used in dipolar wave analysis (Figure 3.3C and Figure S3.4A). The same helices used in the proton Δδ analysis were fit to the same sinusoidal function and the RMSE values (Hz) for these fittings are 2.85, 2.51, 2.08, 1.18, 1.06, 1.31, 2.84, 2.43, 0.69, and 1.42. The outcomes of the RDC data further validate the TALOS-N and $\Delta\delta_{HN}$ chemical shift-based secondary structure identified for the isolated hV1-S1S4 domain in solution at elevated temperatures.

In RDC data, helical distortions can be identified by changes in dipolar wave amplitudes, which are a manifestation of alignment tensor magnitude. Using this metric, the RDC data indicate that hV1-S1S4 in solution has helical distortions in S2, S3, and S4 transmembrane helices consistent with the chemical shift data (Figure 3.3C). RDC analysis of the intracellular S4 helix confirms a lack of helicity at elevated temperature consistent with the $\Delta\delta_{HN}$ data. We note that this region of the S4 segment in both the RDC and $\Delta\delta_{HN}$ data, beginning from L553, do not fit well to any helical subtype, including α-, 3_{10}-, and π helices suggesting that this region in solution at elevated temperature is distinct from that in the rTRPV1 cryo-EM structures.

Amide proton chemical shifts (δ_{HN}) have a characteristic temperature dependence. The relationship between δ_{HN} and temperature is fit to a linear function where the slope of the fit is called the temperature coefficient ($\Delta\delta_{HN}/\Delta T$). $\Delta\delta_{HN}/\Delta T$ values are an indicator of the probability of hydrogen bond formation and generally reflect secondary structure in helical membrane proteins [44, 45]. More specifically, residues that form

intramolecular hydrogen bonds typically have $\Delta\delta_{HN}/\Delta T$ values that are higher than -4.6 ppb/K [44]. The temperature coefficients of the hV1-S1S4 were calculated and plotted against the residue number (Figure 3.3D). Transmembrane helices had an average $\Delta\delta_{HN}/\Delta T$ value of -3.8 ± 0.3 ppb/K, indicating a more structured, hydrogen-bonded state; whereas, the extracellular/intracellular loops had a more negative average $\Delta\delta_{HN}/\Delta T$ value of -5.2 ± 0.5 ppb/K which is indicative of a lack of hydrogen bonding (Figure 3.3D). Coupling the secondary structure analysis of the hV1-S1S4 domain from TALOS-N, $\Delta\delta_{HN}$, and ^{1}H-^{15}N RDCs, with $\Delta\delta_{HN}/\Delta T$ and D/H exchange factor data (Figure 3.1C, D, and Figure 3.3B-D) shows that in solution at elevated temperatures this domain retains the expected transmembrane topology, but with particular changes in helicity that either generally reflect the agonist activated cryo-EM structure or are distinct from the rTRPV1 cryo-EM structures.

3.3.4.2 Temperature-Dependent Distance Changes in hV1-S1S4

To probe the magnitudes and directions of conformational change detected in the temperature titration studies of hV1-S1S4, NMR-detected paramagnetic relaxation enhancement (PRE) distance measurements were made from proton relaxation experiments at 20 °C and 50 °C. These experiments exploit the lone endogenous cysteine residue (C443, S1 helix) in hV1-S1S4 for MTSL labeling, obviating the need to engineer mutations that might impact the potential temperature-dependent structural changes. To ensure the highest possible accuracy of these measurements, six separate samples were prepared, the paramagnetic (three samples) and diamagnetic species (three samples) were each recorded in triplicate at each temperature. To accurately convert the PRE data to

distance information, the rotational correlation times (τ_c) were also directly measured at both temperatures using TRACT (TROSY for rotational correlation times) NMR experiments [46]. Using exclusively the W549 indole amine resonance, which is membrane embedded in the middle of the S4 transmembrane helix, the hV1-S1S4 rotational correlation times at 20 °C and 50 °C were calculated to be 49 ± 3 and 25.6 ± 0.1 ns, respectively (Figure S3.4B, C).

Distances from the residues of the hV1-S1S4 to MTSL-labeled C443 (Figure S3.4D), were obtained at 20 °C and 50 °C. From this data, the differences in PRE distances between 20 °C and 50 °C were calculated ($\Delta PRE_{50\,°C–20\,°C}$) and these values were plotted against as a function of residue number (Figure 3.3E). Given the magnitudes of the temperature-dependent changes in distance, and the proclivity of PRE data to encode both structural and dynamic information, we interpret this data is a qualitative manner. The sign of the ΔPRE values indicate that a given amide proton is moving towards (negative value) or away (positive value) from MTSL-C443. The $\Delta PRE_{50\,°C–20\,°C}$ suggest temperature-driven changes in dynamics or conformational states in the S1-S2 loop, the S2-S3 loop, and the S4 helix C-terminus. The S1-S2 loop has complex data trends suggestive of differences in loop dynamics between temperatures. The S2-S3 loop and S4β helix C-terminus show general trends of movements away from C443. Precise interpretation on these temperature dependent PRE changes are challenging; however, we note that the S1-S2 loop, the S2-S3 loop, and the S4 C-terminus, have been implicated in proton activation [47], ligand binding [20, 23], and ligand coupling [48], respectively.

3.3.4.3 NMR-Detected Temperature-Dependent hV1-S1S4 Changes in Hydration

^{15}N-edited NOESY-TROSY measurements provide through-space distance information between protons up to distances of ~5 Å. NOESY data also provide a measure of solvent exposure via NOE crosspeaks between a given backbone amide proton resonance (H_N) and the water resonance (~4.7 ppm). Since the H_α to H_N distances represent a fixed distance, taking the intensity ratios between the water-H_N cross-peak and the H_α-H_N cross-peak ($I_{water}/I_{H\alpha}$) should reflect a normalized measure of solvent accessibility of a specific backbone amide resonance. Furthermore, taking the difference between the normalized ratios at high and low temperatures ($\Delta NOE_{45\,°C–20\,°C}$) identifies which residues are more (less) solvent exposed to the solvent at a higher (lower) temperature. With this in mind, a positive $\Delta NOE_{45\,°C–20\,°C}$ indicates increased solvent exposure at 45 °C. NOE-based solvent exposure between elevated and lower temperature indicate that for the vast majority (~60% of the observed residues) of hV1-S1S4, the changes in hydration are minimal. However, the S1-S2, S2-S3, and the S3-S4 loops have increased solvent exposure at higher temperatures. Similarly, the S4 helix C-terminus also become more solvent exposed at higher temperatures (Figure 3.3F and Figure S3.5A).

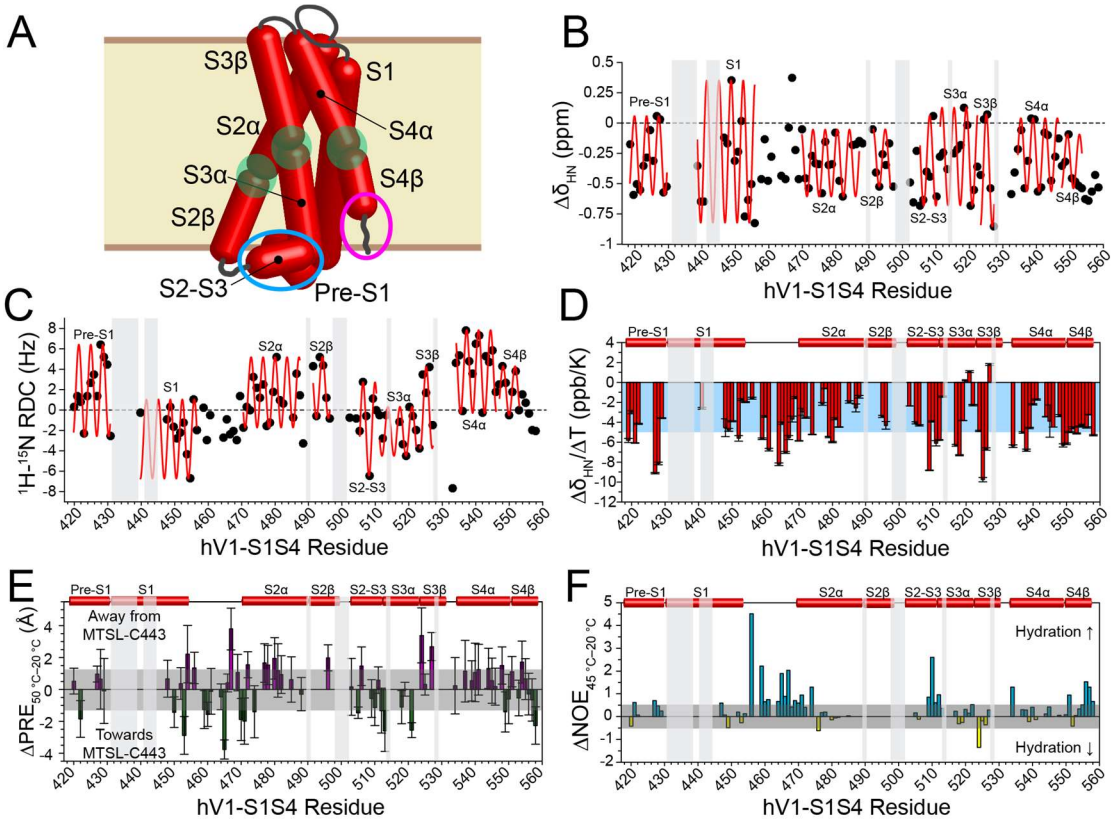

Figure 3.3 hV1-S1S4 undergoes subtle temperature-induced changes in secondary structure, distances, and solvent accessibility. (**A**) A cartoon of hV1-S1S4 secondary structure based on the TALOS-N prediction highlights secondary structural features that are distinct from cryo-EM rTRPV1 structures. Blue and magenta circles indicate increased and decreased helicity, respectively. Breaks in transmembrane helices are shown as transparent green circles. (**B**) Proton Δδ analysis identifies hV1-S1S4 secondary structure at elevated temperature (45 °C). Light grey boxes indicate that these regions where NMR resonances are unassigned. (**C**) Dipolar wave analysis from RDC measurements of the hV1-S1S4 at 45 °C identifies secondary structure. (**D**) A bar plot of the averaged amide proton temperature coefficients ($\Delta\delta_{HN}/\Delta T$) against the hV1-S1S4 residue number. Values greater than -4.6 ppb/K are indicative of hydrogen bonding and are highlighted (blue). (**E**) Temperature dependent differences in distances measured using paramagnetic relaxation enhancement (ΔPRE) of the hV1-S1S4 at 20 °C and 50 °C. The average of the SEM, 1.2 Å, was used as a threshold value and shown in grey. (**F**) Changes in hydration as a function of temperature were measured from normalized H_N–water resonance intensities from ^{15}N-NOESY-TROSY data at 20 °C and 45 °C. The $\Delta NOE_{45\ °C–20\ °C}$ is reflective of changes in hydration where loops and the bottom of S4 helix exhibits increased hydration at elevated temperatures.

3.3.5 The Role of R557 in Coupling between the S1-S4 Domain and the Pore Domain

Our data show that the C-terminus of the S4 helix partially unwinds and becomes more solvent exposed. These movements include the conserved R557, as monitored from the backbone amide with PRE, RDC, chemical shift, and NOESY NMR data. A previous study that R557 in rat TRPV1 is involved in coupling the TRPV1 S1-S4 domain to channel activation in part via a cation-π interaction rearrangement between Y554 and R557 that impacts diverse activation mechanisms, including thermosensing [48]. To probe the role of human R557-TRPV1 in temperature gating, we generated a human TRPV1-R557A mutation for electrophysiology studies. Whole-cell patch-clamp measurements of hTRPV1-R557A corroborate that this mutation inhibits TRPV1 thermosensitivity (Figure 3.4A, B) and using NMR we show that for hV1-S1S4 the R557–water NOE cross-peak is absent at 20 °C and present at 45 °C (Figure 3.4C). These data indicate that R557 in the S4 helix undergoes a temperature dependent change in solvent exposure that is consistent with the ΔPRE measurements. Using NMR temperature titrations with hV1-S1S4-R557A mutant (Figure S3.6A), the resonance intensities retained the sigmoidal two-state model as shown in the representative plot of G548, with a ΔH of 19 ± 2 kcal/mol (Figure 3.4D). Measuring 70 resonance intensities as before with WT, the mean ΔH = 19.7 ± 0.1 kcal/mol and the mean T_{50} = 39 ± 2 °C (Figure 3.4E and Figure S3.6B). We attribute the small decrease in thermosensitivity ($\Delta\Delta H$ = 1.5 ± 0.1 kcal/mol) between the wild-type and R557A mutant of hV1-S1S4 to the loss of the cation-π interaction between R557 and Y554. If R557 couples the S1-S4 domain with the PD, then the R557A mutation should also knock-out capsaicin

activation. Whole-cell patch-clamp electrophysiology of human TRPV1-R557A shows that this mutation indeed silences capsaicin activation (Figure S3.6C). Given the similarities of the thermosensitivity of wild-type and R557A hV1-S1S4, these data suggest that R557 functions to couple motions of the hV1-S1S4 domain and channel gating.

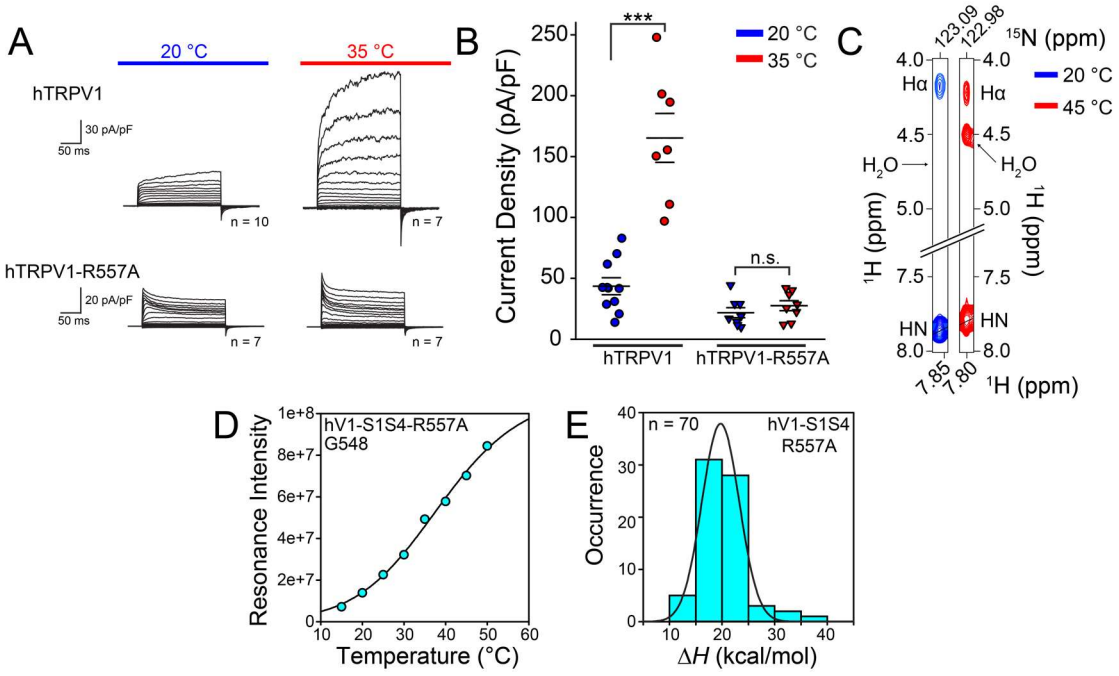

Figure 3.4 R557 is a crucial residue for coupling between the S1-S4 domain to the pore domain. (**A**) and (**B**). Whole-cell patch-clamp electrophysiology data from HEK293 cells show that the wild-type hTRPV1 is heat activated, while the hTRPV1-R557A mutant is not. (**C**) ^{15}N-edited NOESY-TROSY data of R557 water resonance cross peak missing at low temperature but present at elevated temperature, suggesting that R557 amide backbone moves from a membrane embedded to a solvent accessible position in a temperature-dependent manner. (**D**) NMR temperature titration of hV1-S1S4-R557A. G548 in hV1-S1S4-R557A resonance intensities as a function of temperature show two state behavior analogous to the wild-type hV1-S1S4 domain. (**E**) A histogram and a Gaussian distribution fit of ΔH identify a mean $\Delta H = 19.7 \pm 0.1$ kcal/mol for the mutant hV1-S1S4-R557A (n = 70 residues). The data is suggestive of a temperature-dependent conformational change in hV1-S1S4-R557A.

3.4 Discussion

The ability to sense and respond to temperature is fundamental in biology, with a variety of temperature-sensing requirements that vary from low to high temperatures and acute (fast) to environmental (sustained) responses. Acute hot-sensing in higher organisms is sufficiently crucial that the pathway is triply redundant with three distinct heat receptors; the best studied of these is TRPV1 [49]. Similarly, TRPV1 thermosensitivity is tuned in a highly species dependent manner that is correlated with environmental niche. For example, desert dwelling species that are exposed to sustained elevated temperatures are thought to generally have attenuated heat-sensing responses [50]. Many factors have been shown to modulate the temperature response of TRPV1, including chemical ligands, pH, lipids, and proteins. Nonetheless, TRPV1 is intrinsically thermosensitive and the ability to integrate changes in biologically relevant temperatures as a molecular thermometer is a feature inherent to the protein [34]. Despite its importance, the mechanism of TRPV1 thermosensing has been complicated by seemingly contradictory outcomes [1, 2].

In this study, we evaluate the conformational change and thermodynamics of an isolated human TRPV1 S1-S4 domain. We establish that the S1-S4 domain is stable, retains the expected membrane topology, and recapitulates anticipated capsaicin agonist binding, indicating the isolated domain resides in a biologically relevant conformation. These results are consistent with structurally homologous domains studied in isolation from other TRP [51], sodium [52], potassium [42, 53-55], and proton [56] ion channels.

Temperature dependent studies of the hV1-S1S4 monitored by CD, intrinsic tryptophan fluorescence, and solution NMR show that this domain undergoes a two-state temperature-dependent transition, with significant thermosensitivity (ΔH of ~20 kcal/mol). These data also indicate that the domain retains significant structure in both high and low temperature conformations. The energetics associated with this conformational change are large in comparison to other proteins. For example, the enthalpy magnitude of the hV1-S1S4 transition is about twice as large as the well-studied tetrameric hemoglobin system, despite the size of hemoglobin being about four-times larger by mass [29].

Putting hV1-S1S4 thermosensitivity value into the context of the full-length TRPV1 channel will require future studies. The thermosensitivity, or change in enthalpy, between temperature resting and active states of full-length TRPV1, with a consensus value is in the realm of ~100 kcal/mol (see Table S3.1). The value measured here for the full-length human TRPV1 heterologously expressed in mammalian cells is 98 ± 12 kcal/mol or 94 ± 8 kcal/mol, depending on the method used. One challenge with interpreting the thermosensitivity of the isolated hV1-S1S4 relative to the tetrameric TRPV1 in biological conditions is that the cooperativity between monomers during heat-sensing and activation in TRPV1 remains unclear. For hV1-S1S4, which represents ~18% of the channel by mass, could potentially contribute the majority of the thermodynamic driving force (~80%) should the ΔH values of the isolated hV1S1-S4 be additive in nature. On the other hand, if S1-S4 domains allosterically couple very

efficiently in tetrameric channel state, then this domain might contribute as little as ~20 kcal/mol, or ~20% of the thermosensing driving force, to TRPV1 thermosensitivity.

Nonetheless, our results fit in well with the existing literature with the thermodynamic and mechanistic information about TRPV1 and thermosensing in general [18, 32, 36, 57]. For example, studies of a TRPV1 isoform, ΔN-TRPV1, which lacks the majority of the N-terminus, including 5 of 6 ankyrin repeat domains, yet retains sensitivity to physiological changes in temperature, suggests that the core TRPV1 temperature sensing region is isolated to the transmembrane domain [35]. Our data and a recent chimeric study of the Shaker voltage-gated potassium channel (Kv1.2) with the rat TRPV1 pore domain (S5-S6 helices, residues 575-687) suggest that both membrane domains likely contribute to thermosensing. In the chimeric study, the TRPV1 PD was sufficient to transform the chimeric Shaker channel into a thermosensing channel with a thermosensitivity of ~75 kcal/mol as estimated from the reported Q_{10} value [36]. Further studies are required to better contextualize our thermodynamics studies with regards to the full-length channel and to decipher and quantify the cooperativity between membrane domains. If TRPV1 vanilloid ligand activation serves as a guide, concatemer studies have shown that a single capsaicin binding event can fully open the channel; on the other hand, equivalent proton activation studies, show that full activation requires all four TRPV1 proton-sensors [58].

Beyond thermodynamic contributions to TRPV1 thermosensitivity, there are two general views on the mechanisms of thermosensing; first, that state-dependent solvation changes, which have large thermodynamic signatures, drive thermosensing; or second,

that partial unfolding as function of temperature (i.e. TRPV1 is only marginally stable) gives rise to the large thermosensitivity and drives thermosensing [1, 29]. While mechanistic TRPV1 temperature gating details continue to emerge, our studies of hV1-S1S4 domain offer particular mechanistic insights. Our NMR studies of the hV1-S1S4 at elevated temperatures identify structural differences from the cryo-EM structures. For example, chemical shift and RDC data show that the S2, S3, and S4 helices are kinked, a feature absent in all of the current TRPV1 structures. However, S2 helical kinks are found in certain TRPV3, TRPV5, and TRPV6 structures [59-62]. Similarly, helical distortions in S3 [63] and S4 are also found in other TRPV family structures. The most significant structural temperature-dependent changes in distance, hydration, and secondary structure from our studies identify three particular areas: 1) The extracellular juxtamembrane region of the S1 helix, 2) the intracellular S2-S3 loop, and 3) the intracellular S4 helix. Interestingly, these temperature-induced changes we observe are similar to those identified via molecular dynamics simulations of TRPV1 heat activation [64].

The extracellular S1 helix and the S1-S2 loop have been implicated in proton activation, where R455 (in rTRPV1, R456 in hTRPV1) is critical to channel function and R455K causes a gain of function (GOF) mutation [65]. This residue in the cryo-EM structure is buried in the membrane as identified by the OPM server [66] and is in close proximity to lipid molecules (Figure S3.5C) [1]. Moreover, this arginine is proximal to two residues that are crucial for the proton activation, V538 in S4 helix and T633 in pore helix [47]. A recent study that engineered a RTx-sensitive TRPV3 revealed that an

allosteric point mutation in the pore domain (A606V) along with mutations to the vanilloid binding pocket, is necessary for TRPV3 to be both RTx and temperature sensitive, emphasizing the role of this residue in temperature sensitivity and the allosteric modulation of the channel [67]. In TRPV1, the equivalent residue to A606 is V596, and this residue is surrounded by R456, V538, and T633 (Figure S3.5C). With this region of the S1S4 domain clearly important for function, it is interesting that our temperature dependent NMR-studies identify meaningful changes in distance and hydration and suggestive that TRPV1 temperature activation might partially interface with proton activation mechanisms that are coupled to the upper pore gate.

Another area identified in our NMR studies is a difference in helicity of the S2-S3 linker relative to the cryo-EM structures. The S2-S3 linker is central to vanilloid ligand activation of TRPV1 [23, 26, 28] and includes Y511 and S512 that impart specificity by hydrogen bonding to the vanilloid head group of TRPV1 agonists. In the cryo-EM structures, there are helical differences between vanilloid bound and apo-TRPV1 structures. Our NMR data identify an additional helical turn in the S2-S3 linker (Figure 3.1C and Figure 3.3B, C) suggestive that temperature-dependent conformational changes of this domain interface with features key to vanilloid activation.

A common feature of TRPV family structures is a stretch of 3_{10} helix at the intracellular side of the S4 helix. Interestingly, this is not present in our NMR investigations of the hV1-S1S4, instead we see a kinked α-helix where the transition between α- and 3_{10}-helix is found in most TRPV structures. In addition, we see in the RDC data that there is a loss of one helical turn at the S4 C-terminus (Figure 3.3C). This

loss of helix is coupled with a general movement of the S4 helix towards C443 in the S1 helix, as identified in PRE measurements (Figure 3.3E), indicating a concerted movement towards the center of the membrane plane. These changes in secondary structure and distance are concomitant with an increase in hydration of the S4 C-terminus (Figure 3.3F). Similar to the loss of helicity at the C-terminus end of the S4 helix in the hV1-S1S4, the unfurling of the bottom of the S4 helix in the activated state is found in TRPV1, TRPV2 and TRPM8 (Figure S3.7A-C). This helix unfurling is also shown in the apparent TRPM8 ligand-gating mechanism [68]. Upon an agonist binding, the S4 helix undergoes changes in secondary structure from α- to 3_{10} helix, starting around V839, pushing the membrane-bound R850 out the membrane (Figure S3.7C). This R850 in TRPM8 is equivalent to R557 in TRPV1, as the alignment of the S1-S4 domains of TRPV1 and TRPM8 shows that R557 in TRPV1 and R850 in TRPM8 are located in the same region in the membrane (Figure S3.7D).

The C-terminal S4 region is functionally important in coupling the S1-S4 domain to the pore domain [48]. Our data identify that R557 in S4b, which is membrane bound in the cryo-EM structures and at 20 °C in our NOE-detected solvation studies, becomes water accessible at elevated temperatures. This residue is well-conserved, and mutation to lysine (R557K) results in a GOF mutation [48]. The TRPV1 cryo-EM structures have provided molecular insight into the role of R557 in ligand-activated channel coupling. In the apo structure R557 forms a cation-π interaction with Y554 and a lipid separates R557 from interacting with E570 in the S4-S5 linker (Figure 3.5A). Vanilloid binding releases the bound lipid separating R557 from E570 allowing for a switch in R557 conformation

that leads to channel activation (Figure 3.5A) [1]. Our data indicate that heat causes similar conformational changes that would result in the disruption of the cation-π interaction between Y554 and R557, as R557 changes helicity and becomes more solvent accessible at elevated temperatures (Figure 3.5B). Presumably, these changes could couple analogously to vanilloid binding to gate the pore domain. To probe this, we generated an R557A mutant, and electrophysiology studies show that it has both impaired heat and capsaicin sensitivities (Figure S3.6C), consistent with the disruption of S1-S4 domain coupling to gating. The R557A mutation was also incorporated into the isolated hV1-S1S4 and the NMR data show that it retains structure, and only modestly impacts thermosensitivity by ~1.5 kcal/mol relative to the wild-type (Figure S3.6B). Presumably this slight loss of thermosensitivity is from the oblation of the Y554-R557 cation-π interaction. In TRPV4, the residues equivalent to Y554 and R557 in TRPV1 (Y591 and R594) have also been implicated in ligand activation, and mutations in the TRPV4 S3 and S4 helices also impacts heat activation [69]. Taken together these data suggest that R557 functions to couple both heat (Figure 3.4A, B) and ligand (Figure S3.6C) stimuli to the pore domain in gating and is in agreement with a mechanism proposed by Cheng, Julius, and coworkers [1]. We note that R557 is not included in the construct used in a recent study that swapped the TRPV1 PD to the temperature-insensitive Shaker channel (Figure S3.6D) [36], suggesting that in the context of the full-length TRPV1 channel, the PD is not exclusively sufficient to produce thermal activation. Our studies suggest that interplay between these membrane domains are required for heat activation.

Overall, our study provides new insights into the role of the S1-S4 domain in TRPV1 gating. We present the first direct binding measurements of capsaicin to the S1-S4 domain and validate the identity of key residues exhibit specific capsaicin binding. Utilizing various techniques, we show that the S1-S4 domain undergoes a temperature-dependent conformational change with a relatively large magnitude ΔH (thermosensitivity). Mechanistic studies suggest that there is overlap between regions of the S1-S4 domain that have been previously implicated in proton and ligand activation and the conformational changes identified in our study. Taken together our data indicate that the S1-S4 domain contributes to TRPV1 thermosensitivity.

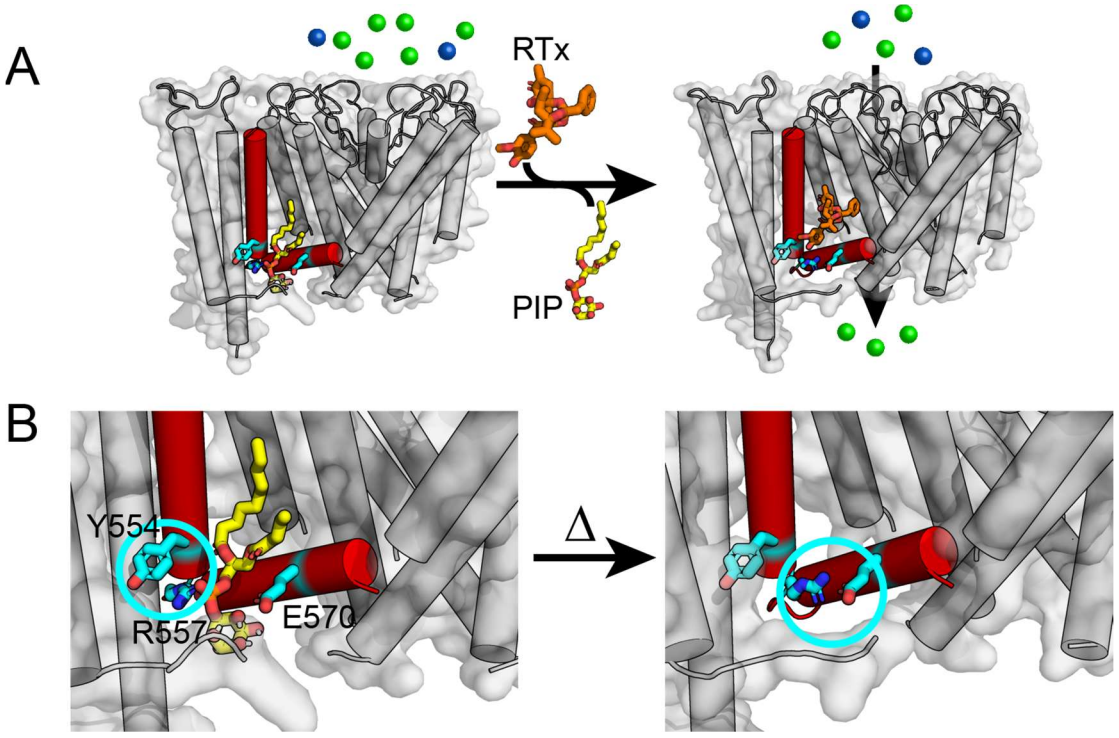

Figure 3.5 A proposed heat-sensing mechanism of TRPV1 involves the interaction between the S4 helix and the S4-S5 linker. (**A**) Structure-based ligand-gated mechanism of TRPV1 is shown in cartoon (PDB ID: 5IRZ and 5IRX). In the resting state, an endogenous lipid (shown in yellow) occludes the canonical vanilloid binding pocket, perturbing the interaction between the R557 in S4 and E570 in S4-S5 linker. As a vanilloid ligand, resiniferatoxin (RTx, orange), binds the S1-S4 domain, the cation-π interaction between R557 and Y554 is disrupted and R557 changes conformation to interact with E570, opening the lower gate. For visual clarity, S3 helix is omitted, and only one S1-S4 domain is shown. (**B**) The close-up views that show the interaction between Y554 and R557 in S4 helix in the resting state (left, highlighted in cyan circle), and the interaction between R557 and E570 in S4-S5 linker (right, shown in cyan circle). Our data suggest that the C-terminal end of the S4 helix undergoes heat-induced movements in this region and lose the helicity. This model is analogous to the ligand activation mechanism and consistent with a heat-activation mechanism proposed by Cheng, Julius, and coworkers [21].

3.5 Materials and Methods

3.5.1 Human TRPV1 S1-S4 domain (hV1-S1S4) Protein Expression and Purification

The hV1-S1S4 (S1-S4, including Pre-S1) was expressed from a synthetic gene engineered from ATUM that encodes the hV1-S1S4, a 141-residue structural domain with an identical amino acid sequence to human TRPV1. The optimized gene was modified to include an N-terminal 10×His tag fused to a thrombin cleavage site subcloned into a pET16b vector. The expressed protein includes residues Pro418-Gly558 from the human TRPV1 channel.

We optimized the fusion hV1-S1S4 expression using *Escherichia coli* strain BL21 (DE3) competent cells. Starter cultures were initiated with 1 transformed colony inoculated in a culture tube containing 3 mL LB and 0.1 mg/mL ampicillin (3 µL of 100 mg/mL stock) (Sigma Aldrich) and incubated for ca. 7 h at 37 °C. 6 mL of starter culture was used to inoculate 1 L of M9 minimal media (12.8 g $Na_2HPO_4 \cdot 7H_2O$ (Sigma Aldrich), 3 g KH_2PO_4 (Thermo Fisher Scientific), 0.5 g NaCl (Thermo Fisher Scientific), 1 mM $MgSO_4 \cdot 7H_2O$ (Sigma Aldrich), 0.1 mM $CaCl_2 \cdot 2H_2O$ (Sigma Aldrich), 4% D-glucose (w/v) (Sigma Aldrich), 1× MEM Vitamin solution (100× solution, Corning)) with 1 g $^{15}NH_4Cl$ (Cambridge Isotope Laboratories) as the sole nitrogen source. The cells were grown at 18 °C and the hV1-S1S4 expression was induced for 48 h by addition of 0.1 mM isopropyl β-D-1-thiogalactopyranoside (IPTG, Research Products International Corp.) at an OD_{600nm} of 0.5-0.6. After 48 h, the cells were harvested by centrifugation at 6,000 ×*g* for 20 min at 4 °C resulting in a cell pellet average of ca. 2.5 g per liter of M9.

The cell pellet was resuspended in 25 mL lysis buffer (75 mM Tris-HCl (Thermo Fisher Scientific), 300 mM NaCl (Thermo Fisher Scientific), 0.5 mM EDTA (Sigma Aldrich), pH 7.7) with 0.01 mg of lysozyme (Sigma Aldrich), 0.01 mg DNase (Sigma Aldrich), 0.01 mg RNase (Sigma Aldrich), 1.25 mg PMSF (Sigma Aldrich), 0.05 mM magnesium acetate (Sigma Aldrich) and 2 mM β-mercaptoethanol (β-ME, Sigma Aldrich). This lysis solution was tumbled at room temperature for 30 min. The mixture was sonicated using an S-4000 Ultrasonic Processor (Qsonica) at 4 °C for 7.5 min at 55% power and 50% duty cycle of 5 sec on and 3 sec off. The resulting whole cell lysate was then tumbled with N,N-dimethyl-N-dodecylglycine (Empigen BB Detergent, BOC Sciences) (3% v/v) for 1 h at 4 °C to solubilize and extract the hV1-S1S4 into micelles. After an hour, the lysate was centrifuged at 38,500 ×*g* for 30 min at 4 °C to pellet non-solubilized cellular debris. The supernatant was collected and tumbled with 1 mL of preequilibrated Ni(II)-NTA Superflow (Qiagen) resin for 1-1.5 h at 4 °C.

The hV1-S1S4-bound resin was packed in a gravity column to a column volume ~ 1 mL and washed with 20 column volumes of Buffer A (40 mM HEPES (Sigma Aldrich), 300 mM NaCl (Thermo Fisher Scientific), 2 mM β-ME (Sigma Aldrich) pH 7.8) with 1.5% (v/v) Empigen detergent (BOC Sciences). The resin was washed with 20 column volumes of wash buffer (40 mM HEPES, 300 mM NaCl, 60 mM Imidazole (Sigma Aldrich), 1.5% (v/v) Empigen, 2 mM β-ME, pH 7.8). With the hV1-S1S4 bound to the resin, the detergent was exchanged into the desirable membrane mimic for further studies with 15 column volumes of rinse buffer (25 mM Na_2HPO_4 (Thermo Fisher Scientific), 0.05% (w/v) lyso-palmitoylphosphatidylglycerol (LPPG, Anatrace), 2 mM β-ME, pH

7.8). Finally, the hV1-S1S4 was eluted with 15 column volumes of elution buffer (25 mM Na_2HPO_4, 300 mM Imidazole, 0.1% (w/v) LPPG, 2 mM BME, pH 7.8).

A variety of membrane mimics were screened by ^{15}N-TROSY-HSQC NMR, including the following: DPC (0.5% (w/v)), TDPC (0.5% (w/v)), LMPC (0.2% (w/v)), LMPG (0.2% (w/v)), LPPC (0.2% (w/v)), and LPPG (0.2% (w/v)) (Fig. S1). Spectra of all tested samples were collected at both 20 °C and 50 °C, and the spectral qualities were compared. The hV1-S1S4 purified in LPPG micelles produced the most well-resolved and dispersed spectra with the appearance of the expected number of resonances and was therefore the membrane mimic chosen for the resulting studies.

After Ni-NTA purification the hV1-S1S4 was buffer exchanged to thrombin cleavage buffer (25 mM Na_2HPO_4, 150 mM NaCl, pH 7.8) using an Amicon Ultra centrifugal ultrafiltration unit (Milipore, 10 kDa cutoff). The concentration of protein was determined using a BCA kit (Thermo Fisher) and 3U thrombin (Novagen) was added for every 1 mg protein. The thrombin-protein cleavage reaction was incubated at room temperature (ca. 23 °C) for 24 h. After the reaction was completed, this mixture was passed over Ni-NTA resin with the flow through containing the thrombin-cleaved hV1-S1S4.

Gel filtration of the cleaved protein was carried out by concentrating to ca. 0.5 mL in NMR buffer (25 mM Na_2HPO_4, 0.5 mM EDTA, pH 6.5), and was eluted with a 1 CV of a Superdex 200 (GE Healthcare Life Sciences) column. The fractions with high A_{280} readings were analyzed with SDS-PAGE. The purified sample was concentrated to a

desired volume. After purification, the average yield of pure hV1-S1S4 per liter of M9 medium was approximately 1.5 mg.

3.5.2 Validation of the hV1-S1S4 Identity

To confirm the identity of purified hV1-S1S4, the SDS-PAGE band was cut and sent to the MS Bioworks, which performed liquid chromatography tandem mass spectrometry (LC-MS/MS). The result revealed that our purified hV1-S1S4 matches the hV1-S1S4 amino acid sequence we provided with 51% coverage (Figure S3.1B).

3.5.3 MTSL Site Directed Spin Labeling

For paramagnetic relaxation enhancements (PRE) maleimide chemistry was used to label the hV1-S1S4 with a nitroxide spin label MTSL (*S*-(1-oxyl-2,2,5,5-tetramethyl-2,5-dihydro-1H-pyrrol-3-yl)methyl methanesulfonothioate, Santa Cruz Biotech) . Only the WT construct containing a lone cysteine in S1 α-helix (C443) was used for PRE. For these reactions, the hV1-S1S4 was prepared as above, except before thrombin cleavage the volume of purified hV1-S1S4 was adjusted to 0.5 mL in 25 mM sodium phosphate buffer at pH 7.2. To maximize nitroxide labeling efficiency, purified hV1-S1S4 was incubated and tumbled with 2.5 mM dithiothreitol (DTT, A Geno Technology, Inc.) for 1-2 h at room temperature to reduce the cysteine sulfhydryl. After the reaction with DTT, a 10:1 MTSL (stock solubilized in DMSO) to protein mole ratio amount of nitroxide spin label was solubilized in DMSO and incubated for 3 h at 37 °C. The reaction was continued at room temperature overnight and was buffer exchanged to 25 mM Na_2HPO_4, pH 7.8. The resulting MTSL-hV1-S1S4 was rebound to Ni-NTA resin and incubated for 1 h at room temperature. MTSL was removed by washing the resin with at least 20

column volumes of rinse buffer (25 mM Na_2HPO_4, 0.05% (w/v) LPPG, pH 7.8). MTSL labeled-hV1-S1S4 was eluted with 5 column volumes of elution buffer (25 mM Na_2HPO_4, 300 mM Imidazole, 0.1% (w/v) LPPG, pH 7.8). After this step, the purification follows as described above with thrombin cleavage and SEC.

3.5.4 Nuclear Magnetic Resonance Spectroscopy

All NMR experiments were recorded with a Bruker 850 MHz ^{1}H spectrometer and Avance III HD console equipped with a 5 mm TCI CryoProbe. All samples included 4 μL D_2O with a total volume of 180 μL in a 3 mm NMR tube. The temperature for these experiments was calibrated using 99% ^{2}H methanol where the difference in chemical shifts (ppm) arising from the two resonances is used as a temperature standard with the ranges of 178 K and 330 K according to $T[K] = 409.0 - 36.54\Delta\delta - 21.85(\Delta\delta)^2$ where $\Delta\delta$ is the difference in Hz between the two peaks [70].

3.5.4.1 NMR Backbone Resonance Assignment

Experiments used for backbone resonance assignment of the hV1-S1S4 were carried out at 45 °C with a 900 μM uniformly ^{15}N, ^{13}C labeled sample in a Bruker shaped NMR tube (Part Number Z106898) with 4% D_2O (v/v). TROSY versions of HSQC, HNCA, HNCOCA, HNCO, HNCACO, HNCACB, and CBCACONH as well as non-TROSY 4D HNCACO and 4D HNCOCA experiments were utilized, and an ^{15}N-edited HSQC-NOESY with a 90 ms mixing time (τ) was used for sequential assignments; table S1 details specific experimental parameters. The nonuniformly sampled data were reconstructed with qMDD and processed in nmrPipe, with analysis and resonance assignment carried out using CcpNMR [71] software (Figure S3.1E-J). The resonance

assignments at 45 °C are deposited in the Biological Magnetic Resonance Bank (BMRB entry 27029).

3.5.4.2 Secondary Structure Calculations and Comparisons with rTRPV1 Cryo-EM Structures

The secondary structure of the hV1-S1S4 at 45 °C was determined using TALOS-N [39] where the secondary structure was plotted as probability of secondary structure vs residue number. The secondary structure was then plotted in Aline [72] alongside rTRPV1 structures determined by cryo-EM. The secondary structure for each of the rTRPV1 structures were specifically determined by analyzing the PDB codes deposited in the Protein Data Bank for requisition numbers 5IRZ, 5IRX, and 5IS0.

3.5.4.3 ^{1}H-^{15}N TROSY-HSQC-Detected Capsaicin Titrations

For the titration with capsaicin (Corden Pharma), stock capsaicin was prepared in 195 proof ethanol (Thermo Scientific), and the mole percent of capsaicin was calculated by the equation below:

$$mol\%\ capsaicin = \frac{(moles\ capsaicin)}{moles\ capsaicin + moles\ LPPG + moles\ hV1S1S4} \times 100\% \quad [1]$$

Using 66 μM hV1-S1S4 in 1.67% LPPG (w/v), ^{1}H-^{15}N TROSY-HSQC spectra of for capsaicin titration were collected at 37 °C, with 32 transients of 2048 direct points and 128 indirect points. The hV1-S1S4 resonance assignments at 45 °C were mapped to 37 °C and used to identify residues that specifically interact with capsaicin (Figure 3.1E).

The mole% capsaicin used were 0.001%, 0.002%, 0.005%, 0.012%, 0.015%, 0.025%, 0.075%, 0.125%, 0.225% and 0.723% (Figure 3.1E). These spectra were processed with nmrPipe [73] and the resonances were analyzed in CcpNmr [71]. Chemical shift perturbations induced by capsaicin were calculated by the equation below:

$$\Delta\delta = \sqrt{(\Delta\delta_H)^2 + \left(0.2(\Delta\delta_N)\right)^2} \quad [2]$$

where $\Delta\delta_H$ is the difference in chemical shift in the proton dimension and $\Delta\delta_N$ is the difference in chemical shift in the nitrogen dimension, and the $\Delta\delta_N$ was multiplied by a scaling factor of 0.2 typically used for nitrogen nuclei [74]. The capsaicin-dependent chemical shift perturbations were plotted as a function of the mole% of added capsaicin and fit to a single site binding model derived from the Langmuir adsorption model commonly used to describe binding in proteins:

$$\Delta\delta(mole\%) = \frac{\Delta\delta_{max} \times mole\%}{K_d + mole\%} \quad [3]$$

where K_d is the dissociation constant and $\Delta\delta_{max}$ is the maximal value of change in chemical shift from perturbation. Using the amide backbone assignment of the hV1-S1S4, the chemical shift perturbations of 72 residues were analyzed and the K_d values for each residue were calculated using *MATLAB R2016a*fit to equation [3].

3.5.4.4 ^{1}H-^{15}N TROSY-HSQC-Detected Temperature Titrations

The ^{1}H-^{15}N TROSY-HSQC experiments of the purified hV1-S1S4 were recorded from 15 °C to 50 °C, at 5 °C increments with all other parameters fixed. Specific types of buffers exhibit pH changes at different temperatures, an effect that could convolute our

analyses. To ensure that the chemical shift perturbations were caused exclusively by temperature changes and not from pH changes of the buffer, ^{1}H-^{15}N-TROSY-HSQC spectra at two different pH values, 6.5 and 6.4, were collected at 37 °C (Figure S3.3G). These two pH values were chosen based on empirical pH changes measured with our NMR buffer as a function of temperature (Table S3.2). No chemical shift perturbations were detected allowing direct analysis for their dependence on temperature dependent resonance changes.

The resonance intensities of several hV1-S1S4 residues were plotted against the temperature, and fit to a sigmoidal two-state model using *MATLAB* scripts relying on the *nlinfit* function with the following equation derived from a Van't Hoff model:

$$I = \frac{\left(I_{active} + I_{resting}\right)e^{\left(-\frac{\Delta H}{R}\left(\frac{1}{T}-\frac{1}{T_m}\right)\right)}}{1 + e^{\left(-\frac{\Delta H}{R}\left(\frac{1}{T}-\frac{1}{T_m}\right)\right)}} \quad [4]$$

From this equation, the changes in enthalpies (ΔH) of 71 residues for WT and 70 residues for the hV1-S1S4-R557A mutant residues were obtained. For the WT, three distinct samples were used for the experiments, yielding three sets of the ΔH values per residue. From the enthalpies, a histogram with bins of 5 kcal/mol was fit to a Gaussian function, $f(\Delta H) = a_{max}\ exp\left(-\frac{(\Delta H-\mu)^2}{2\sigma^2}\right)$, in *MATLAB* for both WT and R557A, where μ and σ are the ensemble average enthalpy and variance respectively.

3.5.4.5 TROSY for Rotational Correlation Times (TRACT) Measurements

To accurately quantify the PRE-derived distances between individual indole amine (W549 and W427) residues and the MTSL-labeled C443, accurate rotational

correlation times (τ_c) are needed at 20 °C and 50 °C. To approximate τ_c, TRACT [75] was collected over a range of time delays from τ = 0 to 100 ms with 4 ms intervals. The pulse program that was used for these experiments was adapted from Lee, D et al [75]. The data were processed and integrated in nmrPipe over a range of 9.6 ppm to 10 ppm, to which a linear baseline correction was applied with the nmrPipe function *BASE* and a defined node list in the noise (fig. S4B). The range that was integrated was selected as it encompassed the W549 indole amine resonance from the S4 transmembrane helix, and only this was integrated since integration over the entire amino region can artificially inflate the effective correlation time [76]. The integrated data was fit using *MATLAB R2015a* with a monoexponential decay function, $f(\tau) = Ae^{-\beta}$, where *A* is a normalized maximum, τ is the time delay, and β is the relaxation decay constant in Hz. The relaxation decays for the α and β state of exclusively the W549 indole amine resonance were used to calculate the approximate effective rotational correlation time (τ_c) due to the rigid body assumption as described previously by Lee, D et al [75].

3.5.4.6 Calculation of Amide Proton Temperature Coefficients

From the NMR temperature titration from 15 °C to 50 °C (288 K to 323 K), the amide proton chemical shifts (δ_{HN}) of assigned resonances at corresponding temperatures were plotted in the same temperature range. Each plot was fit to the linear function, $y = mx + b$, where the slope is the temperature coefficient, $\Delta\delta_{HN}/\Delta T$ (ppb/K).

3.5.4.7 Paramagnetic Relaxation Enhancement (PRE) Measurements

Paramagnetic (MTSL labeled) and diamagnetic (without the MTSL label) proton transverse relaxation (R_2) measurements were recorded using a TROSY-HSQC pulse

program modified to include a relaxation delay before acquisition as described by Clore and coworkers [77]. Four relaxation delays (0, 4, 12, 24 ms) were recorded for the matched paramagnetic and diamagnetic samples at 20 °C (196 scans) and 50 °C (80 scans) with 2048 direct point and 128 indirect points. The spectra were processed using nmrPipe with a Gaussian apodization function, which does not affect the calculated distance to the free electron spin [78]. The resonance intensity values were obtained using CcpNmr and transverse relaxation rates of the paramagnetic state, R_2^{eff}, and the diamagnetic state, R_2, were extracted by fitting the data with a monoexponential decay function, $y = ae^{-bx}$ (Figure S3.4E). The paramagnetic rate enhancements, Γ_2, were calculated by subtracting R_2 from R_2^{eff}, using the relationship of the electron spin-enhanced transverse relaxation rate due to the spin label (R_2^{eff}) is a sum of the intrinsic transverse relaxation rate (R_2) and the contribution from the electron (Γ_2):

$$R_2^{eff} = \Gamma_2 - \mathrm{R}_2 \qquad [5]$$

The errors for R_2^{eff} and R_2 were extracted from fitting errors, and the error of $\delta\Gamma_2$ was calculated using standard the propagation of error:

$$\delta\Gamma_2 = \sqrt{\left(\delta R_2^{eff}\right)^2 + (\delta R_2)^2} \qquad [6]$$

The distance restraints from MTSL-labeled C443 to residues in proximity were calculated by the following relationship:

$$r = \left[\frac{K}{\Gamma_2}\left(4\tau_c + \frac{3\tau_c}{1+\omega_H^2\tau_c^2}\right)\right]^{\frac{1}{6}} \qquad [7]$$

where $\tau_c$is the effective rotational correlation time, ω_H is the Larmor frequency for the nuclear spin (protons), and K is 1.23×10^{-32} cm^6 s^{-2} a constant related to the gyromagnetic ratio (γ), spin quantum number (S), electronic g factor (g), and the Bohr magneton (β) according to $K = \frac{1}{15} S(S+1)\gamma^2 g^2 \beta^2$.

Three separate paramagnetic (MTSL labeled) and diamagnetic (non-MTSL labeled) samples were prepared. Transverse relaxation rates of states were obtained, and using various combinations, 9 paramagnetic enhancement rates were calculated, generating 9 distance restraints per residue. Distances calculated to be higher than 27 Å were disregarded as this is beyond the reliable distance calculation for the atoms involved due to its r^{-6} dependence. The distances at 20 °C and 50 °C were averaged, and the temperature dependent change in distances (ΔPRE) were calculated by subtracting 20 °C (resting state, initial) from 50 °C (active state, final) ($\Delta PRE_{50\,°C - 20\,°C}$). We interpreted that the residues with negative ΔPREs are moving closer to MTSL-C443, and the residues with positive ΔPREs are moving away from MTSL-C443. The errors of distance restraints were the standard error of the mean (SEM).

3.5.4.8 NOESY at Two Different Temperatures

^{15}N-edited TROSY-HSQC-NOESY spectra of the hV1-S1S4 were collected with 96 scans and 48 scans with the mixing time of 90 ms at 20 °C and 45 °C, respectively. Using the amide resonance assignments and temperature titration resonances, amide NOESY crosspeaks were assigned to corresponding Hα and water cross-peaks. Using peak volumes, the ratio (I) between the water and Hα cross-peaks were calculated by

dividing the water cross-peak by Hα cross-peak at both temperatures. Then the differences of $I_{water}/I_{H\alpha}$ at 45 °C and 20 °C ($\Delta NOE_{45\,°C - 20\,°C}$) were calculated for all well resolved resonances to observe if the hV1-S1S4 undergoes changes in hydration as a function of temperature. The $\Delta NOE_{45\,°C - 20\,°C}$ was plotted against the residue number and the cutoff value of 0.5 was used to evaluate the changes in hydration per residue.

3.5.4.9 Deuterium/Hydrogen Exchange Factor Analysis of the hV1-S1S4 at 50 °C

The H_2O/D_2O exchange measurement for the hV1-S1S4 was carried out at 50 °C. To vary the concentration of D_2O in the sample, the NMR buffer was prepared in D_2O. This was done by lyophilizing 500 µL of NMR buffer and resuspending it in 500 µL of D_2O. To make 10% D_2O/90% H_2O, 18 uL of NMR buffer in D_2O was added to the sample, and the sample was incubated for approximately 12 hours to ensure that the exchange between the proton and deuterium is completed. ^{1}H-^{15}N TROSY-HSQC was collected as described above with 32 scans. For the higher concentration of D_2O titration points, the sample with 10% D_2O/90% H_2O was concentrated down to approximately 100 µL, and 80 µL of the NMR buffer in D_2O was added to the concentrated sample to make a 40% D_2O/60% H_2O sample. For the further D_2O points, the same method was used.

The resulting data was analyzed with a method developed by Opella et al. [79]. The relative peak volumes of resonances were normalized to those from the 2.2% D_2O spectrum. The mole fraction of water (χ_{water}) was calculated for each data point and plotted against the normalized peak volumes. The decay in resonance intensity as a function of χ_{water} is linearly dependent on the exchange factor *m*. All D/H assigned exchange factors were plotted against the residue number for further analysis.

3.5.4.10 Residual Dipolar Coupling (RDC)

A neutral 3.8% polyacrylamide gel comprising 3.8% (w/v) copolymer was generated using acrylamide (stock 40% w/v, Sigma-Aldrich), bis-acrylamide (stock 2%, Sigma-Aldrich), 10% APS, and 4 μL of TEMED in a casting solution of 10 mL of 250 mM imidazole at pH 6.5. These gels were cast in a 3D printed plastic block with a custom 6 mm inner diameter polytetrafluoroethylene (PTFE, Teflon) tube insertion. Prior to adding TEMED, the solution was filtered using 0.22 μm filter (Millipore) to eliminate any polymerized acrylamide. The polymerization reaction was carried out for 24 hours. Once polymerization was complete, the gel was soaked in ddH_2O for ~12 h initially, then it was dialyzed in the NMR buffer for 48 hours with a gentle nutating at room temperature; with buffer changes every 12-18 h. Once the dialysis was complete, the gel was cut to 1.7 mm length; the length was empirically chosen to span the probe coil within a 5 mm NMR tube. The cut gel was partially dehydrated by incubating at 37 °C for 3.5 h, which was then soaked in 1 mL of a purified 177 μM hV1-S1S4 sample for approximately 48 h. The concentration of the protein solution outside of the gel was measured every 24 h to monitor absorption into the gel. Once concentration plateaued, the protein-soaked gel was stretched into a 5 mm NMR tube with an inner diameter of 4.4 mm using Tygon tubing attached to the NMR tube and a syringe, the difference in gel and tube diameter stretched the gel to ~4 mm. Residual dipolar couplings were measured using Amide RDC's by TROSY Spectroscopy (ARTSY) by taking the ratio of assigned amino acid intensities from attenuated spectra and reference spectra [80]. The dipolar

couplings were then plotted as a function of residue number and fit according to the following equation:

$$\delta_{NH} = A \cdot \sin\left[\frac{2\,\pi}{T}(x - x_0) + \varphi\right] + A_{mean} \quad [8]$$

where *T* is the period of the wave, *x* is the amino acid identity, *x0* is the first amino acid to be fit in a given range, A_{mean} is the average of the couplings in a given range, and *A* represents a function of the alignment tensor according to:

$$A = \frac{2\,D_a \cos^2[\delta]\cos^2[\theta] - \cos^2 D_a \cos^2[\delta]\sin^2[\theta] + \frac{3}{2}\,D_a\,R\cos^2[\delta]\sin^2[\theta]\cos^2[\phi]}{\sin[\varphi]} \quad [9]$$

where *R* and D_a are the rhombicity and axial symmetry of the alignment tensor, respectively. The angles θ and ϕ correspond to the amide bond vector angles with respect to the Y- and Z- axes, and δ the angle that the amide bond vector makes with the chain axis [81]. The first equation is a good approximation for ideal α-helices and 3_{10} -helices as previously described [81, 82] RMSE was calculated according to:

$$RMSE = \sqrt{\frac{\sum_{t=1}^{T}(\hat{y}_t - y_t)^2}{T}} \quad [10]$$

where $\hat{y}_t$ corresponds to predicted values of y_t over *T* observations.

3.5.5 Far-Ultraviolet Circular Dichroism (Far-UV CD)

Far-UV CD measurements were carried out on a 0.2 mg/ml hV1-S1S4 sample in 0.1% (w/v) LPPG micelles in 200 µL in 25 mM Na_2PO_4 buffer at pH 6.5. CD spectra were obtained with a Jasco J-710 spectropolarimeter using a 1.0 mm path length cell. The

temperature was controlled with a Peltier device (Jasco PTC-424S). All experiments were measured from 250 nm to 190 nm and 5 scans from 10 °C to 57 °C in 1 °C increments. The blank (25 mM Na_2HPO_4, pH 6.5, containing 0.1% (w/v) LPPG) measurement values were subtracted from the protein measurement values, and the units of CD values were converted into mean residue ellipticity using the equation:

$$[\theta]_{MR} = 100 \times \frac{\theta}{C \times N \times l} \quad [11]$$

where $[\theta]_{MR}$ is the mean residue ellipticity, θ is ellipticity in millidegrees, C is the concentration of protein in molar (M), N is the number of amino acid residues of protein, and l is the path length in centimeters. The hV1-S1S4 CD values at 222 nm were plotted against temperature (Figure 3.2B).

3.5.6 Temperature Study Using Intrinsic Tryptophan Fluorescence Measurement

Fluorescence emission spectra were measured on a QM-4/2005SE Spectrofluorometer (PTI, NJ) using 295 nm excitation to minimize contributions from tyrosine residues [38]. The temperature was controlled over a range of ca. 7 °C – 50 °C using a water circulation system and a calibrated thermocouple was used to measure the temperature of the sample inside the cuvette. To account for light scattering contributions, a sample of LPPG micelles and buffer was used as a blank and subtracted from the measurements containing hV1-S1S4. The blank signals are relatively small and their magnitude and position do not change with temperature (Figure S3.4G). In contrast, for the hV1-S1S4 samples, increasing temperature resulted in both a decrease in

fluorescence intensity and a spectral shift to higher wavelengths. We characterize fluorescence spectral shifts in terms of the average emission wavelength, ⟨λ⟩:

$$\langle\lambda\rangle = \frac{\sum I(\lambda_i)\lambda_i}{\sum I(\lambda_i)} \quad [12]$$

where $I(\lambda)_i$ is the intensity measured at wavelength λ_i. This quantity is more precise and less sensitive to instrumental noise than the peak maximum (λ_{max}) because the calculation reflects data from the entire spectrum rather than a single point [83].

3.5.7 Cell Culture

HEK-293 cells (ATCC cell line CRL-1573) were cultured in 35 mm dishes at 37 °C in DMEM with 10% fetal bovine serum, 2 mM L-glutamine, 4.5 mg ml^{-1} glucose, and 100 mg ml^{-1} each of penicillin and streptomycin in the presence of 5% CO_2. All reagents were obtained from Life Technologies.

3.5.8 Plasmid and Mammalian Cell Transfection

The full-length human TRPV1 gene was subcloned into a pIRES-2 plasmid also containing the EGFP gene. This construct produces bicistronic mRNA containing an internal ribosome entry site (IRES) between the two genes, allowing for the independent translation of TRPV1 and the EGFP reporter. TRPV1-R557A was generated in the same plasmid using standard site-directed mutagenesis. Cells were transiently transfected with 0.4 µg DNA using FuGENE 6 transfection reagent (Promega) in a 1:3 µg DNA:µL FuGENE ratio 48 h before electrophysiology measurements were performed.

3.5.9 Electrophysiology

Transfected cells were released from the culture dish surface by briefly exposing them to 0.25% trypsin-EDTA (Thermo) and resuspending in supplemented DMEM. Cells were plated on glass coverslips and incubated for 1-2 h at 37 °C. Whole-cell voltage-clamp measurements were performed with an Axopatch 200B amplifier and pClamp 10.3 software (Molecular Devices). Data was acquired at 2 kHz, filtered at 1 kHz, and digitized using a Digidata 1440a digitizer (Molecular Devices). Patch pipettes were pulled from borosilicate glass capillaries (World Precision Instruments) using a P-2000 laser puller (Sutter Instruments) and heat polished with a MF-830 microforge (Narashige), resulting in resistances of 2-5 MΩ. A reference electrode was inserted into a salt bridge composed of 2% agar in extracellular solution. Glass coverslips plated with cells were placed in a chamber and covered with extracellular solution containing 132 mM NaCl, 5 mM KCl, 1 mM $MgCl_2$, 2 mM $CaCl_2$, 10 mM HEPES, and 5 mM glucose. The pH of the solution was adjusted to 7.4 using NaOH and osmolality was adjusted to 310 mOsm using sucrose. Pipette solution contained 315 mM K^+ gluconate, 5 mM KCl, 1 mM $MgCl_2$, 5 mM EGTA, and 10 mM HEPES, with pH adjusted to 7.2 using KOH and osmolality adjusted to 300 mOsm using sucrose. Osmolality was measured using a Vapro 5600 vapor pressure osmometer (Wescor). Temperature was controlled by perfusing preheated or cooled extracellular solution using an HCPC perfusion system and HCT-10 temperature controller (ALA Scientific), which heats or cools solution by supplying a specified voltage to a Peltier device through which perfusion solution flows. Temperature was calibrated by measuring the temperature of the solution exiting the HCPC at a given

voltage. Currents were recorded at +60 mV and normalized to cell membrane capacitance.

3.6 References

1. Hilton, J.K., et al., Understanding thermosensitive transient receptor potential channels as versatile polymodal cellular sensors. *Biochemistry,* 2015. **54**(15): p. 2401-13.

2. Voets, T., TRP channels and thermosensation. *Handb. Exp. Pharmacol.,* 2014. **223**: p. 729-41.

3. Caterina, M.J., et al., The capsaicin receptor: a heat-activated ion channel in the pain pathway. *Nature,* 1997. **389**(6653): p. 816-24.

4. Kim, A.Y., et al., Pirt, a phosphoinositide-binding protein, functions as a regulatory subunit of TRPV1. *Cell,* 2008. **133**(3): p. 475-85.

5. Klein, R.M., et al., Determinants of molecular specificity in phosphoinositide regulation. Phosphatidylinositol (4,5)-bisphosphate (PI(4,5)P2) is the endogenous lipid regulating TRPV1. *J Biol Chem,* 2008. **283**(38): p. 26208-16.

6. Tominaga, M., et al., The Cloned Capsaicin Receptor Integrates Multiple Pain-Producing Stimuli. *Neuron,* 1998. **21**(3): p. 531-543.

7. Fernandes, E.S., M.A. Fernandes, and J.E. Keeble, The functions of TRPA1 and TRPV1: moving away from sensory nerves. *Br J Pharmacol,* 2012. **166**(2): p. 510-21.

8. Julius, D., TRP channels and pain. *Annu. Rev. Cell. Dev. Biol.,* 2013. **29**: p. 355-84.

9. Moran, M.M., et al., Transient receptor potential channels as therapeutic targets. *Nat Rev Drug Discov,* 2011. **10**(8): p. 601-20.

10. Fernandes, E.S., et al., TRPV1 deletion enhances local inflammation and accelerates the onset of systemic inflammatory response syndrome. *J. Immunol.,* 2012. **188**(11): p. 5741-51.

11. Razavi, R., et al., TRPV1 sensory neurons control beta cell stress and islet inflammation in autoimmune diabetes. *Cell,* 2006. **127**(6): p. 1123-35.

12. Lee, L.Y. and Q. Gu, Role of TRPV1 in inflammation-induced airway hypersensitivity. *Curr Opin Pharmacol,* 2009. **9**(3): p. 243-9.

13. Motter, A.L. and G.P. Ahern, TRPV1-null mice are protected from diet-induced obesity. *FEBS Lett.,* 2008. **582**(15): p. 2257-62.

14. Suri, A. and A. Szallasi, The emerging role of TRPV1 in diabetes and obesity. *Trends Pharmacol Sci,* 2008. **29**(1): p. 29-36.

15. Riera, C.E., et al., TRPV1 pain receptors regulate longevity and metabolism by neuropeptide signaling. *Cell,* 2014. **157**(5): p. 1023-36.

16. Mistretta, F., et al., Bladder cancer and urothelial impairment: the role of TRPV1 as potential drug target. *Biomed Res Int,* 2014. **2014**: p. 987149.

17. Stock, K., et al., Neural precursor cells induce cell death of high-grade astrocytomas through stimulation of TRPV1. *Nat. Med.,* 2012. **18**(8): p. 1232-8.

18. Hilton, J.K., M. Kim, and W.D. Van Horn, Structural and Evolutionary Insights Point to Allosteric Regulation of TRP Ion Channels. *Acc Chem Res,* 2019.

19. Liao, M., et al., Structure of the TRPV1 ion channel determined by electron cryo-microscopy. *Nature,* 2013. **504**(7478): p. 107-12.

20. Cao, E., et al., TRPV1 structures in distinct conformations reveal activation mechanisms. *Nature,* 2013. **504**(7478): p. 113-8.

21. Gao, Y., et al., TRPV1 structures in nanodiscs reveal mechanisms of ligand and lipid action. *Nature,* 2016. **534**(7607): p. 347-51.

22. Yang, F., et al., The conformational wave in capsaicin activation of transient receptor potential vanilloid 1 ion channel. *Nat Commun,* 2018. **9**(1): p. 2879.

23. Jordt, S.-E. and D. Julius, Molecular Basis for Species-Specific Sensitivity to "Hot" Chili Peppers. *Cell,* 2002. **108**(3): p. 421-430.

24. Gavva, N.R., et al., Molecular determinants of vanilloid sensitivity in TRPV1. *J. Biol. Chem.,* 2004. **279**(19): p. 20283-95.

25. Sutton, K.G., et al., Functional characterisation of the S512Y mutant vanilloid human TRPV1 receptor. *Br J Pharmacol,* 2005. **146**(5): p. 702-11.

26. Yang, F., et al., Structural mechanism underlying capsaicin binding and activation of the TRPV1 ion channel. *Nat. Chem. Biol.,* 2015. **11**(7): p. 518-24.

27. Hanson, S.M., et al., Capsaicin interaction with TRPV1 channels in a lipid bilayer: molecular dynamics simulation. *Biophys J,* 2015. **108**(6): p. 1425-34.

28. Elokely, K., et al., Understanding TRPV1 activation by ligands: Insights from the binding modes of capsaicin and resiniferatoxin. *Proc Natl Acad Sci U S A,* 2016. **113**(2): p. E137-45.

29. Clapham, D.E. and C. Miller, A thermodynamic framework for understanding temperature sensing by transient receptor potential (TRP) channels. *Proc. Natl. Acad. Sci. USA,* 2011. **108**(49): p. 19492-7.

30. Liu, B., K. Hui, and F. Qin, Thermodynamics of Heat Activation of Single Capsaicin Ion Channels VR1. *Biophysical Journal,* 2003. **85**(5): p. 2988-3006.

31. Yao, J., B. Liu, and F. Qin, Kinetic and energetic analysis of thermally activated TRPV1 channels. *Biophys. J.,* 2010. **99**(6): p. 1743-53.

32. Chowdhury, S., B.W. Jarecki, and B. Chanda, A molecular framework for temperature-dependent gating of ion channels. *Cell,* 2014. **158**(5): p. 1148-1158.

33. Lolicato, M., et al., Transmembrane helix straightening and buckling underlies activation of mechanosensitive and thermosensitive K(2P) channels. *Neuron,* 2014. **84**(6): p. 1198-212.

34. Cao, E., et al., TRPV1 channels are intrinsically heat sensitive and negatively regulated by phosphoinositide lipids. *Neuron,* 2013. **77**(4): p. 667-79.

35. Zaelzer, C., et al., DeltaN-TRPV1: A Molecular Co-detector of Body Temperature and Osmotic Stress. *Cell Rep,* 2015. **13**(1): p. 23-30.

36. Zhang, F., et al., Heat activation is intrinsic to the pore domain of TRPV1. *Proc Natl Acad Sci U S A,* 2018. **115**(2): p. E317-E324.

37. Greenfield, N.J., Using circular dichroism collected as a function of temperature to determine the thermodynamics of protein unfolding and binding interactions. *Nat. Protoc.,* 2006. **1**(6): p. 2527-35.

38. Royer, C.A., Probing protein folding and conformational transitions with fluorescence. *Chem Rev,* 2006. **106**(5): p. 1769-84.

39. Shen, Y. and A. Bax, Protein structural information derived from NMR chemical shift with the neural network program TALOS-N. *Methods Mol Biol,* 2015. **1260**: p. 17-32.

40. Asakura, T., et al., The relationship between amide proton chemical shifts and secondary structure in proteins. *J Biomol NMR,* 1995. **6**(3): p. 227-36.

41. Zhou, N.E., et al., Relationship between amide proton chemical shifts and hydrogen bonding in amphipathic .alpha.-helical peptides. *Journal of the American Chemical Society,* 1992. **114**(11): p. 4320-4326.

42. Shenkarev, Z.O., et al., NMR structural and dynamical investigation of the isolated voltage-sensing domain of the potassium channel KvAP: implications for voltage gating. *J Am Chem Soc,* 2010. **132**(16): p. 5630-7.

43. Mesleh, M.F., et al., Dipolar waves map the structure and topology of helices in membrane proteins. *J Am Chem Soc,* 2003. **125**(29): p. 8928-35.

44. Baxter, N.J. and M.P. Williamson, Temperature dependence of 1H chemical shifts in proteins. *Journal of Biomolecular NMR,* 1997. **9**(4): p. 359-369.

45. Doyle, C.M., et al., Concurrent Increases and Decreases in Local Stability and Conformational Heterogeneity in Cu, Zn Superoxide Dismutase Variants Revealed by Temperature-Dependence of Amide Chemical Shifts. *Biochemistry,* 2016. **55**(9): p. 1346-61.

46. Lee, D., et al., Effective rotational correlation times of proteins from NMR relaxation interference. *J Magn Reson,* 2006. **178**(1): p. 72-6.

47. Ryu, S., et al., Uncoupling proton activation of vanilloid receptor TRPV1. *J Neurosci,* 2007. **27**(47): p. 12797-807.

48. Boukalova, S., et al., Conserved residues within the putative S4-S5 region serve distinct functions among thermosensitive vanilloid transient receptor potential (TRPV) channels. *J. Biol. Chem.,* 2010. **285**(53): p. 41455-62.

49. Vandewauw, I., et al., A TRP channel trio mediates acute noxious heat sensing. *Nature,* 2018. **555**(7698): p. 662-666.

50. Laursen, W.J., et al., Low-cost functional plasticity of TRPV1 supports heat tolerance in squirrels and camels. *Proc Natl Acad Sci U S A,* 2016. **113**(40): p. 11342-11347.

51. Rath, P., et al., Implications of Human Transient Receptor Potential Melastatin 8 (TRPM8) Channel Gating from Menthol Binding Studies of the Sensing Domain. *Biochemistry,* 2016. **55**(1): p. 114-24.

52. Paramonov, A.S., et al., NMR investigation of the isolated second voltage-sensing domain of human Nav1.4 channel. *Biochim Biophys Acta Biomembr,* 2017. **1859**(3): p. 493-506.

53. Butterwick, J.A. and R. MacKinnon, Solution structure and phospholipid interactions of the isolated voltage-sensor domain from KvAP. *J Mol Biol,* 2010. **403**(4): p. 591-606.

54. Peng, D., et al., Purification and structural study of the voltage-sensor domain of the human KCNQ1 potassium ion channel. *Biochemistry,* 2014. **53**(12): p. 2032-42.

55. Ng, H.Q., et al., Purification and structural characterization of the voltage-sensor domain of the hERG potassium channel. *Protein Expr Purif,* 2012. **86**(2): p. 98-104.

56. Takeshita, K., et al., X-ray crystal structure of voltage-gated proton channel. *Nat Struct Mol Biol,* 2014. **21**(4): p. 352-7.

57. Sosa-Pagan, J.O., E.S. Iversen, and J. Grandl, TRPV1 temperature activation is specifically sensitive to strong decreases in amino acid hydrophobicity. *Sci Rep,* 2017. **7**(1): p. 549.

58. Hazan, A., et al., The pain receptor TRPV1 displays agonist-dependent activation stoichiometry. *Sci Rep,* 2015. **5**: p. 12278.

59. Singh, A.K., L.L. McGoldrick, and A.I. Sobolevsky, Structure and gating mechanism of the transient receptor potential channel TRPV3. *Nat Struct Mol Biol,* 2018. **25**(9): p. 805-813.

60. Hughes, T.E.T., et al., Structural basis of TRPV5 channel inhibition by econazole revealed by cryo-EM. *Nat Struct Mol Biol,* 2018. **25**(1): p. 53-60.

61. Singh, A.K., et al., Mechanism of calmodulin inactivation of the calcium-selective TRP channel TRPV6. *Sci Adv,* 2018. **4**(8): p. eaau6088.

62. Singh, A.K., et al., Structural bases of TRP channel TRPV6 allosteric modulation by 2-APB. *Nat Commun,* 2018. **9**(1): p. 2465.

63. Huynh, K.W., et al., Structure of the full-length TRPV2 channel by cryo-EM. *Nat Commun,* 2016. **7**: p. 11130.

64. Wen, H. and W. Zheng, Decrypting the Heat Activation Mechanism of TRPV1 Channel by Molecular Dynamics Simulation. *Biophys J,* 2018. **114**(1): p. 40-52.

65. Boukalova, S., J. Teisinger, and V. Vlachova, Protons stabilize the closed conformation of gain-of-function mutants of the TRPV1 channel. *Biochim Biophys Acta,* 2013. **1833**(3): p. 520-8.

66. Lomize, M.A., et al., OPM database and PPM web server: resources for positioning of proteins in membranes. *Nucleic Acids Res,* 2012. **40**(Database issue): p. D370-6.

67. Zhang, F., K.J. Swartz, and A. Jara-Oseguera, Conserved allosteric pathways for activation of TRPV3 revealed through engineering vanilloid-sensitivity. *Elife,* 2019. **8**.

68. Yin, Y., et al., Structural basis of cooling agent and lipid sensing by the cold-activated TRPM8 channel. *Science,* 2019. **363**(6430).

69. Vriens, J., et al., Determinants of 4 alpha-phorbol sensitivity in transmembrane domains 3 and 4 of the cation channel TRPV4. *J Biol Chem,* 2007. **282**(17): p. 12796-803.

70. Ammann, C., P. Meier, and A. Merbach, A simple multinuclear NMR thermometer. *Journal of Magnetic Resonance (1969),* 1982. **46**(2): p. 319-321.

71. Vranken, W.F., et al., The CCPN data model for NMR spectroscopy: development of a software pipeline. *Proteins,* 2005. **59**(4): p. 687-96.

72. Bond, C.S. and A.W. Schuttelkopf, ALINE: a WYSIWYG protein-sequence alignment editor for publication-quality alignments. *Acta Crystallogr D Biol Crystallogr,* 2009. **65**(Pt 5): p. 510-2.

73. Delaglio, F., et al., NMRPipe: a multidimensional spectral processing system based on UNIX pipes. *J Biomol NMR,* 1995. **6**(3): p. 277-93.

74. Williamson, M.P., Using chemical shift perturbation to characterise ligand binding. *Prog Nucl Magn Reson Spectrosc,* 2013. **73**: p. 1-16.

75. Lee, D., et al., Effective rotational correlation times of proteins from NMR relaxation interference. *J. Magn. Reson.,* 2006. **178**(1): p. 72-6.

76. Gautier, A., et al., Structure determination of the seven-helix transmembrane receptor sensory rhodopsin II by solution NMR spectroscopy. *Nature Struct. Mol. Biol.,* 2010. **17**(6): p. 768-74.

77. Iwahara, J., C. Tang, and G. Marius Clore, Practical aspects of (1)H transverse paramagnetic relaxation enhancement measurements on macromolecules. *J. Magn. Reson.,* 2007. **184**(2): p. 185-95.

78. Van Horn, W.D., et al., The impact of window functions on NMR-based paramagnetic relaxation enhancement measurements in membrane proteins. *Biochim Biophys Acta,* 2010. **1798**(2): p. 140-9.

79. Veglia, G., et al., Deuterium/Hydrogen Exchange Factors Measured by Solution Nuclear Magnetic Resonance Spectroscopy as Indicators of the Structure and Topology of Membrane Proteins. *Biophysical Journal,* 2002. **82**(4): p. 2176-2183.

80. Fitzkee, N.C. and A. Bax, Facile measurement of (1)H-(1)5N residual dipolar couplings in larger perdeuterated proteins. *J Biomol NMR,* 2010. **48**(2): p. 65-70.

81. Mascioni, A. and G. Veglia, Theoretical analysis of residual dipolar coupling patterns in regular secondary structures of proteins. *J Am Chem Soc,* 2003. **125**(41): p. 12520-6.

82. Mesleh, M.F., et al., Dipolar waves as NMR maps of protein structure. *Journal of the American Chemical Society,* 2002. **124**(16): p. 4206-4207.

83. Royer, C.A., C.J. Mann, and C.R. Matthews, Resolution of the fluorescence equilibrium unfolding profile of trp aporepressor using single tryptophan mutants. *Protein Sci,* 1993. **2**(11): p. 1844-52.

3.7 Supplementary Materials

3.7.1 Details of the Thermodynamic Framework for Interpreting Temperature-Dependent Studies

NMR resonance intensities are inversely proportional to the resonance linewidth ($\Delta\upsilon_{FWHH}$, full-width at half-height). For the Lorentzian shaped signals observed in NMR, the intensities and linewidths reflect the transverse relaxation rates (R_2) of the molecule, which can be estimated from the linewidth, $\Delta\upsilon_{FWHH} = R_2/\pi$ [1]. R_2 is in turn sensitive to the dynamic properties of the protein in solution, including nanosecond timescale rotational motion, and picosecond to millisecond internal motions, including protein conformational change. Thus, NMR peak intensity should report on the conformational state of a protein. In the hV1-S1S4 temperature-dependent NMR studies we leverage the common framework employed in CD to assess the thermosensitivity in terms of change in enthalpy (ΔH) as described below.

Far-UV CD is commonly used to measure the change in enthalpy (ΔH) between folded or conformational states [2]. This assumes that the change in measured ellipticity as a function of temperature is directly proportional to the change in protein states. Early studies have shown for two state behavior that there is good correlation between calorimetric and CD measurements of thermodynamic values (c.f.) [3]. To evaluate the ΔH for the transition between protein states, one generally assumes a two-state model. In the context of TRP channels this is certainly an oversimplification, but adequately captures accurate thermodynamic values, as has been noted in previous studies [4]. Briefly, for temperature-dependent equilibrium, CD data at a given wavelength, usually at 222 nm for helical proteins, exhibit clear changes between two states (i.e. the data are sigmoidal in nature). At a given temperature the relative concentrations of conformational states 1 and 2 will be related to the equilibrium constant K, which can be written as the fraction of the concentration of conformational state 2 (α):

$$K = \frac{[State\ 2]}{[State\ 1]} = \frac{\alpha}{1-\alpha} \qquad [1]$$

K is also related to the change in standard state free energy ($\Delta G°$) between conformational states and noted in the Gibbs-Helmholtz equation:

$$\Delta G° = -RT\ ln\ K \qquad [2]$$

which is in turn is related to the changes in enthalpy ($\Delta H°$) and entropy ($\Delta S°$) between states:

$$\Delta G° = \Delta H° - T\Delta S° \qquad [3]$$

At the midpoint of the transition between temperature-dependent conformational states (T_{50}), or the melting temperature (T_m) in folding studies, the concentrations of the two structural states are equal and $K = 1$ and $\Delta G° = 0$, resulting in the following identity:

$$\Delta S° = \frac{\Delta H°}{T_{50}} \quad [4]$$

Combining equations 2, 3, and 4, K can be written in a modified form of the van't Hoff equation using only terms of temperature (T), midpoint temperature (T_{50}), and the change in enthalpy ($\Delta H°$):

$$K = e^{\left[\left(\frac{\Delta H°}{RT}\right)\left(\left(\frac{T}{T_{50}}\right)-1\right)\right]} \quad [5]$$

Rearrangement of Equation 1 gives:

$$\alpha = \frac{K}{(1+K)} \quad [6]$$

A mathematical description of the assumption above, that the observed ellipticity at a given temperature (θ_{obs}) is directly proportional to the ellipticity of conformational states 1 (θ_1) and 2 (θ_2) gives the following relationship:

$$\theta_{obs} = \alpha(\theta_1 - \theta_2) + \theta_1 \quad [7]$$

To calculate the values of ΔH and T_{50} that best describe the experimental data, initial estimates of ΔH, T_{50}, θ_1, and θ_2 are used as initial parameters to non-linear least squares fitting of Equation 5, 6, and 7 to the raw data. The authors used SigmaPlot to perform

non-linear least squared fitting of the CD data which resulted in a $\Delta H = 19 \pm 1$ kcal/mol and $T_{50} = 37 \pm 1$ °C.

The method described above assumes that change in the heat capacity (ΔC_p) is negligible. In the context of TRP channel thermosensors, it has been suggested that this may not be the case [5]. Indeed, Chanda and coworkers have used protein design principles that attempt to increase the magnitude of ΔC_p for the Shaker voltage-gated potassium channel, a non-thermosensing ion channel, to successfully convert it to a thermosensing ion channel [6]. Chanda's study clearly indicates that modifying the change in heat capacity can perturb the thermosensitivity of a given protein. However, for wild-type TRP channels at biologically relevant temperatures, it seems that ΔC_p is relatively small in magnitude. When ΔC_p changes as a function of temperature then both ΔH and ΔS will change significantly as a function of temperature [5, 7]. However, as reviewed elsewhere [8], existing studies of TRP channel thermosensitivity suggest that ΔH (and thus ΔS) are fairly constant as a function of temperature indicating that ΔC_p is small in magnitude [4, 8-12].

The above described method is completely general for extracting ΔH from equilibrium data that can be approximated by a simple two state model. To this end, these same procedures were used to estimate the ΔH from temperature-dependent whole-cell patch-clamp electrophysiology steady state currents (Figure 3.2A), where θ_1, and θ_2 were modified to maximal and minimal current values. The resulting electrophysiology values are consistent with previously published TRPV1 thermodynamic values (Table S3.1).

Similarly, NMR resonance intensity as a function of temperature exhibit two-state behavior which was also fit to the above equilibrium thermodynamic model, yielding a ΔH value that is similar in magnitude to the CD determined value from the hV1-S1S4 (Figure 3.2B and Figure S3.3E). Lastly, this general two-state equation was also used to interpret the temperature-dependence of the intrinsic tryptophan fluorescence in terms of the average emission wavelength ($\langle\lambda\rangle$), which yielded values of hV1-S1S4 that are consistent with both NMR and CD.

3.7.2 Supplementary References

1. Cavanagh, J.F., W. J.; Palmer III, A. G.; Rance, M.; Skelton, N. J., *Protein NMR Spectroscopy: Principles and Practice (Second Edition)*. 2007: Elsevier Academic Press.

2. Greenfield, N.J., Using circular dichroism collected as a function of temperature to determine the thermodynamics of protein unfolding and binding interactions. *Nat. Protoc.,* 2006. **1**(6): p. 2527-35.

3. Privalov, P.L. and S.A. Potekhin, Scanning microcalorimetry in studying temperature-induced changes in proteins. *Methods Enzymol.,* 1986. **131**: p. 4-51.

4. Voets, T., et al., The principle of temperature-dependent gating in cold- and heat-sensitive TRP channels. *Nature,* 2004. **430**(7001): p. 748-54.

5. Clapham, D.E. and C. Miller, A thermodynamic framework for understanding temperature sensing by transient receptor potential (TRP) channels. *Proc. Natl. Acad. Sci. USA,* 2011. **108**(49): p. 19492-7.

6. Chowdhury, S., B.W. Jarecki, and B. Chanda, A molecular framework for temperature-dependent gating of ion channels. *Cell,* 2014. **158**(5): p. 1148-1158.

7. Prabhu, N.V. and K.A. Sharp, Heat capacity in proteins. *Annu. Rev. Phys. Chem.,* 2005. **56**: p. 521-48.

8. Voets, T., TRP channels and thermosensation. *Handb. Exp. Pharmacol.,* 2014. **223**: p. 729-41.

9. Yang, F., et al., Thermosensitive TRP channel pore turret is part of the temperature activation pathway. *Proc. Natl Acad. Sci. USA,* 2010. **107**(15): p. 7083-8.

10. Yao, J., B. Liu, and F. Qin, Kinetic and energetic analysis of thermally activated TRPV1 channels. *Biophys. J.,* 2010. **99**(6): p. 1743-53.

11. Yao, J., B. Liu, and F. Qin, Modular thermal sensors in temperature-gated transient receptor potential (TRP) channels. *Proc. Natl Acad. Sci. USA,* 2011. **108**(27): p. 11109-14.

12. Voets, T., et al., TRPM8 voltage sensor mutants reveal a mechanism for integrating thermal and chemical stimuli. *Nat. Chem. Biol.,* 2007. **3**(3): p. 174-82.

3.7.3 Supplementary Figures

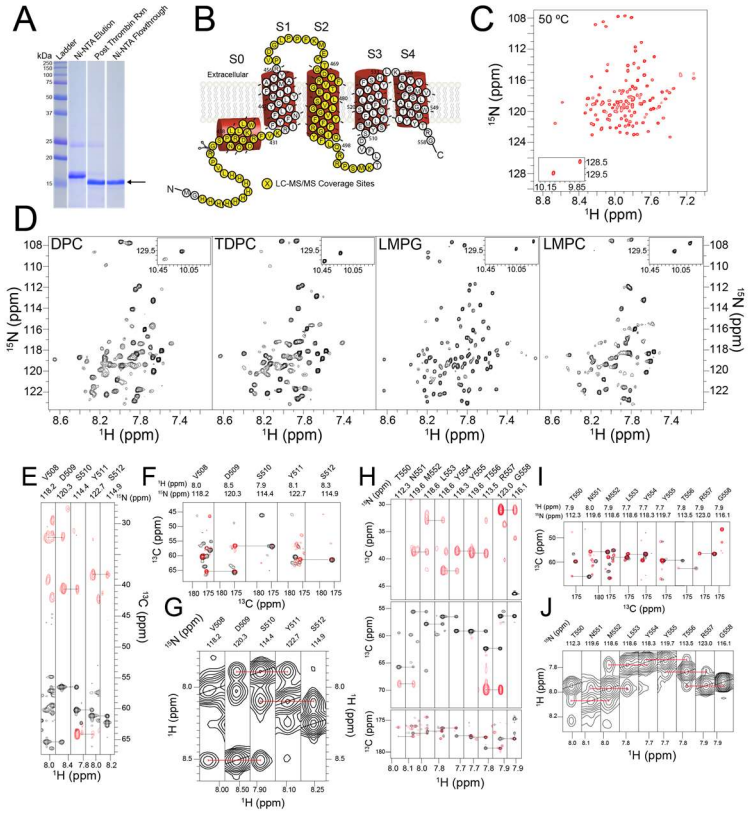

Figure S3.1 The expression and NMR amide backbone assignment of the hV1-S1S4. **(A)** SDS-PAGE gel of the hV1-S1S4 samples of Ni^{2+}-NTA affinity chromatography purification, post-thrombin reaction, and 10×His-tag cleaved hV1-S1S4 (lanes 2, 3, and 4 respectively). (**B**) The highlighted residues on the hV1-S1S4 membrane topology represent the coverage for LC-MS/MS as a means to verify the identity of hV1-S1S4 (51% amino acid coverage). (**C**) hV1-S1S4 reconstituted in LPPG micelles results in a high quality ^{1}H-^{15}N TROSY-HSQC NMR spectrum at elevated temperatures (50 °C). (**D**) Optimization of the micellar conditions for the hV1-S1S4 using NMR. To identify a suitable membrane mimic for hV1-S1S4, five membrane mimics were tested. LPPG was chosen to be the most suitable membrane mimic for the hV1-S1S4 as shown in (**C**) after analyzing the number of resonances observed, spectral resolution, and homogeneity of resonance intensities. (**E**) Residues in the TRPV1 S2-S3 loop have been implicated in vanilloid ligand binding and activation. A strip plot of HNCA and HNCOCA from V508 to S512 in the S2-S3 loop is shown on the left (**E**), and this assignment is confirmed by the 4D HNCA and HNCOCA (**F**) and ^{15}N-edited NOESY-TROSY (**G**). (**H**) Backbone resonance assignment of T550 to G558 in S4 helix, shown with HNCA (black) and HNCACB (red), 4D HNCACO (**I**, black) and ^{15}N-edited NOESY-TROSY (**J**).

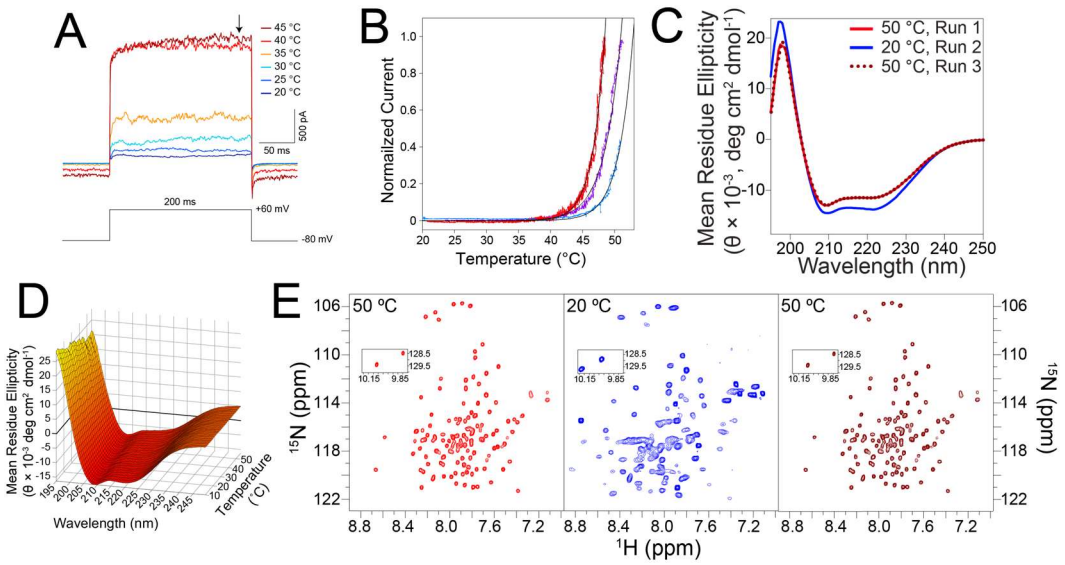

Figure S3.2 Temperature-dependent data of TRPV1 and hV1-S1S4. (**A**) The electrophysiology temperature measurement of the human TRPV1. Increased temperature evoked increased current magnitudes, and the data points at the black arrow were plotted against the temperature to generate the plot in Fig. 2A. (**B**) Three individual temperature ramp current values obtained from HEK-293 cells transiently transfected with hTRPV1. Cells were subjected to a temperature ramp from 20 to 50 °C over the course of ca. 35 seconds. The ΔH values from each line (red, purple and teal) are obtained from fitting to a pseudo-steady state model (see Methods), resulting in values of 106.8 ± 0.4, 80.1 ± 0.3, and 94.3 ± 0.5 kcal/mol, respectively. (**C**) The reversibility of the hV1-S1S4 was tested with CD between 20 °C and 50 °C. The CD spectra recover to mean residue ellipticity when re-heated. The data shown are of a temperature cycle of elevated, decreased, and returned elevated temperature spectra. (**D**) Superimposed circular dichroism spectra from 10 °C to 57 °C for the hV1-S1S4. The spectra show that key α-helical secondary structure features are generally retained as a function of temperature, which is consistent with the NMR and fluorescence data that the hV1-S1S4 remains seemingly structured over this temperature range. (**E**) The thermal reversibility of the hV1-S1S4 tested with NMR between 20 °C and 50 °C. Like the reversibility shown with CD in (**C**), the hV1-S1S4 that underwent the cycle of heating and cooling retains the initial resonances as shown in the first 50 °C spectrum (red, left), and the second 50 °C spectrum (dark red, right), showing that this domain does not exhibit hysteresis.

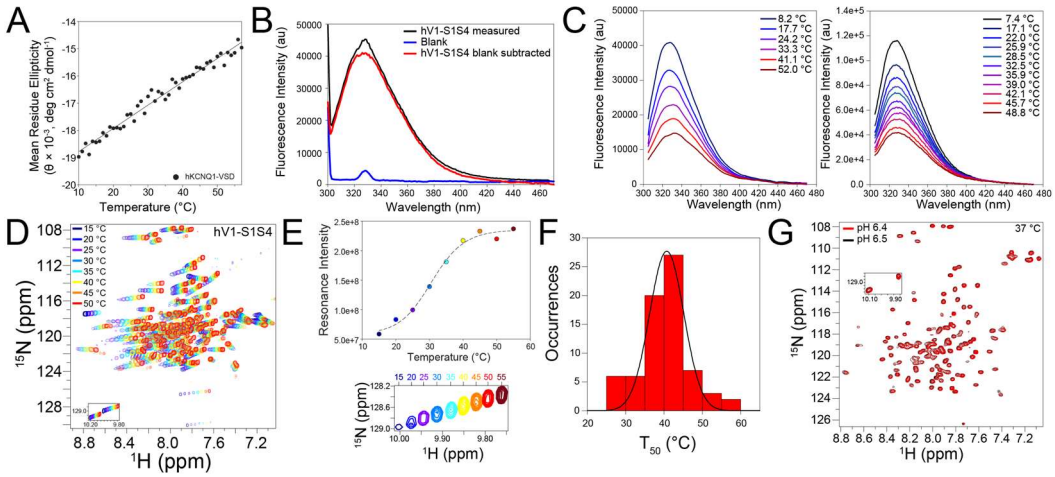

Figure S3.3 Additional data supporting the thermodynamic analyses of the hV1-S1S4 using various biophysical methods. (**A**) Non-temperature sensitive human KCNQ1 voltage-sensing domain was used as a negative control. As expected, the human KCNQ1-VSD shows a linear trend in mean residue ellipticity compared to the hV1-S1S4 data, which shows a clear sigmoidal shape. (**B**) The superimposition of the emission spectra of intrinsic tryptophan fluorescence of the hV1-S1S4, buffer (blank) and the hV1-S1S4 black subtracted. (**C**) The superimposition of the emission spectra of the hV1-S1S4 at varying temperature. Two distinct hV1-S1S4 samples were used for these measurements. (**D**) Superimposed ^{1}H-^{15}N TROSY-HSQC spectra of hV1-S1S4 as a function of temperature show significant chemical shift perturbations. The changes in chemical shift as a function of temperature reflect the thermal expansion of the hydrogen bonding of the secondary structure such that peaks that move less reside in more structured predominantly helical regions. The intensity changes as a function of temperature can be explained by the internal dynamics of the individual amide nuclei, which experience linewidth changes that are suitable for thermodynamic analysis. (**E**) Representative NMR data from W549; as the temperature changes, the intensity data has a sigmoidal shape which reflects a two-state transition and can be fit to extract thermodynamic parameters (see Methods). (**F**) The histogram distribution of melting temperatures (T_{50}) calculated from the NMR temperature titration. This was calculated from fitting the sigmoidal curve. The mean T_{50} of 71 resonances was calculated to be 40.7 ± 0.6 °C. (**G**) The ^{1}H-^{15}N TROSY-HSQC spectra at pH 6.5 and pH 6.4, which is in the range of pH change for the buffer that was used as a function of the temperature ramp, are identical when superimposed. This indicates that temperature induced buffer pH changes are not responsible for the hV1-S1S4 temperature dependent observations noted by NMR and CD experiments.

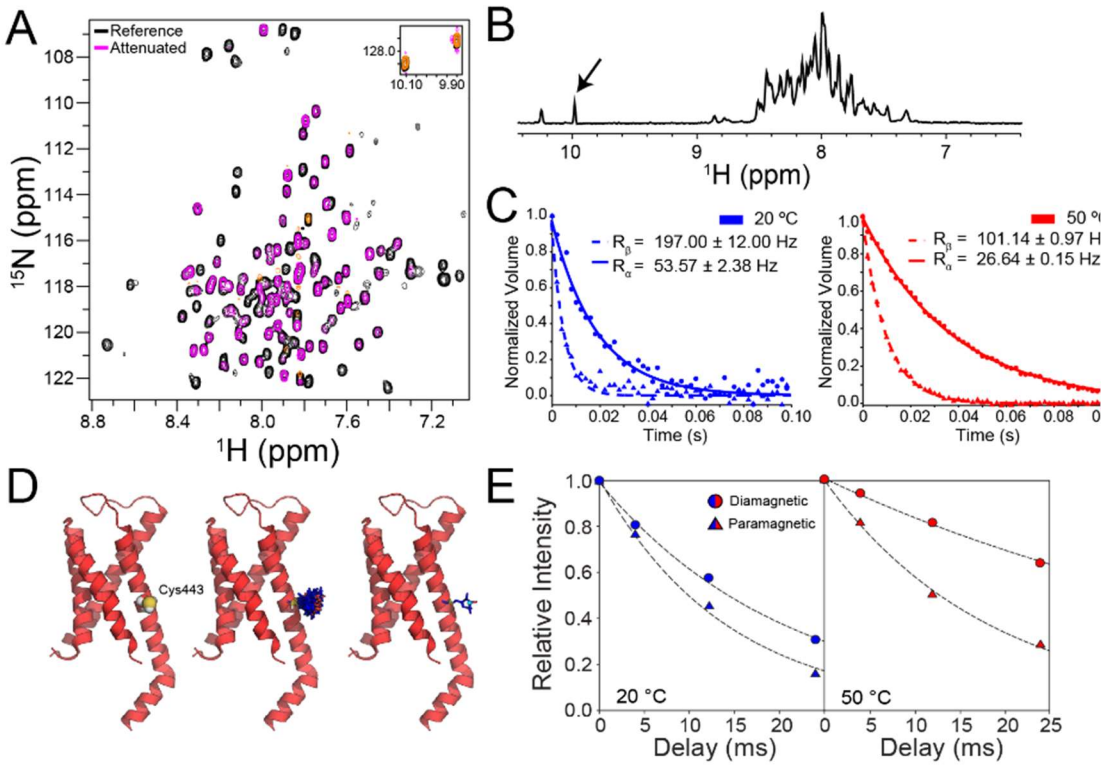

Figure S3.4 Supporting data for RDC and PRE NMR measurements. **(A)** The reference (black) and attenuated (magenta) ARTSY spectra of the hV1-S1S4 used for the RDC measurements. (**B**) A representative hV1-S1S4 proton NMR spectrum. The indole amine from the S4 helix residue W549, highlighted with an arrow, was used for analysis in the TRACT experiment (see Methods) due to potential artifacts that can arise from dynamic regions in the protein. (**C**) The relaxation rates for TROSY and Anti-TROSY relaxation states from the W549 indole amine at 20 °C and 50 °C. The relaxation rates were calculated by fitting to a monoexponential decay from which the rates were used to calculate the rotational correlation time (τ_c). (**D**) The location of a lone cysteine in the S1 helix of the hV1-S1S4, C443, was labeled with a maleimide paramagnetic nitroxide spin label, MTSL. The middle structure represents the MTSL-labeled S1-S4 domain (rTRPV1. PDB ID: 5IRZ) computationally, with 85 rotameric states of the MTSL modeled in PyMol (see Methods) and right structure displaying the centroid position of all the rotameric states of the MTSL. (**E**) The representative proton relaxation curves for paramagnetic and diamagnetic states at 20 °C and 50 °C for W427.

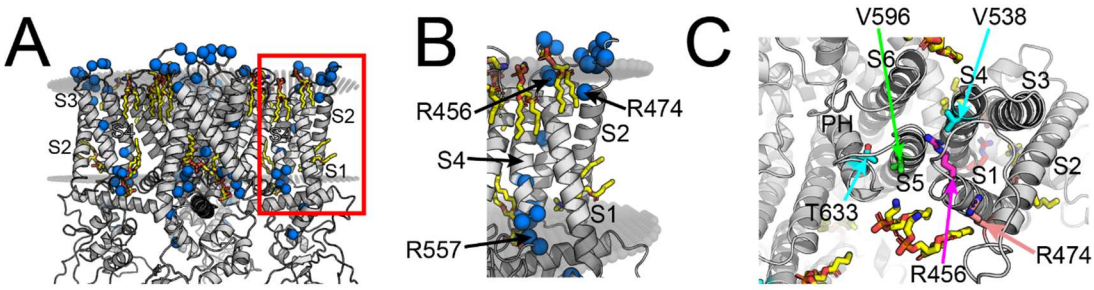

Figure S3.5 Mapping of the residues that show temperature-dependent movement. (**A**) The structure of TRPV1 (PDB ID: 5IRZ) in OPM membranes that highlights the residues that show increased solvent accessiblity at 45 °C, highlighted with marine. The main chains of the residues with increased solvation are shown in spheres. The S1-S4 domain is displayed in red box. The lipid molecules are shown in yellow sticks. (**B**) A close-up view of the S1-S4 domain. It is clear that the R456 and R557 are embedded in the membrane. All three residues, R456, R474 and R557, have high values of $\Delta NOE_{45°C–20°C}$ and appear to have temperature-dependent movements. (**C**) Top view of the TRPV1 structure (PDB ID: 5IRZ) that highlights key residues in heat and proton activation. R456 (S1 helix, magenta) is known to be crucial in channel function and gating and is interacting with V538 (S4 helix, cyan). V538 and T633 (pore helix, cyan) are important for proton activation. V596 (S5 helix, green) is a potential key residue for temperature activation, and this residue is surrounded by R456, V538 and T633.

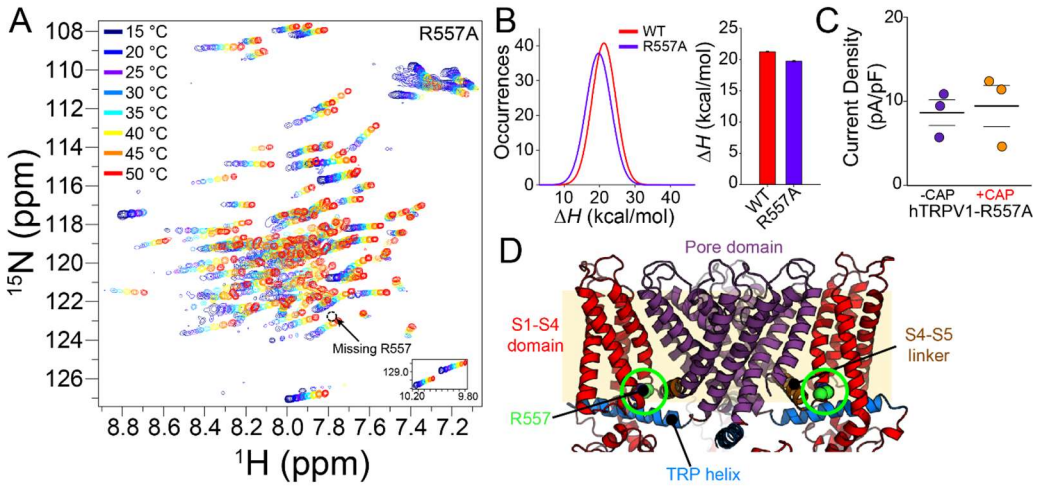

Figure S3.6 The hTRPV1-R557A mutant becomes insensitive to both temperature and capsaicin, but the hV1-S1S4-R557A retains the temperature sensitivity. (**A**) Superimposed ^{1}H-^{15}N HSQC spectra of the hV1-S1S4-R557A at temperatures from 15 to 50 °C. As expected the R557 resonance is missing in the R557A mutatnt spectra. (**B**) Comparison in Δ*H* between the WT and the hV1-S1S4-R557A mutant. The Gaussian fittings of the Δ*H* histograms (left) show a leftward shift, indicating that the R557A (purple line) is slightly less temperature sensitive than the WT (red line), consistent with the loss of a cation-π interaction. The ensemble average enthalpy from the respective WT and R557A Gaussian fits and resulting variance are shown in a bar plot (right). (**C**) The jittered plot of hTRPV1-R557A of whole-cell patch-clamp electrophysiology in the presence and absence of capsaicin. Consistent with R557A acting as a coupling mutation, the mutant is insensitive to capsaicin activation at a concentration (1 μM) that would saturate WT hTRPV1. (**D**) Structure of the rat TRPV1 (PDB ID: 5IRZ) that highlights each structural domain. The S1-S4 domains are highlighted in red. The PD that was implanted to the Shaker is demonstrated in purple. We note that R557 (highlighted in green) is not included in the chimeric study, and the phenotypes of this residue indicate that R557 is central to coupling the S1-S4 domain with the PD in channel gating.

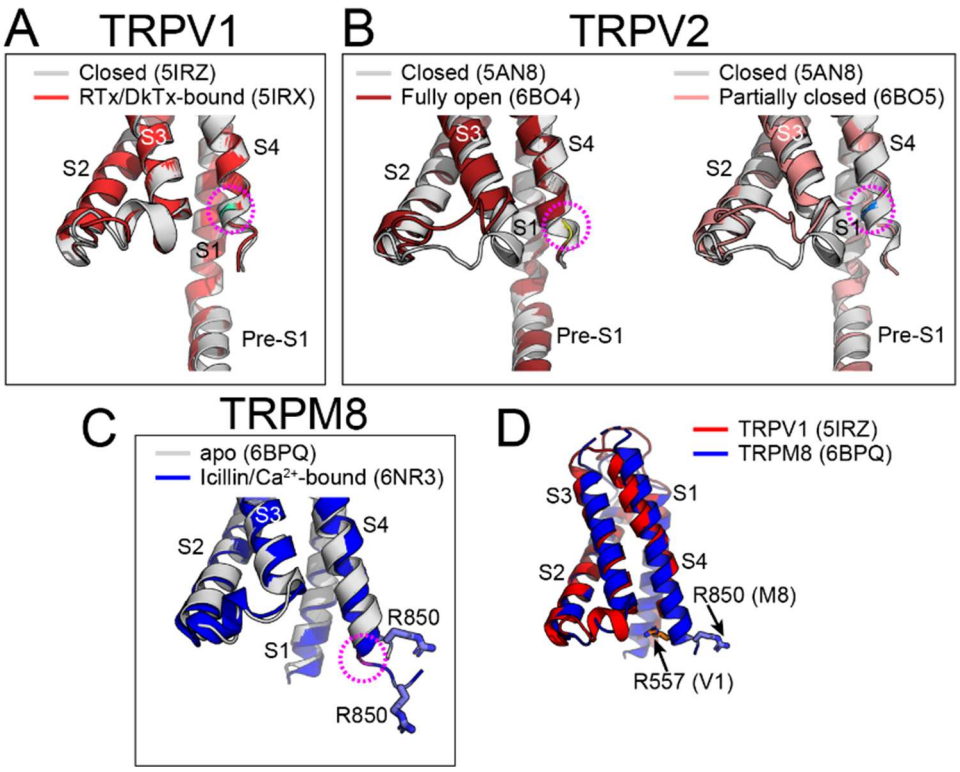

Figure S3.7 Structural examples of S4 helix motions in TRP channel activation. (**A**) Superimposed structures of TRPV1 in its resting (PDB ID: 5IRZ, light grey) and active states (RTx/DkTx-bound, PDB ID: 5IRX, red). In the active state, starting around Y555 (light blue, highlighted with magenta circle), the bottom of the S4 helix starts unfurling. (**B**) The same unfurling trend found in TRPV2. The fully-closed structure of TRPV2 (PDB ID: 5AN8) is superimposed with the fully open state that includes the pore turret (PDB ID: 6BO4, dark red on the left), and partially closed state which does not include the pore turret (PDB ID: 6BO5, pink on the right). In both alignments, the unfurling of the S4 begins at the bottom of the S4 helix (highlighted in yellow and marine, with magenta circle). (**C**) Superimposed structures of the apo TRPM8 (PDB ID: 6BPQ, light grey), and the icillin/Ca^{2+}-bound TRPM8 (PDB ID: 6NR3, blue). In TRPM8, the bottom of the S4 helix undergoes an extreme conformational change, induced by the α- to 3_{10}-helix transition, starting at the residue highlighted in magenta. This difference can be verified by the displacement of R850, as it travels further down the membrane when TRPM8 is activated. (**D**) The alignment of the S1-S4 domains of TRPV1 (red) and TRPM8 (blue). Although the orientation is different, R557 in TRPV1 and R850 in TRPM8 are located in the C-terminal end of the S4 helix, near the membrane bilayer.

3.7.4 Supplementary Tables

Supplementary Table S3.1. Measured thermosensitivity values (Δ*H)* of TRPV1 temperature studies.

Δ*H* (kcal/mol)	Potential (mV)	Method	TRPV1 species	Protein Origin/ Membrane Type	Reference
98 ± 12	+60	Whole-cell	Human	HEK293/HEK293	**This Study (Steady state)**
94 ± 8	+60	Whole-cell	Human	HEK293/HEK293	**This Study (Temp ramp)**
64.9[a]	-70	Whole-cell	Rat	HEK293/HEK293	**Vlachová et al., 2003**
150 ± 13	-60	Inside-out	Rat	*X. laevis*/ *X. laevis*	**Liu et al., 2003**
26.8	+80	Inside-out	Murine	HEK293/HEK293	**Yang et al., 2010**
101 ± 4 65 ± 6	-60, +60	Outside-out	Rat	HEK293/HEK293	**Yao et al., 2010**
90 ± 3	-60	Whole-cell	Rat	HEK293/HEK293	**Yao et al., 2011**
86.2 ± 3.9[b]	-60	Proteoliposome patch	Rat	Sf9 Insect cells/Soybean polar lipids	**Cao et al., 2013**
155	+100	Single-channel planar lipid bilayers	Rat	HEK293/3:1 POPC:POPE	**Sun and Zakharian, 2015**
65 ± 5.7[a]	-60	Whole-cell	Rat	*X. laevis*/ *X. laevis*	**Zhang et al., 2017**

88 ± 8	+60	Inside-out	Rat	HEK293/HEK293	**Sánchez-Moreno et al., 2018**

[a]*The reported temperature coefficient (Q_{10}) was converted to ΔH according to* $\Delta H \approx 20 ln Q_{10}$ [29].
[b] *Protein was purified and reconstituted in proteoliposomes.*

Supplementary Table S3.2 Buffer pH stability as a function of temperature.

Temperature (°C)[a]	pH[b]
10	6.49
15	6.50
20	6.49
25	6.48
30	6.46
35	6.41
40	6.41
45	6.38
50	6.36
55	6.40
60	6.39

[a] *Temperature measured with Fluke 52 II thermometer with 80PK-1 beaded type-K thermocouple; according to the instrument specifications, in this temperature range, should produce a maximum temperature error of ±0.4 °C.*
[b] *This data is for the phosphate buffer used in CD, fluorescence and NMR measurements (see Methods).*

3.7.5 NMR Processing Scripts

```
#!/bin/csh

bruk2pipe -in ./ser \
  -bad 0.0 -ext -aswap -AMX -decim 1960 -dspfvs 20 -grpdly 67.9862976074219  \
  -xN              2048  -yN              128  \
  -xT              1024  -yT               64  \
  -xMODE            DQD  -yMODE  Echo-AntiEcho  \
  -xSW        10204.082  -ySW         2585.315  \
  -xOBS         850.279  -yOBS          86.168  \
  -xCAR           4.641  -yCAR         117.953  \
  -xLAB              HN  -yLAB             15N  \
  -ndim               2  -aq2D         Complex  \
  -out ./test.fid -verb -ov

sleep 1

#!/bin/csh

nmrproc.com Script for nmrDraw

set nodelist = (  11ppm 6ppm  )

set lbHz    =  1.0
set g1      =  15
set g2      =  20
set off     =  0.33
set pow     =  2
set p0      =  -67.8
set p1      =   0.0
set c       =   0.5
set extX1   = 11.0ppm
set extXN   = 6.5ppm

nmrPipe -in test.fid \
| nmrPipe -fn POLY -time                          \
#| nmrPipe -fn LP -b -pred 20  -fix -ord                    \
| nmrPipe  -fn GM -g1 $g1 -g2 $g2 -g3 0.05 -c 0.75 -one          \
| nmrPipe  -fn ZF -zf 2 -auto                        \
| nmrPipe  -fn FT -auto                       \
| nmrPipe -fn BASE -nl $nodelist                     \
| nmrPipe  -fn PS -p0 $p0  -p1 $p1 -di -verb       \
| nmrPipe  -fn POLY -auto                      \
| nmrPipe -fn EXT -x1 $extX1 -xn $extXN -sw         \
| nmrPipe  -fn TP                                \
```

```
#| nmrPipe -fn LP -fb -pred 50 -ord                    \
| nmrPipe  -fn SP -off $off -end 0.98 -pow $pow -c 0.5      \
| nmrPipe  -fn ZF -zf 2 -auto                          \
| nmrPipe  -fn FT -auto                          \
| nmrPipe  -fn PS -p0 90.00 -p1 0.00 -di -verb       \
#| nmrPipe  -fn POLY -auto                          \
       -ov -out test.ft2
```

3.7.6 NMR-Detected Thermosensitivity Analysis MatLab Script

```
if exist('fit_data','dir') == 7
   disp('data exits')
else
   mkdir fit_data
   mkdir plots
end

tic
clear all
clc
close all

warning('off')
files=dir('*.txt');
j=readtable(files(1).name,'Delimiter','\t');
n=size(files);




t=[15 20 25 30 35 40 45 50];


fit2=@(b,x) 1+(b(1)-b(2))*exp(b(3)./(1.98E-3.*x).*(x./b(4)-1))./(1+exp(b(3)./(1.98E-
3*x).*(x./b(4)-1)));


% b(1) = max b(2)=min b(3)=DelH b(4)=tm

figure
hold on
tmp=readtable(files(1).name,'Delimiter','\t');
r=1.98E-3; %kcal/mol/K
```

```
a=tmp.Height;
beta20=[max(a) min(a) 10 300];
[xData yData]=prepareCurveData(t,a)
[beta2,R2,J2,CovB2,MSE2]=nlinfit(xData+273.15,a,fit2,beta20);
xfit2=linspace(min(t),max(t))+273.15;
fig=plot(xData+273.15,a,'o', xfit2,fit2(beta2,xfit2));
legend([fig],['\Delta H =  ' sprintf('%.2f',beta2(3)) ' kcal/mol/K '  ],'Location','Best');


clear a
figure
for i=1:n(1);
   try
   hold on
   tmp=readtable(files(i).name,'Delimiter','\t');
   a=tmp.Height;
   b(:,i)=a;
   [xData yData]=prepareCurveData(t+273.15,a);
   fit=@(b,x) b(1)*x+b(2);
   beta20=[max(a) min(1) 10 300];
   [beta2,R2,J2,CovB2,MSE2]=nlinfit(xData,a,fit2,beta20)
   stdev=sqrt(diag(CovB2));

   delh(:,i)=beta2(3);
%    delh=delh';
   tm(:,i)=beta2(4);
   error(:,i)=stdev(3);
   fig=figure;
   plot(xData,a,'o', xfit2,fit2(beta2,xfit2));
   saveas(fig,sprintf('./plots/FIG%d.png',i)); % will create FIG1, FIG2,...
   close
   catch
   end
end

% movegui(t,'southwest')
%save('fit_data/enthalpy.txt','delh','-ascii');
%save ('fit_data/tm.txt','tm','-ascii');

%% Histogram with Gaussian fit
Delta_H=delh;
clear fit
h1=length(find(Delta_H>5 & Delta_H<10));
h2=length(find(Delta_H>10 & Delta_H<15));
```

```
h3=length(find(Delta_H>15 & Delta_H<20));
h4=length(find(Delta_H>20 & Delta_H<25));
h5=length(find(Delta_H>25 & Delta_H<30));
h6=length(find(Delta_H>30 & Delta_H<35));
h7=length(find(Delta_H>35 & Delta_H<40));
fig=length(find(Delta_H>40 & Delta_H<45));
x=linspace(0,45,10)+2.5;
y=[0 h1 h2 h3 h4 h5 h6 h7 fig 0];
rng default
figure
hold on
[xData yData]=prepareCurveData(x,y);
f=fit(xData,yData,'gauss1');
fit=@(g,x) g(1).*exp(-((x-g(2))./g(3)).^2);
beta0=[f.a1 f.b1 f.c1];
[beta,R,J,CovB,MSE]=nlinfit(xData,yData,fit,beta0);
standev=sqrt(diag(CovB));
SEM=standev/sqrt(length(yData));
SSresidual=sum(R.^2);
SStotal=sum((y-mean(y)).^2);
rsquare=1-(SSresidual/SStotal);
bar(x,y,1);
p=plot(f);
legend([p],['\Delta H =  ' sprintf('%.2f',beta(2)) '  \pm  ' sprintf('%.2f',SEM(2)) ' kcal/mol '
],'Location','Best');
xlabel('\DeltaH (kcal/mol)')
ylabel('Occurences')
set(gca,'TickDir','out')
print('-painters','-deps','histogram_fit_delta_H_v2')
% print -painters -dpdf -r800 histogram_fit_delta_H_v2.eps

%% Histogram for tm

t50=tm-273.15;
clear fit
b0=length(find(t50<30));
b1=length(find(t50>30 & t50<35));
b2=length(find(t50>35 & t50<40));
b3=length(find(t50>40 & t50<45));
b4=length(find(t50>45 & t50<50));
b5=length(find(t50>50 & t50<55));
b6=length(find(t50>55 & t50<60));
fig=length(find(t50>60));
x=linspace(0,45,10)+22.5;
```

```
y=[0 b0 b1 b2 b3 b4 b5 b6 fig 0];
rng default
figure
hold on
[x y]=prepareCurveData(x,y);
f=fit(x,y,'gauss1');
fit=@(g,x) g(1).*exp(-((x-g(2))./g(3)).^2);
beta0=[f.a1 f.b1 f.c1];
[beta,R,J,CovB,MSE]=nlinfit(x,y,fit,beta0);
standev=sqrt(diag(CovB));
SEM=standev/sqrt(length(yData));
SSresidual=sum(R.^2);
SStotal=sum((y-mean(y)).^2);
rsquare=1-(SSresidual/SStotal);
bar(x,y,1);
p=plot(f);
legend([p],['\t50 =  ' sprintf('%.2f',beta(2)) '  \pm  ' sprintf('%.2f',SEM(2)) ' degC '
],'Location','Best');
xlabel('\tm (degC)')
ylabel('Occurences')
set(gca,'TickDir','out')
print('-painters','-deps','histogram_fit_tm_v2')
% print -painters -dpdf -r800 histogram_fit_delta_H_v2.eps
```

3.7.7 NMR-Detected Temperature Coefficient Analysis MatLab Script

```
if exist('fit_data','dir') == 7
   disp('data exits')
else
   mkdir fit_data
end

tic
clear all
close all
clc

delete('decays_ppb_tempCoeff.txt')
warning('off')
files=dir('*.txt');
j=readtable(files(1).name,'Delimiter','\t');
n=size(files);
Dd=zeros(8,n(1));
```

```
for i=1:n(1)
   try
   h=readtable(files(i).name,'Delimiter','\t');
   H=h.PositionF2;
   N=h.PositionF1;
   DdH=power((H-H(end)),2);
   ddh(:,i)=DdH;
   DdN=power(((N-N(end))/5),2);
   Dd(:,i)=sqrt(DdH+DdN);
   catch
   end
end

work=zeros(8,n(1));
for i=1:n(1)
   try
   h=readtable(files(i).name,'Delimiter','\t');
   H=h.PositionF2;
   work(:,i)=H;
   catch
   end
end

t=[15 20 25 30 35 40 45 50];
figure
for i=1:n(1);
   hold on
   [xData yData]=prepareCurveData(t,ddh(:,i));
   fit=@(b,x) b(1)*x+b(2);
   beta0=[0 0];
   [beta,R,J,CovB,MSE]=nlinfit(xData,yData,fit,beta0);
   xfit=linspace(min(xData),max(xData));
   plot(xData,yData,'o', xfit,fit(beta,xfit) );
   decay(:,i)=beta(1)*1000;
   residuals(:,i)=R;

end
figure
for i=1:n(1);
   hold on
   [xData yData]=prepareCurveData(t,Dd(:,i));
   fit=@(b,x) b(1)*x+b(2);
   beta0=[0 0];
   [beta,R,J,CovB,MSE]=nlinfit(xData,yData,fit,beta0);
```

```
    xfit=linspace(min(xData),max(xData));
    plot(xData,yData,'o', xfit,fit(beta,xfit) );
    deldel(:,i)=beta(1)*1000;

end
figure
for i=1:n(1);
    hold on
    [xData yData]=prepareCurveData(t,work(:,i));
    fit=@(b,x) b(1)*x+b(2);
    beta0=[0 0];
    [beta,R,J,CovB,MSE]=nlinfit(xData,yData,fit,beta0);
    xfit=linspace(min(xData),max(xData));
    plot(xData,yData,'o', xfit,fit(beta,xfit) );
    prot(:,i)=beta(1)*1000;

end
figure
for i=1:n(1);
    [p,S] = polyfit(xData,residuals(:,i),2);
    paraParm(:,i)=p(1);
    x1 = linspace(min(xData),max(xData));
    y1 = polyval(p,x1);
    P(:,i)=p(1);
    plot(xData,residuals(:,i),'o')
    hold on
    plot(x1,y1)

end
```

CHAPTER 4

THE S1-S4 DOMAIN OF HUMAN TRPV1 BINDS VARIOUS CHEMICAL AGONISTS AND ANTAGONISTS

4.1 Introduction

The taste of spicy foods arises primarily from vanilloid compounds that chemically activate the TRPV1 (transient receptor potential vanilloid 1) heat receptor [1]. The vanilloid compound capsaicin, is the cognate ligand for TRPV1 and the molecular mechanism of capsaicin activation has come into focus in recent years through structural and functional studies [2-6]. The first study that identified the capsaicin-sensitive region in TRPV1 utilized the capsaicin-insensitive chicken TRPV1 ortholog (genus *Gallus gallus*, gTRPV1) [7]. Despite the family name vanilloid, other TRPV channels (TRPV2-6) are insensitive to vanilloid compounds. Using the capsaicin insensitivities from gTRPV1 and rTRPV2, the key residue for capsaicin sensitivity was identified to be Y511 in S3 helix of the S1-S4 domain [7]. The ligand-bound TRPV1 structures, combined with computational modeling, has elucidated the capsaicin-dependent gating mechanism [2-6]. The vanilloid moiety of capsaicin is thought to form hydrogen bonds with Y511 in S3 helix and E570 in S4-S5 linker, and the neck of capsaicin, where the amide group is located, forms a hydrogen bond with T550 in S4 helix, interacting with the S1-S4 domain in head-down, tail-up orientation [4]. The binding of capsaicin induces the movement of S4-S5 linker towards the S1-S4 domain, and this movement exerts mechanical force to pull the S6 helix in the pore domain, initiating the opening of the lower gate [4].

Due to its responsiveness to noxious stimuli, TRPV1 has been therapeutic target for pain for decades [8, 9]. For instance, capsaicin cream can be found over the counter at any pharmacy as a pain reliever. Generally when capsaicin is administered topically, activated TRPV1 eventually leads to channel desensitization of this pain receptor, causing the therapeutic analgesic effect [10]. Another target of TRPV1-mediated pain relief is through the development of specific antagonists [8, 11]. Broadly, two types of TRPV1 antagonists include competitive and orthosteric antagonists. In particular, competitive antagonists bind to the orthosteric agonist binding site, forcing channel closure; whereas, orthosteric antagonists bind to the region that is distant to the agonist binding site, eventually leading to inhibition [12]. These TRPV1 antagonists can block temperature hypersensitivity that is induced by inflammation, which can be effective in pain relief [8]. However, a major side effect of TRPV1 antagonism is the changes in core body temperature (either hyperthermia or hypothermia), which in significant cases could be fatal [13, 14]. Therefore, it is crucial to understand how TRPV1 interacts with various chemical compounds at the molecular level to better understand how chemical binding is coupled to channel activation, which would set a foundation to dissect distinct TRPV1 modes of activation that include capsaicin, heat, and protons [15].

TRPV1 is modulated by various ligands including canonical vanilloids, endogenous and exogenous cannabinoids, and synthetic antagonists [16-18]. To illustrate the interesting pharmacology of TRPV1 chemical activation, consider capsiate, a vanilloid that activates TRPV1 [16]. The chemical structure of capsiate is nearly identical to capsaicin; except for the chemical linkage between the vanilloid head group and

aliphatic in capsaicin is an amide; whereas, capsiate has an ester linkage. Unlike capsaicin, which is extremely pungent, capsiate is not pungent [16]. A more complete understanding of how capsaicin, capsiate and other TRPV1 regulating chemicals should provide an explanation for phenotypes including the lack of capsaicin pungency. In addition to the discovery of an endogenous cannabinoid molecule, anandamide (AEA), one study showed that some cannabinoids from cannabis regulation TRPV1 function, suggestive that cannabinoid compounds can be novel therapeutic target for inflammation and pain [17, 19].

Various cryo-EM structures of ligand-bound TRP channels have identified the putative ligand binding sites. From these studies,TRPV1 vanilloid agonists including capsaicin (CAP) and resiniferatoxin (RTx), bind to the canonical vanilloid binding site, as confirmed by the ligand-bound cryo-EM structures [2, 3]. Remarkably, with a few mutations, the canonical vanilloid binding pocket was also engineered to the vanilloid-insensitive TRPV2 and TRPV3, emphasizing the importance of key residues that form the binding pocket and presumably mechanistic conservation among family members [20-22]. Additionally, other chemical ligands also bind the canonical vanilloid binding pocket including capsazepine, a TRPV1 vanilloid mimic that is missing a methoxy group in the head group and functions as an antagonist [3], and econazole, an inhibitor of TRPV5 and TRPV1 [23, 24]. Interestingly, 2-aminoethoxydiphenyl borate (2-APB), a common modulator of a number of TRP channels [25-27], binds to multiple regions in TRPV3, introducing a potential allosteric modulation mechanism [28]. Unfortunately, molecular mechanism of how other agonists and antagonists modulate TRPV1 still

remains elusive. Understanding how TRPV1 interacts with different ligands is anticipated to provide new insights into TRPV1 therapeutic intervention.

The four-helix bundle S1-S4 membrane domain of human TRPV1 is central to the vanilloid ligand sensitivity, where binding occurs and then the binding energy is transduced to the pore domain resulting in channel gating [2, 3, 5, 7, 29]. This domain is structurally homologous to the voltage sensing domain (VSD) of voltage-gated potassium ion channels (VGICs). In VGICs, the VSD senses the changes in membrane potential across the membrane, eliciting a conformational change that initiates the gating event [30]. In TRPV channels, this domain appears to undergo a movement as a response to ligand binding [31]. For instance, in TRPV3, binding of 2-APB causes the S1-S4 domain to tilt toward the pore domain [28]. Similar to TRPV3, the S1-S4 domain of TRPV5 tilts away from the PD when the inhibitor econazole binds in the canonical vanilloid binding pocket, closing the lower gate [23]. The S1-S4 domains of other TRPVs, TRPV2, TRPV4 and TRPV6, show distinct movements such as rotation, S3 helix movement, and the movement of S4 and S4-S5 linker helices, respectively [31]. Currently, the structural data indicate that there is limited to no conformational change in TRPV1 upon agonist binding [2, 3]; however, given the related TRPV channels undergo conformational change, it remains to be determined what the magnitude and direction of conformational changes in the TRPV1 S1-S4 domain that underlie channel activation and gating.

Our recent study indicates that the S1-S4 membrane domain of human TRPV1 (hV1-S1S4) is efficiently reconstituted in a lysolipid membrane mimic, and specifically binds capsaicin. Here, we performed a comprehensive analysis on capsaicin binding to

hV1-S1S4, and probed the effect of temperature differences on capsaicin binding. Additionally, the role of S4-S5 linker in capsaicin binding was investigated. Next, we explored the interaction between the hV1-S1S4 and various ligands such as capsiate, cannabinoids, cholesteryl hemisuccinate, and ABT-102. Lastly, we inspected the inhibition mode of a TRPV1 antagonists, ABT-102, and its influence in temperature activation.

4.2 Materials and Methods

4.2.1 Capsaicin Titration of hV1-S1S4 Using NMR Spectroscopy

The hV1-S1S4 was prepared following previously established protocol [32]. The protein concentration was calculated by BSA assay because the concentrations of protein and detergent determine the amount of ligands to add in units of mole%. The mole% of the ligand was calculated as an equation [1]:

$$[ligand](mol\%) = \frac{n_{ligand}}{n_{ligand} + n_{LPPG} + n_{S1S4}} \times 100\% \quad [1]$$

One thing to note is that the equation [1] does not consider the critical micelle concentration (CMC). Desired ligands were prepared in organic solvents including ethanol, DMSO, and chloroform depending on the solubility. Specifically, stock solutions of capsaicin, capsiate, resiniferatoxin, cannabidiol, cannabigerol, anandamide, and ABT-102 were solubilized in 200 proof EtOH. Capsazepine and 2-APB stock solutions were prepared in DMSO and cholesteryl hemisuccinate in chloroform. All the protein samples were prepared in 180 μL volume common to a 3 mm NMR tube. For the initial titration point, ^{1}H-^{15}N TROSY-HSQC or Best-TROSY-HSQC experiments were acquired on a

Bruker 850 MHz (^{1}H) spectrometer with a 5 mm TCI cryoprobe and Avance III HD console. Depending on the protein concentration, the number of transients varied, but for ^{1}H-^{15}N TROSY-HSQC, 2048 points in the direct dimension and 128 points in the indirect dimension were collected, and for ^{1}H-^{15}N Best-TROSY-HSQC, 1024 points in the direct dimension and 256 points in the indirect dimension were recorded. Most of the titrations were carried out at 37 °C after a calibration using deuterated MeOH (± 0.1 °C) [32]. Additionally for capsaicin, titrations were performed at 25 °C and 50 °C. To continue a titration, the sample was ejected from the spectrometer, and calculated volumes of ligand for each titration point were added to the NMR tube, and the ligand was mixed by inverting the NMR tube 3 times. The same ^{1}H-^{15}N TROSY-HSQC or Best-TROSY spectrum was collected at each titration point, until the ligand was determined to be at its respective saturating concentration. Between titration points, there was no significant incubation time. For capsaicin, capsiate, cannabidiol, and anandamide, the following titration points were used: 0.001, 0.002, 0.005, 0.012, 0.015, 0.025, 0.075, 0.125, 0.225, and 0.723 mol%. For cannabigerol (CBG), one additional point, 1.22 mol%, was added to ensure that CBG is at its saturating concentration, and for capsazepine, an additional point of 0.0005 mol% was used because capsazepine has been shown to be a potent competitive antagonist against capsaicin. For 2-APB, prepared in DMSO, the titration points included 0.001, 0.002, 0.005, 0.012, 0.017, 0.030, 0.080, 0.180, 0.380 and 0.875 mol%. Cholesteryl hemisuccinate (CHS) was prepared in chloroform, and the following titration points were used: 0.001, 0.002, 0.005, 0.012, 0.015, 0.025 and 0.075 mol%. Resiniferatoxin (RTx) and ABT-102 are known to be much more potent than capsaicin.

To date, majority of the ligand sensitivity to TRPV1 has been measured with the EC_{50} (or IC_{50}), the concentration of a ligand at the half of the maximal (inhibitory) response. This is an indirect method to measure the affinity of an agonist/antagonist, and it is different from the binding dissociation constant (K_d), which measures the direct association between the ligand and the target. From previous functional measurements, the EC_{50} of RTx and the IC_{50} of ABT-102 against capsaicin have been reported to be in the low nano-molar range [7, 13, 29]. Therefore, much smaller titration points were used; for RTx, 0.01, 0.02, 0.05, 0.07, 0.1, 0.5, 1, 5, 10 μmol% were used, and for ABT-102, 0.5, 1, 2, 7, 12, 22, 72, 122, 222, 722, 1222 nmol% were used.

Collected spectra were processed using NMRPipe and analyzed with CcpNmr Analysis. The changes in chemical shift ($\Delta\delta_{obs}$) that were produced by the addition of ligands were calculated using equation [2] below,

$$\Delta\delta_{obs} = \sqrt{(\Delta\delta_H)^2 + \frac{1}{5}(\Delta\delta_N)^2} \qquad [2]$$

Calculated chemical shift perturbations were plotted as a function of ligand concentration, and the binding dissociation constants (K_d) were calculated using the nlinfit function in *Matlab R2016a* and a single binding site model with the following equation:

$$f(x) = \frac{x \cdot B_{max}}{K_D + x} \qquad [3]$$

where B_{max} is the maximal change in $\Delta\delta_{obs}$ for a given resonance of the hV1-S1S4 upon saturation with ligands, K_d is the dissociation constant, x is the concentration of ligand in mol% [32-34].

Since chemical shift perturbations were observed from the majority of resonances, more thorough analysis was done to isolate the binding region in the hV1-S1S4. This could indicate that there might be a global conformational change in the hV1-S1S4 upon ligand binding. In NMR ligand titrations, a larger magnitude $\Delta\delta$ implies involvement in the binding site, and smaller K_d indicates tighter binding; therefore, large $\Delta\delta/K_d$ values should identify residues that are near the respective ligand binding site. Residues with very small K_d values, less than 1 mmol%, were disregarded because those K_d values mean very tight binding, but this may not be measurable via NMR because the timescale of the off-rate would be out of range that can be detected by NMR [34], or the ratio between the ligand and the protein may not be reasonable (i.e., not 1:1 ratio) [34]. This "tight" binding could be the result of slow-exchange between the ligand-bound state and ligand-free state, which cannot be fit to equation [3]. Additionally, the ratios between fitting error and K_d values were calculated, and those with a fitting error to K_d ratio higher than 40% were similarly discarded. The $\Delta\delta/K_d$ values after a thorough analysis were plotted against the hV1-S1S4 residue number, and the cutoff value for residues involved in binding was determined to be the sum of the average $\Delta\delta/K_d$ and one standard deviation to make sure that strong binding residues are not within the noise.

Binding of capsaicin without a vehicle solvent seemed to exhibit an intermediate exchange because the plot of chemical shift perturbation as a function of capsaicin

showed sigmoidal curves rather than hyperbolic curves. Especially for Y511 and S512, the binding curves were fitted using the Hill equation,

$$f(x) = \frac{x^n}{K_d^n + x^n} \quad [4]$$

where *n* is the Hill coefficient, which informs the degree of cooperativity between ligand and protein.

4.2.2 Capsaicin Titration at Different Temperatures

NMR-detected capsaicin titrations of the hV1-S1S4 were conducted at 25, 37 and 50 °C to calculate the changes in enthalpy (ΔH) in binding. In these binding experiments, the unit of K_d is in mol% because there are multiple components in the system such as protein, detergent molecules and ligand molecule. Because the hV1-S1S4 is surrounded by a significant amount of LPPG detergent micelles, and hydrophobic capsaicin molecule tends to get partitioned into the membrane, using the traditional molarity to measure the K_d is not meaningful, therefore, mole ratio, or mole percent, is a more accurate way to measure the K_d. To calculate the changes in free energy (ΔG) of binding, K_d values in mol% at different temperatures were converted to molarity (M) under the assumption that the protein concentration is 50 μM and the concentration of LPPG is 0.1 wt%. Using the gas constant 1.987×10^{-3} kcal·mol^{-1}·K^{-1}, the ΔG of binding at different temperatures were calculated using a following equation:

$$\Delta G = RT ln K_d \quad [5]$$

Because the dissociation constant is the reciprocal of the association constant ($K_d = \frac{1}{K_a}$), the negative sign was canceled from the inverse of K_a. The lnK_d values from capsaicin binding at three temperatures were plotted against 1000/T (1/K). If $\Delta H°$ and $\Delta S°$ are independent to the temperature changes, the change in heat capacity, $\Delta C_p°$, would be zero. In this case, the lnK_d would be directly proportional to temperature, and this relationship can be fit to the classical van't Hoff equation below:

$$lnK_{eq} = -\frac{\Delta H°}{RT} + \frac{\Delta S°}{R} \quad [5]$$

From this equation, slope values from the linear progression fitting were used to calculate the $\Delta H°$. However, if $\Delta H°$ and $\Delta S°$ are dependent on the temperature, $\Delta C_p°$ is not equal to zero, and the lnK_d vs temperature plot can be fit to the polynomial function [35]:

$$lnK_d = a + \frac{b}{T} + \frac{c}{T^2} + \frac{d}{T^3} + \cdots \quad [6]$$

From the fitting using equation [6], the parameter values can be obtained and used to calculate $\Delta G°$, $\Delta H°$, $\Delta S°$ and $\Delta C_p°$ using the following equations [35]:

$$\Delta G° = -R\left(aT + b + \frac{c}{T} + \frac{d}{T^2}\right) \quad [7]$$

$$\Delta H° = -R(b + \frac{2c}{T} + \frac{3d}{T^2}) \quad [8]$$

$$\Delta S° = R\left[a - \left(\frac{C}{T^2} + \frac{2d}{T^3}\right)\right] \quad [9]$$

$$\Delta C_p^\circ = 2R\left(\frac{c}{T^2} + \frac{3d}{T^3}\right) \quad [10]$$

4.2.3 Capsaicin Titration of hV1-S1S4 Mutants

A number of point mutations of the hV1-S1S4 were generated using a Q5 cloning kit. The mutants include Y511A, R557A, Y511A/R557A, D459A, E467A and E467A/Y511A, and the success of mutagenesis was confirmed by DNA Sanger sequencing. The mutations were also validated by comparing mutant protein NMR spectra to the wild-type amide backbone assigned spectrum. The NMR-detected capsaicin titrations for these mutants were carried out using the same capsaicin titration points, and the resulting spectra were processed and analyzed as described in the section 4.2.1.

4.3 Results

4.3.1 Capsaicin Induces the Conformational Change of the S1-S4 Domain

We have previously performed the NMR-detected capsaicin titration with the hV1-S1S4 in the lysolipid membrane memetic. Since capsaicin is a lipophilic molecule, an organic solvent needed to be chosen, and ethanol was selected as a vehicle. As capsaicin solution was added to the hV1-S1S4, chemical shift perturbations were detected (Figure 4.1A). Key capsaicin-binding residues, Y511, S512 and T550, presented saturable, specific capsaicin binding as previously shown (Figure 4.1B). In addition to these residues, majority of the hV1-S1S4 resonances displayed chemical shift perturbations that could indicate that other regions in the S1-S4 domain may bind capsaicin. Analyzing the other assigned resonances suggests that capsaicin also binds

outside of the vanilloid binding pocket, mainly in the extracellular S1-S2 loop, and top of the S2 and S3 helices (Figure 4.1C).

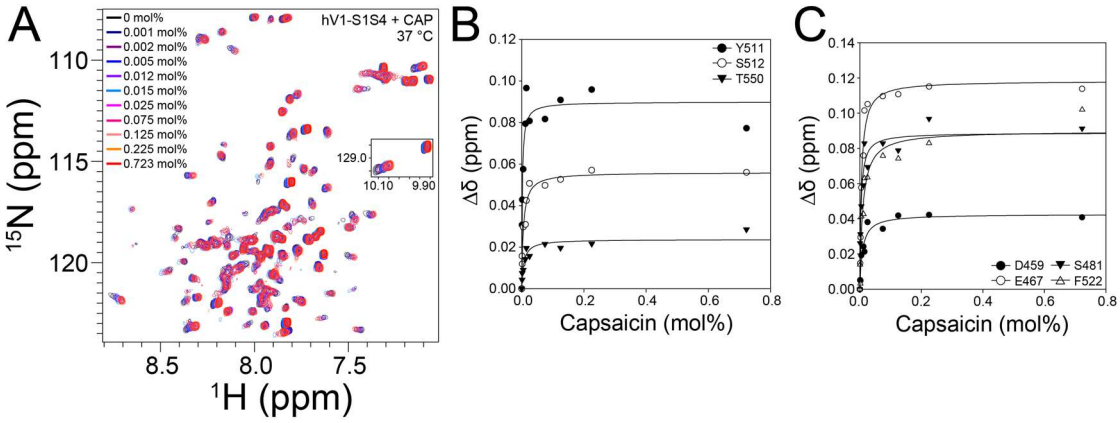

Figure 4.1 NMR-detected capsaicin titration with the S1-S4 domain of hTRPV1. (A) Superimposed ^{1}H-^{15}N TROSY-HSQC spectra of capsaicin titration with the hV1-S1S4 at 37 °C. Global chemical shift perturbations were detected as increasing capsaicin concentration. (B) Binding isotherms of key capsaicin binding residues, Y511, S512 and T550. Calculated binding dissociation constants (Kd) for Y511, S512 and T550 are 2.0 ± 0.5 mmol%, 5.4 ± 1.1 mmol%, and 6.7 ± 2.1 mmol%, respectively. (C) Binding isotherms of other residues that bind capsaicin. D459 and E467 reside in the extracellular S1-S2 loop, S481 is in the S2 helix, and F522 is in the S3 helix. The K_d values for these residues are 8.6 ± 2.1 mmol%, 5.1 ± 0.8 mmol%, 3.8 ± 0.9 mmol%, and 9.6 ± 2.7 mmol%, respectively.

To ensure that the global chemical shift perturbations were not induced by ethanol, specific control experiments were conducted. First, the hV1-S1S4 was subjected to the ethanol titration, using the same volume of ethanol added for the capsaicin titration. Increasing amount of ethanol caused chemical shift perturbations; however, ethanol didn't bind specifically to the hV1-S1S4 (Figure 4.2A). Analysis of Y511 against the mole% of EtOH and increasing volume of EtOH did not show saturable, hyperbolic curves, indicating that EtOH does not bind to the S1-S4 domain (Figure 4.2B, C). It is noteworthy that the volume of ethanol added to the sample at each titration point matches

to the amount that was needed for the titration using capsaicin prepared in ethanol solution. When the volume of ethanol was converted to mole%, the titration points were close to be 100 mole% (Figure 4.2B), displaying no specific binding, whereas capsaicin seemed to show a saturable specific binding [32]. Second, saturating amount of capsaicin was directly incorporated into the hV1-S1S4, and series of dilutions reflected the changes in chemical shifts (Figure 4.3A). While majority of resonances showed typical hyperbolic binding isotherms in the presence of ethanol, the absence of ethanol resulted in the binding curves that resemble sigmoidal curves. Fitting these curves of Y511 and S512 to the Hill equation resulted in different K_d values 3.5 ± 0.4 mol%, and 3.4 ± 0.2 mol%, respectively, with the Hill coefficients of 2.0 ± 0.3 and 1.6 ± 0.1, respectively (Figure 4.3B). From this experiment, there were resonances that did not show the specific binding to capsaicin. Instead, some residues exhibited intriguing trends in line widths as a function of capsaicin. For example, E467, a residue in the extracellular S1-S2 loop, showed increasing line widths (line broadening) as the concentration of capsaicin increased, but at the end, the line width decreased at the final saturating concentration of capsaicin. Additionally, some residues such as T526 in the S3 helix and S540 in the S4 helix, which are close in proximity, showed decreasing line widths as capsaicin reached the saturating concentration (Figure 4.3C).

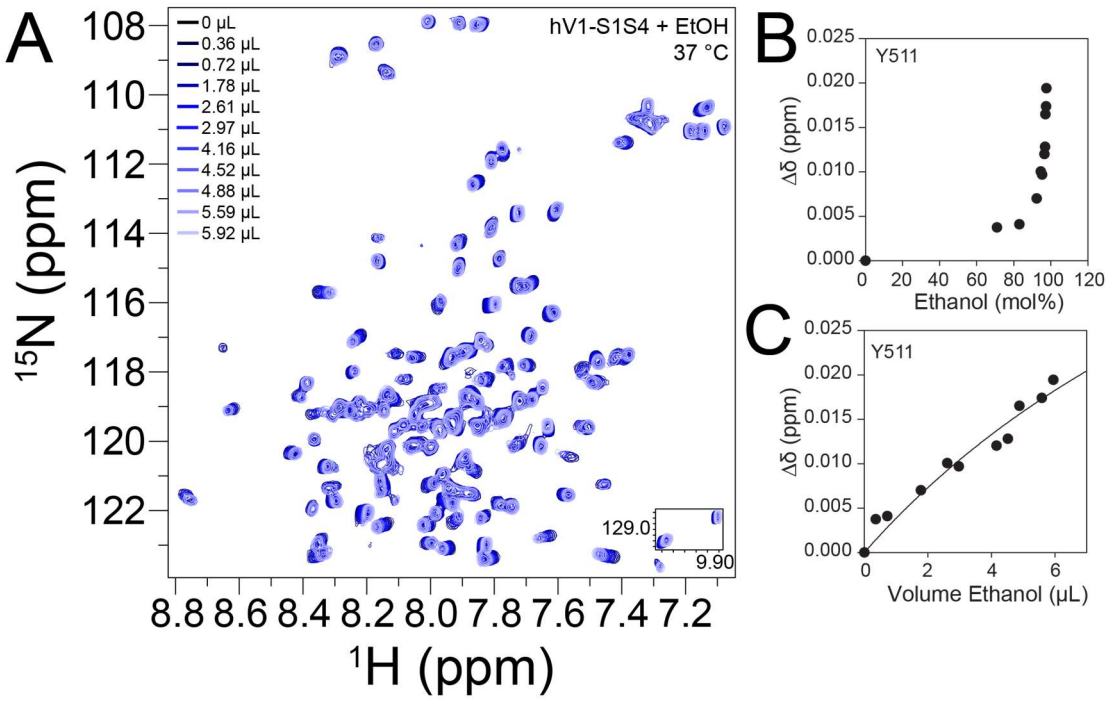

Figure 4.2 NMR-detected EtOH titration with the hV1-S1S4. (A) Superimposed hV1-S1S4 HSQC spectra as increasing volume of ethanol. (B) Calculated mole% values of EtOH was plotted against the chemical shift perturbations (CSPs) of Y511. (C) The CSPs of Y511 was plotted against the added volume of EtOH, which seemed to show a generally linear relationship indicative of non-specific binding.

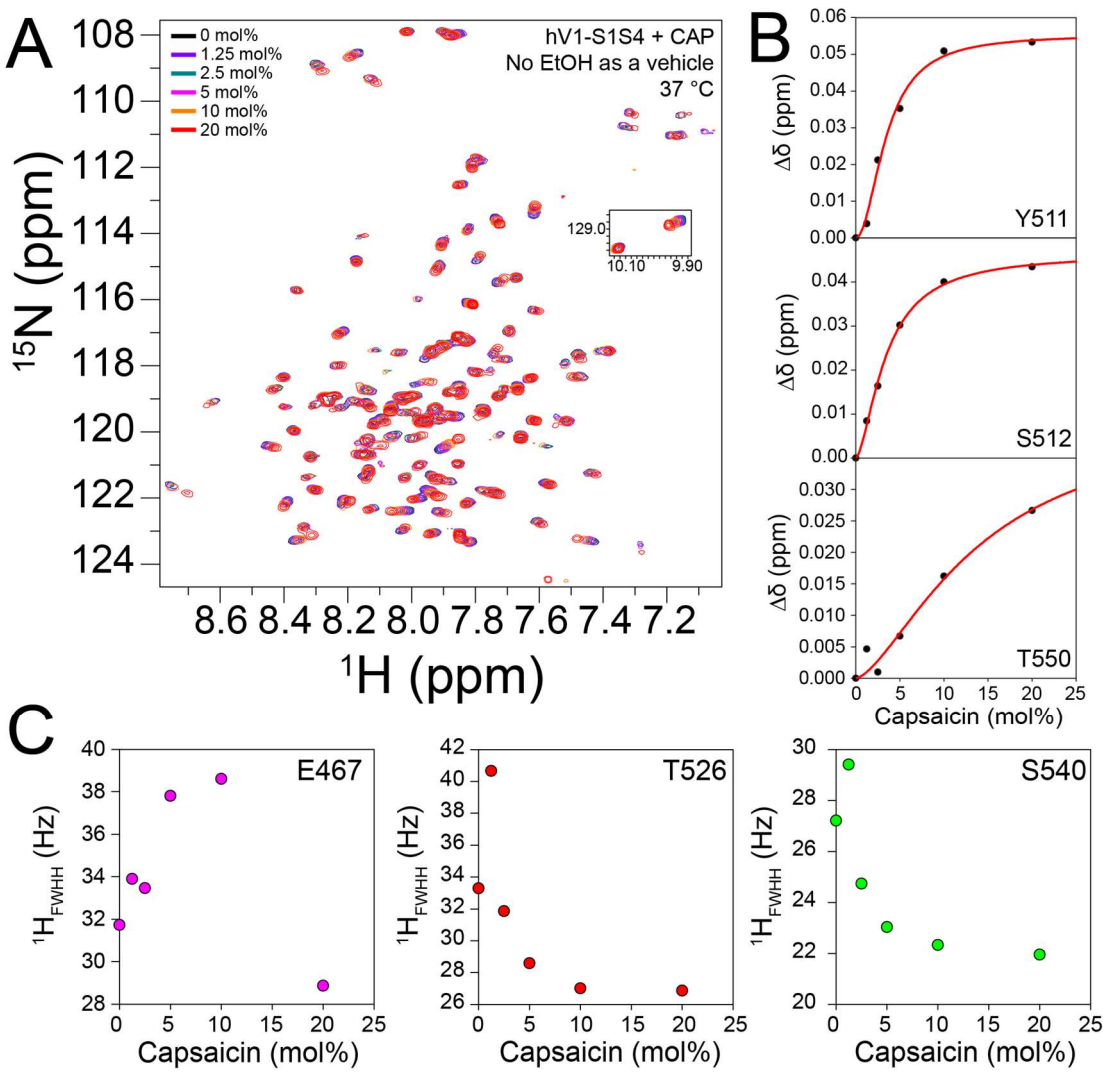

Figure 4.3 NMR-detected capsaicin titration with the S1-S4 domain of hTRPV1. (A) NMR-detected capsaicin titration with the hV1-S1S4 without ethanol. Global CSPs were also observed similar to the previous titration with capsaicin stock prepared in ethanol. (B) Binding curves of Y511, S512 and T550 from the capsaicin titration without the use of vehicle. These curves were fitted using the Hill equation instead of the equation used for one-site saturation binding. The resulting K_d values were 3.5 ± 0.4 mol%, 3.4 ± 0.2 mol%, and 14 ± 13 mol%, respectively. (C) Changes in linewidth (full-width at half height, FWHH) as a function of capsaicin concentration. Instead of the line broadening upon ligand binding, different trends were observed. For example, the linewidths E467 in the S1-S2 loop increased with the increasing capsaicin concentration, but at the final, saturating concentration, the linewidth decreased drastically, which could indicate an intermediate exchange. Additionally, T526 in S3 helix and S540 in S4 helix showed gradually decreasing linewidth, which could indicate slow exchange systems.

4.3.2 The Mutants of the hV1-S1S4 Binds Capsaicin but with Decreased Affinities

Y511 in S3 helix has been designated to be a key molecular determinant of capsaicin interaction. When Y511 of the rat TRPV1 was mutated to alanine (rTRPV1-Y511A), the mutant channel showed no response to capsaicin [7]. To test this, the hV1-S1S4-Y511A was generated, and this mutant was subjected to the same NMR-detected capsaicin titration experiments, using both capsaicin solutions prepared in ethanol, and capsaicin directly incorporated in protein solution. These two distinct approaches led to slightly different results. First, the magnitudes of chemical shift perturbations (Δδ) were compared to the WT. When capsaicin prepared in ethanol was used, the overall magnitude of Δδ of the hV1-S1S4-Y511A was much smaller than that of WT. Despite the smaller Δδ values, when each resonance was analyzed, majority of the resonances displayed the saturable, specific capsaicin binding with the overall K_d of 16.7 ± 0.7 mmol%, which is approximately 2.3 times weaker than the WT. On the other hand, when the capsaicin was directly incorporated into the hV1-S1S4-Y511A solution, the magnitude of Δδ was similar to that from the WT, and some resonances showed tighter binding to capsaicin (Figure 4.4).

Our previous work showed that the R557A is a coupling mutant in temperature sensing [32], and we further investigated the role of this residue in capsaicin sensitivity. First, we probed the effect of this mutation in the full-channel using the whole-cell patch clamp electrophysiology. Compared to the WT hTRPV1, hTRPV1-R557A showed no responses to capsaicin, indicating that R557 could be also involved in coupling between the S1-S4 domain and pore domain in capsaicin gating. To test if the R557A mutant in

the S1-S4 domain would reflect the same result as the functional measurement, the hV1-S1S4-R557A was generated and the same capsaicin titration was carried out. Somewhat expected, the hV1-S1S4-R557A bound capsaicin, with the average K_d of 26.1 ± 10.2 mmol%.

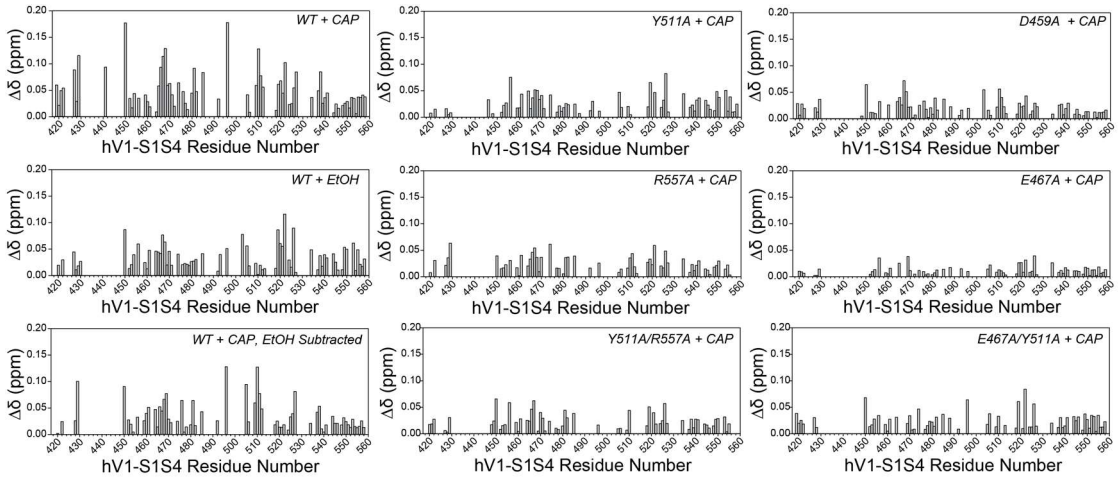

Figure 4.4 Comparison in Δδ magnitudes from the capsaicin titration with hV1-S1S4 and its mutants. All of these titrations were performed using capsaicin stock prepared in ethanol. To compare, the Δδ values from ethanol was plotted as well. Overall, the Δδ values from the mutants are much smaller than the wild-type.

To evaluate the contributions of Y511 and R557 in capsaicin binding, a double-mutant, hV1-S1S4-Y511A/R557A was created and was subjected to the capsaicin titration. Compared to the single mutants, the overall Δδ values were slightly smaller, however, many residues still seemed to bind specifically to capsaicin, yielding the overall K_d of 21.3 ± 1.4 mmol%. The Y511A, R557A mutants and the Y511A/R557A double mutant allowed us to perform double mutant cycle analysis [32]. Using the averaged K_d values of the WT, Y511A, R557A and Y511A/R557A, double mutant cycle analysis was performed. The change in free energy *(ΔG*) were calculated from the converted K_d values

from mol% to Molarity, and the differences in ΔGs were further calculated (Table 4.1). Unfortunately, the quality of R557A data was inferior than the others, resulting in a huge error compared to others. It will be worth collecting the R557A data in the future studies. The calculated ΔG values are listed in Figure 4.4, and the coupling energy between Y511 and R557 ($\Delta\Delta G$) was calculated to be –0.6 ± 0.3 kcal/mol (Figure 4.5).

Table 4.1 Averaged Binding Dissociation Constants of the hV1-S1S4 WT, Y511A, R557A and Y511A/R557A.

	WT	Y511A	R557A	Y511A/R557A
Averaged K_d (mmol%)	7.2 ± 0.1	16.7 ± 0.1	26.1 ± 10.2	21.3 ± 1.4
Converted K_d (μM)	1.0 ± 0.1	2.3 ± 0.1	3.6 ± 1.4	3.0 ± 0.2
ΔG (kcal/mol)	-8.5 ± 0.1	-8.0 ± 0.1	-7.7 ± 0.2	-7.9 ± 0.1

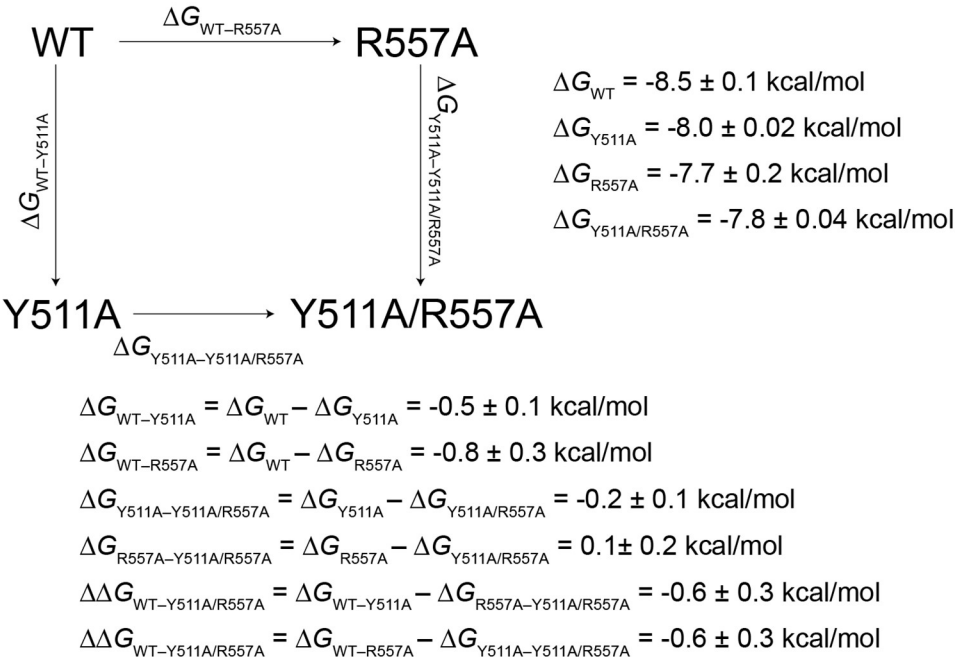

Figure 4.5 Double mutant cycle analysis for capsaicin binding. From this double mutant cycle analysis, $\Delta G_{WT-R557A} \neq \Delta G_{Y511A-Y511A/R557A}$ and $\Delta G_{WT-Y511A} \neq \Delta G_{R557A-Y511A/R557}$, indicating that these two mutations, Y511A and R557A, are not independent of each other. Furthermore, the coupling energy between Y511 and R557, $\Delta\Delta G_{int}$ was calculated to be $-0.6 \pm 0.3\ kcal/mol$.

We noticed that many residues in the S1-S2 loop show an apparent specific interaction with capsaicin. To test if the extracellular S1-S2 loop is crucial in capsaicin binding, the following mutations were created, D459A and E467. These two mutants resulted in even smaller Δδ at the saturating concentration of capsaicin than the other mutants, Y511A, R557A, and Y511A/R557A, and the ethanol (Figure 4.4). The overall averages of the K_d values for the D459A and E467A were 16.7 ± 0.9 mmol% and 13.2 ± 0.9 mmol%, respectively, which are weaker than the WT by approximately 4-5 folds (Figure 4.4).

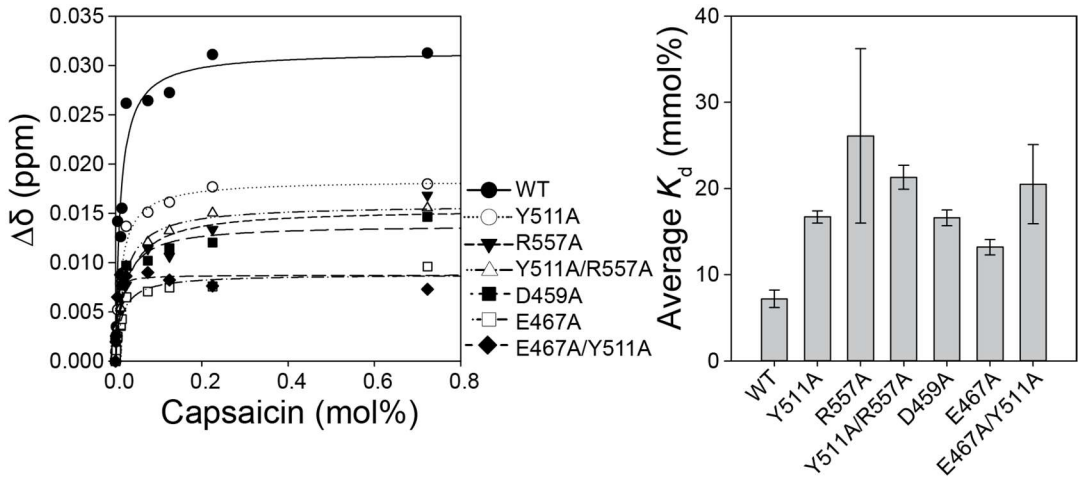

Figure 4.6 Comparison among capsaicin binding to the hV1-S1S4. On the left is representative binding isotherms of a residue W549. This is the indole amine of W549, and the binding isotherms of the mutants were plotted to compare the affinities to capsaicin. The bar plot on the right represents the averaged K_d values in mmol% for all the constructs that were tested. The error for the R557A mutant is quite large due to the poor fitting from the poor quality of data. The smaller values of K_d indicates a tighter binding, and this confirms that the wild type has a tighter interaction with capsaicin than the mutants.

Furthermore, we hypothesized that mutating one of the residues in the S1-S2 loop and Y511 might knock out the capsaicin sensitivity, and another double mutant, hV1-S1S4-E467A/Y511A, was made, and was tested for capsaicin binding. The magnitude of Δδ was somewhat decreased, and majority of resonances retained saturable specific binding (Figure 4.6). The same double mutant cycle analysis was performed, using E467A and Y511A single mutants and an E467A/Y511A double mutant, and the free energy of coupling between E467 and Y11 was calculated. All the values are listed in Figure 4.7.

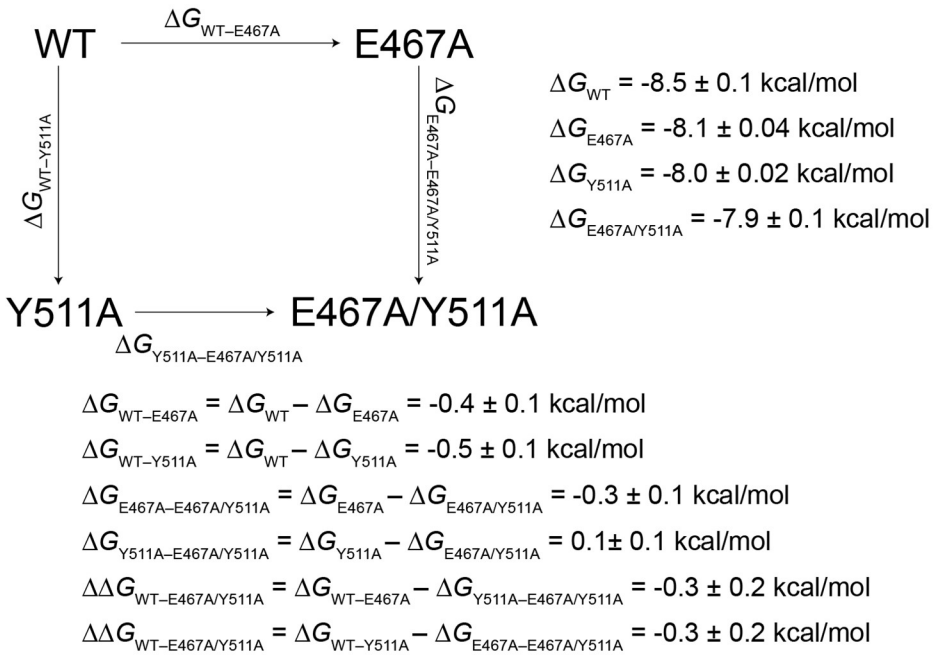

Figure 4.7 Double mutant cycle analysis for residues E467 and Y511. From this double mutant cycle analysis, $\Delta G_{WT-E467A} \neq \Delta G_{Y511A-E467A/Y511A}$ and $\Delta G_{WT-Y511A} \neq \Delta G_{E467A-E467\ /Y511A}$. Similar to Y511 and R557, these two residues E467 and Y511 are also not independent of each other. The free energy of coupling between E467 and Y511, $\Delta\Delta G_{int}$ was calculated to be $-0.3\ \pm 0.2\ kcal/mol$, which is smaller than $\Delta\Delta G_{int}$ from Y511 and R557, and this value is presumably insignificant at the quality of the current data.

4.3.3 Capsaicin Binding at Different Temperatures

Previously, we have shown that the S1-S4 domain undergoes temperature dependent conformational changes. If the hV1-S1S4 were to have different conformations at different temperatures, capsaicin may interact with the hV1-S1S4 differently at each temperature. To test this hypothesis, capsaicin titrations at 3 different temperatures, 25, 37 and 50 °C were carried out. Due to the coalesces of resonances, the K_d values of some residues could not be obtained. Overall, capsaicin bound with the tightest affinity at 25 °C relative to the other two temperatures, when the averages of all

binding dissociation constants were compared. The plot of lnK_d against the inverse of temperature ($1/T \times 10^3$) demonstrated a nonlinear trend (Figure 4.8), which deviates from the classical van't Hoff model. However, this trend was not conserved when individual residues were analyzed. Some residues showed decrease in binding affinities as temperature increased, but most residues didn't show a specific trend. In general, the classical van't Hoff's equation assumes that the $\Delta H°$ and $\Delta S°$ are independent to temperature changes (i.e., $\Delta H°$ and $\Delta S°$ are constant over temperature changes), which means that the heat capacity ($\Delta C_p°$) is zero. In this case, classical van't Hoff equation as shown in equation [5] (in Materials and Methods) could provide the H° value from the slope. However, the plot shown in Figure 4.8 can be better analyzed by fitting using the nonlinear van't Hoff's equation. The nonlinear van't Hoff's model assumes that the ΔH° and ΔS° are dependent on changes in temperature, and the $\Delta C_p°$ is not zero [35]. Depending on the curvature of the curve, the sign of $\Delta C_p°$ changes, and the heat-sensitive nature of TRPV1 would result in the negative value of $\Delta C_p°$ [37, 38].

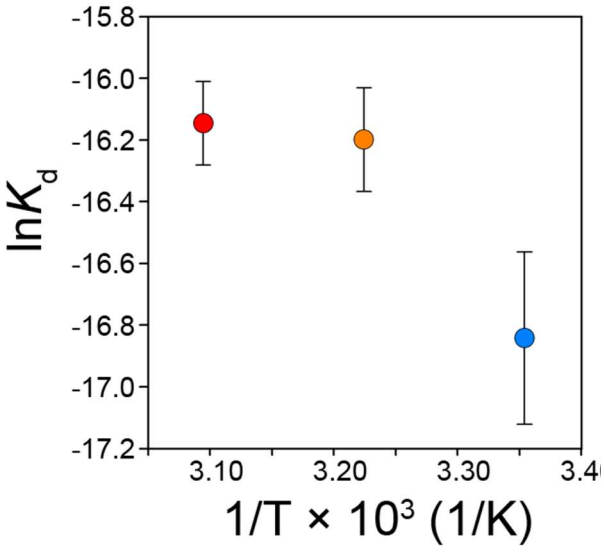

Figure 4.8 Thermodynamic analysis of capsaicin binding to the hV1-S1S4. The averaged K_d values of capsaicin binding at 25 (blue circle), 37 (orange circle) and 50 °C (red circle), independently, were converted to molar unit. Then natural log (*ln*) of K_d were calculated, and plotted against $1/T \times 10^3$ in Kalvin. Since this plot does not follow the classical van't Hoff's equation, it will be fitted to the nonlinear van't Hoff's equation in future studies. From the fitting, $\Delta C_p°$ value can be obtained.

4.3.4 Role of the S4-S5 Linker in Ligand Interaction

Another important residue in capsaicin binding is E570 in S4-S5 linker, as this residue also forms a hydrogen bond with the vanilloid head group. This interaction is crucial specifically because it causes the movement of the S4-S5 linker, initiating the gating event. To validate that the S4-S5 linker enhances the ligand interaction, the hV1-S1S4-S4-S5 linker construct was generated. Using the same expression and purification condition, the hV1-S1S4-linker yielded an HSQC spectrum of which the spectral quality was as great as that of the hV1-S1S4. Extra residues were detected, and the C-terminal residues of the S4 helix were disappeared as expected. Next, the capsaicin was tested to for the differences in the magnitudes of the binding affinities. The capsaicin stock solutions with much smaller concentrations were prepared, and the NMR-based titration showed that Y511 and T550 in the linker construct showed much higher affinity to capsaicin than that of the hV1-S1S4 construct, with the affinities 0.26 ± 0.09 μmol% and 0.30 ± 0.1 μmol%, respectively (Figure 4.9). Compared to the hV1-S1S4, the binding affinities for these two residues of the hV1-S1S4 with the S4-S5 linker are approximately 130 fold and 45 fold tighter.

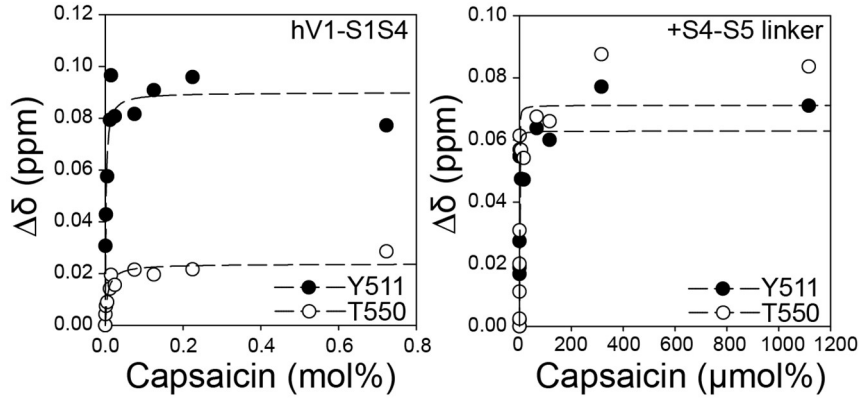

Figure 4.9 Binding isotherms of capsaicin with the hV1-S1S4 and the hV1-S1S4 with the S4-S5 linker. The dissociation constants from the capsaicin binding with the S4-S5 linker construct were much smaller than those from the S1-S4 domain, which means that the S4-S5 linker construct interacts with capsaicin much more tightly.

4.3.5 The hV1-S1S4 Interacts with Various Types of Ligands

4.3.5.1 Vanilloid Compounds

Next, we tested other ligands that may interact with the hV1-S1S4. First, other vanilloid analogues such as capsiate and resiniferatoxin were subjected to the binding experiment, and the key residues were monitored. In NMR-detected ligand studies, residues that bind to the ligand tend to show higher magnitude of chemical shift perturbations that are induced by the specific binding event [34]. To observe differences in binding region, the $\Delta\delta/K_d$ plots were compared, and these plots revealed similarities and differences in vanilloids binding sites (Figure 4.10A-C). One residue that bound to all vanilloid compounds was K468 in the extracellular S1-S2 loop, closer to the S2 helix. Besides, residues that bind to each ligand were mapped on the structure (Figure 4.10D). Interestingly, only capsaicin did have a high $\Delta\delta/K_d$ value for Y511, but when the binding isotherms were plotted for both capsiate and RTx, Y511 did bind specifically to these

ligands; capsiate bound to Y511 with a K_d of 13 ± 3 mmol%, which is approximately six folds weaker than capsaicin, and RTx bound to Y511 with a K_d of 125 ± 38 nmol%, which is much more potent than capsaicin.

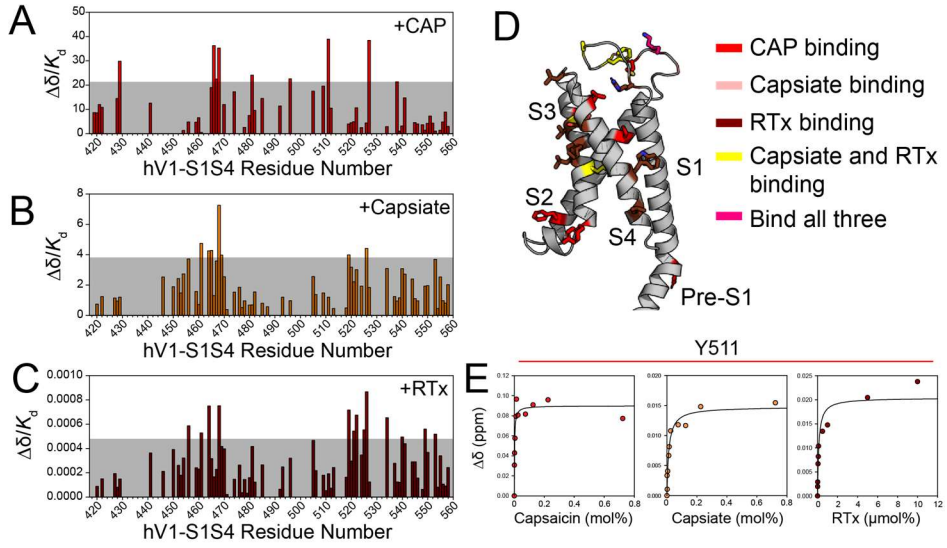

Figure 4.10 Comparison among vanilloid ligands that interact with the hV1-S1S4. The $\Delta\delta/K_d$ values from the capsaicin (A), capsiate (B), and resiniferatoxin (C) titrations were plotted against the hV1-S1S4 residue number. The grey boxes in these plots mean that the residues in this area are not meaningful. The residues that are above the cutoff values (above the grey boxes) are mapped on the structure (D, S1-S4 domain of rTRPV1, PDB ID: 5IRZ) (E) Binding isotherms of Y511 with the vanilloid ligands. All three ligands show saturable specific interactions with Y511.

4.3.5.2 Cannabinoids

There was a recent TRPV2 cryo-EM structured determined in the presence of cannabinoid (CBD) [39]. This work introduced the CBD binding site that is outside of the canonical vanilloid binding pocket formed by residues in the S3, S4 helices and the S4-S5 linker [39]. In particular, the amino acid residues that bind CBD include hydrophobic and aromatic residues located in S5 and S6 helices [39]. Given that the insensitivity to

vanilloid ligands in TRPV2 comes from some sequential differences between TRPV1 and TRPV2, TRPV1 may be interacting with cannabinoid compounds in a different matter. To test this hypothesis, the hV1-S1S4 was subjected to the titrations with cannabinoid compounds, cannabidiol (CBD), cannabigerol (CBG), and anandamide (AEA), an endogenous endocannabinoid molecule, which are prepared in ethanol for the titrations. The same thorough analysis described in section 4.3.1 was performed, and the binding residues for each cannabinoids were mainly distributed in the S1-S2 loop and the S2 helix (Figure 4.11A-C). Three residues that all CBD, CBG and AEA commonly bound to the hV1-S1S4 were R456 in the S1-S2 loop, Q519 and T526 in the S3 helix (Figure 4.11D). As an example, the isotherms from R456 residue were plotted and the binding affinities of CBD, CBG and AEA to this residue were fairly similar (Figure 4.11E, F).

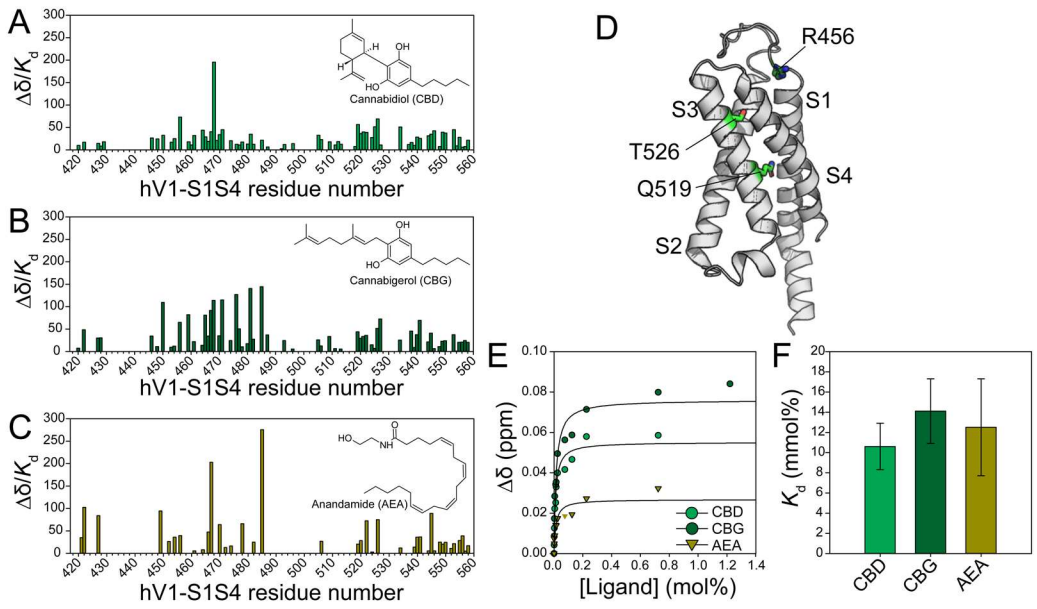

Figure 4.11 Cannabinoids binding with the hV1-S1S4. The plots between the $\Delta\delta/K_d$ values and the hV1-S1S4 residue number were generated for each cannabinoid ligand (A-C). (D) Three residues in the hV1-S1S4 bound to all three ligands, and these residues are mapped on the structure (PDB ID: 5IRZ). (E) Binding isotherms of R456 with CBD (green), CBG (dark green), and AEA (olive). The K_d values of CBD, CBG and AEA are 11 ± 2 mmol%, 14 ± 3 mmol%, and 13 ± 5 mmol%, respectively. These values are also plotted in (F).

4.3.5.3 2-APB

2-aminoethoxydiphenyl borate, 2-APB, is a well-known modulator of diverse TRP channels, including TRPV1. It has been shown to activate TRPV1-TRPV4; whereas, it inhibits TRPV5 and TRPV6 [25, 26, 40]. There are two TRP channel structures with 2-APB, TRPV3 and TRPV6 [28, 41]. Interestingly, 2-APB-bound TRPV3 structure demonstrated multiple binding sites, and one binding site overlaps with the 2-APB binding site in TRPV6. Among these three binding sites, two resides in the S1-S4 domain, one is near the space formed by the S1 and S2 helices, and the other is where the cholesterol is shown to bind in the lower pocket (Figure 4.12A). To date, neither the

binding site of 2-APB in TRPV1 nor the mechanism of 2-APB activation of TRPV1 have been identified. 2-APB stock was prepared in DMSO, and was titrated to the hV1-S1S4 solution. First, regions in hV1-S1S4 that are equivalent to two 2-APB binding site found in TRPV3 were analyzed (Figure 4.12B). Residues A452 and R456 in S1 helix and S481 in S2 helix, which are in close proximity to 2-APB binding sites, displayed specific binding with the average K_d of 10.4 ± 3.3 mmol% (Figure 4.12C). Interestingly, 2-APB in the putative cholesterol binding site is very close to Y555 in S4, and this residue also bound 2-APB well, with 13.8 ± 1.6 mmol% K_d (Figure 4.12C). Although 2-APB wasn't detected in the vanilloid binding pocket in TRPV3 cryo-EM structures, both S510 and Y511 seemed to bind 2-APB as well, with the affinities 8.9 ± 3.0 mmol% and 10.4 ± 3.2 mmol%, respectively (Figure 4.12D), indicating that the 2-APB binding and vanilloid binding sites may overlap.

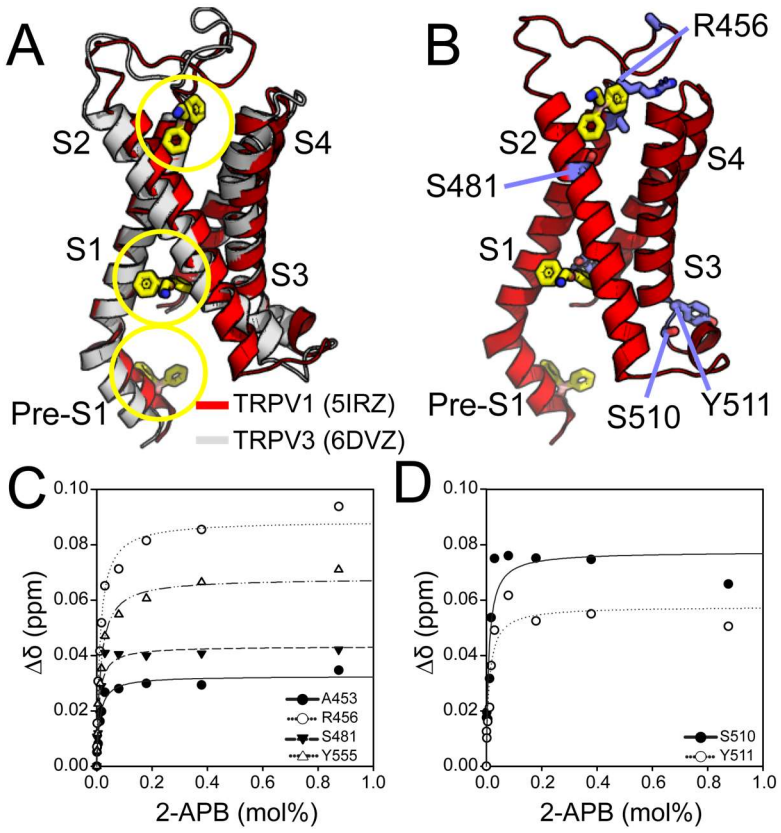

Figure 4.12 2-APB binds the hV1-S1S4. (A) The cryo-EM structure of rat TRPV1 (PDB ID: 5IRZ, red) and 2-APB bound mouse TRPV3 (PDB ID: 6DVZ, grey) were aligned in PyMOL using the cealign algorithm, and only S1-S4 domain are shown to better demonstrate the 2-APB binding sites in TRPV3 as highlighted in yellow circles. (B) Residues that are good 2-APB binding candidates are highlighted in midblue, and 2-APB molecules are also shown to show the proximity. (C) Binding isotherms of residues A453, R456, S481 and Y555 with 2-APB that show nice saturating curves. For Y555, it appears to be a little bit distant from the binding sites, but the 2-APB molecule located between the bottom of S1 and S2 helices is in close proximity to Y555, and the K_d of this residue was 14 ± 2 mmol% (open triangle). (D) 2-APB is not expected to bind in the canonical vanilloid binding pocket, but residues S510 and Y511 showed decent binding to 2-APB.

4.3.5.4 Cholesteryl Hemisuccinate

Many TRP channels have been shown to be modulated by endogenous lipids. Cholesterol is an important component of mammalian membranes, and the concentration

of cholesterol in the membrane influences the membrane fluidity and trafficking of the membrane proteins [42, 43]. Some studies have suggested that TRPV1 is negatively modulated by cholesterol, and putative cholesterol binding sites have been introduced [44, 45]. Cholesteryl hemisuccinate (CHS) is a cholesterol derivative that is widely used in experiments because it is much easier to handle. In the recent years, a few TRP channel structures have been determined in the presence of cholesteryl hemisuccinate. In TRPV2, the electron density that resembles a cholesterol molecule was detected in the crevice formed by S1 and S2 helices in the S1-S4 domain [46]. Given that TRPV1 and TRPV2 have approximately 50% sequential homology, cholesterol may bind in the similar region in the S1-S4 domain of TRPV1. Furthermore, TRPM4 structure revealed three putative CHS binding sites; first binding site was in the canonical vanilloid ligand binding pocket in the intracellular side between the S3, S4 helices and the S4-S5 linker, second was in the extracellular side where double-knot toxin binds in TRPV1, and third was in the space formed between the S1, S4 helices and the neighboring S5 helix [47]. Aligning the structures of TRPV1 and TRPM4, the lipidic molecule binding regions can be compared (Figure 4.13A)

Other than the structural evidence, cholesterol binding site can be predicted by observing the amino acid sequence. The cholesterol binding motif is called CRAC domain (cholesterol recognition amino acid consensus), which consists of a hydrophobic residue, leucine or valine, followed by 1 to 5 residues, an aromatic residue, tyrosine or phenylalanine, followed by 1 to 5 residues, and finally, a basic residue, lysine or arginine [48]. CARC domain is the mirror image of the CRAC domain. In TRPV1 S1-S4 domain,

a few CRAC/CARC domains were spotted, V482-Y487-R491 in the S2 helix, L534-Y537- in the N-terminal S4 helix, and L553-Y555-R557 in the C-terminal S4 helix (Figure 4.13B). After the titration with CHS solubilized in chloroform, some residues that are confidently assigned and are clearly distinguishable at 37 °C were analyzed, and they exhibited saturating specific binding with the average K_d of 7.4 ± 1.8 mmol% (Figure 4.13C).

In the closed-state TRPV1 cryo-EM structure (PDB ID: 5IRZ), there appears to be three regions that lipids may bind. One site is where the vanilloid ligands bind, second site is the pocket formed between the S1 and S2 helices, where the cholesterol binding site is in TRPV2, and third site is the extracellular region between the S1-S4 domain and the PD. To examine if the residues near the third lipid binding site interact with CHS, the residues that are within 5 Å from the lipid molecule (6OE) were selected [3], among these residues were Y454 and R456 in the S1 helix, which showed saturable specific binding (Figure 4.13D).

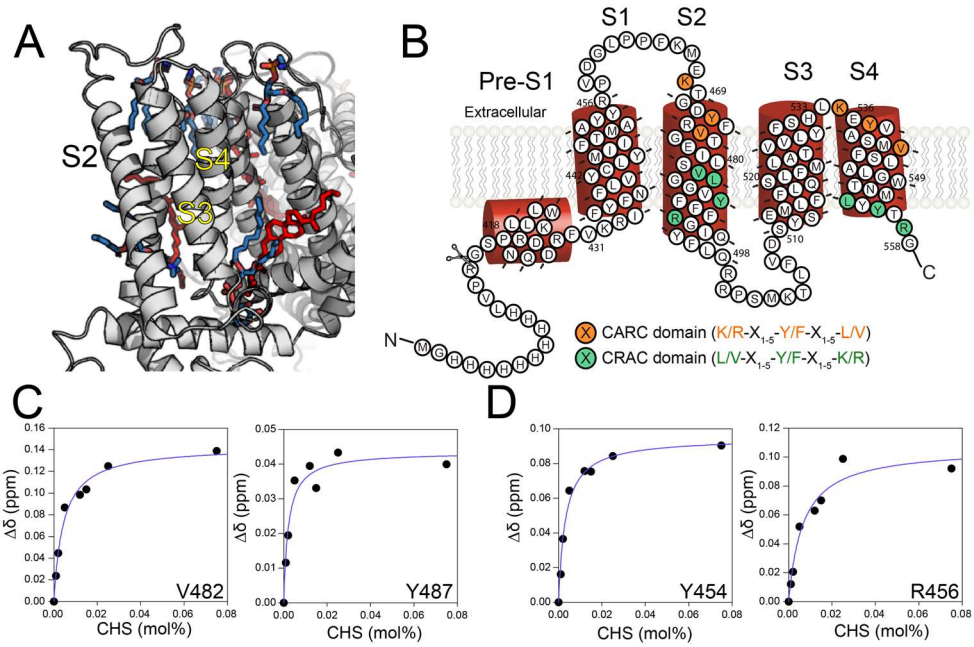

Figure 4.13 Cholesteryl hemissucinate (CHS) interacts with the hV1-S1S4. (A) The putative locations of lipidic molecules in TRPV1. The molecules in blue stick are lipidic molecules bound to TRPV1, and molecules in red stick represent the CHS bound in TRPM4. (B) The membrane topology of the hV1-S1S4, highlighting the CRAC/CARC domains. The CARC domains are highlighted in orange, and the CRAC domains are highlighted in green. (C) Binding isotherms of two residues that form the CRAC domain in the S2 helix, V482 and Y487. These two residues show saturable specific binding with K_d values 4.4 ± 0.7 mmol% and 2.1 ± 0.6 mmol%, respectively. (D) Binding isotherms of the residues in the extracellular S1-S2 loop region. This region is close to the lipid molecule binding site in TRPV1, and these two residues, Y454 and R456, bind specifically to CHS with K_d values 3.2 ± 0.5 mmol% and 6.6 ± 1.9 mmol%, respectively.

4.3.5.5 Antagonists

Antagonists of TRPV1 have been synthesized and tested by numerous pharmaceutical companies for the novel drug development [8, 11]. Capsazepine (CPZ), a commonly used TRPV1 antagonist, functions as a competitive inhibitor against capsaicin, with the IC_{50} in high nano-molar to low micro-molar range [49]. The CPZ-bound TRPV1 cryo-EM structure (PDB ID: 5IS0) hinted that CPZ serves as a competitive inhibitor as

the structure showed that it binds in the vanilloid binding pocket [3]. To dissect the interaction between CPZ and the hV1-S1S4, the NMR-based titration was performed using the CPZ solution prepared in DMSO. Overall, decent chemical shift perturbations were observed as the concentration of CPZ increased, and more thorough analysis was conducted to isolate the binding site of CPZ in the S1-S4 domain. CPZ is not considered as a vanilloid compound because of its lack of vanilloid moiety, though the only difference in the head group is the presence of two hydroxyl group in CPZ instead of one hydroxyl and an ester (Figure 4.14A). The structure (PDB ID: 5IS0) indicates that Y511 is not hydrogen bonded to CPZ, but S512 may be forming a hydrogen bond with CPZ (Figure 4.14B). When these two residues were carefully analyzed, only S512 showed a saturable hyperbolic binding isotherm indicative of specific binding. Another key residue T550 showed a specific binding to CPZ (Figure 4.13C-F).

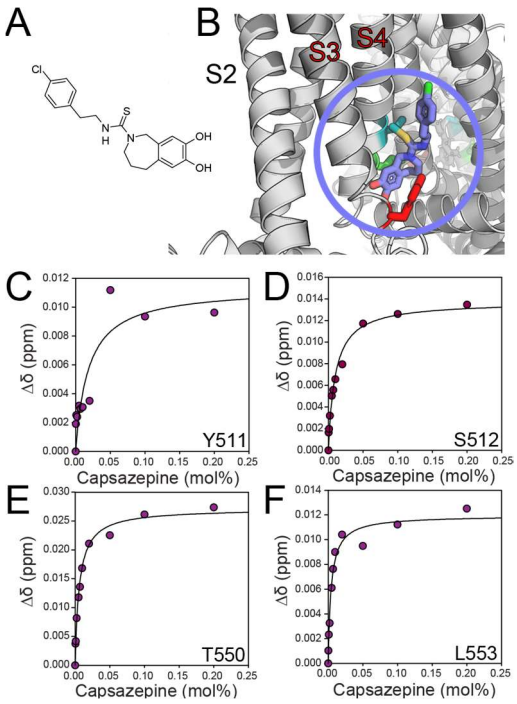

Figure 4.14 Capsazepine (CPZ) titration with the hV1-S1S4. (A) Chemical structure of CPZ. There is a slight change in the vanilloid moiety from an ester to a hydroxyl group. (B) CPZ-bound structure of rTRPV1 (PDB ID: 5IRZ). CPZ molecule is shown in midblue stick, Y511 is shown in red, T550 is shown in cyan, and L553 is shown in green. (C) CPZ binding isotherm of Y511 residue. Given that the fitting is not as great as other isotherms, S512 (D), T550 (E), and L553 (F), it can be concluded that Y511 doesn't bind well to CPZ.

ABT-102 is another synthesized antagonist of TRPV1, which is much more potent antagonist than capsazepine. ABT-102 has been used as a pain reliever, but one major drawback of this molecule includes the cause of hyperthermia that could be fatal [13]. Our preliminary experiment tested the effect of ABT-102 against capsaicin activation and heat activation, where ABT-102 can efficiently inhibit the capsaicin activation with the nano-molar IC_{50}, whereas it failed to block the heat-activation (Figure 4.15A). Although it is not clear where ABT-102 binds in TRPV1, we hypothesized that ABT-102 may bind in the S1-S4 domain based on the evidence that a variety of distinct chemical ligands bind to this domain and that ABT-102 is a potent inhibitor against capsaicin, which in turn binds the S1-S4 domain. A titration was carried out using NMR, and it turns out Y511 doesn't display specific binding to ABT-102 (Figure 4.15D). Instead, residues in the S3 helix and T550 showed specific binding (Figure 4.15E).

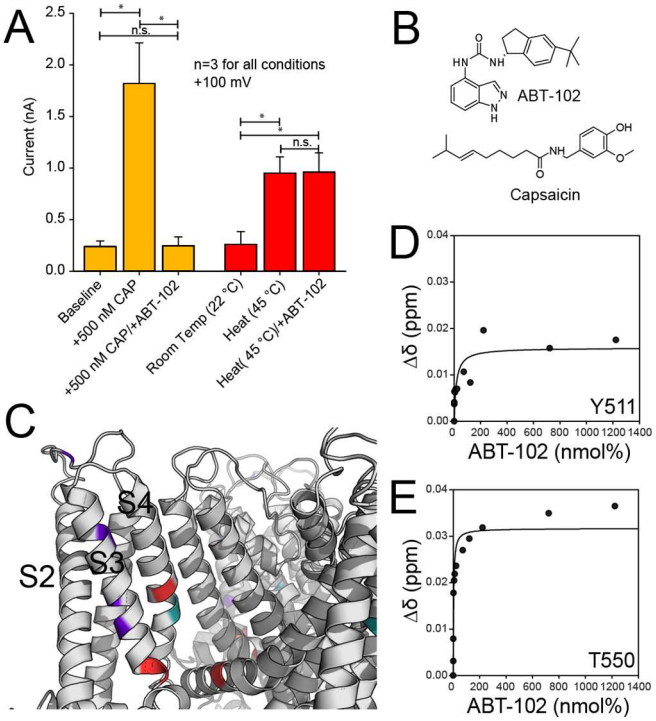

Figure 4.15 ABT-102 binds outside of the vanilloid binding site. (A) ABT-102 inhibits the capsaicin-activated TRPV1, while it doesn't hinder the heat-activated TRPV1. (B) Chemical structures of ABT-102 and capsaicin. (C) Exhibition of independent binding sites of ABT-102 (purple) and capsaicin (red). T550 binds to both ligands. (D) Y511 doesn't bind well to ABT-102. (E) T550 binds very well to ABT-102, with the binding affinity of 3.3 ± 1.0 nmol%.

4.3.6 Evaluating Ligand Interactions as a Function of Temperature

To investigate how ligands affect thermosensitivity of the hV1-S1S4, NMR-based temperature titrations in the presence of ligands, 4 mole% capsaicin, 1.2 mmole% ABT-102, 30 mmole% PIP_2 and 30 mmole% cholesteryl hemisuccinate, were performed. The mean ΔH of the apo hV1-S1S4 was 21.2 ± 0.1 kcal/mol. Compared to this, the binding of capsaicin caused a significant left-shift in the mean ΔH, whereas other ligands, ABT-102, PIP_2 and CHS, showed smaller magnitude of right-shifts in the mean ΔH (Figure 4.16).

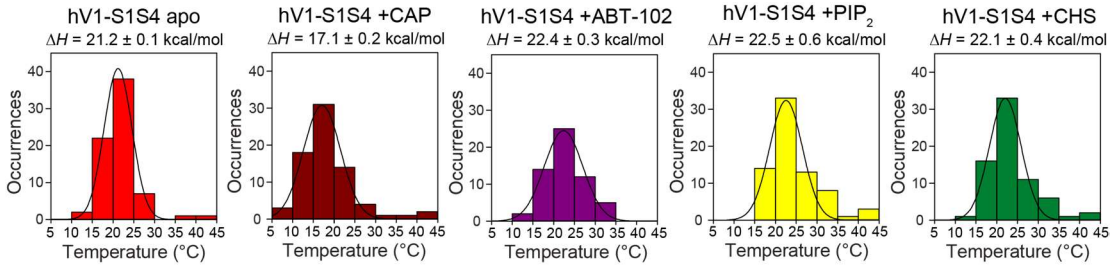

Figure 4.16 The effect of various ligands in the hV1-S1S4 thermosensitivity. Compared to the hV1-S1S4 wild type (WT), which has ΔH = 21.2 ± 0.1 kcal/mol, only capsaicin causes decrease in thermosensitivity to ΔH = 17.1 ± 0.2 kcal/mol. Though there are slight differences, other ligands didn't have significant differences in ΔH values from the WT.

Because there was a significant decrease in thermosensitivity when capsaicin was bound to the hV1-S1S4, the thermosensitivities of the mutants were compared in the absence and presence of capsaicin. Compared to the WT, Y511A, R557A and Y511A/R557A mutants showed slight decrease in thermosensitivity. These mutants also do not show significant differences in thermosensitivities with the addition of capsaicin (Figure 4.17).

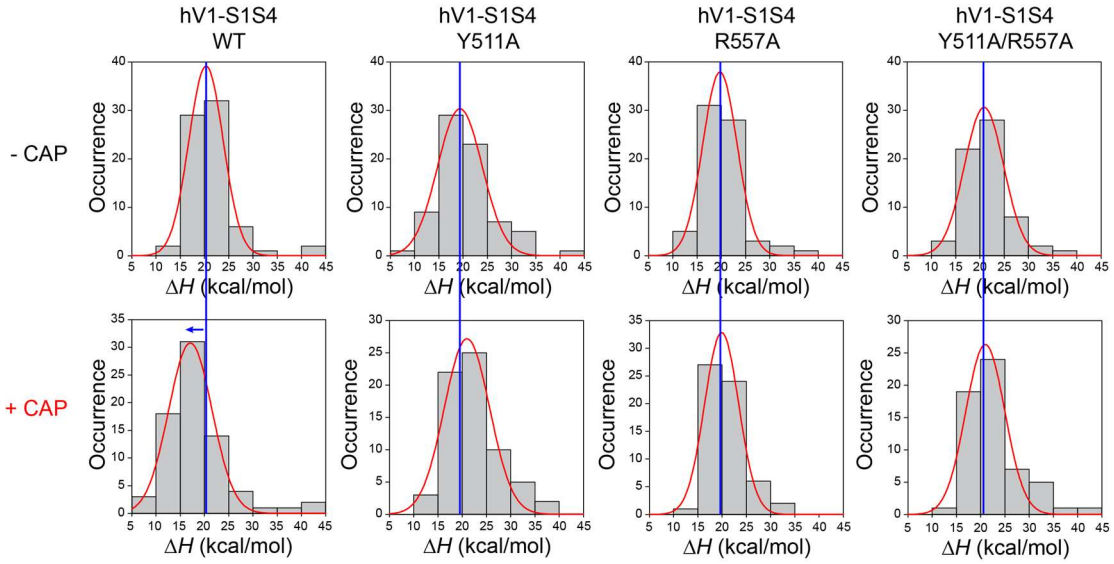

Figure 4.17 Comparison of temperature sensitivity of the WT and mutants and the effect of capsaicin in thermosensitivities. The blue lines indicate the mean of the ΔH values. The mutants of hV1-S1S4, Y511A, R557A and Y511A/R557A, didn't show significant shifts as shown in the WT.

4.4 Discussion

In this study, we explored how the S1-S4 domain of TRPV1 responds to the canonical TRPV1 agonist, capsaicin, as well as a variety of chemical ligands. One challenge with these binding studies is that because all of these ligands are lipophilic, the use of organic solvents as a vehicle was inevitable. Consequently, there could be two species of chemical shift perturbations that evolve at the same time; one arose from the solvent and the other from the ligand. As shown in Figure 4.2, ethanol induces chemical shift perturbations, with fairly meaningful magnitudes, and the ethanol seemed to influence the magnitude of the capsaicin affinity as shown in Figures 4.1 and 4.3. For example, Y511 had K_d values of 2.0 ± 0.5 mmol% when capsaicin solution in ethanol was titrated, but when capsaicin was directly incorporated, the K_d values of Y511 was

approximately 5 mol%, yielding about 2,500 fold difference (Figure 4.1 and 4.3). In both cases, the hyperbolic curves did reach the saturating point, Previous studies indicated that the alcohol potentiates TRPV1 activation. For example, when capsaicin prepared in the alcoholic solution was administered to patients, the ethanol-induced potentiation of TRPV1 was observed [50]. The tighter affinities to capsaicin with ethanol could support the previous results that ethanol enhances the potentiation of TRPV1.

Another interesting trend observed in these studies was the change in exchange rate. From the capsaicin with ethanol titration, a lot of residues displayed the binding isotherms that would represent the fast exchange between the ligand and the protein. However, the capsaicin titration without ethanol showed interesting sigmoidal binding curve, which is indicative of an intermediate exchange. Rather than fitting this sigmoidal binding curve to the classic binding fitting equation, the Hill equation fits much better with higher correlation value. For example, fitting Y511 data to the Hill equation resulted in $K_d = 3.5 \pm 0.4$ mol% with the Hill coefficient of 2.0 ± 0.3 and $R^2 = 0.9884$, which is 1,750 fold different compared to the other fitting method that adopts 1:1 ratio between ligand and protein.

One residue that had both a large $\Delta\delta$ and a saturable binding curve was E467 located in the S1-S2 loop, closer to the S2 helix. Without ethanol as a vehicle, it seemed to have a non-specific binding at higher concentration of capsaicin as it did not have a saturating curve. However, there was an interesting trend found in changes in line width as a function of capsaicin. Line shape analysis can be monitored to see if the protein undergoes a conformational change as ligand bind. In the fast exchange regime, if the

ligand binding induces the conformational change, the protein will experience consistent line broadening as the concentration of ligand increases. In contrast, if the protein binds the ligand with an intermediate exchange rate, the line width would increase at first, but it will decrease at the saturating concentration of ligand, indicating that the protein is in the ligand-bound conformation [34]. This trend was observed from this residue. These results suggest that capsaicin binding to the S1-S4 domain causes the global conformational change, which could provide a more detailed explanation of capsaicin-induced gating mechanism. Furthermore, a previous study performed molecular dynamic simulations to understand how capsaicin enters and settles in the vanilloid binding pocket [51]. This simulation pointed out that capsaicin enters through the S1-S2 loop and flips on its way to occupy the binding pocket. Given that the residues in the S1-S2 loop bind well to capsaicin, we could test the role of the hV1-S1S4 as a flipase. We also note that a lot of titrations had relatively smaller $\Delta\delta$. In general, the ligand binding residues produce large chemical shift perturbations [34], but the mixture of fast and intermediate exchange between the ligands and the S1-S4 domain could explain the smaller magnitudes.

As a protein undergoes a conformational change due to ligand binding, the trend of chemical shift perturbations could be nonlinear. This trend was detected from a previously performed titration between calmodulin (CaM) and calcium, where the resonances of CaM resembled circular motions as calcium concentration increased [52]. This similar trajectory of chemical shift perturbations was also detected in the hV1-S1S4 titration with capsaicin in EtOH. T450 in the S1 helix and S510 in the S2-S3 loop showed

this trend (Figure 4.18A), and Y511 also shows a nonlinear chemical shift perturbation, suggesting that the S1-S4 domain may undergo a conformational change (Figure 4.18B).

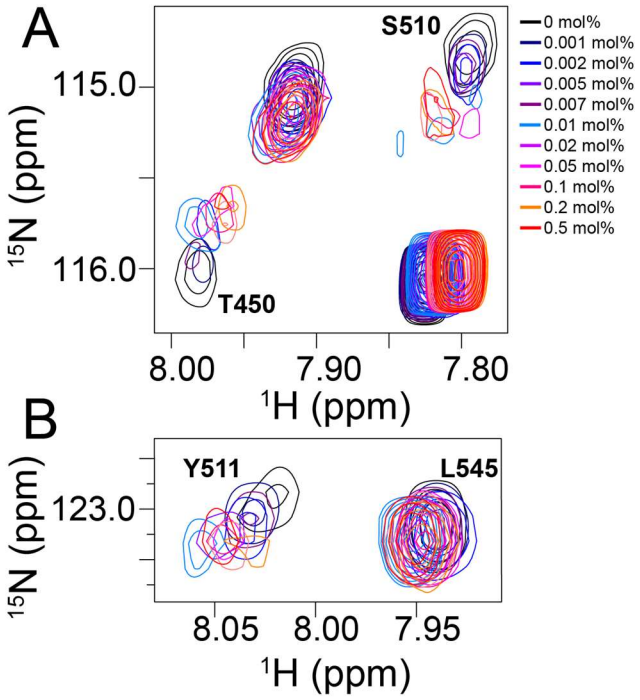

Figure 4.18 Nonlinear chemical shift perturbations detected from the capsaicin titration with the hV1-S1S4. (A) T450 and S510 show unique chemical shift perturbations. There seem to be differences in linewidths for these resonances based on differences in resonance intensities. (B) Y511 also displays a nonlinear chemical shift perturbation. Rather, Y511 showed somewhat inconsistent chemical shift perturbations. Nonetheless, these trends could indicate that the hV1-S1S4 experiences a conformational change or a change in dynamics.

Despite the concern, ethanol doesn't seem to disrupt the interactions between the hV1-S1S4 and various ligands. The majority of ligands were prepared in ethanol, including capsiate, RTx, CBD, CBG, AEA, and ABT-102. Regardless of the similarities in the magnitudes of $\Delta\delta$, the resulting K_d values for each ligand were different, indicating that the ligands in ethanol interact with the S1-S4 domain distinctively. Although the binding sites seemed to be quite similar among all the ligands that were tested, some differences were observed. Comparing just vanilloid ligands, capsaicin, capsiate and RTx, general binding sites overlapped, which are located in the extracellular S1-S2 loop

and the S3 helix. However, RTx seemed to interact with the residues in S4 helix more than capsaicin and capsiate. Between capsaicin and capsiate, the only difference in chemical structures is the neck; capsaicin has an amide group, whereas capsiate has an ester. Because the neck of capsaicin forms a hydrogen bond with T550 in S4 helix, it can be expected that capsiate may not interact with T550 due to its lack of amide in the neck. Our titration data with capsiate indicates that T550 interacts with capsiate. Compared to capsaicin (K_d = 7 ± 2 mmol%), capsiate binds T550 with almost three folds weaker affinity (K_d = 19 ± 3 mmol%). Other than decreased affinity, few differences in binding site were observed from capsiate relative to capsaicin.

The data presented here indicate that cannabinoids bind in the S1-S4 domain of TRPV1, contradicting the results from TRPV2 where cannabidiol (CBD) binds in the pore domain [39]. There was no indication that the S1-S4 domain of TRPV2 does not seem to bind CBD, and this could be because of the majority of amino acid sequence differences between TRPV1 and TRPV2 in the S2 to S4 helices, which are central to ligand binding in TRPV1. Previously, a few studies have shown that in TRPV2, equivalent amino acid residues to the key residues in the vanilloid binding pocket, Y511, S512, M547 and T550, differ [20, 21]. Given that mutation of these residues in TRPV2 reversed the sensitivity to vanilloid ligands, it may be possible that cannabinoids might bind the S1-S4 domain of engineered TRPV2. Cannabinoids have a hydroxyl group that could potentially form hydrogen bonds with Y511 in the vanilloid binding pocket. Given that the chemical structures of CBD and CBG are similar, it was expected that the binding sites for these two molecules may be similar. After a thorough analysis, three

residues, R456, Q519 and T526, are found to be binding all three cannabinoid ligands. Both CBD and CBG bound specifically to Y511, but AEA does not appear to interact with Y511, indicating that binding sites for AEA may be different from that of vanilloids and plant-based cannabinoids.

One common feature in ligand binding with the hV1-S1S4 is the interaction in the extracellular S1-S2 loop. For Cholesterol and 2-APB, binding at this loop was somewhat expected because of the predicted CARC domain in the extracellular region (Figure 4.13B), and the 2-APB bound structure (PDB ID: 6DVZ, Figure 4.12A). For cholesteryl hemisuccinate (CHS), the hV1-S1S4 residues that form the CARC domain at the top of the S2 and S4 helices did exhibit specific binding. There are a few TRP channel structures that include cholesterol molecules, which revealed multiple binding sites [46, 47]. These binding sites include canonical vanilloid binding site, a crevice formed between the S2 and S3 helices, an extracellular space between the S1-S4 domain and the pore domain, and near TRP helix [3, 46, 47]. Similar to this, residues of the hV1-S1S4 near these putative cholesterol binding sites displayed specific binding to CHS. However, the global chemical shift perturbations detected from the ligand binding titration with CHS could have been potentially induced by changes in membrane fluidity. Similarly, 2-APB also seemed to cause global chemical shift perturbations and the large majority of the resonances did show saturable, specific binding to the hV1-S1S4. From the 2-APB bound TRPV3 structure, three binding sites are found near the S1-S4 domain, so our data seem to be in agreement with the structural data. Collectively, binding to both S1-S2 loop

and the intracellular side could indicate that the hV1-S1S4 functions as a flipase for other ligands as well. Further experiments would have to be performed to test this hypothesis.

Beyond binding with many ligands, the relationship between the ligand and temperature activation was also explored. Our previous work involved robust thermodynamic analysis of the S1-S4 domain using solution NMR, far-UV CD and intrinsic tryptophan fluorescence, where we showed that the average ΔH of the hV1-S1S4 as changes in temperature was ~20 kcal/mol. When capsaicin was bound, there was a decrease in ΔH, from 21.2 ± 0.1 kcal/mol to 17.1 ± 0.2 kcal/mol (Figure 4.17). However, it is intriguing that the thermosensitivity of the mutants wasn't influenced by the existence of capsaicin, which could indicate that capsaicin doesn't bind to the mutants. As the capsaicin titrations showed, the hV1-S1S4 mutants remain capsaicin sensitive, though the affinities are smaller than the wildtype. It is possible that capsaicin binding energies from these mutants are not strong enough to encourage the channel gating, and this could explain why the hTRPV1-Y511A and hTRPV1-R557A mutants lost capsaicin sensitivity.

When other ligands, ABT-102, PIP_2 and cholesteryl hemisuccinate were tested for their influence in thermosensitivity, the differences were insignificant, meaning that these compounds do not affect the thermosensitivity. In the case of ABT-102, this information and the binding study of ABT-102 can be used to decouple the ligand and temperature activation. If there is a residue that binds to ABT-102, but doesn't affect the temperature activation, this region could be a new target for the pain medication without causing fatal hyperthermia, which one major side effect of current ABT-102 treatment.

Current hypothesis on the thermosensing is that an endogenous phospholipid occupies the vanilloid binding pocket, and as heat is applied, the phospholipid is evacuated from the binding pocket, and the gating event starts. With current cryo-EM and MD simulations, this is challenging to test experimentally, and the temperature titration in the presence of PIP_2 and CHS could be a good method to test this hypothesis. Our results showed that addition of these lipidic molecules caused no significant differences in thermosensitivities, which could indicate that the lipids may not modulate temperature sensing mechanism, or they have allosteric influence on the channel modulation.

Lastly, we investigated the function of the S4-S5 linker in the ligand interaction. From the computational docking, presence of the S4-S5 linker exhibited higher free energies from the ligand binding for capsaicin, capsiate, capsazepine and resiniferatoxin. The NMR ligand titrations of the hV1-S1S4-linker with capsaicin was performed using much smaller titration points (μmol% range), and these ligands bound tighter to the linker domain. More analysis need to be done on this, and one essential analysis for this experiment is the assignment of the resonances for the S4-S5 linker. Because there are additional resonances, three resonances that formed the S4 helix of the hV1-S1S4 construct, T556 and R557 and G558, need to be re-assigned.

In conclusion, this work provides putative binding regions of various ligands. Binding studies suggest that the S1-S4 domain may experience a change in dynamics related to several conformational ensemble, induced by the ligand binding, and this conformational change could be crucial to complete the ligand activation mechanism. Given that specific binding was observed in the extracellular loop region, this raises the

possibility of the S1-S4 domain serving as a flipase. Temperature titration experiments in the absence and presence of capsaicin explains that the capsaicin and temperature activation may be inherently thermodynamically coupled, but that may not be the case for other ligands such as ABT-102, PIP_2 and CHS. Although more analysis needs to be done, the S4-S5 linker seems to enhance the interaction with capsaicin. Besides the role in ligand activation, it will also be interesting to investigate how this linker plays a role in temperature activation. Lastly, this study suggests that the S1-S4 domain can be a platform to screen drugs to investigate both the binding location and the affinities of the drugs, which could be beneficial to develop a novel drug.

4.5 Supplementary Information

4.5.1 MatLab Script to Extract K_d Values from a High Volume of Data

```
clc
close all
clear all
warning('off')
files=dir('*.txt');
j=readtable(files(1).name,'Delimiter','\t');
n=size(files);

for i = 1:n
   j=readtable(files(i).name,'Delimiter','\t');
   N=j.PositionF1;
   H=j.PositionF2;
   dH=(H(:)-H(1)).^2;
   dN=0.2*(N(:)-N(1)).^2;
   Dd(:,i)=sqrt(dH+dN);
end
%%

x=[0 1.00E-03 2.00E-03 5.00E-03 0.012 0.015 0.025 0.075 0.125 0.225 0.723];

fit=@(b,x) b(1).*x./(b(2)+x);
xData=x(:);
```

```
yData=Dd(:,1);
beta0=[max(yData),0];
[beta,R,J,CovB,MSE]=nlinfit(xData,yData,fit,beta0)


%%

for i=1:n
   [xData yData]=prepareCurveData(xData,Dd(:,i));

   fit=@(b,x) b(1).*x./(b(2)+x);
   yData=Dd(:,i);
   beta0=[max(yData),0];
   [beta,R,J,CovB,MSE]=nlinfit(xData,yData,fit,beta0)
   standev=sqrt(diag(CovB));
   SEM=standev/sqrt(length(yData))
   SSresidual=sum(R.^2);
   SStotal=sum((yData-mean(yData)).^2);
   rsquare=1-(SSresidual/SStotal)

   h=figure;
   xfit=linspace(min(xData),max(xData));
   plot(xData,yData,'o',xfit,fit(beta,xfit));
   kd(:,i)=beta(:,2);
   standard_error(:,i)=standev(2);
   saveas(h,sprintf('./plots/FIG%d.png',i)); % will create FIG1, FIG2,...
   close
end
disp('done')
```

4.6 References

1. Caterina, M.J., et al., The capsaicin receptor: a heat-activated ion channel in the pain pathway. *Nature,* 1997. **389**(6653): p. 816-24.

2. Cao, E., et al., TRPV1 structures in distinct conformations reveal activation mechanisms. *Nature,* 2013. **504**(7478): p. 113-8.

3. Gao, Y., et al., TRPV1 structures in nanodiscs reveal mechanisms of ligand and lipid action. *Nature,* 2016. **534**(7607): p. 347-51.

4. Yang, F., et al., Structural mechanism underlying capsaicin binding and activation of the TRPV1 ion channel. *Nat Chem Biol,* 2015. **11**(7): p. 518-524.

5. Elokely, K., et al., Understanding TRPV1 activation by ligands: Insights from the binding modes of capsaicin and resiniferatoxin. *Proc Natl Acad Sci U S A,* 2016. **113**(2): p. E137-45.

6. Yang, F., et al., The conformational wave in capsaicin activation of transient receptor potential vanilloid 1 ion channel. *Nat Commun,* 2018. **9**(1): p. 2879.

7. Jordt, S.-E. and D. Julius, Molecular Basis for Species-Specific Sensitivity to "Hot" Chili Peppers. *Cell,* 2002. **108**(3): p. 421-430.

8. Jara-Oseguera, A., S. Simon, and T. Rosenbaum, TRPV1: On the Road to Pain Relief. *Current Molecular Pharmacology,* 2008. **1**(3): p. 255-269.

9. Szallasi, A., F. Cruz, and P. Geppetti, TRPV1: a therapeutic target for novel analgesic drugs? *Trends Mol Med,* 2006. **12**(11): p. 545-54.

10. O'Neill, J., et al., Unravelling the mystery of capsaicin: a tool to understand and treat pain. *Pharmacol Rev,* 2012. **64**(4): p. 939-71.

11. Brandt, M.R., C.E. Beyer, and S.M. Stahl, TRPV1 Antagonists and Chronic Pain: Beyond Thermal Perception. *Pharmaceuticals (Basel),* 2012. **5**(2): p. 114-32.

12. Brito, R., et al., TRPV1: A Potential Drug Target for Treating Various Diseases. *Cells,* 2014. **3**(2): p. 517-45.

13. Surowy, C.S., et al., (R)-(5-tert-butyl-2,3-dihydro-1H-inden-1-yl)-3-(1H-indazol-4-yl)-urea (ABT-102) blocks polymodal activation of transient receptor potential vanilloid 1 receptors in vitro and heat-evoked firing of spinal dorsal horn neurons in vivo. *J Pharmacol Exp Ther,* 2008. **326**(3): p. 879-88.

14. Varga, A., et al., Effects of the novel TRPV1 receptor antagonist SB366791 in vitro and in vivo in the rat. *Neurosci Lett,* 2005. **385**(2): p. 137-42.

15. Garami, A., et al., Contributions of different modes of TRPV1 activation to TRPV1 antagonist-induced hyperthermia. *J Neurosci,* 2010. **30**(4): p. 1435-40.

16. Iida, T., et al., TRPV1 activation and induction of nociceptive response by a non-pungent capsaicin-like compound, capsiate. *Neuropharmacology,* 2003. **44**(7): p. 958-967.

17. De Petrocellis, L., et al., Effects of cannabinoids and cannabinoid-enriched Cannabis extracts on TRP channels and endocannabinoid metabolic enzymes. *Br J Pharmacol,* 2011. **163**(7): p. 1479-94.

18. Garami, A., et al., Transient Receptor Potential Vanilloid 1 Antagonists Prevent Anesthesia-induced Hypothermia and Decrease Postincisional Opioid Dose Requirements in Rodents. *Anesthesiology,* 2017. **127**(5): p. 813-823.

19. Muller, C., P. Morales, and P.H. Reggio, Cannabinoid Ligands Targeting TRP Channels. *Front Mol Neurosci,* 2018. **11**: p. 487.

20. Yang, F., et al., Rational design and validation of a vanilloid-sensitive TRPV2 ion channel. *Proc Natl Acad Sci U S A,* 2016. **113**(26): p. E3657-66.

21. Zhang, F., et al., Engineering vanilloid-sensitivity into the rat TRPV2 channel. *Elife,* 2016. **5**.

22. Zhang, F., K.J. Swartz, and A. Jara-Oseguera, Conserved allosteric pathways for activation of TRPV3 revealed through engineering vanilloid-sensitivity. *Elife,* 2019. **8**.

23. Hughes, T.E.T., et al., Structural basis of TRPV5 channel inhibition by econazole revealed by cryo-EM. *Nat Struct Mol Biol,* 2018. **25**(1): p. 53-60.

24. Mathivanan, S., et al., Effect of econazole and benzydamine on sensory neurons in culture. *J Physiol Pharmacol,* 2016. **67**(6): p. 851-858.

25. Colton, C.K. and M.X. Zhu, 2-Aminoethoxydiphenyl borate as a common activator of TRPV1, TRPV2, and TRPV3 channels. *Handb Exp Pharmacol,* 2007(179): p. 173-87.

26. Hu, H., et al., Two amino acid residues determine 2-APB sensitivity of the ion channels TRPV3 and TRPV4. *Proc Natl Acad Sci U S A,* 2009. **106**(5): p. 1626-31.

27. Hu, H.Z., et al., 2-aminoethoxydiphenyl borate is a common activator of TRPV1, TRPV2, and TRPV3. *J Biol Chem,* 2004. **279**(34): p. 35741-8.

28. Singh, A.K., L.L. McGoldrick, and A.I. Sobolevsky, Structure and gating mechanism of the transient receptor potential channel TRPV3. *Nat Struct Mol Biol,* 2018. **25**(9): p. 805-813.

29. Gavva, N.R., et al., Molecular determinants of vanilloid sensitivity in TRPV1. *J Biol Chem,* 2004. **279**(19): p. 20283-95.

30. Jensen, M.O., et al., Mechanism of voltage gating in potassium channels. *Science,* 2012. **336**(6078): p. 229-33.

31. Hilton, J.K., M. Kim, and W.D. Van Horn, Structural and Evolutionary Insights Point to Allosteric Regulation of TRP Ion Channels. *Acc Chem Res,* 2019. **52**(6): p. 1643-1652.

32. Kim, M., et al., Evidence that the TRPV1 S1-S4 Membrane Domain Contributes to Thermosensing. 2019.

33. Van Horn, W.D., et al., Solution nuclear magnetic resonance structure of membrane-integral diacylglycerol kinase. *Science,* 2009. **324**(5935): p. 1726-9.

34. Williamson, M.P., Using chemical shift perturbation to characterise ligand binding. *Prog Nucl Magn Reson Spectrosc,* 2013. **73**: p. 1-16.

35. Vieira, E.D., L.G. Basso, and A.J. Costa-Filho, Non-linear van't Hoff behavior in pulmonary surfactant model membranes. *Biochim Biophys Acta Biomembr,* 2017. **1859**(6): p. 1133-1143.

36. Horovitz, A., Double-mutant cycles: a powerful tool for analyzing protein structure and function. *Folding and Design,* 1996. **1**(6): p. R121-R126.

37. Chowdhury, S., B.W. Jarecki, and B. Chanda, A molecular framework for temperature-dependent gating of ion channels. *Cell,* 2014. **158**(5): p. 1148-1158.

38. Clapham, D.E. and C. Miller, A thermodynamic framework for understanding temperature sensing by transient receptor potential (TRP) channels. *Proc Natl Acad Sci U S A,* 2011. **108**(49): p. 19492-7.

39. Pumroy, R.A., et al., Molecular mechanism of TRPV2 channel modulation by cannabidiol. *Elife,* 2019. **8**.

40. Kovacs, G., et al., Inhibition of the human epithelial calcium channel TRPV6 by 2-aminoethoxydiphenyl borate (2-APB). *Cell Calcium,* 2012. **52**(6): p. 468-80.

41. Singh, A.K., et al., Structural bases of TRP channel TRPV6 allosteric modulation by 2-APB. *Nat Commun,* 2018. **9**(1): p. 2465.

42. Grouleff, J., et al., The influence of cholesterol on membrane protein structure, function, and dynamics studied by molecular dynamics simulations. *Biochim Biophys Acta,* 2015. **1848**(9): p. 1783-95.

43. Lippincott-Schwartz, J. and R.D. Phair, Lipids and cholesterol as regulators of traffic in the endomembrane system. *Annu Rev Biophys,* 2010. **39**: p. 559-78.

44. Morales-Lazaro, S.L. and T. Rosenbaum, Cholesterol as a Key Molecule That Regulates TRPV1 Channel Function. *Adv Exp Med Biol,* 2019. **1135**: p. 105-117.

45. Picazo-Juarez, G., et al., Identification of a binding motif in the S5 helix that confers cholesterol sensitivity to the TRPV1 ion channel. *J Biol Chem,* 2011. **286**(28): p. 24966-76.

46. Huynh, K.W., et al., Structure of the full-length TRPV2 channel by cryo-EM. *Nat Commun,* 2016. **7**: p. 11130.

47. Duan, J., et al., Structure of full-length human TRPM4. *Proc Natl Acad Sci U S A,* 2018. **115**(10): p. 2377-2382.

48. Di Scala, C., et al., Relevance of CARC and CRAC Cholesterol-Recognition Motifs in the Nicotinic Acetylcholine Receptor and Other Membrane-Bound Receptors. *Curr Top Membr,* 2017. **80**: p. 3-23.

49. Bevan, S., et al., Capsazepine: a competitive antagonist of the sensory neurone excitant capsaicin. *Br J Pharmacol,* 1992. **107**(2): p. 544-52.

50. Geppetti, P. and M. Trevisani, Activation and sensitisation of the vanilloid receptor: role in gastrointestinal inflammation and function. *Br J Pharmacol,* 2004. **141**(8): p. 1313-20.

51. Hanson, S.M., et al., Capsaicin interaction with TRPV1 channels in a lipid bilayer: molecular dynamics simulation. *Biophys J,* 2015. **108**(6): p. 1425-1434.

52. Arai, M., J.C. Ferreon, and P.E. Wright, Quantitative analysis of multisite protein-ligand interactions by NMR: binding of intrinsically disordered p53 transactivation subdomains with the TAZ2 domain of CBP. *J Am Chem Soc,* 2012. **134**(8): p. 3792-803.

CHAPTER 5

BEYOND HUMAN TRPV1 S1-S4 DOMAIN: EXPRESSION AND PURIFICATION OF VITAMIN K EPOXIDE REDUCTASE (VKOR)

This chapter include additional work that I studied during my PhD.

5.1 Introduction

Vitamin K is involved in production of blood coagulation factor from post-translational modification of vitamin K-dependent proteins (VKD). Since vitamin K is minimal in human diet, it needs to be recycled for appropriate functions. Vitamin K exists as a quinone in human body and it is reduced to vitamin K-hydroquinone (KH_2) [1]. Next, hydroquinone is oxidized to vitamin K-epoxide, which then should be reduced to vitamin K-quinone (Figure 5.1) [1]. Two enzymes that are responsible for this recycle are γ-glutamyl carboxylase (GGCX), and vitamin K epoxide reductase (VKOR). GGCX aids γ-carboxylation of glutamic acid (Gla) residues, which is essential for post-translational modification of VKD proteins, and VKOR is responsible for reducing vitamin K-epoxide to vitamin K-quinone (Figure 5.1). If vitamin K-epoxide is not reduced to the quinone form, concentration of inactive vitamin K will increase, which will decrease the production of coagulation factors [1]. This cycle is crucial for blood coagulation and VKOR has been identified as a therapeutic target of anticoagulant, warfarin.

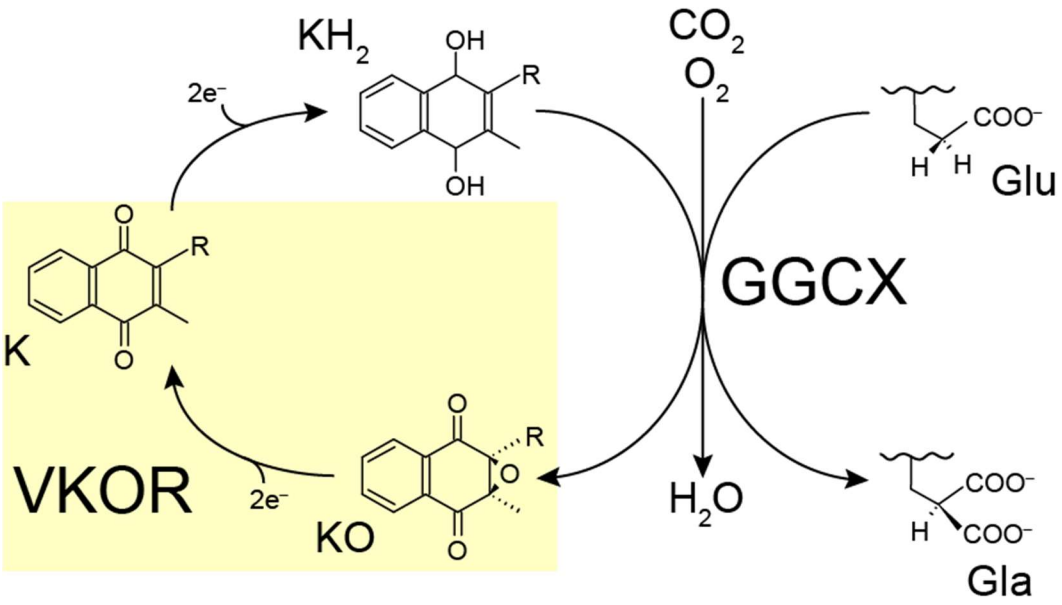

Figure 5.1 Vitamin K cycle. Vitamin K is reduced to KH_2, and an enzyme gamma-glutamyl carboxylase (GGCX) drives the carboxylation reaction, which leads to the generation of Vitamin K oxide (KO). This KO needs to be reduced again to produce vitamin K, and the enzyme responsible for this is vitamin K epoxide reductase (VKOR).

Warfarin is the most widely used oral anticoagulant to treat diseases such as thromboembolic disorders and stroke. Despite its efficiency in anticoagulation, the difficulties in warfarin therapy still remain due to warfarin's narrow therapeutic range that arose from single nucleotide polymorphisms (SNPs) [2, 3]. Depending on types of SNPs, one can be extremely sensitive to warfarin that even a small dose of warfarin could lead to extreme bleeding, or some SNPs could cause the resistance to warfarin, and higher dosage of warfarin would be needed while carefully monitoring the patients. Although it is known that warfarin inhibits the VKOR activity, the binding pocket of warfarin in VKOR was a mystery when this project was ongoing. So far, the available structures of VKOR are via X-ray crystallography

Even though VKOR has been acknowledged since early 1940s, the discovery of VKORC1 gene has not been until quite recent, which was in 2004 by Li and coworkers [4]. Many groups have been trying to purify the protein, but it has been very challenging to purify, concluding that VKOR might be a multi-subunit complex [1]. VKOR homologues can be found in many other species including rats, bacteria, insects, and plants, but its function in different species has not been specified.

In 2010, Rapoport's group resolved the crystal structure of bacterial homologue of VKOR [5]. This structure has provided new insights into a putative warfarin binding site and electron transfer mechanism that is important for the VKOR activity. However, to date, the membrane topology of human VKOR (hVKOR) has been an ongoing debate. The homology model of hVKOR was built based on the bacterial VKOR, which includes four transmembrane helices, this model was used to study the warfarin binding to hVKOR via computational method [6]. In contrast, some predicted that hVKOR may have three transmembrane helices instead of 4-TM [7].

Another protein of interest related to this project was human VKOR-like 1 protein (hVKORL1). As a paralog of hVKOR, meaning that these two genes derived from the same ancestor [8], hVKORL1 shares approximately 74% similarities in protein sequences to hVKOR, and its sensitivity and resistant to warfarin has been studied [9]. Even though these two genes are paralogs, VKOR is expressed in liver, while VKORL1 is expressed in extrahepatic tissues [10, 11]. Because VKORL1 has much higher resistance to warfarin than VKOR, VKORL1 activity still remains active at a concentration of warfarin that

inhibits VKOR activity. However, the mechanism of VKORL1 in warfarin inhibition still needs to be elucidated.

One bacterial species that shares the homology of hVKOR is *Mycobacterium tuberculosis*, which is a human pathogen that causes tuberculosis. Beckwith and coworkers have shown that MtVKOR is essential for the formation of disulfide bond, which is important for the virulence, and for the growth of cells [12]. In addition, both vitamin K antagonists and antibiotics can interrupt the VKOR activity [12]. By determining the structure of MtVKOR and investigating the interaction between anticoagulants and MtVKOR, the mechanism of action of VKOR in human can also be understood. Furthermore, observing the binding of antibiotics to MtVKOR can lead to another way of developing new antibiotics for this pathogenic *M. tuberculosis*.

5.2 Materials and Methods

5.2.1 Expression Testing of MtVKOR, hVKOR and hVKORL1

To identify the best expression condition, five components were considered; expression cell line, temperature, concentration of IPTG to induce, $OD_{600\,nm}$ to induce, and the induction time. For this study, tested genes included *Mycobacterium tuberculosis* VKOR (MtVKOR), human VKOR (hVKOR) and human VKOR-Like 1 (hVKORL1). MtVKOR gene was obtained from the DNA repository system, DNASU, and codon-optimized hVKOR and hVKORL1 constructs were obtained from DNA2.0. These genes were cloned into either pET16b or pET21b expression vector. The difference between these two expression vectors was the location of hexa-Histidine tag; pET16b possessed

an N-terminal 6×His-tag, and pET21b included a C-terminal 6×His-tag. All of these constructs were subjected to the expression testing.

To begin, each construct was transformed into seven expression cell lines, BL21 (DE3), BL21 (DE3) Star, C41 (DE3), C43 (DE3) Rosetta 2, Rosetta 2 (DE3), BL21 (DE3) pLysS, and BL21 (DE3) CodonPlus RP. The expression vectors pET16b and pET21b had ampicillin resistant gene, and some cell lines, C43 (DE3) Rosetta 2, Rosetta 2 (DE3), BL21 (DE3) pLysS, and BL21 (DE3) CodonPlus RP had chloramphenicol resistant characteristic. The medium that was chosen for expression testing was M9 minimal medium because the objective of this project was to perform structural studies using NMR. For starter cultures, single colony from each transformation was picked with a pipette tip, and was inoculated to LB rich media with appropriate antibiotics; for 18 and 25 °C, the starter cultures of 3 mL LB and 3 µL antibiotics were initiated in the morning, and were grown for approximately 7 h, and for 37 °C, 5 mL LB and 5 µL antibiotics were used and were grown overnight. For each cell line, 100 mL M9 medium (1.28 g $Na_2HPO_4 \cdot 7H_2O$, 0.3 g K_2HPO_4, 0.05 g NaCl, 0.1 g NH_4Cl, pH adjusted to 7.0) was made and was autoclaved. Before inoculating starter cultures, 100 µL 1 M $MgSO_4 \cdot 7H2O$, 100 µL 0.1 M $CaCl_2 \cdot 2H_2O$, 1 mL MEM vitamin mix, 2 mL 20% glucose, and 100 µL antibiotics were added to 100 mL M9 minimal media. For fast growing cell lines, 1.5 mL of starter cultures were added, and for slow growing cell lines, 3 mL of starter cultures were inoculated. When $OD_{600\ nm}$ reached between 0.7 and 0.8, the cells were induced with three different concentrations of IPTG, 0.3 mM, 0.5 mM and 1 mM. Induction periods varied at different temperatures, 48 h at 18 °C, 24 h at 25 °C, and 4 h at 37 °C.

After the whole process, final $OD_{600\,nm}$ values were recorded, and 1 mL of each expression condition was collected in epi-tube, which was harvested by centrifuging at 6,000 × g for 20 min at room temperature.

5.2.2 SDS-PAGE and Western Blot

Harvested cell pellets were resuspended in lysis buffer mix (50 mM Na_2HPO_4, 300 mM NaCl, 0.5 (w/v)% n-decyl β-D-maltopyranoside (DM), pH 7-8), lysozyme, DNase, RNase, 0.5 $Mg(CH_3COO)_2$), using the normalized amount based on the final OD_{600nm}. Followed by 10 min incubation at room temperature, 1 (w/v)% lauroylsarcosine was added. For SDS-PAGE and Western blot, appropriate amount of 6X SDS loading dye (0.375 M Tris-HCl, 6 mg bromophenol blue, 12% SDS, 0.6 M DTT, 60% glycerol, pH 6.8) was added. The samples were run on duplicates for both SDS-PAGE and Western blot. SDS-PAGE was run using 12% polyacrylamide gel at 120 V, and protein samples were transferred to the nitrocellulous membrane. After the incubation in the blocking buffer (5% dry milk in 1× Tris-Base Saline (TBS)) at room temperature, the membrane was washed with 1× TBSTT (1× TBS with 0.1% Tween 20 and 0.2% Triton X-100) twice, followed by one 1× TBS wash. Next, the membrane was incubated with the penta-His antibody in blocking buffer with 1:6,000 dilutions for 1 h, and three washes were repeated (twice with TBSTT and once with TBS). The membrane was then incubated with AP-linked anti-mouse secondary antibody for 1 h. Finally, the membrane was washed with TBSTT four times, and it was incubated with BCIP/NBT solution for 2-3 min.

5.2.3 Protein Purification

Three protein constructs transformed into corresponding cell lines that yielded the best expression. For MtVKOR, the best expression condition was in BL21 (DE3) Star, grown and induced with 1 mM IPTG for 48 h at 18 °C. After the bacterial cell culture, harvested cell pellets were suspended in lysis buffer (70 mM Tris-HCl, 300 mM NaCl, 0.2 mM EDTA, pH 7.7), with the addition of PMSF, LDR mix and Mg acetate. Per 1 g of cell pellet, 10 mL lysis buffer was used. The lysate was further sonicated with 50% power, and 50% duty cycle for better opening of the cells.

For whole cell extraction, 3% (v/v) Empigen was added the sonicated cell lysate, and the mixture was tumbled for 1 h at 4 °C. To separate the solubilized membrane protein and the insoluble cell debris, lysate and Empigen mixture was centrifuged at 20,000 × g for 20 min at 4 °C. The supernatant was mixed with the 1 mL Ni-NTA slurry that was equilibrated while centrifugation, and the protein + Ni-NTA slurry mixture was tumbled for 1-1.5 h at 4 °C. The VKOR-bound Ni-NTA was collected by running through the protein and Ni-NTA slurry mixture through the column. The resin was washed with the EmpA buffer to wash out the unbound protein. The impurities were washed by flowing through 10 CV of wash buffer (EmpA with 30 mM imidazole, pH 7.8). Next, the resin was washed with 15 CV of Rinse/Exchange buffer (25 mM Na_2HPO_4, 0.2% (w/v) DPC, pH 7.8), and the protein was eluted by 10 CV of Elution buffer (25 mM Na_2HPO_4, 300 mM imidazole, 0.5% (w/v) DPC, pH 7.8).

For both inclusion body wash and membrane fraction extraction purification, the sonicated cell lysate was centrifuged at 20,000 × g for 20 min at 4 °C. To extract

membrane fraction, supernatant was collected from the first centrifugation, and was proceed for ultracentrifugation at 100,000 × g for 2 h at 4 °C. After the ultracentrifugation, the supernatant was discarded, and the pellet was resuspended with the binding buffer (25 mM Na_2HPO_4, pH 7.8) and the addition of 3 % (v/v) Empigen. The membrane fraction was tumbled at 4 °C for solubilization, and the next day, same Ni-NTA purification protocol was used. For inclusion body wash, the pellet after the first centrifugation was resuspended in lysis buffer, sonicated, and centrifuged. This cycle was repeated twice more, and the final supernatant was collected to proceed. This supernatant was continued onto the remaining purification protocol.

5.3 Results and Discussion

The Western blot analysis of hundreds of expression condition isolated a few strong candidates based on the intensity of bands. Expression of the MtVKOR was great for all the expression conditions that were tested. In general, bacterial proteins express better than the human proteins, so the expression of hVKORL1 were not as great as that of MtVKOR. Unfortunately, the expression of hVKOR was so low that this construct was not continued. For each construct, best expression conditions are summarized in Table 5.1.

Table 5.1 Summary of best expression conditions for MtVKOR, hVKOR, and hVKORL1

	MtVKOR	hVKOR	hVKORL1
Expression cell line	BL21 (DE3) Star	N/A	BL21 (DE3) CodonPlus RP
Induction [IPTG]	1.0 mM	N/A	1.0 mM

Temperature	18 °C	N/A	18 °C

For MtVKOR, many attempts had done to optimize the purification condition. Among the whole-cell extraction, inclusion body wash and membrane fraction purifications, membrane fraction purification yielded the most pure MtVKOR protein, but the yield was quite low. The second best purification was the inclusion body wash; the yield seemed to be higher than the membrane fraction purification, but the purity was also a problem. Furthermore, it seemed that a lot of protein from the inclusion body wash didn't bind to the Ni-NTA resin because a strong band was detected from the flow-through fraction (Figure 5.3, Western blot lane 9).

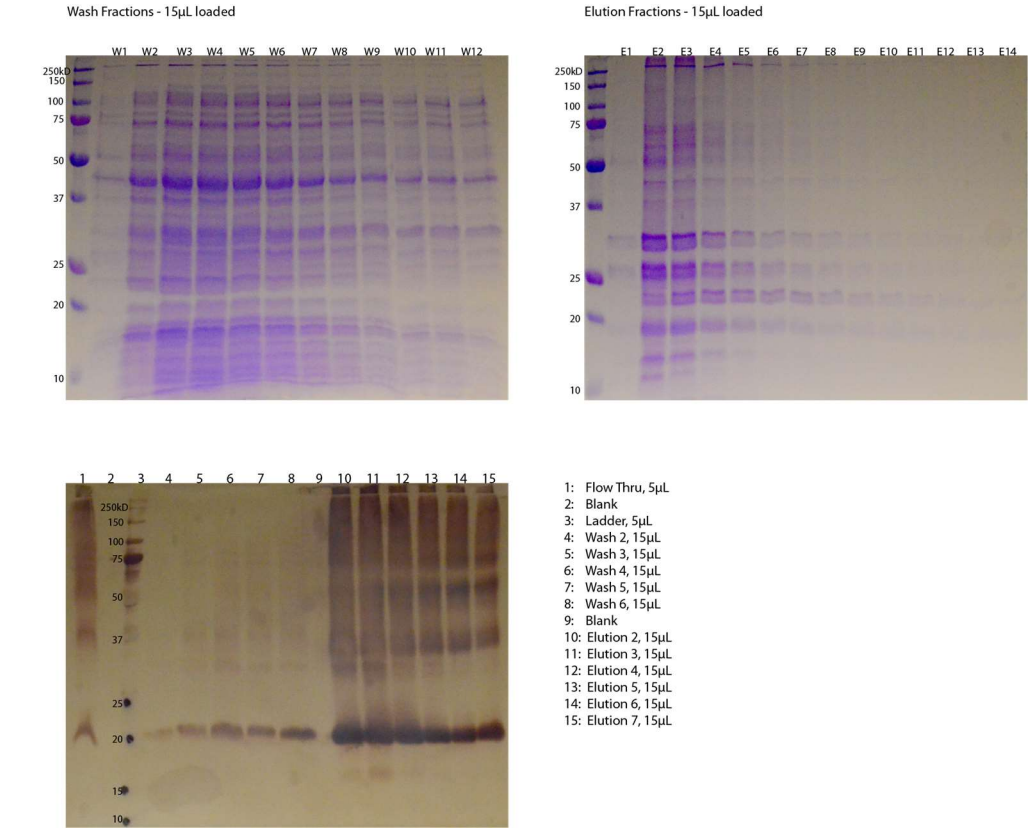

Figure 5.2 Whole cell purification of MtVKOR expressed in BL21 (DE3) Star *E. coli* competent cell line, induced with 1 mM IPTG and grown at 18 °C. The MtVKOR protein seems to exist in elution fractions, but the purity of the elution fractions was very low.

MtVKOR pET16b BL21 (DE3) Star 1.0mM IPTG 18°C - Membrane Fraction & Inclusion Body Purification (Empigen to LDAO)
Induced at OD = 0.721 Mass of Pellet = 4.52g $[imidazole]_{wash}$ = 15mM, $[imidazole]_{elution}$ = 300mM (12/21/13)

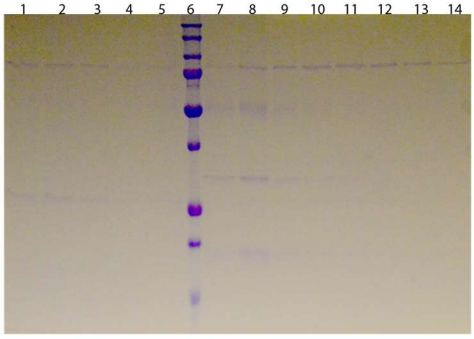

1: Membrane Fraction, Wash 1, 15µL
2: Membrane Fraction, Wash 2, 15µL
3: Membrane Fraction, Wash 3, 15µL
4: Membrane Fraction, Wash 4, 15µL
5: Membrane Fraction, Wash 5, 15µL
6: Ladder, 5µL
7: Membrane Fraction, Elution 1, 15µL
8: Membrane Fraction, Elution 2, 15µL
9: Membrane Fraction, Elution 3, 15µL
10: Membrane Fraction, Elution 4, 15µL
11: Membrane Fraction, Elution 5, 15µL
12: Membrane Fraction, Elution 6, 15µL
13: Membrane Fraction, Elution 7, 15µL
14: Membrane Fraction, Elution 8, 15µL

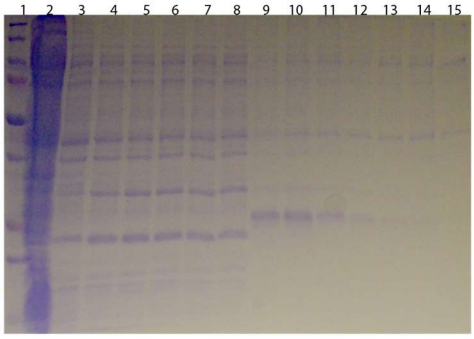

1: Ladder, 5µL
2: Inclusion Body, Flow Thru, 5µL
3: Inclusion Body, Wash 1, 15µL
4: Inclusion Body, Wash 2, 15µL
5: Inclusion Body, Wash 3, 15µL
6: Inclusion Body, Wash 4, 15µL
7: Inclusion Body, Wash 5, 15µL
8: Inclusion Body, Wash 6, 15µL
9: Inclusion Body, Elution 1, 15µL
10: Inclusion Body, Elution 2, 15µL
11: Inclusion Body, Elution 3, 15µL
12: Inclusion Body, Elution 4, 15µL
13: Inclusion Body, Elution 5, 15µL
14: Inclusion Body, Elution 6, 15µL
15: Inclusion Body, Elution 7, 15µL

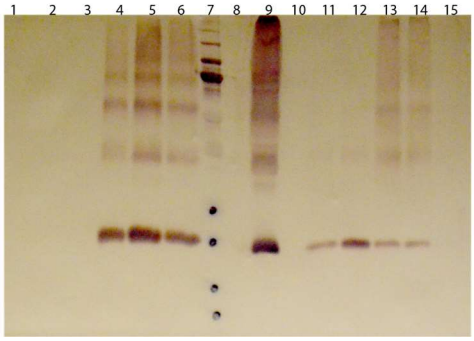

1: Membrane Fraction, Flow Thru, 5µL
2: Blank
3: Membrane Fraction, Wash 2, 15µL
4: Membrane Fraction, Elution 1, 15µL
5: Membrane Fraction, Elution 2, 15µL
6: Membrane Fraction, Elution 3, 15µL
7: Ladder, 5µL
8: Blank
9: Inclusion Body, Flow Thru, 5µL
10: Blank
11: Inclusion Body, Wash 2, 15µL
12: Inclusion Body, Wash 3, 15µL
13: Inclusion Body, Elution 1, 15µL
14: Inclusion Body, Elution 2, 15µL
15: Inclusion Body, Elution 3, 15µL

Figure 5.3 Membrane fraction and inclusion body wash purifications of MtVKOR expressed in BL21 (DE3) Star *E. coli* competent cell line, induced with 1 mM IPTG and grown at 18 °C. The elution fractions from the membrane fraction purifications seemed pure, but the yield was a lot lower compared to the whole cell extraction purification and inclusion body purification.

After the Ni-NTA affinity chromatography purifications of MtVKOR, eluted proteins were not very pure, and the yield was quite low (Figure 5.2). For MtVKOR, preliminary ^{1}H-^{15}N TROSY-HSQC spectra were collected. The detergent 1,2-diheptanoyl-sn-glycero-3-phosphocholine (DHPC) was used as the membrane mimic. A few issues with the sample were the low concentration of the sample, and the poor spectral quality (Figure 5.4). In addition, the purification results were not reproducible, and it was very costly to make a nice NMR sample to continue the project.

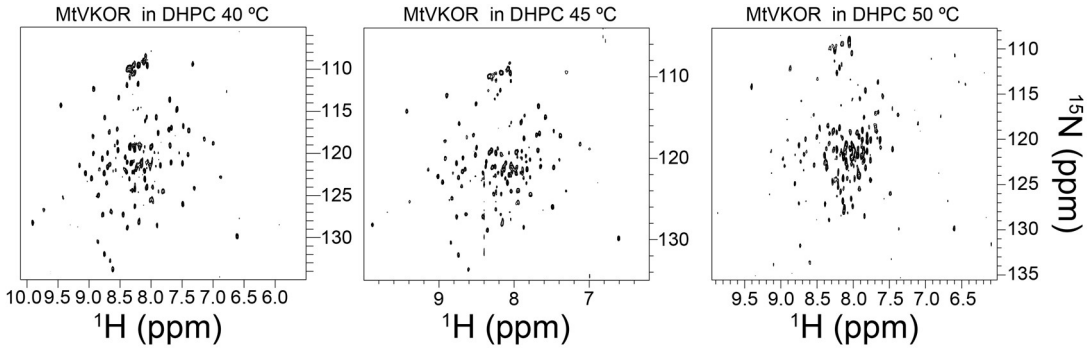

Figure 5.4 ^{1}H-^{15}N TROSY-HSQC spectra of MtVKOR in DHPC micelles. The sample was in a low concentration, therefore, to collect one spectrum, a large number of transient had to be inputted. Unfortunately, this spectrum could not be reproduced, presumably because of the challenges in protein purification.

Compared to MtVKOR, hVKORL1 seemed to be slightly easier to purify, but the expression level was a lot lower. To optimize the purification condition, the imidazole concentrations of the wash buffer were varied, but there was no significant difference from different conditions.

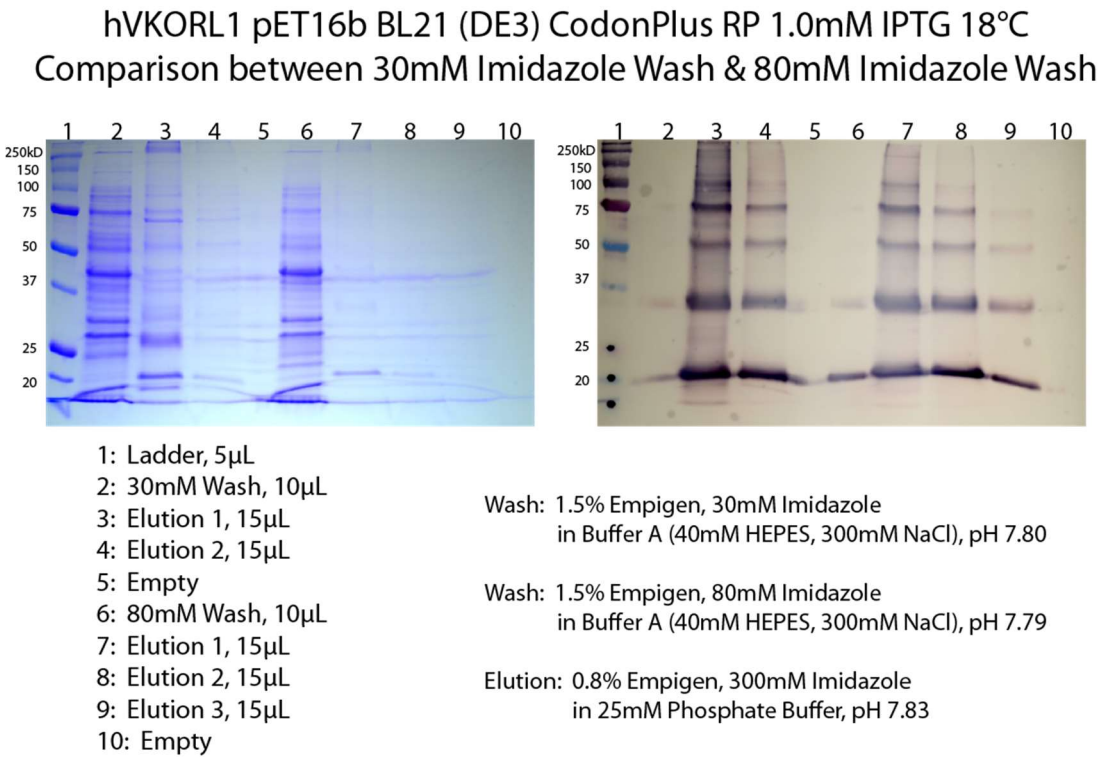

Figure 5.5 Whole cell purification of hVKORL1 expressed in BL21 (DE3) CodonPlus RP, induced with 1.0 mM IPTG, grown at 18 °C. Similar to the purifications of MtVKOR, the purity and the yield after purification were very poor.

Even though this project is very intriguing and is very worth studying, the project was progressing too slowly to be pursued further. A lot of purification conditions were tested including varying the imidazole concentration, changing the detergent for elution, changing the pH of binding and eluting, and different extraction methods. If more efforts are put into, it may be possible to get a decent amount of pure protein to continue characterize, and it will be powerful to perform NMR-detected ligand titration to determine the location of warfarin binding and the binding dissociation constants.

5.4 Supplementary materials

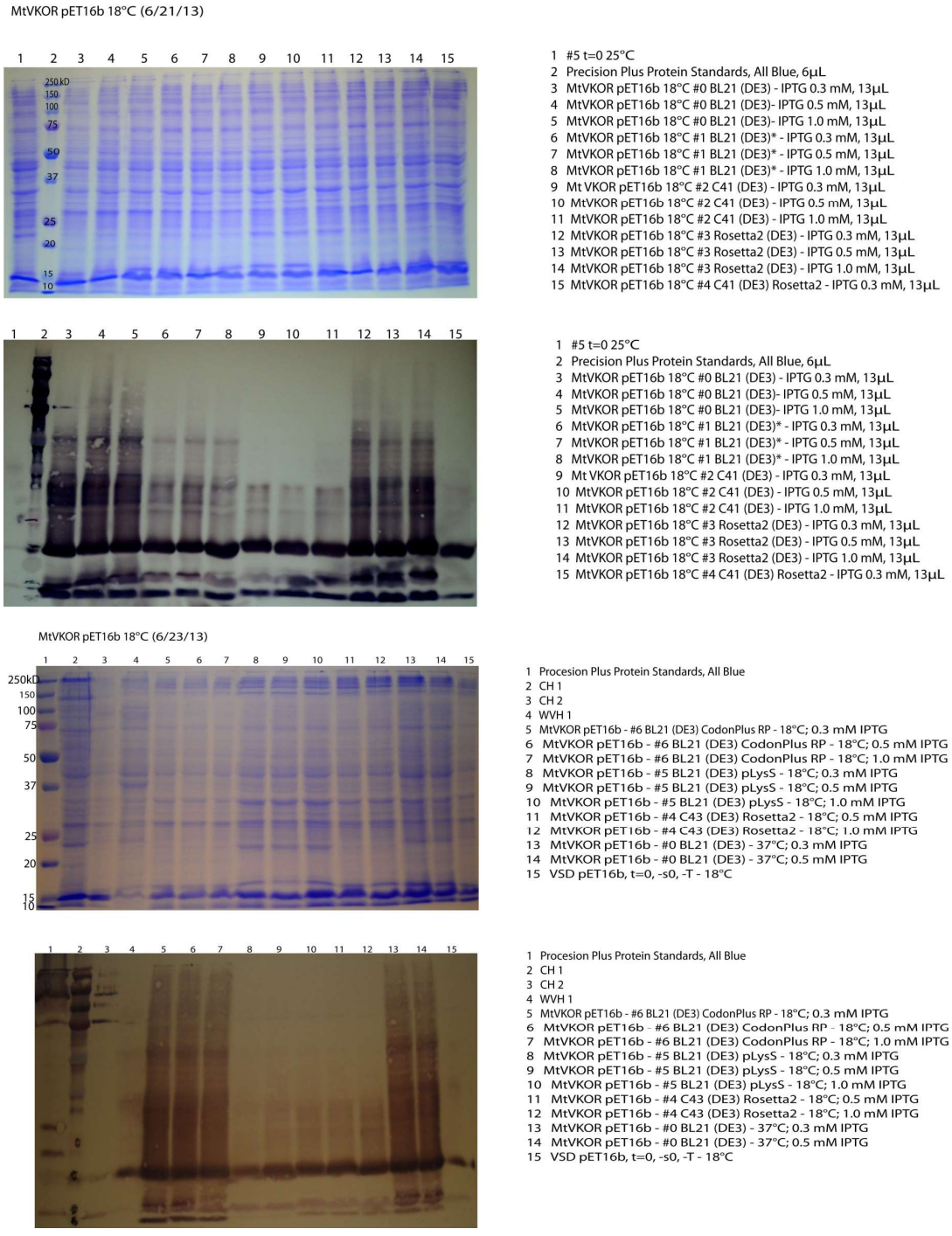

Figure S5.1 First part of expression testing of MtVKOR pET16b. A lot of conditions exhibit good expression of this protein.

MtVKOR pET16b (6/23/13)

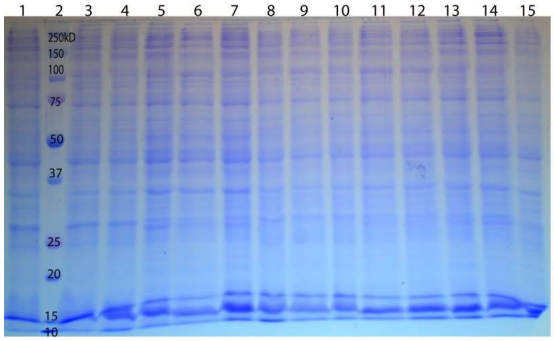

1 MtVKOR pET16b - #1 BL21 (DE3), 0.3 mM IPTG, 37°C
2 Precision Plus Protein Standards, All Blue
3 MtVKOR pET16b - #1 BL21 (DE3), 0.5 mM IPTG, 37°C
4 MtVKOR pET16b - #1 BL21 (DE3), 1.0 mM IPTG, 37°C
5 MtVKOR pET16b - #2 BL21 (DE3)*, 0.3 mM IPTG, 37°C
6 MtVKOR pET16b - #2 BL21 (DE3)*, 0.5 mM IPTG, 37°C
7 MtVKOR pET16b - #2 BL21 (DE3)*, 1.0 mM IPTG, 37°C
8 MtVKOR pET16b - #3 C41 (DE3), 0.3 mM IPTG, 37°C
9 MtVKOR pET16b - #3 C41 (DE3), 0.5 mM IPTG, 37°C
10 MtVKOR pET16b - #3 C41 (DE3), 1.0 mM IPTG, 37°C
11 MtVKOR pET16b - #4 C43 (DE3) Rosetta2, 0.3 mM IPTG, 37°C
12 MtVKOR pET16b - #4 C43 (DE3) Rosetta2, 0.5 mM IPTG, 37°C
13 MtVKOR pET16b - #4 C43 (DE3) Rosetta2, 1.0 mM IPTG, 37°C
14 MtVKOR pET16b - #5 BL21 (DE3) pLysS, 0.3 mM IPTG, 37°C
15 VSD pET16b #5 - S0, -T, 37°C

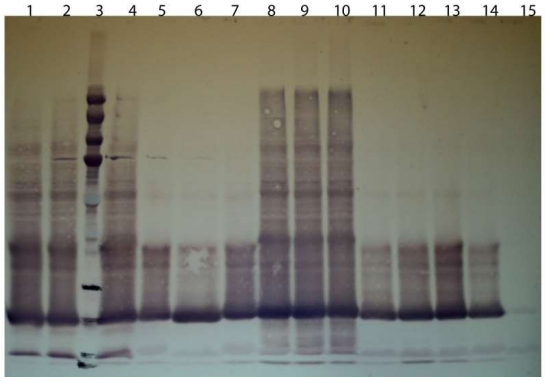

1 MtVKOR pET16b - #1 BL21 (DE3), 0.3 mM IPTG, 37°C
2 Precision Plus Protein Standards, All Blue
3 MtVKOR pET16b - #1 BL21 (DE3), 0.5 mM IPTG, 37°C
4 MtVKOR pET16b - #1 BL21 (DE3), 1.0 mM IPTG, 37°C
5 MtVKOR pET16b - #2 BL21 (DE3)*, 0.3 mM IPTG, 37°C
6 MtVKOR pET16b - #2 BL21 (DE3)*, 0.5 mM IPTG, 37°C
7 MtVKOR pET16b - #2 BL21 (DE3)*, 1.0 mM IPTG, 37°C
8 MtVKOR pET16b - #3 C41 (DE3), 0.3 mM IPTG, 37°C
9 MtVKOR pET16b - #3 C41 (DE3), 0.5 mM IPTG, 37°C
10 MtVKOR pET16b - #3 C41 (DE3), 1.0 mM IPTG, 37°C
11 MtVKOR pET16b - #4 C43 (DE3) Rosetta2, 0.3 mM IPTG, 37°C
12 MtVKOR pET16b - #4 C43 (DE3) Rosetta2, 0.5 mM IPTG, 37°C
13 MtVKOR pET16b - #4 C43 (DE3) Rosetta2, 1.0 mM IPTG, 37°C
14 MtVKOR pET16b - #5 BL21 (DE3) pLysS, 0.3 mM IPTG, 37°C
15 VSD pET16b #5 - S0, -T, 37°C

MtVKOR pET16b (6/23/13)

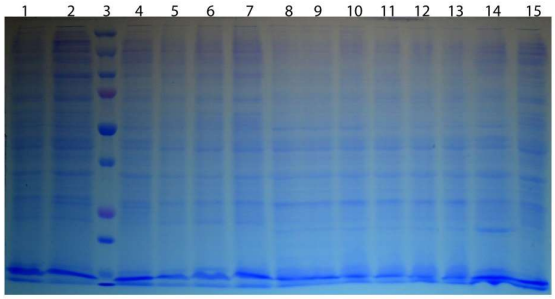

1 MtVKOR pET16b - #0 BL21 (DE3), 1.0 mM IPTG, 37°C
2 MtVKOR pET16b - #5 BL21 (DE3) pLysS, 0.5 mM IPTG, 37°C
3 Precision Plus Protein Standards, All Blue
4 MtVKOR pET16b - #5 BL21 (DE3) pLysS, 1.0 mM IPTG, 37°C
5 MtVKOR pET16b - #6 BL21 (DE3) CodonPlus RP, 0.3 mM IPTG, 37°C
6 MtVKOR pET16b - #6 BL21 (DE3) CodonPlus RP, 0.5 mM IPTG, 37°C
7 MtVKOR pET16b - #6 BL21 (DE3) CodonPlus RP, 1.0 mM IPTG, 37°C
8 MtVKOR pET16b - #0 BL21 (DE3), 0.3 mM IPTG, 25°C
9 MtVKOR pET16b - #0 BL21 (DE3), 0.5 mM IPTG, 25°C
10 MtVKOR pET16b - #0 BL21 (DE3), 1.0 mM IPTG, 25°C
11 MtVKOR pET16b - #1 BL21 (DE3)*, 1.0 mM IPTG, 25°C
12 MtVKOR pET16b - #1 BL21 (DE3)*, 1.0 mM IPTG, 25°C
13 MtVKOR pET16b - #1 BL21 (DE3)*, 1.0 mM IPTG, 25°C
14 MtVKOR pET16b - #2 C41 (DE3), 0.3 mM IPTG, 25°C
15 VSD pET16b - #5 - S0 -T 37°C

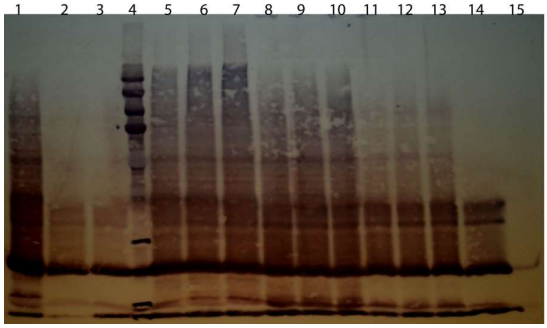

1 MtVKOR pET16b - #0 BL21 (DE3), 1.0 mM IPTG, 37°C
2 MtVKOR pET16b - #5 BL21 (DE3) pLysS, 0.5 mM IPTG, 37°C
3 MtVKOR pET16b - #5 BL21 (DE3) pLysS, 1.0 mM IPTG, 37°C
4 Precision Plus Protein Standards, All Blue
5 MtVKOR pET16b - #6 BL21 (DE3) CodonPlus RP, 0.3 mM IPTG, 37°C
6 MtVKOR pET16b - #6 BL21 (DE3) CodonPlus RP, 0.5 mM IPTG, 37°C
7 MtVKOR pET16b - #6 BL21 (DE3) CodonPlus RP, 1.0 mM IPTG, 37°C
8 MtVKOR pET16b - #0 BL21 (DE3), 0.3 mM IPTG, 25°C
9 MtVKOR pET16b - #0 BL21 (DE3), 0.5 mM IPTG, 25°C
10 MtVKOR pET16b - #0 BL21 (DE3), 1.0 mM IPTG, 25°C
11 MtVKOR pET16b - #1 BL21 (DE3)*, 1.0 mM IPTG, 25°C
12 MtVKOR pET16b - #1 BL21 (DE3)*, 1.0 mM IPTG, 25°C
13 MtVKOR pET16b - #1 BL21 (DE3)*, 1.0 mM IPTG, 25°C
14 MtVKOR pET16b - #2 C41 (DE3), 0.3 mM IPTG, 25°C
15 VSD pET16b - #5 - S0 -T 37°C

Figure S5.2 Second part of expression testing of MtVKOR pET16b.

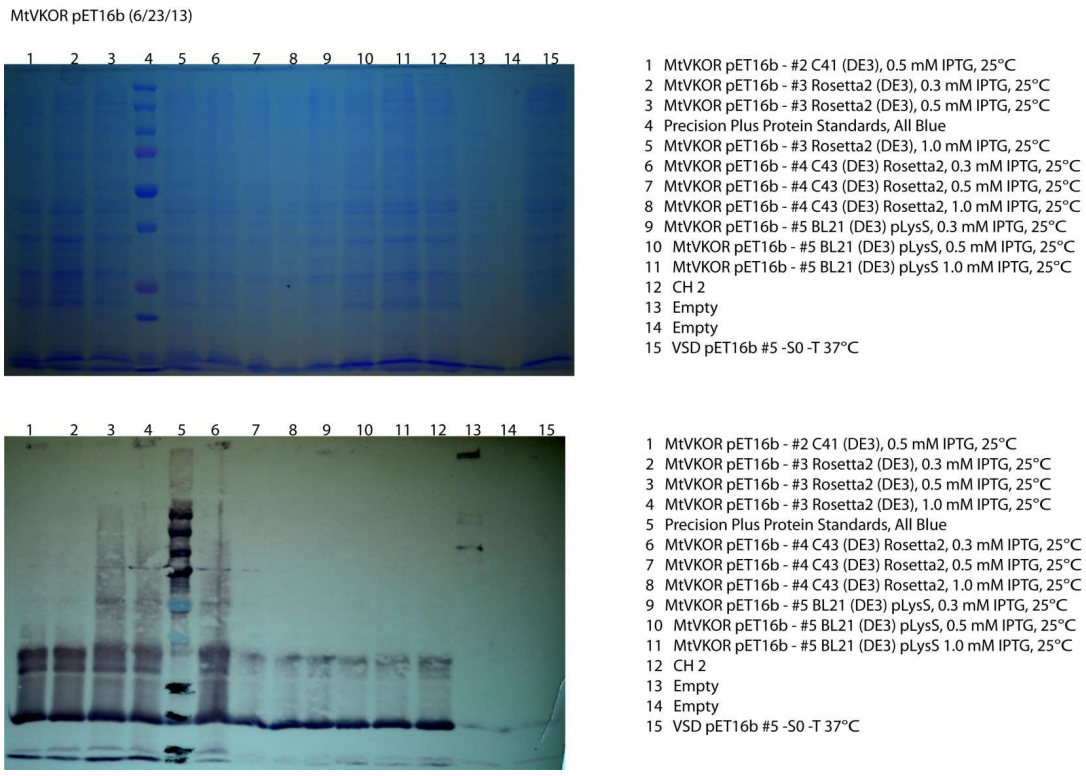

Figure S5.3 Third part of expression testing of MtVKOR pET16b. Overall, MtVKOR seems to express the best when the cells were grown at lower temperature.

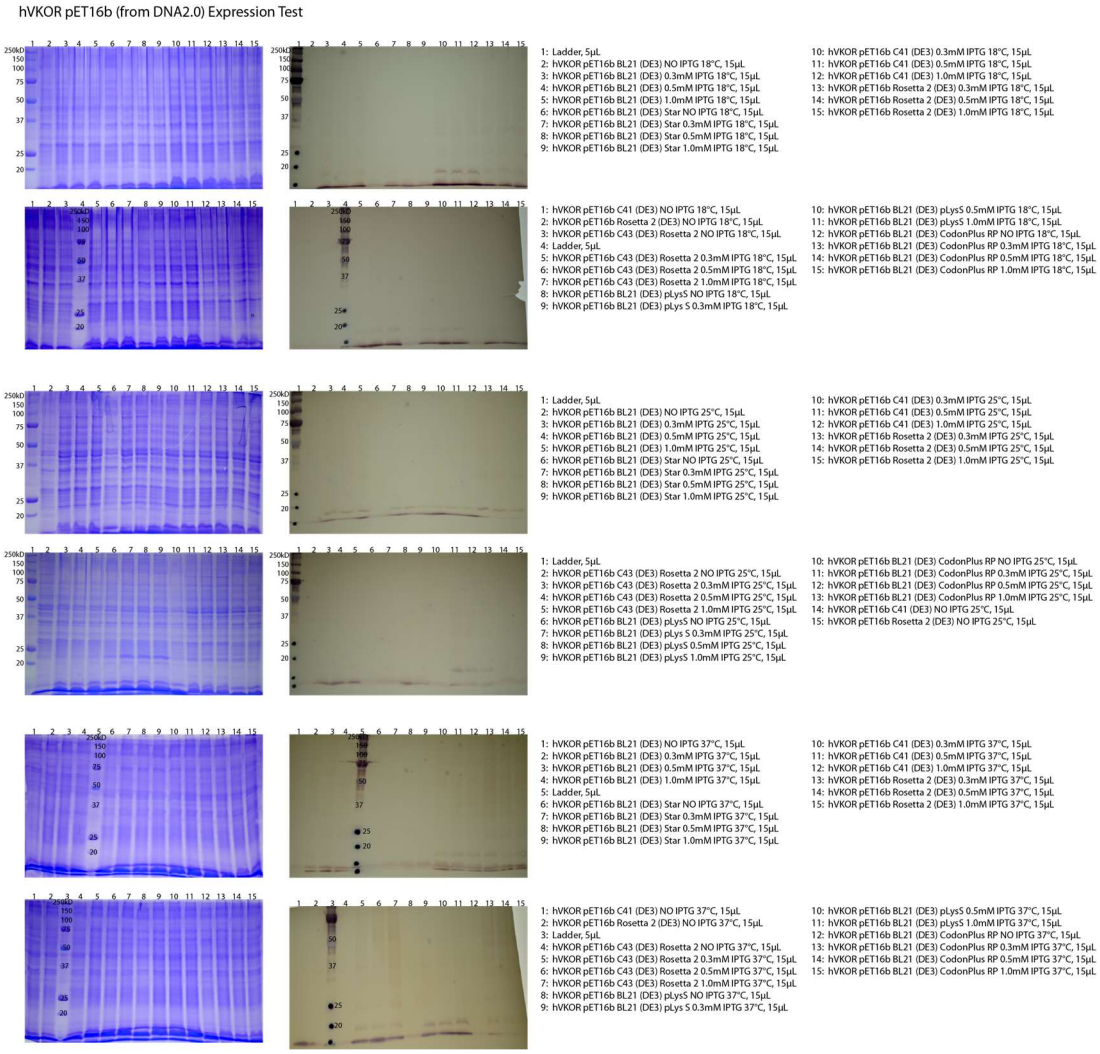

Figure S5.4 Expression testing of hVKOR pET16b. The expression of this protein in all the tested conditions was very low, and it was decided not to pursue this protein.

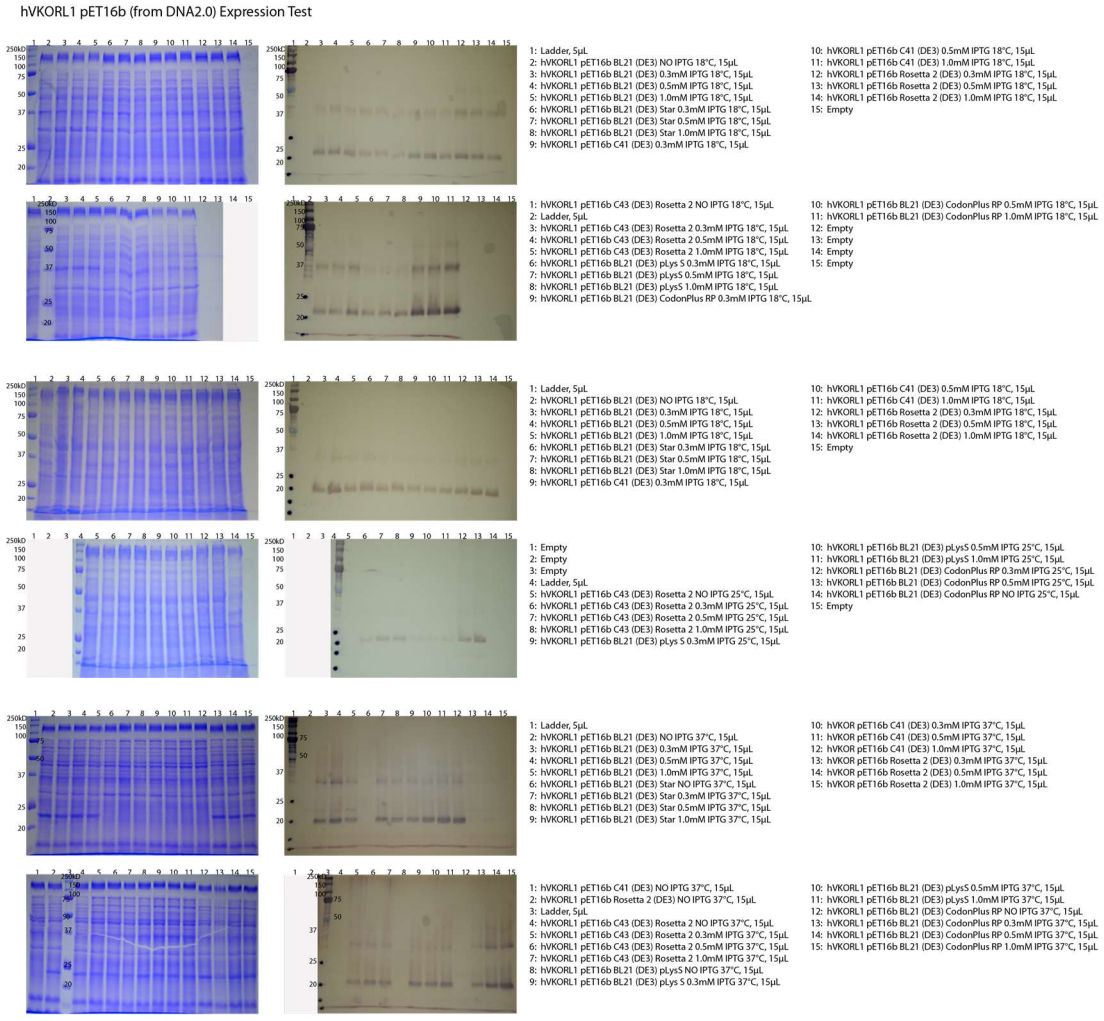

Figure S5.5 Expression testing of hVKORL1 pET16b. hVKORL1 expressed better than hVKOR and the condition BL21 (DE3) CodonPlus RP and1.0 mM IPTG at 18 °C was chosen to be the best expression condition.

5.5 References

1. Oldenburg, J., et al., The Vitamin K Cycle. 2008. **78**: p. 35-62.

2. Limdi, N.A., et al., Warfarin pharmacogenetics: a single VKORC1 polymorphism is predictive of dose across 3 racial groups. *Blood,* 2010. **115**(18): p. 3827-34.

3. Zhu, Y., et al., Estimation of warfarin maintenance dose based on VKORC1 (-1639 G>A) and CYP2C9 genotypes. *Clin Chem,* 2007. **53**(7): p. 1199-205.

4. Li, T., et al., Identification of the gene for vitamin K epoxide reductase. *Nature,* 2004. **427**(6974): p. 541-4.

5. Li, W., et al., Structure of a bacterial homologue of vitamin K epoxide reductase. *Nature,* 2010. **463**(7280): p. 507-12.

6. Wu, S., et al., Warfarin and vitamin K epoxide reductase: a molecular accounting for observed inhibition. *Blood,* 2018. **132**(6): p. 647-657.

7. Tie, J.K., D.Y. Jin, and D.W. Stafford, Human vitamin K epoxide reductase and its bacterial homologue have different membrane topologies and reaction mechanisms. *J Biol Chem,* 2012. **287**(41): p. 33945-55.

8. Van Horn, W.D., Structural and functional insights into human vitamin K epoxide reductase and vitamin K epoxide reductase-like1. *Crit Rev Biochem Mol Biol,* 2013. **48**(4): p. 357-72.

9. Shen, G., et al., Stabilization of warfarin-binding pocket of VKORC1 and VKORL1 by a peripheral region determines their different sensitivity to warfarin inhibition. *J Thromb Haemost,* 2018. **16**(6): p. 1164-1175.

10. Hammed, A., et al., VKORC1L1, an enzyme rescuing the vitamin K 2,3-epoxide reductase activity in some extrahepatic tissues during anticoagulation therapy. *J Biol Chem,* 2013. **288**(40): p. 28733-42.

11. Vermeer, C. and K. Hamulyak, Vitamin K: lessons from the past. *J Thromb Haemost,* 2004. **2**(12): p. 2115-7.

12. Wang, X., et al., Membrane topology and mutational analysis of Mycobacterium tuberculosis VKOR, a protein involved in disulfide bond formation and a homologue of human vitamin K epoxide reductase. *Antioxid Redox Signal,* 2011. **14**(8): p. 1413-20.

CHAPTER 6

CLOSING REMARKS

With the innovation of cryo-EM and technology, the functions of TRPV1 are elucidated little by little, yet, this intriguing protein still possesses unresolved mysteries. A plenty of studies in the TRPV1 research involve the functional studies of the full channel instead of working with one isolated domain of the channel. The work involving the S1-S4 transmembrane domain presented in this dissertation provides new insights into temperature and ligand activation of human TRPV1 ion channel.

Chapter 1 provides a general information about TRP channels, focusing on the thermodynamics of temperature sensing, and the ligand activation. Since this work heavily uses nuclear magnetic resonance spectroscopy, basic theory of NMR and ligand titration is described.

Chapter 2 is the overview of recently determined TRP channel structures via cryo-electron microscopy. This review focused on the allosteric modulation of TRP channels, revealed by the cryo-EM structures in diverse states induced by ligand binding. It also covers the evolutionarily perspective of TRP channels, and summarizes the gating mechanisms that have been proposed from many ligand-bound TRP structures. Finally, it addresses currently known information in temperature activation of thermoTRPs, and concludes that the core thermosensitivity of TRP channels arises from the transmembrane domain (TMD).

Chapter 3 includes the work that characterized the S1-S4 domain and investigated the role of this evolutionary domain in temperature sensing. Many groups have been

putting tremendous efforts into understanding the mechanism of thermosensation. These groups focused on different domains of TRPV1 to probe TRPV1 thermosensing mechanism, but this work focused on the S1-S4 domain, a crucial domain for ligand binding. Despite in isolation, the S1-S4 domain is in biologically relevant state in that it binds capsaicin as monitored by the solution NMR. When this domain was subjected to temperature studies, it exhibited a reversible temperature-dependent conformational change, which led to the thermodynamic studies of the S1-S4 domain. From three biophysical techniques, the changes in enthalpy were obtained and it was decided that the S1-S4 domain provides meaningful thermodynamic signature to aid channel gating. Because a wide range of temperature is accessible via NMR, temperature-dependent movement could also be detected, which could be the origin of the large thermodynamic signature. This study is the first to show the direct interaction between capsaicin and TRPV1, and is the first to attempt to understand the thermosensing mechanism using a direct biophysical and thermodynamic analysis.

In Chapter 4, the S1-S4 domain was subjected to binding studies with various chemical ligands that have been shown to be the agonists and antagonists of TRPV1. This work performed more detailed analysis on capsaicin binding. So far, the cryo-EM structure indicates there is only one capsaicin binding site, but the data presented here suggest that there may be multiple binding sites of capsaicin in the S1-S4 domain. Another possibility is that the NMR titration detected global changes in dynamics or a conformational change that is induced by capsaicin binding. A variety of ligands such as capsiate, resiniferatoxin, capsazepine, cannabinoids, lipidic molecules and ABT-102 are

tested if the binding sites of these ligands reside in the S1-S4 domain. These ligands do bind to the S1-S4 domain with different affinities, and binding sites appeared to be overlapping with slight differences. This work also explored the method to decouple the temperature activation and ligand activation. Especially for ABT-102, it inhibits the capsaicin-activated TRPV1 very efficiently, meanwhile it isn't effective against the heat-activated TRPV1. This work shows that ABT-102 binds in the S1-S4 domain, but not in the canonical vanilloid binding site, and it did not change the thermosensitivity when the temperature titration of the S1-S4 domain was performed in the presence of ABT-102. This work could open up the new avenue to find a way to decouple different modes of activation.

Chapter 5 is the work that was conducted on vitamin K epoxide reductase, a membrane protein enzyme that is the molecular target for an anticoagulant, warfarin. The goal was to express and purify the VKOR proteins from human and bacterial orthologs, but the purification was extremely challenging with very low expression. Nonetheless, a little bit of data that were collected are presented in this chapter.

From these studies, the S1-S4 domain can be further investigated for its role in temperature, ligand activation, as well as proton activation. The contribution of the S1-S4 domain in proton activation has not been explored, and it will be interesting to observe the changes in S1-S4 domain as a function of changes in pH. Currently, approximately 87% of the amide backbone of the S1-S4 domain has been assigned, and it would be useful to obtain the full assignment, along with the side chain assignment. Incorporating both temperature and ligand interaction data, more detailed analysis to decouple the

temperature- and ligand- activation would need to be achieved. With the S4-S5 linker, the thermosensitivity hasn't been studied much, and it will be helpful to get the assignment of the extra residues in the S4-S5 linker, and get some structural information from the PRE and RDC measurements. Furthermore, the involvement of the S4-S5 linker in other ligand gating would provide more detailed mechanistic insights.

REFERENCES

1. Nilius, B. and G. Owsianik, The transient receptor potential family of ion channels. *Genome Biol,* 2011. **12**(3): p. 218.

2. Hilton, J.K., M. Kim, and W.D. Van Horn, Structural and Evolutionary Insights Point to Allosteric Regulation of TRP Ion Channels. *Acc Chem Res,* 2019. **52**(6): p. 1643-1652.

3. Caterina, M.J., et al., The capsaicin receptor: a heat-activated ion channel in the pain pathway. *Nature,* 1997. **389**(6653): p. 816-24.

4. Jordt, S.E., M. Tominaga, and D. Julius, Acid potentiation of the capsaicin receptor determined by a key extracellular site. *Proc Natl Acad Sci U S A,* 2000. **97**(14): p. 8134-9.

5. Tominaga, M., et al., The Cloned Capsaicin Receptor Integrates Multiple Pain-Producing Stimuli. *Neuron,* 1998. **21**(3): p. 531-543.

6. Lukacs, V., et al., Dual regulation of TRPV1 by phosphoinositides. *J Neurosci,* 2007. **27**(26): p. 7070-80.

7. Kim, A.Y., et al., Pirt, a phosphoinositide-binding protein, functions as a regulatory subunit of TRPV1. *Cell,* 2008. **133**(3): p. 475-85.

8. Suri, A. and A. Szallasi, The emerging role of TRPV1 in diabetes and obesity. *Trends Pharmacol Sci,* 2008. **29**(1): p. 29-36.

9. Weber, L.V., et al., Expression and functionality of TRPV1 in breast cancer cells. *Breast Cancer (Dove Med Press),* 2016. **8**: p. 243-252.

10. Kim, J.H., The Emerging Role of TRPV1 in Airway Inflammation. *Allergy Asthma Immunol Res,* 2018. **10**(3): p. 187-188.

11. Yoshida, A., et al., TRPV1 is crucial for proinflammatory STAT3 signaling and thermoregulation-associated pathways in the brain during inflammation. *Sci Rep,* 2016. **6**: p. 26088.

12. Cao, E., et al., TRPV1 channels are intrinsically heat sensitive and negatively regulated by phosphoinositide lipids. *Neuron,* 2013. **77**(4): p. 667-79.

13. Feng, Q., Temperature sensing by thermal TRP channels: thermodynamic basis and molecular insights. *Curr Top Membr,* 2014. **74**: p. 19-50.

14. Yang, F., et al., Thermosensitive TRP channel pore turret is part of the temperature activation pathway. *Proc Natl Acad Sci U S A,* 2010. **107**(15): p. 7083-8.

15. Liu, B., K. Hui, and F. Qin, Thermodynamics of Heat Activation of Single Capsaicin Ion Channels VR1. *Biophysical Journal,* 2003. **85**(5): p. 2988-3006.

16. Vlachová, V., et al., Functional Role of C-Terminal Cytoplasmic Tail of Rat Vanilloid Receptor 1. *The Journal of Neuroscience,* 2003. **23**(4): p. 1340-1350.

17. Yao, J., B. Liu, and F. Qin, Kinetic and energetic analysis of thermally activated TRPV1 channels. *Biophys J,* 2010. **99**(6): p. 1743-53.

18. Clapham, D.E. and C. Miller, A thermodynamic framework for understanding temperature sensing by transient receptor potential (TRP) channels. *Proc Natl Acad Sci U S A,* 2011. **108**(49): p. 19492-7.

19. Chowdhury, S., B.W. Jarecki, and B. Chanda, A molecular framework for temperature-dependent gating of ion channels. *Cell,* 2014. **158**(5): p. 1148-1158.

20. Brauchi, S., et al., A hot-sensing cold receptor: C-terminal domain determines thermosensation in transient receptor potential channels. *J Neurosci,* 2006. **26**(18): p. 4835-40.

21. Liao, M., et al., Structure of the TRPV1 ion channel determined by electron cryo-microscopy. *Nature,* 2013. **504**(7478): p. 107-12.

22. Zhang, F., et al., Heat activation is intrinsic to the pore domain of TRPV1. *Proc Natl Acad Sci U S A,* 2018. **115**(2): p. E317-E324.

23. Liu, B. and F. Qin, Single-residue molecular switch for high-temperature dependence of vanilloid receptor TRPV3. *Proc Natl Acad Sci U S A,* 2017. **114**(7): p. 1589-1594.

24. Wen, H. and W. Zheng, Decrypting the Heat Activation Mechanism of TRPV1 Channel by Molecular Dynamics Simulation. *Biophys J,* 2018. **114**(1): p. 40-52.

25. Zaelzer, C., et al., DeltaN-TRPV1: A Molecular Co-detector of Body Temperature and Osmotic Stress. *Cell Rep,* 2015. **13**(1): p. 23-30.

26. Laursen, W.J., et al., Species-specific temperature sensitivity of TRPA1. *Temperature (Austin),* 2015. **2**(2): p. 214-26.

27. Jabba, S., et al., Directionality of temperature activation in mouse TRPA1 ion channel can be inverted by single-point mutations in ankyrin repeat six. *Neuron,* 2014. **82**(5): p. 1017-31.

28. Moparthi, L., et al., Human TRPA1 is intrinsically cold- and chemosensitive with and without its N-terminal ankyrin repeat domain. *Proc Natl Acad Sci U S A,* 2014. **111**(47): p. 16901-6.

29. Jordt, S.-E. and D. Julius, Molecular Basis for Species-Specific Sensitivity to "Hot" Chili Peppers. *Cell,* 2002. **108**(3): p. 421-430.

30. Spyridaki, A., et al., The natural product capsaicin inhibits photosynthetic electron transport at the reducing side of photosystem II and purple bacterial reaction center: structural details of capsaicin binding. *Biochimica et Biophysica Acta (BBA) - Bioenergetics,* 2000. **1459**(1): p. 69-76.

31. Gavva, N.R., et al., Molecular determinants of vanilloid sensitivity in TRPV1. *J Biol Chem,* 2004. **279**(19): p. 20283-95.

32. Cao, E., et al., TRPV1 structures in distinct conformations reveal activation mechanisms. *Nature,* 2013. **504**(7478): p. 113-8.

33. Gao, Y., et al., TRPV1 structures in nanodiscs reveal mechanisms of ligand and lipid action. *Nature,* 2016. **534**(7607): p. 347-51.

34. Yang, F., et al., Structural mechanism underlying capsaicin binding and activation of the TRPV1 ion channel. *Nat Chem Biol,* 2015. **11**(7): p. 518-524.

35. Yang, F., et al., The conformational wave in capsaicin activation of transient receptor potential vanilloid 1 ion channel. *Nat Commun,* 2018. **9**(1): p. 2879.

36. Shen, Y. and A. Bax, Protein backbone and sidechain torsion angles predicted from NMR chemical shifts using artificial neural networks. *J Biomol NMR,* 2013. **56**(3): p. 227-41.

37. Williamson, M.P., Using chemical shift perturbation to characterise ligand binding. *Prog Nucl Magn Reson Spectrosc,* 2013. **73**: p. 1-16.

38. Rohacs, T., Phosphoinositide regulation of TRP channels. *Handb Exp Pharmacol,* 2014. **223**: p. 1143-76.

39. Ciardo, M.G. and A. Ferrer-Montiel, Lipids as central modulators of sensory TRP channels. *Biochim Biophys Acta Biomembr,* 2017. **1859**(9 Pt B): p. 1615-1628.

40. Numazaki, M., et al., Direct phosphorylation of capsaicin receptor VR1 by protein kinase Cepsilon and identification of two target serine residues. *J Biol Chem,* 2002. **277**(16): p. 13375-8.

41. Bhave, G., et al., Protein kinase C phosphorylation sensitizes but does not activate the capsaicin receptor transient receptor potential vanilloid 1 (TRPV1). *Proc Natl Acad Sci U S A,* 2003. **100**(21): p. 12480-5.

42. Studer, M. and P.A. McNaughton, Modulation of single-channel properties of TRPV1 by phosphorylation. *J Physiol,* 2010. **588**(Pt 19): p. 3743-56.

43. Liu, J., et al., Phosphorylation of TRPV1 by cyclin-dependent kinase 5 promotes TRPV1 surface localization, leading to inflammatory thermal hyperalgesia. *Exp Neurol,* 2015. **273**: p. 253-62.

44. Hellwig, N., et al., Homo- and heteromeric assembly of TRPV channel subunits. *J Cell Sci,* 2005. **118**(Pt 5): p. 917-28.

45. Staruschenko, A., N.A. Jeske, and A.N. Akopian, Contribution of TRPV1-TRPA1 interaction to the single channel properties of the TRPA1 channel. *J Biol Chem,* 2010. **285**(20): p. 15167-77.

46. Bidaux, G., et al., Regulation of activity of transient receptor potential melastatin 8 (TRPM8) channel by its short isoforms. *J Biol Chem,* 2012. **287**(5): p. 2948-62.

47. Shin, Y.C., et al., TRIP database 2.0: a manually curated information hub for accessing TRP channel interaction network. *PLoS One,* 2012. **7**(10): p. e47165.

48. Hilton, J.K., et al., Understanding thermosensitive transient receptor potential channels as versatile polymodal cellular sensors. *Biochemistry,* 2015. **54**(15): p. 2401-13.

49. Hilton, J.K., et al., Phosphoinositide-interacting regulator of TRP (PIRT) has opposing effects on human and mouse TRPM8 ion channels. *J Biol Chem,* 2018. **293**(24): p. 9423-9434.

50. Montell, C. and G.M. Rubin, Molecular characterization of the drosophila trp locus: A putative integral membrane protein required for phototransduction. *Neuron,* 1989. **2**(4): p. 1313-1323.

51. Lange, M., et al., The Transient Receptor Potential (TRP) Channel Family in Colletotrichum graminicola: A Molecular and Physiological Analysis. *PLoS One,* 2016. **11**(6): p. e0158561.

52. Majhi, R.K., et al., Expression of temperature-sensitive ion channel TRPM8 in sperm cells correlates with vertebrate evolution. *PeerJ,* 2015. **3**: p. e1310.

53. Myers, B.R., Y.M. Sigal, and D. Julius, Evolution of thermal response properties in a cold-activated TRP channel. *PLoS One,* 2009. **4**(5): p. e5741.

54. Ovchinnikov, S., et al., Large-scale determination of previously unsolved protein structures using evolutionary information. *Elife,* 2015. **4**: p. e09248.

55. Nicoludis, J.M. and R. Gaudet, Applications of sequence coevolution in membrane protein biochemistry. *Biochim Biophys Acta Biomembr,* 2018. **1860**(4): p. 895-908.

56. Zubcevic, L., et al., Cryo-electron microscopy structure of the TRPV2 ion channel. *Nat Struct Mol Biol,* 2016. **23**(2): p. 180-186.

57. Hughes, T.E.T., et al., Structural basis of TRPV5 channel inhibition by econazole revealed by cryo-EM. *Nat Struct Mol Biol,* 2018. **25**(1): p. 53-60.

58. McGoldrick, L.L., et al., Opening of the human epithelial calcium channel TRPV6. *Nature,* 2018. **553**(7687): p. 233-237.

59. Autzen, H.E., et al., Structure of the human TRPM4 ion channel in a lipid nanodisc. *Science,* 2018. **359**(6372): p. 228-232.

60. Samanta, A., et al., Structural insights into the molecular mechanism of mouse TRPA1 activation and inhibition. *J Gen Physiol,* 2018. **150**(5): p. 751-762.

61. Demeuse, P., R. Penner, and A. Fleig, TRPM7 channel is regulated by magnesium nucleotides via its kinase domain. *J Gen Physiol,* 2006. **127**(4): p. 421-34.

62. Iordanov, I., et al., The proposed channel-enzyme transient receptor potential melastatin 2 does not possess ADP ribose hydrolase activity. *Elife,* 2016. **5**.

63. Bandell, M., et al., High-throughput random mutagenesis screen reveals TRPM8 residues specifically required for activation by menthol. *Nat Neurosci,* 2006. **9**(4): p. 493-500.

64. Voets, T., et al., TRPM8 voltage sensor mutants reveal a mechanism for integrating thermal and chemical stimuli. *Nat Chem Biol,* 2007. **3**(3): p. 174-82.

65. Rath, P., et al., Implications of Human Transient Receptor Potential Melastatin 8 (TRPM8) Channel Gating from Menthol Binding Studies of the Sensing Domain. *Biochemistry,* 2016. **55**(1): p. 114-24.

66. Bidaux, G., et al., Epidermal TRPM8 channel isoform controls the balance between keratinocyte proliferation and differentiation in a cold-dependent manner. *Proc Natl Acad Sci U S A,* 2015. **112**(26): p. E3345-54.

67. Yin, Y., et al., Structural basis of cooling agent and lipid sensing by the cold-activated TRPM8 channel. *Science,* 2019.

68. Takaishi, M., et al., Reciprocal effects of capsaicin and menthol on thermosensation through regulated activities of TRPV1 and TRPM8. *J Physiol Sci,* 2016. **66**(2): p. 143-55.

69. Wright, C.E., et al., Identification of the L-menthol binding site in guinea-pig lung membranes. *Br J Pharmacol,* 1998. **123**(3): p. 481-6.

70. Macpherson, L.J., et al., More than cool: promiscuous relationships of menthol and other sensory compounds. *Mol Cell Neurosci,* 2006. **32**(4): p. 335-43.

71. Karashima, Y., et al., Bimodal action of menthol on the transient receptor potential channel TRPA1. *J Neurosci,* 2007. **27**(37): p. 9874-84.

72. Colton, C.K. and M.X. Zhu, 2-Aminoethoxydiphenyl borate as a common activator of TRPV1, TRPV2, and TRPV3 channels. *Handb Exp Pharmacol,* 2007(179): p. 173-87.

73. Kovacs, G., et al., Inhibition of the human epithelial calcium channel TRPV6 by 2-aminoethoxydiphenyl borate (2-APB). *Cell Calcium,* 2012. **52**(6): p. 468-80.

74. Singh, A.K., et al., Structural bases of TRP channel TRPV6 allosteric modulation by 2-APB. *Nat Commun,* 2018. **9**(1): p. 2465.

75. Singh, A.K., L.L. McGoldrick, and A.I. Sobolevsky, Structure and gating mechanism of the transient receptor potential channel TRPV3. *Nat Struct Mol Biol,* 2018. **25**(9): p. 805-813.

76. Zubcevic, L., et al., Conformational ensemble of the human TRPV3 ion channel. *Nat Commun,* 2018. **9**(1): p. 4773.

77. Hu, H., et al., Two amino acid residues determine 2-APB sensitivity of the ion channels TRPV3 and TRPV4. *Proc Natl Acad Sci U S A,* 2009. **106**(5): p. 1626-31.

78. Zakharian, E., et al., Inorganic polyphosphate modulates TRPM8 channels. *PLoS One,* 2009. **4**(4): p. e5404.

79. Voets, T., et al., The principle of temperature-dependent gating in cold- and heat-sensitive TRP channels. *Nature,* 2004. **430**(7001): p. 748-54.

80. Gavva, N.R., et al., Transient receptor potential melastatin 8 (TRPM8) channels are involved in body temperature regulation. *Mol Pain,* 2012. **8**: p. 36.

81. Ma, S., et al., Activation of the cold-sensing TRPM8 channel triggers UCP1-dependent thermogenesis and prevents obesity. *J Mol Cell Biol,* 2012. **4**(2): p. 88-96.

82. Rossato, M., et al., Human white adipocytes express the cold receptor TRPM8 which activation induces UCP1 expression, mitochondrial activation and heat production. *Mol Cell Endocrinol,* 2014. **383**(1-2): p. 137-46.

83. Matos-Cruz, V., et al., Molecular Prerequisites for Diminished Cold Sensitivity in Ground Squirrels and Hamsters. *Cell Rep,* 2017. **21**(12): p. 3329-3337.

84. Yao, J., B. Liu, and F. Qin, Modular thermal sensors in temperature-gated transient receptor potential (TRP) channels. *Proc Natl Acad Sci U S A,* 2011. **108**(27): p. 11109-14.

85. Zheng, W. and H. Wen, Heat activation mechanism of TRPV1: New insights from molecular dynamics simulation. *Temperature,* 2019: p. 1-12.

86. Sosa-Pagan, J.O., E.S. Iversen, and J. Grandl, TRPV1 temperature activation is specifically sensitive to strong decreases in amino acid hydrophobicity. *Sci Rep,* 2017. **7**(1): p. 549.

87. Pertusa, M., et al., Critical role of the pore domain in the cold response of TRPM8 channels identified by ortholog functional comparison. *J Biol Chem,* 2018. **293**(32): p. 12454-12471.

88. Velisetty, P., et al., Expression and Purification of the Pain Receptor TRPV1 for Spectroscopic Analysis. *Sci Rep,* 2017. **7**(1): p. 9861.

89. Zagotta, W.N., et al., Measuring distances between TRPV1 and the plasma membrane using a noncanonical amino acid and transition metal ion FRET. *J Gen Physiol,* 2016. **147**(2): p. 201-16.

90. Steinberg, X., et al., Conformational dynamics in TRPV1 channels reported by an encoded coumarin amino acid. *Elife,* 2017. **6**: p. e28626.

91. Voets, T., TRP channels and thermosensation. *Handb. Exp. Pharmacol.,* 2014. **223**: p. 729-41.

92. Kim, A.Y., et al., Pirt, a phosphoinositide-binding protein, functions as a regulatory subunit of TRPV1. *Cell,* 2008. **133**(3): p. 475-85.

93. Klein, R.M., et al., Determinants of molecular specificity in phosphoinositide regulation. Phosphatidylinositol (4,5)-bisphosphate (PI(4,5)P2) is the endogenous lipid regulating TRPV1. *J Biol Chem,* 2008. **283**(38): p. 26208-16.

94. Fernandes, E.S., M.A. Fernandes, and J.E. Keeble, The functions of TRPA1 and TRPV1: moving away from sensory nerves. *Br J Pharmacol,* 2012. **166**(2): p. 510-21.

95. Julius, D., TRP channels and pain. *Annu. Rev. Cell. Dev. Biol.,* 2013. **29**: p. 355-84.

96. Moran, M.M., et al., Transient receptor potential channels as therapeutic targets. *Nat Rev Drug Discov,* 2011. **10**(8): p. 601-20.

97. Fernandes, E.S., et al., TRPV1 deletion enhances local inflammation and accelerates the onset of systemic inflammatory response syndrome. *J. Immunol.,* 2012. **188**(11): p. 5741-51.

98. Razavi, R., et al., TRPV1 sensory neurons control beta cell stress and islet inflammation in autoimmune diabetes. *Cell,* 2006. **127**(6): p. 1123-35.

99. Lee, L.Y. and Q. Gu, Role of TRPV1 in inflammation-induced airway hypersensitivity. *Curr Opin Pharmacol,* 2009. **9**(3): p. 243-9.

100. Motter, A.L. and G.P. Ahern, TRPV1-null mice are protected from diet-induced obesity. *FEBS Lett.,* 2008. **582**(15): p. 2257-62.

101. Suri, A. and A. Szallasi, The emerging role of TRPV1 in diabetes and obesity. *Trends Pharmacol Sci,* 2008. **29**(1): p. 29-36.

102. Riera, C.E., et al., TRPV1 pain receptors regulate longevity and metabolism by neuropeptide signaling. *Cell,* 2014. **157**(5): p. 1023-36.

103. Mistretta, F., et al., Bladder cancer and urothelial impairment: the role of TRPV1 as potential drug target. *Biomed Res Int,* 2014. **2014**: p. 987149.

104. Stock, K., et al., Neural precursor cells induce cell death of high-grade astrocytomas through stimulation of TRPV1. *Nat. Med.,* 2012. **18**(8): p. 1232-8.

105. Sutton, K.G., et al., Functional characterisation of the S512Y mutant vanilloid human TRPV1 receptor. *Br J Pharmacol,* 2005. **146**(5): p. 702-11.

106. Hanson, S.M., et al., Capsaicin interaction with TRPV1 channels in a lipid bilayer: molecular dynamics simulation. *Biophys J,* 2015. **108**(6): p. 1425-34.

107. Lolicato, M., et al., Transmembrane helix straightening and buckling underlies activation of mechanosensitive and thermosensitive K(2P) channels. *Neuron,* 2014. **84**(6): p. 1198-212.

108. Greenfield, N.J., Using circular dichroism collected as a function of temperature to determine the thermodynamics of protein unfolding and binding interactions. *Nat. Protoc.,* 2006. **1**(6): p. 2527-35.

109. Royer, C.A., Probing protein folding and conformational transitions with fluorescence. *Chem Rev,* 2006. **106**(5): p. 1769-84.

110. Shen, Y. and A. Bax, Protein structural information derived from NMR chemical shift with the neural network program TALOS-N. *Methods Mol Biol,* 2015. **1260**: p. 17-32.

111. Asakura, T., et al., The relationship between amide proton chemical shifts and secondary structure in proteins. *J Biomol NMR,* 1995. **6**(3): p. 227-36.

112. Zhou, N.E., et al., Relationship between amide proton chemical shifts and hydrogen bonding in amphipathic .alpha.-helical peptides. *Journal of the American Chemical Society,* 1992. **114**(11): p. 4320-4326.

113. Shenkarev, Z.O., et al., NMR structural and dynamical investigation of the isolated voltage-sensing domain of the potassium channel KvAP: implications for voltage gating. *J Am Chem Soc,* 2010. **132**(16): p. 5630-7.

114. Mesleh, M.F., et al., Dipolar waves map the structure and topology of helices in membrane proteins. *J Am Chem Soc,* 2003. **125**(29): p. 8928-35.

115. Baxter, N.J. and M.P. Williamson, Temperature dependence of 1H chemical shifts in proteins. *Journal of Biomolecular NMR,* 1997. **9**(4): p. 359-369.

116. Doyle, C.M., et al., Concurrent Increases and Decreases in Local Stability and Conformational Heterogeneity in Cu, Zn Superoxide Dismutase Variants Revealed by Temperature-Dependence of Amide Chemical Shifts. *Biochemistry,* 2016. **55**(9): p. 1346-61.

117. Lee, D., et al., Effective rotational correlation times of proteins from NMR relaxation interference. *J Magn Reson,* 2006. **178**(1): p. 72-6.

118. Ryu, S., et al., Uncoupling proton activation of vanilloid receptor TRPV1. *J Neurosci,* 2007. **27**(47): p. 12797-807.

119. Boukalova, S., et al., Conserved residues within the putative S4-S5 region serve distinct functions among thermosensitive vanilloid transient receptor potential (TRPV) channels. *J. Biol. Chem.,* 2010. **285**(53): p. 41455-62.

120. Vandewauw, I., et al., A TRP channel trio mediates acute noxious heat sensing. *Nature,* 2018. **555**(7698): p. 662-666.

121. Laursen, W.J., et al., Low-cost functional plasticity of TRPV1 supports heat tolerance in squirrels and camels. *Proc Natl Acad Sci U S A,* 2016. **113**(40): p. 11342-11347.

122. Paramonov, A.S., et al., NMR investigation of the isolated second voltage-sensing domain of human Nav1.4 channel. *Biochim Biophys Acta Biomembr,* 2017. **1859**(3): p. 493-506.

123. Butterwick, J.A. and R. MacKinnon, Solution structure and phospholipid interactions of the isolated voltage-sensor domain from KvAP. *J Mol Biol,* 2010. **403**(4): p. 591-606.

124. Peng, D., et al., Purification and structural study of the voltage-sensor domain of the human KCNQ1 potassium ion channel. *Biochemistry,* 2014. **53**(12): p. 2032-42.

125. Ng, H.Q., et al., Purification and structural characterization of the voltage-sensor domain of the hERG potassium channel. *Protein Expr Purif,* 2012. **86**(2): p. 98-104.

126. Takeshita, K., et al., X-ray crystal structure of voltage-gated proton channel. *Nat Struct Mol Biol,* 2014. **21**(4): p. 352-7.

127. Hazan, A., et al., The pain receptor TRPV1 displays agonist-dependent activation stoichiometry. *Sci Rep,* 2015. **5**: p. 12278.

128. Singh, A.K., et al., Mechanism of calmodulin inactivation of the calcium-selective TRP channel TRPV6. *Sci Adv,* 2018. **4**(8): p. eaau6088.

129. Huynh, K.W., et al., Structure of the full-length TRPV2 channel by cryo-EM. *Nat Commun,* 2016. **7**: p. 11130.

130. Boukalova, S., J. Teisinger, and V. Vlachova, Protons stabilize the closed conformation of gain-of-function mutants of the TRPV1 channel. *Biochim Biophys Acta,* 2013. **1833**(3): p. 520-8.

131. Lomize, M.A., et al., OPM database and PPM web server: resources for positioning of proteins in membranes. *Nucleic Acids Res,* 2012. **40**(Database issue): p. D370-6.

132. Vriens, J., et al., Determinants of 4 alpha-phorbol sensitivity in transmembrane domains 3 and 4 of the cation channel TRPV4. *J Biol Chem,* 2007. **282**(17): p. 12796-803.

133. Ammann, C., P. Meier, and A. Merbach, A simple multinuclear NMR thermometer. *Journal of Magnetic Resonance (1969),* 1982. **46**(2): p. 319-321.

134. Vranken, W.F., et al., The CCPN data model for NMR spectroscopy: development of a software pipeline. *Proteins,* 2005. **59**(4): p. 687-96.

135. Bond, C.S. and A.W. Schuttelkopf, ALINE: a WYSIWYG protein-sequence alignment editor for publication-quality alignments. *Acta Crystallogr D Biol Crystallogr,* 2009. **65**(Pt 5): p. 510-2.

136. Delaglio, F., et al., NMRPipe: a multidimensional spectral processing system based on UNIX pipes. *J Biomol NMR,* 1995. **6**(3): p. 277-93.

137. Gautier, A., et al., Structure determination of the seven-helix transmembrane receptor sensory rhodopsin II by solution NMR spectroscopy. *Nature Struct. Mol. Biol.,* 2010. **17**(6): p. 768-74.

138. Iwahara, J., C. Tang, and G. Marius Clore, Practical aspects of (1)H transverse paramagnetic relaxation enhancement measurements on macromolecules. *J. Magn. Reson.,* 2007. **184**(2): p. 185-95.

139. Van Horn, W.D., et al., The impact of window functions on NMR-based paramagnetic relaxation enhancement measurements in membrane proteins. *Biochim Biophys Acta,* 2010. **1798**(2): p. 140-9.

140. Veglia, G., et al., Deuterium/Hydrogen Exchange Factors Measured by Solution Nuclear Magnetic Resonance Spectroscopy as Indicators of the Structure and Topology of Membrane Proteins. *Biophysical Journal,* 2002. **82**(4): p. 2176-2183.

141. Fitzkee, N.C. and A. Bax, Facile measurement of (1)H-(1)5N residual dipolar couplings in larger perdeuterated proteins. *J Biomol NMR,* 2010. **48**(2): p. 65-70.

142. Mascioni, A. and G. Veglia, Theoretical analysis of residual dipolar coupling patterns in regular secondary structures of proteins. *J Am Chem Soc,* 2003. **125**(41): p. 12520-6.

143. Mesleh, M.F., et al., Dipolar waves as NMR maps of protein structure. *Journal of the American Chemical Society,* 2002. **124**(16): p. 4206-4207.

144. Royer, C.A., C.J. Mann, and C.R. Matthews, Resolution of the fluorescence equilibrium unfolding profile of trp aporepressor using single tryptophan mutants. *Protein Sci,* 1993. **2**(11): p. 1844-52.

145. Cavanagh, J.F., W. J.; Palmer III, A. G.; Rance, M.; Skelton, N. J., *Protein NMR Spectroscopy: Principles and Practice (Second Edition)*. 2007: Elsevier Academic Press.

146. Privalov, P.L. and S.A. Potekhin, Scanning microcalorimetry in studying temperature-induced changes in proteins. *Methods Enzymol.,* 1986. **131**: p. 4-51.

147. Prabhu, N.V. and K.A. Sharp, Heat capacity in proteins. *Annu. Rev. Phys. Chem.,* 2005. **56**: p. 521-48.

148. Jara-Oseguera, A., S. Simon, and T. Rosenbaum, TRPV1: On the Road to Pain Relief. *Current Molecular Pharmacology,* 2008. **1**(3): p. 255-269.

149. Szallasi, A., F. Cruz, and P. Geppetti, TRPV1: a therapeutic target for novel analgesic drugs? *Trends Mol Med,* 2006. **12**(11): p. 545-54.

150. O'Neill, J., et al., Unravelling the mystery of capsaicin: a tool to understand and treat pain. *Pharmacol Rev,* 2012. **64**(4): p. 939-71.

151. Brandt, M.R., C.E. Beyer, and S.M. Stahl, TRPV1 Antagonists and Chronic Pain: Beyond Thermal Perception. *Pharmaceuticals (Basel),* 2012. **5**(2): p. 114-32.

152. Brito, R., et al., TRPV1: A Potential Drug Target for Treating Various Diseases. *Cells,* 2014. **3**(2): p. 517-45.

153. Surowy, C.S., et al., (R)-(5-tert-butyl-2,3-dihydro-1H-inden-1-yl)-3-(1H-indazol-4-yl)-urea (ABT-102) blocks polymodal activation of transient receptor potential vanilloid 1 receptors in vitro and heat-evoked firing of spinal dorsal horn neurons in vivo. *J Pharmacol Exp Ther,* 2008. **326**(3): p. 879-88.

154. Varga, A., et al., Effects of the novel TRPV1 receptor antagonist SB366791 in vitro and in vivo in the rat. *Neurosci Lett,* 2005. **385**(2): p. 137-42.

155. Garami, A., et al., Contributions of different modes of TRPV1 activation to TRPV1 antagonist-induced hyperthermia. *J Neurosci,* 2010. **30**(4): p. 1435-40.

156. Iida, T., et al., TRPV1 activation and induction of nociceptive response by a non-pungent capsaicin-like compound, capsiate. *Neuropharmacology,* 2003. **44**(7): p. 958-967.

157. De Petrocellis, L., et al., Effects of cannabinoids and cannabinoid-enriched Cannabis extracts on TRP channels and endocannabinoid metabolic enzymes. *Br J Pharmacol,* 2011. **163**(7): p. 1479-94.

158. Garami, A., et al., Transient Receptor Potential Vanilloid 1 Antagonists Prevent Anesthesia-induced Hypothermia and Decrease Postincisional Opioid Dose Requirements in Rodents. *Anesthesiology,* 2017. **127**(5): p. 813-823.

159. Muller, C., P. Morales, and P.H. Reggio, Cannabinoid Ligands Targeting TRP Channels. *Front Mol Neurosci,* 2018. **11**: p. 487.

160. Mathivanan, S., et al., Effect of econazole and benzydamine on sensory neurons in culture. *J Physiol Pharmacol,* 2016. **67**(6): p. 851-858.

161. Hu, H.Z., et al., 2-aminoethoxydiphenyl borate is a common activator of TRPV1, TRPV2, and TRPV3. *J Biol Chem,* 2004. **279**(34): p. 35741-8.

162. Jensen, M.O., et al., Mechanism of voltage gating in potassium channels. *Science,* 2012. **336**(6078): p. 229-33.

163. Kim, M., et al., Evidence that the TRPV1 S1-S4 Membrane Domain Contributes to Thermosensing. 2019.

164. Van Horn, W.D., et al., Solution nuclear magnetic resonance structure of membrane-integral diacylglycerol kinase. *Science,* 2009. **324**(5935): p. 1726-9.

165. Vieira, E.D., L.G. Basso, and A.J. Costa-Filho, Non-linear van't Hoff behavior in pulmonary surfactant model membranes. *Biochim Biophys Acta Biomembr,* 2017. **1859**(6): p. 1133-1143.

166. Horovitz, A., Double-mutant cycles: a powerful tool for analyzing protein structure and function. *Folding and Design,* 1996. **1**(6): p. R121-R126.

167. Pumroy, R.A., et al., Molecular mechanism of TRPV2 channel modulation by cannabidiol. *Elife,* 2019. **8**.

168. Grouleff, J., et al., The influence of cholesterol on membrane protein structure, function, and dynamics studied by molecular dynamics simulations. *Biochim Biophys Acta,* 2015. **1848**(9): p. 1783-95.

169. Lippincott-Schwartz, J. and R.D. Phair, Lipids and cholesterol as regulators of traffic in the endomembrane system. *Annu Rev Biophys,* 2010. **39**: p. 559-78.

170. Morales-Lazaro, S.L. and T. Rosenbaum, Cholesterol as a Key Molecule That Regulates TRPV1 Channel Function. *Adv Exp Med Biol,* 2019. **1135**: p. 105-117.

171. Picazo-Juarez, G., et al., Identification of a binding motif in the S5 helix that confers cholesterol sensitivity to the TRPV1 ion channel. *J Biol Chem,* 2011. **286**(28): p. 24966-76.

172. Duan, J., et al., Structure of full-length human TRPM4. *Proc Natl Acad Sci U S A,* 2018. **115**(10): p. 2377-2382.

173. Di Scala, C., et al., Relevance of CARC and CRAC Cholesterol-Recognition Motifs in the Nicotinic Acetylcholine Receptor and Other Membrane-Bound Receptors. *Curr Top Membr,* 2017. **80**: p. 3-23.

174. Bevan, S., et al., Capsazepine: a competitive antagonist of the sensory neurone excitant capsaicin. *Br J Pharmacol,* 1992. **107**(2): p. 544-52.

175. Geppetti, P. and M. Trevisani, Activation and sensitisation of the vanilloid receptor: role in gastrointestinal inflammation and function. *Br J Pharmacol,* 2004. **141**(8): p. 1313-20.

176. Arai, M., J.C. Ferreon, and P.E. Wright, Quantitative analysis of multisite protein-ligand interactions by NMR: binding of intrinsically disordered p53 transactivation subdomains with the TAZ2 domain of CBP. *J Am Chem Soc,* 2012. **134**(8): p. 3792-803.

177. Oldenburg, J., et al., The Vitamin K Cycle. 2008. **78**: p. 35-62.

178. Limdi, N.A., et al., Warfarin pharmacogenetics: a single VKORC1 polymorphism is predictive of dose across 3 racial groups. *Blood,* 2010. **115**(18): p. 3827-34.

179. Zhu, Y., et al., Estimation of warfarin maintenance dose based on VKORC1 (-1639 G>A) and CYP2C9 genotypes. *Clin Chem,* 2007. **53**(7): p. 1199-205.

180. Li, T., et al., Identification of the gene for vitamin K epoxide reductase. *Nature,* 2004. **427**(6974): p. 541-4.

181. Li, W., et al., Structure of a bacterial homologue of vitamin K epoxide reductase. *Nature,* 2010. **463**(7280): p. 507-12.

182. Wu, S., et al., Warfarin and vitamin K epoxide reductase: a molecular accounting for observed inhibition. *Blood,* 2018. **132**(6): p. 647-657.

183. Tie, J.K., D.Y. Jin, and D.W. Stafford, Human vitamin K epoxide reductase and its bacterial homologue have different membrane topologies and reaction mechanisms. *J Biol Chem,* 2012. **287**(41): p. 33945-55.

184. Van Horn, W.D., Structural and functional insights into human vitamin K epoxide reductase and vitamin K epoxide reductase-like1. *Crit Rev Biochem Mol Biol,* 2013. **48**(4): p. 357-72.

185. Shen, G., et al., Stabilization of warfarin-binding pocket of VKORC1 and VKORL1 by a peripheral region determines their different sensitivity to warfarin inhibition. *J Thromb Haemost,* 2018. **16**(6): p. 1164-1175.

186. Hammed, A., et al., VKORC1L1, an enzyme rescuing the vitamin K 2,3-epoxide reductase activity in some extrahepatic tissues during anticoagulation therapy. *J Biol Chem,* 2013. **288**(40): p. 28733-42.

187. Vermeer, C. and K. Hamulyak, Vitamin K: lessons from the past. *J Thromb Haemost,* 2004. **2**(12): p. 2115-7.

188. Wang, X., et al., Membrane topology and mutational analysis of Mycobacterium tuberculosis VKOR, a protein involved in disulfide bond formation and a homologue of human vitamin K epoxide reductase. *Antioxid Redox Signal,* 2011. **14**(8): p. 1413-20.

APPENDIX A

PUBLISHED PORTIONS

Two portions of this dissertation have been previously published. These portions were included with permission from all co-authors.

Chapter 2:

Reproduced with permission from Hilton, J. K., Kim, M., and Van Horn, W. D. Structural and Evolutionary Insights Point to Allosteric Regulation of TRP Ion Channels. *Acc Chem Res* 2019, 52(6):1643-1652. Copyright 2019 American Chemical Society.

Chapter 3:

This study was originally published in bioRxiv preprint server., and this chapter is reproduced with permission from all co-authors.
Kim, M., et al., Evidence that the TRPV1 S1-S4 Membrane Domain Contributes to Thermosensing. 2019. https://doi.org/10.1101/711499